Titre: Title:	Experimental study of small-scaling effects on the mechanical behavior of coarse granular materials
Auteur: Author:	Gilbert Girumugisha
Date:	2025
Type:	Mémoire ou thèse / Dissertation or Thesis
Référence: Citation:	Girumugisha, G. (2025). Experimental study of small-scaling effects on the mechanical behavior of coarse granular materials [Thèse de doctorat, Polytechnique Montréal]. PolyPublie. https://publications.polymtl.ca/65790/

POLYTECHNIQUE MONTRÉAL
affiliée à l'Université de Montréal

Experimental study of small-scaling effects on the mechanical behavior of coarse granular materials

GILBERT GIRUMUGISHA
Département de génie civil, géologique, et des mines

Thèse présentée en vue de l'obtention du diplôme de *Philosophiæ Doctor*
Génie minéral

Avril 2025

POLYTECHNIQUE MONTRÉAL
affiliée à l'Université de Montréal

Cette thèse intitulée :

Experimental study of small-scaling effects on the mechanical behavior of coarse granular materials

présentée par **Gilbert GIRUMUGISHA**
en vue de l'obtention du diplôme de *Philosophiæ Doctor*
a été dûment acceptée par le jury d'examen constitué de :

Li LI, président
Carlos OVALLE, membre et directeur de recherche
Hans Henning STUTZ, membre et codirecteur de recherche
Michel AUBERTIN, membre
Gonzalo ZAMBRANO NARVAEZ, membre externe

DEDICATION

À mon père et à ma mère,
À mes frères Thierry et Jimmy, et ma soeur Josiane,
–Votre fils et votre frère.

À ma fiancée Winnie I.,
–Ton fiancé.

Finally, to the reader,
–Enjoy at its best!

ACKNOWLEDGEMENTS

Chaque fois que je me sentais épuisé ces mots retentissaient en voix haute:

> *Ceux qui sèment avec larmes moissonneront avec chants d'allégresse. Celui qui marche en pleurant, quand il porte la semence, revient avec allégresse, quand il porte ses gerbes.*
> *–Psaume 126:5,6.*

J'en suis très reconnaissant pour l'encouragement tiré et envers celles et ceux qui ont rendu paisible cette aventure.

Je saisis cette occasion pour exprimer ma profonde gratitude au Professeur Carlos OVALLE, mon directeur de recherche, pour son mentorat, ses conseils, son accompagnement, son temps, son leadership, sa confiance, sa patience, ainsi que pour l'exposition académique et professionnelle qu'il m'a offerte — sans laquelle cette thèse n'aurait pas vu le jour. *¡Gracias!*

I want to thank Professor Hans Henning STUTZ, my co-supervisor, for the opportunity to work together and his insightful feedback throughout the course of the project. *Vielen Danke für alles!*

J'adresse mes remerciements au Professeur Li LI pour avoir accepté de présider le jury de ma soutenance de thèse. Je suis particulièrement reconnaissant au Professeur émérite Michel AUBERTIN ainsi qu'au Professeur Gonzalo ZAMBRANO NARVAEZ pour le temps consacré, leurs commentaires, et leur disponibilité à siéger comme membres du jury de ma thèse doctorale. *Merci !*

Je remercie chaleureusement Dr. Serge OUELLET de la Mine Canadian Malartic pour sa collaboration, ses échanges, ses précieux conseils, et pour m'avoir offert l'excellente opportunité de réaliser des expérimentations in situ sous sa direction. Je suis également reconnaissant envers M. Gabriel CAYA, ing., et M. Sylvain OUELLET, ing., pour leur soutien remarquable lors de la campagne de tests in situ, ainsi qu'à Mme Elsa Maria MONGO, ing., pour avoir capté d'excellentes photographies adaptées à la publication.

To Mr. Holger REITH, Mrs. Pia GÖLZ, Mr. Nebil DEMIRAL and Mr. Henning BOROWSKI, for the technical support during my stay in Germany. *Dankeschön!*

To the Noltze family, Hedi NOLTZE, Dr. Achim NOLTZE and Pascal NOLTZE, for hosting and giving me a family experience during my stay in Germany. Thank you for allowing me to fully experience Germany, for integrating me, and for the Rummy! *Ich vermisse Sie!*

I would also like to thank all my colleagues at Polytechnique Montréal and KIT for the engaging table talks and the lasting souvenirs. My sincere gratitude goes to the GMMG team members—Paula, Florian, Quyen, Carolina, Zahra, Sergio, David, and Lina—as well as to my officemates Yuyu, Samy, and Santiago, and our friendly neighbors: Khawla, Arij, Zahia, Sirine, Madison, Ilhem, Afaf, Wiem, Karine, Abu, Hamed, and Sadjat. A special thanks to Florian BEHLKE for his impactful advice during my writing process and data organization, and to Karim POUYE for his valuable contributions during his internship. I am also grateful to Bereket and Carlos at KIT for their support. Finally, I truly thank Noura El-HARRACK, Monica MONZON, and Patrick BERNÈCHE for their invaluable technical assistance.

To my loving fiancée WINNIE, for her unwavering love, trust, support, prayers and encouragement, and the continual support of her family. *Ndabigushimira, asante sana!*

To my FAMILY, for the inherited bravery, for whispering encouragements, showing love, support, and solidarity from far away. Mostly for the echoing proverbial tone from my parents–*Umugisha uhora uhishe abahanga bakawushakisha!*–suggesting that true blessings or good fortune are not easily found, even by the wise, and must be sought with effort.

Lastly, I extend my deepest gratitude to my extended ecclesiastical family for your prayers and unwavering support: the Tuyizere family, Grandma Margaret, Grandma Évelyne, Pastor & Sister Cousins, Godspower, John, Mugisha, Andy, Guy, Priscilla, Shem, Derrick, Azarias, Tito, Nestor, Kevin, Arnold, Auntie Pat, and the Seaman family in France, and Gloria and the Veclici family in Germany. Thank you all—*we are finally there!*

This research study was possible thanks to the financial support of the Canadian Malartic Mine, the Mitacs Globalink scholarship [Ref. FR118496], the Institute of Soil Mechanics and Rock Mechanics (IBF) at Karlsruhe Institute of Technology, the Natural Sciences and Engineering Research Council of Canada (NSERC) [Ref. RGPIN-2019-06118], the *Fonds de recherche du Québec - Nature et technologies* (FRQNT) through the *Programme de recherche en partenariat sur le développement durable du secteur minier-II* [Ref. 2020-MN-281267] and the industrial partners of the Research Institute on Mines and the Environment (RIME) (http://www.irme.ca/en).

RÉSUMÉ

Pour effectuer des analyses de stabilité des haldes à stériles miniers, il est essentiel de caractériser la résistance critique au cisaillement des roches stériles. Cependant, la présence de fragments rocheux surdimensionnés limite les essais de cisaillement à de petites éprouvettes, qui doivent être préparés à l'aide de techniques de mise à l'échelle granulométrique. Pour garantir que les éprouvettes testés soient représentatives du matériau original sur le terrain, la réduction de la taille des particules doit être effectué au minimum. Cependant, cela nécessite des appareils d'essai très grands qui sont très rares ou indisponibles. Sinon, on ne peut faire confiance qu'à la fiabilité des techniques de mise à l'échelle reduite. Depuis les travaux pionniers sur les essais triaxiaux à grande échelle menés dans les années 1960 au Mexique, aux États-Unis et en Allemagne, la fiabilité des techniques de mise à petite échelle pour les sols grossiers et les matériaux d'enrochement est restée un sujet de grand intérêt. Au fil des années, de nombreuses méthodes expérimentales ont été proposées et des données significatives ont été compilées. Cependant, les chercheurs ont souvent rapporté des observations expérimentales contradictoires, conduisant à des contradictions apparentes concernant les effets de taille sur le comportement mécanique des matériaux grossiers.

Cette étude vise à élucider les facteurs à l'origine des effets de taille. Sur la base d'un vaste programme d'essais à grande échelle en laboratoire et in-situ sur des stériles miniers, des enrochements et des sols graveleux, les effets de plusieurs propriétés des matériaux et conditions d'essai sont systématiquement étudiés. Les essais ont été réalisés dans deux laboratoires et sur un site minier : les laboratoires d'Environnement Minier à Polytechnique Montréal (Canada) et de l'*Institut für Bodenmechanik und Felsmechanik* (IBF) (Institut de Mécanique des Sols et de Mécanique des Roches) du *Karlsruhe Institute of Technology* (Allemagne), ainsi que sur le terrain à la Mine Canadian Malartic (Québec, Canada). Le programme expérimental évalue les effets de l'échelle granulométrique, de la taille de l'éprouvette, du volume élémentaire représentatif (REV), des effets des conditions aux frontières sur le comportement des éprouvettes soumises aux essais de compression triaxiale, et des paramètres d'état. Près de 170 essais triaxiaux de grande taille et une douzaine d'essais de cisaillement direct ont été réalisés, à partir d'éprouvettes triaxiaux de laboratoire de diamètres variés, de 100 à 800 mm, et d'une boîte de cisaillement direct non standard parmi les plus grandes au monde, de dimensions $1200 \times 1200 \times 380\ mm^3$. La configuration initiale et les formes caractéristiques des particules ont été caractérisées afin d'établir une base de comparaison entre des éprouvettes allant de l'état lâche à dense, et des particules grossières allant de subanguleuses à

arrondies. Des niveaux de contrainte de confinement variant de $\sigma'_3 = 45$ à 600 kPa ont été appliqués. Le changement d'échelle alterne entre les techniques de granulométrie tronquée et de courbes granulométriques parallèles. Les analyses reévaluent les effets d'échelle, de la taille de l'éprouvette et des conditions de bord sur les propriétés mécaniques caractéristiques, notamment la dilatance, le module de déformation, la résistance au cisaillement au pic et les états critiques.

La contribution principale de ce projet doctoral comprend une base de données étendue et quantitative, issue d'une large gamme de matériaux granulaires grossiers testés à différentes échelles d'éprouvettes. Les résultats suggèrent qu'un volume elementaire representatif de matériau grossier ne peut être obtenu que si la taille maximale des particules est limitée à environ 1/12 du diamètre de l'éprouvette de l'essai de compression triaxiale, ce qui est plus restrictif que les normes géotechniques en vigueur aux États-Unis et en Europe. De plus, pour garantir que les méthodes de mise à l'échelle sont représentatives, il est essentiel de confirmer que la forme caractéristique des particules des éprouvettes mis à l'échelle reste cohérente avec celle du matériau grossier d'origine. D'autre part, l'imbrication et la rugosité élevées des roches grossières concassées renforcent les effets de bord dans les éprouvettes soumises aux essais de compression triaxiale. Par conséquent, les éprouvettes à petite échelle présentent souvent une dilatance plus élevée que le matériau grossier d'origine, et des extrémités lubrifiées doivent être systématiquement utilisées dans les sols grossiers. Dans ces conditions, la résistance critique au cisaillement des éprouvettes grossiers peut être correctement caractérisée à l'aide de techniques de granulométries tronquées et de granulométrie parallèle.

Il est essentiel de comprendre les limites des techniques de mise à l'échelle reduite pour éviter les estimations optimistes des propriétés des sols grossiers, afin de garantir des conceptions d'ingénierie géotechnique sécuritaire pour les structures telles que les barrages en enrochements et les haldes à stériles miniers. Les recherches futures devraient se concentrer sur l'examen des effets de taille dans les matériaux granulaires à fractions fines importantes, l'exploration de divers chemins de contrainte et l'étude du comportement cyclique des sols grossiers. Pour évaluer la nécessité d'essais à grande échelle pour un projet spécifique, il est essentiel d'évaluer les propriétés intrinsèques des matériaux et de considérer leur influence potentielle sur les résultats. Bien qu'ils soient rares et coûteux, les essais à grande échelle restent inestimables, offrant des informations essentielles qui améliorent la compréhension des sols grossiers.

ABSTRACT

To conduct stability analyses of mine waste rock (WR) piles, it is essential to characterize the critical shear strength of loose WR material. However, the presence of oversized rock clasts limits shear testing to small specimens, which must be prepared using grading scaling techniques. To ensure the tested specimens closely resemble the field material, particle size reduction should be kept to a minimum. However, this requires very large testing devices that are very scarce or unavailable. Otherwise, one can only trust in the reliability of small-scale techniques. Since the pioneering works on large triaxial testing conducted in the 1960s in Mexico, the USA and Germany, the reliability of small-scale techniques for coarse-grained soils and rockfill materials has remained a subject of great interest. Over the years, numerous experimental methods have been proposed and significant data have been compiled. However, researchers have often reported conflicting experimental observations, leading to apparent contradictions regarding size effects on the mechanical behavior of coarse-grained materials.

This doctoral project aims to elucidate the factors at the source of size effects. Based on comprehensive large-scale laboratory and in-situ tests on mine waste rock, rockfills and gravelly soils, the effects of several material properties and testing conditions are systematically studied. The tests were carried out at two laboratories and one mine site: the laboratories of Mining Environment at Polytechnique Montreal (Canada) and the *Institut für Bodenmechanik und Felsmechanik* (IBF) (Institute of Soil Mechanics and Rock Mechanics) at the Karlsruhe Institute of Technology (Germany), and in the field at the Canadian Malartic Mine (Quebec, Canada). The experimental program assesses the effects of grading scaling, specimen size, representative elementary volume (REV), triaxial specimen boundary effects and state parameters. Nearly 170 large-scale triaxial tests and a dozen large direct shear tests were conducted using laboratory specimens with diameters ranging from 100 to 800 mm. A non-standard direct shear box–among the largest in the world–was also used, with dimensions $1200 \times 1200 \times 380$ mm^3. The packing properties and characteristic particle shapes of the materials were characterized to establish a comparable basis, ranging from loose to dense specimens and subangular to rounded coarse particles. Mean stress levels used varied from $\sigma'_3 = 45 - 600$ kPa. The material scaling methods applied were scalping grading, parallel grading and truncation (replacement) techniques. The analyses revise the effects of scaling, grading and end-restraint on the characteristic mechanical behaviors, including dilatancy, strain moduli, peak shear strength and critical states.

The main contribution of this doctoral project lies in the extensive and quantitative dataset obtained from a wide range of coarse-grained materials, tested at different specimen scales. The findings suggest that a REV of coarse material can only be achieved if the maximum particle size is limited to approximately 1/12 of the triaxial specimen diameter, which is more restrictive than current geotechnical standards in the USA and Europe. Several crucial parameters must be controlled to enable small-scale reliability and representativeness. The characteristic particle shapes should be verified prior to scaling. The triaxial end caps in coarse-grained materials testing should be lubricated properly to enhance free dilation due to the high interlocking and roughness of crushed coarse particles. Otherwise, small-scale specimens often exhibit higher dilatancy than the original prototype coarse material. Furthermore, equivalent relative densities are imperative. Under these conditions, it is shown that scalping grading, parallel grading and truncation (replacement) techniques can provide reliable mechanical behavior of coarse materials in small-scale specimens.

Understanding the limitations of small-scale techniques is crucial to avoid optimistic soil property estimates and ensure reliable geotechnical engineering designs for structures such as rockfill and earth dams, and mine waste rock piles. Future research should focus on examining size effects in granular materials with significant fine fractions, exploring various stress paths, and investigating the cyclic behavior of coarse-grained soils. To assess the necessity of large-scale testing for a specific project, it is essential to evaluate the intrinsic properties of the materials and consider their potential influence on the results. Despite being rare and costly, large-scale tests remain invaluable, offering critical insights that enhance the understanding of coarse-grained materials.

TABLE OF CONTENTS

LIST OF TABLES

LIST OF FIGURES

LIST OF ACRONYMS AND SYMBOLS

ASTM	American Society for Testing and Materials
BS	British Standards
CD	Consolidated drained
CLS	Column-like structures
CTC	Conventional triaxial compression
CSL	Critical state line
CU	Consolidated undrained
DAQ	Data acquisition
DEM	Discrete element method
DIN	Deutsches Institut für Normung
DST	Direct shear test
FS	Factor of safety
GDP	Gross domestic product
IBF	Institut für Bodenmechanik und Felsmechanik (Institute of Soil Mechanics and Rock Mechanics)
JGS	Japanese Geotechnical Society
KIT	Karlsruhe Institute of Technology
MERN	Ministère de l'Énergie et des Ressources naturelles
PWP	Pore water pressure
REV	Representative elementary volume
RIME	Research Institute in Mining and Environment
SEM	Scanned Electronic Microscope
UCS	Uniaxial compression strength
UK	United Kingdom
UQAT	Université du Québec en Abitibi-Témiscamingue
USA	United States of America
UU	Unconsolidated undrained
WR	Mine waste rock
WRP	Waste rock piles
XRD	X-Ray diffraction

α	Sample aspect ratio [–]
δu	Pore water pressure increment [$ML^{-1}T^{-2}$]
$\varepsilon_1,\ \varepsilon_a$	Axial strain (interchangeably) [%]
$d\varepsilon_1,\ d\varepsilon_a$	Axial strain increment (interchangeably) [%]
ε_r	Radial strain [%]
ε_v	Volumetric strain [%]
$d\varepsilon_v$	Volumetric strain increment [%]
γ_d	Dry density [$ML^{-2}T^{-2}$]
$\gamma_{d_{max}},\ \gamma_{d_{min}}$	Maximum and minimum dry densities [$ML^{-2}T^{-2}$]
ν	Poisson's ratio [–]
ϕ'	Effective internal friction angle [°]
ϕ'_{cr}	Effective internal critical friction angle [°]
$\phi'_{max},\ \phi'_p$	Effective internal maximum or peak friction angle (interchangeably) [°]
ψ_{max}	Dilatancy angle [°]
σ'_n	Effective normal stress [$ML^{-1}T^{-2}$]
$\sigma_1,\ \sigma_2,\ \sigma_3$	Total principal stresses [$ML^{-1}T^{-2}$]
$\sigma'_1,\ \sigma'_2,\ \sigma'_3$	Effective principal stresses [$ML^{-1}T^{-2}$]
σ_{cp}	Back pressure [$ML^{-1}T^{-2}$]
τ	Shear stress [$ML^{-1}T^{-2}$]
d	Characteristic size diameter [L]
$d_{10},\ d_{30},\ d_{60}$	Particle diameter with 10%, 30%, and 60% passings [L]
d_{50}	Average particle size [L]
d_{max}	Maximum particle size [L]
D_r	Relative density [%]
e	Void ratio [–]
e_{cr}	Critical state void ratio [–]
$e_{max},\ e_{min}$	Maximum and minimum void ratios [–]
E	Initial (Young) modulus [$ML^{-1}T^{-2}$]
E_i	Characteristic modulus [$ML^{-1}T^{-2}$]
E_{50}	Secant strain modulus [$ML^{-1}T^{-2}$]
F	Scaling factor [–]
F_h	Horizontal pulling force [MLT^{-2}]
F_v	Vertical loading force [MLT^{-2}]
G	Shear modulus [$ML^{-1}T^{-2}$]
h	Horizontal displacement [L]
I_D	Density index [%]

$L,\ D,\ H,\ W$	Sample length, diameter, height, and width [L]
p'	Mean effective stress [$\mathrm{ML^{-1}T^{-2}}$]
q	Deviatoric stress [$\mathrm{ML^{-1}T^{-2}}$]
R	Particle roundness [–]
S_{WL}	Particle width-to-length sphericity [–]
u	Pore water pressure [$\mathrm{ML^{-1}T^{-2}}$]
X	Characteristic sample size [L]
B	Skempton coefficient [–]
B_g	Marsal's breakage ratio index [%]
C_c	Curvature coefficient [–]
C_u	Uniformity coefficient [–]

CHAPTER 1 INTRODUCTION

1.1 Research background and context

In order to develop reliable and safe operational geotechnical criteria to improve the designs of mine waste rock piles, rockfill structures and earth dams, the stress-strain properties of coarse gravels and crushed rock materials should be evaluated. This is mainly done through comprehensive experimental testing. However, because of the size limitations of existing testing facilities and devices, physical testing of coarse-grained material is not always achievable, resulting in data scarcity. Designs and decisions are based on a limited number of data, mostly taken from tests on small-scale specimens of the *prototype* field material. In this work, we refer to coarse-grained materials (soils, waste rock, or rockfills) as those that contain particle sizes in the range of gravels ($5 < d < 80mm$) and/or oversized particles boulders ($d > 80mm$).

Typically, practitioners reduce the characteristic particle size of the material using grading scaling methodologies. A so-called specimen aspect ratio ($\alpha = X/d_{max}$, where X is the characteristic specimen size and d_{max} is the maximum particle size) should be defined to satisfy the minimum value recommended by international testing standards. In other words, scaling involves altering the particle size distribution (PSD) of the field material. Within the framework of the critical state soils mechanics, it has been shown that the PSD has a strong effect on the stress-strain behavior, while it does not affect the effective internal critical friction angle (ϕ'_{cr}), provided that grain mineralogy, surface roughness and particle shape remain the same across size fractions. However, the literature documents contradictory trends with scaling and grading effects, raising uncertainties about the accuracy and representativeness of small specimens to capture the behavior of coarser field materials. Yet, due to the limitations to handle oversized particles, the sources of these contradictions remain poorly understood. Qualitative and quantitative investigations are imperative to properly understand the effects of scaling in coarse-grained materials, in order to enhance the reliability and representativeness of testing on relatively small-scale specimens.

This doctoral project encompasses the characterization of the mechanical behavior of coarse soils, rockfill materials and mine waste rocks (WR). Based on extensive previous research, this study establishes additional data and qualitative tools to tackle this topic.

1.1.1 Research questions

This thesis intends to answer the following questions:

- What properties must be controlled to prepare a small-scale representative specimen that reliably replicates the mechanical behavior of a coarse-grained prototype field material?
- If there is a reliable scaling method, do we still need large and expensive tests?

1.1.2 Hypotheses

The following hypotheses are raised to answer the research questions.

- Mechanical tests on specimens with relatively low values of the specimen aspect ratio (α) result in inconsistent mechanical behavior.
- The minimum α recommended by common geotechnical standards might be too low to ensure a representative elementary volume (REV) and mitigate specimen scale effects; this could partially explain the apparent contradictions of size effects found in the literature.
- Within a given coarse-grained material, particle shapes could change across different particle sizes. Therefore, a small-scale specimen could have different characteristic particle shapes compared to the coarser material, impacting its mechanical behavior and representativeness.
- Due to the mobilization of relatively high frictional stress components in coarse angular soils compared to sands and fine soils, specimen boundary effects might be enhanced.

1.1.3 Objectives

The main objective of this doctoral project is to assess the reliability of small-scaling techniques for coarse-grained materials, in order to evaluate their mechanical behavior.

To achieve the main objective, the following specific objectives (SO) are proposed:

- SO1. Evaluate the effects of specimen size, specimen aspect ratio and grading on the strain-stress relationship of mine waste rock material, quarry rockfill and coarse gravel soils, tested under conventional triaxial compression (CTC).

- SO2. Develop a large in-situ testing technique to characterize the critical shear strength of coarse waste rock materials.
- SO3. Investigate the impacts of boundary effects on the mechanical behavior of small-scale quarry rockfill specimens in CTC.
- SO4. Provide practical recommendations on testing methods and specimen preparation for testing coarse granular materials, as well as data interpretation to evaluate potential size effects.

1.2 Structure of the manuscript

This manuscript is written in English since international researchers are involved through collaboration and review, namely Prof. Hans Henning Stutz of Karlsruhe Institute of Technology (KIT) in Germany (co-director of this doctoral project), and Prof. Gonzalo Zambrano Narvaez from the University of Alberta (external member of the jury). As a whole, the manuscript is divided into eight (8) Chapters and three Appendices containing additional figures of the test results of WR specimens in the laboratory (*Appendix A*), at in-situ (*Appendix B*), and for quarry rockfill specimens tested in the laboratory (*Appendix C*).

- *Chapter* 1 presents the introduction and the project overview, detailing the research questions, hypothesis and objectives.
- *Chapter* 2 consists of a comprehensive literature review aiming to situate the reader in the general framework of soil mechanical characterization, with particular emphasis on coarse soils. The following technical topics are recalled:
  - context of waste rocks in mining;
  - fundamental concepts of critical soil mechanics;
  - testing methods to assess the mechanical behavior of soils;
  - small-scaling techniques utilized to characterize oversized soils and rockfills, and their impacts on deformation and strength properties;
  - finally, the highlights of the review are recapitulated to introduce the motivation for this research.
- The methodologies followed throughout this research study are described in *Chapter* 3.

- *Chapter* 4 is the subject of ARTICLE 1 "Grading scalping and specimen size effects on critical shear strength of mine waste rock through laboratory and in-situ testing", published in the *International Journal of Rock Mechanics and Mining Sciences*. This work arises from the collaboration with the Canadian Malartic Mine (Quebec, Canada), in the framework of a research project supported by the Research Institute in Mining and Environment (RIME) UQAT-Polytechnique. The article assesses the impact of scaling and grading on the mechanical behavior of loose WR, detailing:

  - the development of one of the largest reported shear boxes in the world ($[1200 \times 1200] \times 380$) mm^3 (cross-sectional area $\times$ depth);
  - 57 laboratory tests performed using triaxial specimens of diameter ($D = 150$ and 300 mm) to assess size effect;
  - the effect of specimen aspect ratio (α) under varying sizes.

- *Chapter* 5 presents ARTICLE 2: "End-restraint effects in triaxial tests on H:D=2:1 specimens of rockfill material". This work has been submitted to *Geotechnique Letters* Journal. The main objective is to assess the effects of triaxial end boundary conditions on the mechanical response of coarse angular soil. Different end-platen setups are examined, including the standard rough platens and enlarged lubricated ends. This endeavor is undertaken in the context of grading influence by varying d_{max} in specimens of quarry rockfill material. The article presents a total of 79 monotonic tests on specimens with slenderness height-to-diameter H:D=2:1.

- *Chapter* 6 presents the ARTICLE 3: "Effects of triaxial specimen scaling on the mechanical behavior of alluvial gravels." This work has been submitted to the *Journal of Geotechnical and Geoenvironmental Engineering*. It stems from the collaboration with the *Institut für Bodenmechanik und Felsmechanik* (IBF) (Institute of Soil Mechanics and Rock Mechanics) at the Karlsruhe Institute of Technology, in Germany. The paper details the grading effects by varying the uniformity coefficient (C_u) in three devices to test specimens of $D = 100$, 150 and 800 mm, and H:D=1:1. A total of 20 monotonic triaxial compression shearing tests are carried out and analyzed.

- *Chapter* 7 presents a synthesis and a general discussion of the results of Chapters 4−6, totalizing more than 170 triaxial and direct shear tests. Observations from *Chapter* 2 are revisited during the discussion.

- Finally, *Chapter* 8 presents the conclusions and an assessment of the research objectives, followed by practical recommendations and perspectives for future work.

1.3 Disclaimer

The results of this thesis have been partially published and presented in the following conferences:

- Girumugisha, G., Ovalle, C., Stutz H.H., (2025). Small-scaling effects on the stress dilatancy response of coarse gravel soils. The 78th Canadian Geotechnical Conference, *GeoManitoba 2025*. Submitted.
- Girumugisha, G., Ovalle, C., Ouellet, S. (2024). specimen Size Effect on Shear Strength of Mine Waste Rock Material Using the Scalping Method. *Geo-Congress 2024*, Vancouver, Canada, February 25-28, pp. 313-320. https://ascelibrary.org/doi/abs/10.1061/9780784485309.032
- Quiroz-Rojo, P., Ovalle, C., Girumugisha, G., Cantor, C., Azéma, E., Renouf, M. (2024). Particle size effects on critical strength of granular soils through numerical and laboratory testing. 17th Pan-American Conference on Soil Mechanics and Geotechnical Engineering *XVII PCSMGE*, November 12-12, 2024, La Serena, Chile. https://www.issmge.org/publications/online-library
- Ovalle, C., Girumugisha, G., Cantor, D. & Ouellet, S. (2023). Size effects assessment of mine waste-rock shear strength combining numerical, laboratory and in-situ approaches. In PM Dight (ed.), *SSIM 2023*: Third International Slope Stability in Mining Conference, Australian Centre for Geomechanics, Perth, pp. 291-300. https://doi.org/10.36487/ACG_repo/2335_16

CHAPTER 2 LITERATURE REVIEW

2.1 Mine waste

The mining industry plays an important role in local and international economies and societies. For instance, Statistics Canada (2022) reports that the contribution of mining to the gross domestic product (GDP) is of 6%, with more than half related to metallic minerals. Additionally, declining ore grades and increasing demand for metals during society's energy transformation drive increased mining operations worldwide. This situation poses significant challenges to managing the relentless increase in mine waste, which is produced mainly as waste rock (WR) and tailings. WRs are sterile material without economic value, which has to be blasted and excavated to access the ore (*Figure* 2.1). In open-pit hard rock mining, nearly $\sim 2/3$ of the mined rock is WR, whereas in underground mining it is around 10% (Hawley & Cunning, 2017; SME, 2011). However, these ratios can vary greatly depending on the WR lithology (Aubertin et al., 1996, 2013). On the other hand, the ore process includes grinding and milling to recover minerals, generating slurry tailings (as illustrated in *Figure* 2.1) with non-plastic sandy-silt particles (Aubertin et al., 2013; Bussière, 2007; Lèbre et al., 2017). Tailings are stored in facilities confined by dams or dykes (Aachib et al., 2004; Aubertin et al., 2013; Lèbre et al., 2017). WR and tailings storage facilities must be designed to minimize their environmental impacts, and to guarantee their chemical, hydrogeological and mechanical stability (Aubertin et al., 1996, 2021; Blight, 2009; Bussière & Guittonny, 2020; Chapuis et al., 1993).

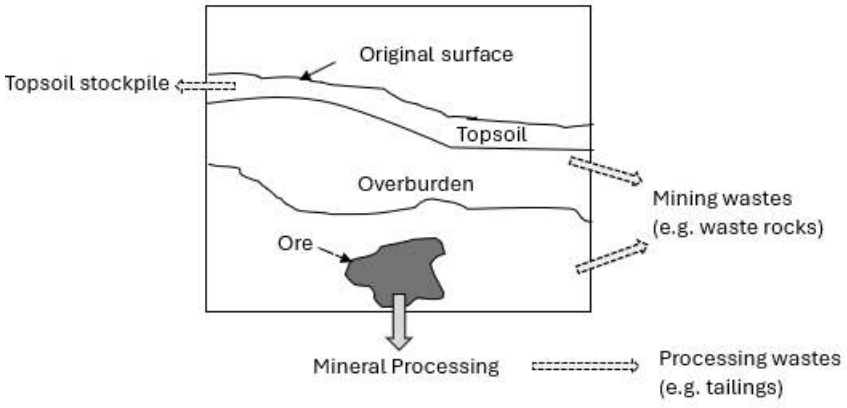

Figure 2.1 Schematic illustration of mine waste streams at a metallic mine, *modified* after Lottermoser (2010).

WR volume production increases proportionally with the current high market demand for minerals (USGS, 2022). Around 15 Gt/year of mined waste is reported globally (Lottermoser, 2010). For instance, the largest open-pit gold mine in Canada, the Canadian Malartic Mine, reported more than 30 million tonnes extracted in 2020, corresponding to 85 000 tonnes per day (tpd) [1]. The largest copper mines in Chile extract more than 200 000 tpd (Linero et al., 2007; Quezada & Villavicencio, 2024), with WR piles (WRP) of unprecedented heights beyond 500 m (Bard et al., 2011; Linero et al., 2007; Quezada & Villavicencio, 2024; Valenzuela et al., 2008), making WRPs among the highest structures built by man (Aubertin et al., 2021; Bard et al., 2011; Garcia-Torres et al., 2024; Linero et al., 2007; Quezada & Villavicencio, 2024; Valenzuela et al., 2008; Zevgolis, 2018). For example, *Figure* 2.2a shows the Antamina East WRP dump (in Peru) of 500 m high, covering 240 ha and approximately 1 billion tonnes of material (Hawley & Cunning, 2017). The sidehill fill in Antamina Tucush Valley is shown in elevation in Figure 2.2(b), illustrating WR material resting at its angle of repose.

[1] https://canadianmalartic.com/wp-content/uploads/canadian-malartic-mine-sr2020.pdf

(a)

(b)

Figure 2.2 WRPs at Antamina Mine in Peru (Hawley & Cunning, 2017): (a) East WRP; (b) sidehill fills in the Tucush Valley.

2.1.1 Waste rock material

- Particle size distribution

WR blasting and excavation generate coarse subangular and angular rock clasts, that can easily reach around 1 m in diameter (d). As shown in *Figure* 2.3, WRs from hard rock mines typically have well-graded particle size distributions (PSD), containing boulders ($d > 300$ mm), cobbles ($d = 75 - 300$ mm), gravelly sandy fractions and a limited amount ($\approx$ 5-20%) of silt-sized fines ($d \leq 80\mu$m). McKeowen et al. (2000) reported the characteristic properties of the PSDs analyzed below boulders of 1 m from WR of hard rock mines with uniformity coefficient ($C_u = d_{60}/d_{10}$) between 8 and 610. Essayad (2021) described $d_{10} = 0.02 - 3.5$ mm,

$d_{60} = 1.8 - 86$ mm and $C_u = 14 - 217$ of WR from the Canadian Malartic Mine (MCM) in Canada. Typical characteristic properties have been documented from the same and other hard rock mines in Quebec, Canada (Gamache-Rochette, 2004; Hernandez-Orellana, 2007; Peregoedova, 2012). On the other hand, as shown in the same figure (2.3), slurry tailings are finer than WRs (below $d < 1$ mm) (Aubertin et al., 1996; Bussière, 2007). Essayad and Aubertin (2021) reported $d_{10} = 0.004 \pm 0.0005$ and $d_{60} = 0.04 \pm 0.01$ mm ($C_u = 9.3$) on MCM tailings. Furthermore, due to the presence of heavy metal minerals, the specific gravity of tailings is reported between $G_s = 2.6 - 4.2$ (Aubertin et al., 2013; Essayad, 2021; Grimard, 2018; James, 2009). For instance, James (2009) reported $G_s = 4 \pm 0.35$ for LaRonde Mine in Quebec (Canada).

- *Hydrogeotechnical properties*

The widely distributed particle sizes of WR and the disposal and dumping operations lead to significant heterogeneity in the internal structure of WRPs (Anterrieu et al., 2010; Aubertin et al., 2013; Azam et al., 2007; Dawood & Aubertin, 2009; Fala, 2008; Lahmira et al., 2016). Therefore, hydrogeotechnical properties vary greatly depending on different lithologies (Aubertin, Bussière, & Bernier, 2002; Aubertin, Fala, et al., 2002; Essayad, 2021; Fala, 2008; Fala et al., 2006; Hernandez-Orellana, 2007; Maknoon, 2016; Martin, 2003; Peregoedova, 2012), as well as fine fractions due to particle crushing and degradation (Bard et al., 2011; Valenzuela et al., 2008). The typical range reported for the saturated hydraulic conductivity (k_{sat}) of WR materials is shown in *Figure* 2.4 after Peregoedova (2012), varying between $k_{sat} = 10^{-2}$ and 10^{-5} cm/s. Similar range is reported elsewhere on several WR materials in Canada (Aubertin, Fala, et al., 2002; Aubertin et al., 2005; Morin et al., 1991) and internationally (e.g: (Azam et al., 2011; Franklin et al., 2008)). Peregoedova (2012) showed systematically that the high k_{sat} values of WRs are associated with large macropores, in which the water retention capacity and the air entry values (AEV) remain very low ($AEV < 10$ cm or 1 kPa). *Figure* 2.5 presents the variation of the AEV with d_{10} (*left-plot*) without any definite clear trend due to prominent material heterogeneities (Azam et al., 2007; Dimech et al., 2019; Fredlund & Xing, 1994; Martin et al., 2019; Peregoedova, 2012). However, the relatively low residual suction values (Ψ_r) increase with decreasing d_{10} (*right-plot*). It is important to mention that if the WR lithology contains active sulfide minerals, contact with oxygen and water would trigger chemical processes such as acid mine drainage (Amos et al., 2015; Aubertin, Bussière, & Bernier, 2002; Aubertin, Fala, et al., 2002; Azam et al., 2007; Bao et al., 2022; Bussière & Guittonny, 2020; Fala et al., 2006; Raymond et al., 2021; Smith et al., 2013). This literature review does not discuss further these geochemical and hydrogeological aspects of WR materials, since the current doctoral research project focuses

on their mechanical properties.

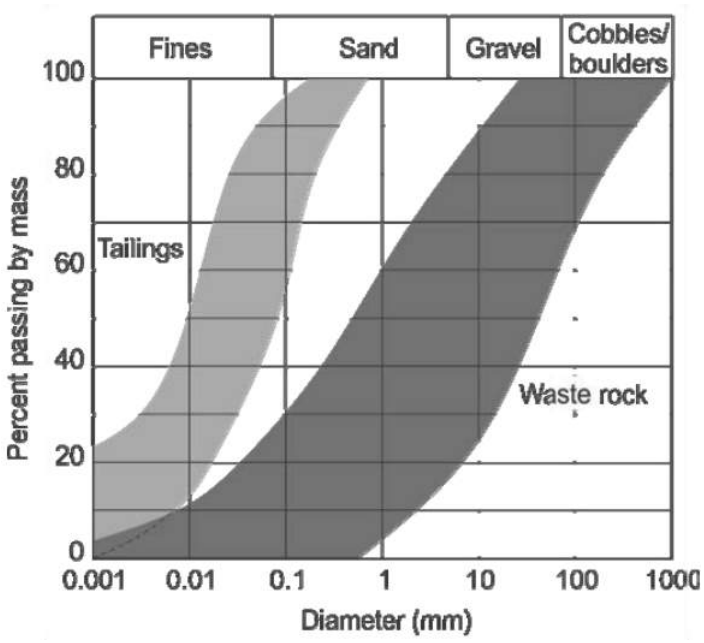

Figure 2.3 Typical PSDs encountered in WRP and tailings, after Bussière (2007), Gamache-Rochette (2004), and James et al. (2013).

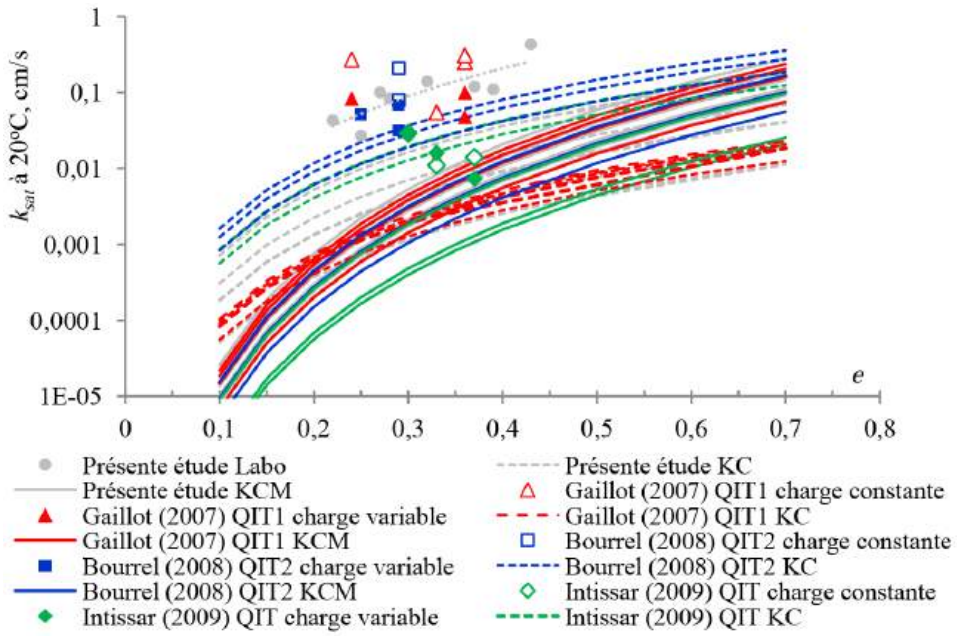

Figure 2.4 Variation of k_{sat} with e after Peregoedova (2012).

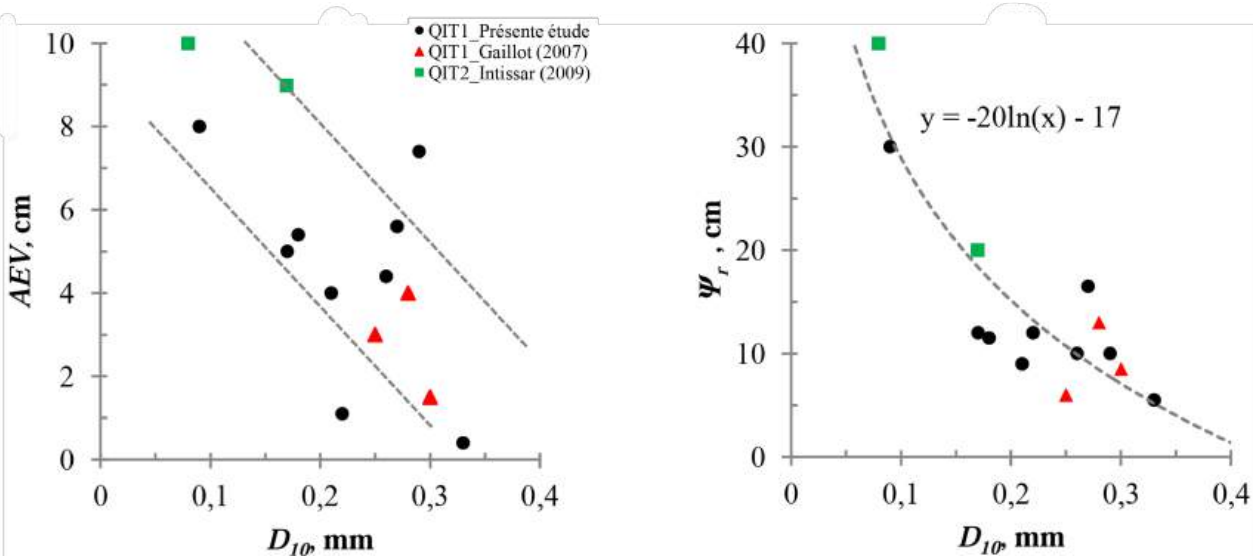

Figure 2.5 Variation of AEV (*left*) and Ψ_r (*right*) with d_{10} after Peregoedova (2012).

- *Dry unit weight*

When constructing WRPs, the material is generally dumped without compaction, other than the passage of machinery (trucks and dozers). Thus, WR remains relatively loose on the surface and densifies by its weight once the pile rises. Essayad (2021) reported dry unit weight (γ_d) values of around $\gamma_d = 19 - 23\ kN/m^3$ measured using in-situ nuclear density gauge (NDG) at the MCM site. Additionally, in-situ density measurements with replacement techniques using calibrated material were carried-out, as illustrated in *Figure* 2.6. First, the surface excavation is made (see *Figure* 2.6a-b), followed by bash installation in the excavated trench. The mass of the excavated WR is weighed and, following ASTM D5030, a known water volume is progressively replaced and filled, as shown in *Figure* 2.6c-d. Alternatively, plastic beads of uniform size and shape were also used as replacement material instead of water (see *Figure* 2.6e-f). The beads were first characterized in the laboratory to estimate their unit weight for in-situ proper estimates. Compaction was provided through vibration using plexiglass tubes. The estimate of the results of both NDG and replacement by water is shown in *Table* 2.1; all the values are in the typical range reported pf $\gamma_d = 19 - 23\ kN/m^3$.

Similar values are reported in the literature for WRPs. *Figure* 2.7 presents γ_d estimates in WRPs as a function of effective stresses and their equivalent heights. These values were estimated after oedometric compression tests on coarse specimens of WR from a large copper mine by Bard et al. (2007) and Valenzuela et al. (2008). γ_d is in the order of 18-24 kN/m^3, corresponding to void ratios of e= 0.5 to 0.15, respectively.

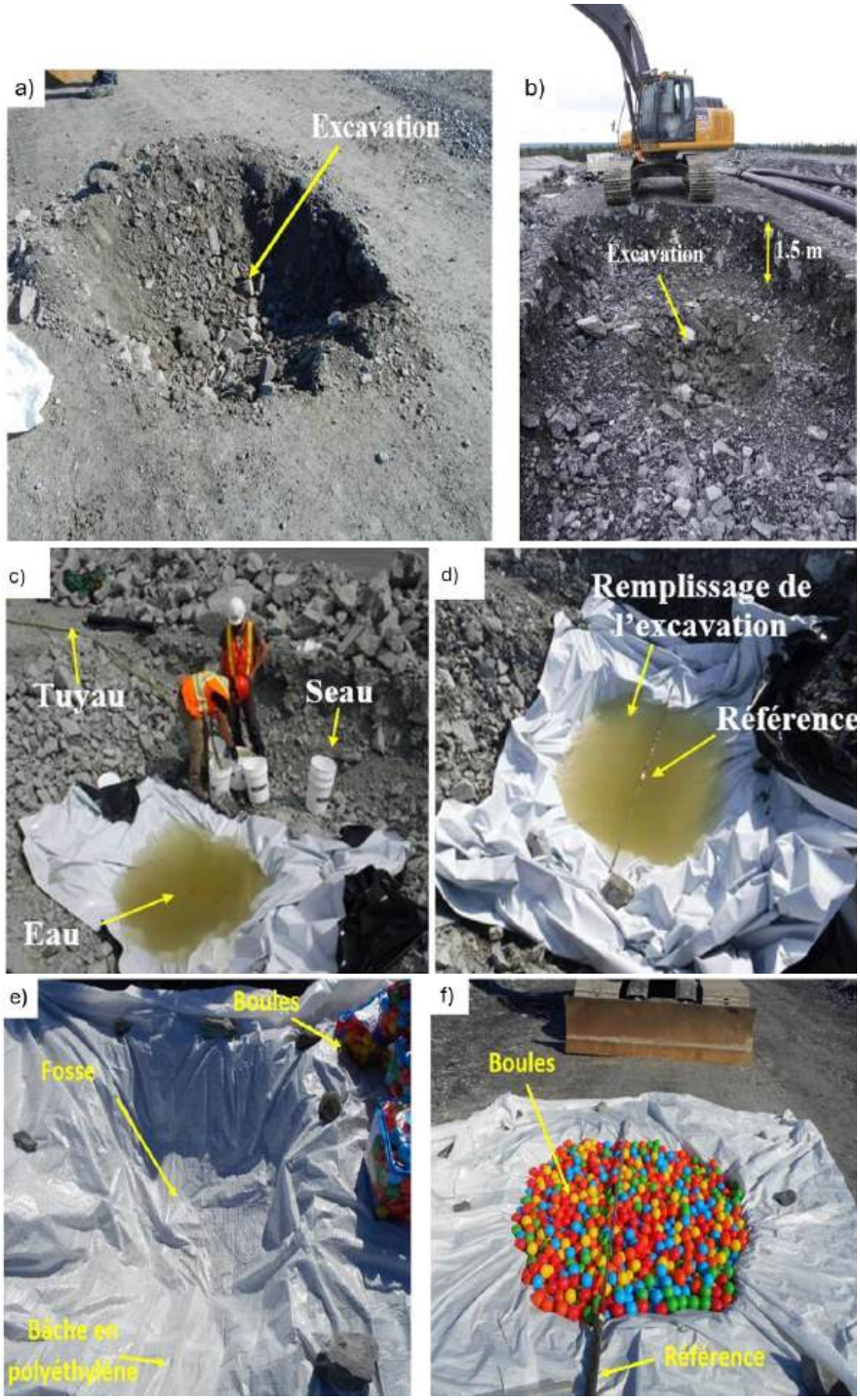

Figure 2.6 In-situ density estimate after Essayad (2021).

Table 2.1 In-situ dry unity weight estimates for WR material using nuclear density gauge (NDG) and calibrated material replacement after Essayad (2021).

WRI	Method	Depth (m)	Dry unit weight γ_d (kN/m^3)	Total porosity n (-)
6	NDG	(h = 0.3 m)	19.4 – 23	0.17 – 0.30
9	NDG	(h = 0.3 m)	20.50 – 23.10	0.16 – 0.26
D.O	NDG	(h = 0.3 m)	18.4 – 23	0.17 – 0.34
12	NDG	(h = 0.3 m)	21 – 23	0.17 – 0.24
		(h > 1 – 1.5 m)	18 – 22.40	0.19 – 0.35
	In situ density tests: water replacement method	(h = 0.5 m)	23	0.17
		(h > 1 – 1.5 m)	15 – 19.5	0.29 – 0.46*

*Unrealistically high value (discarded from the calculations)

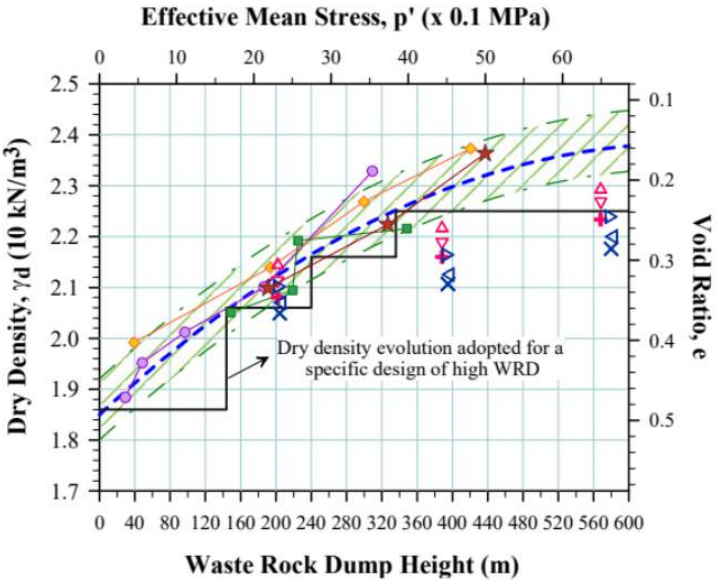

Figure 2.7 Variation of e with WRP height after Bard et al. (2007).

- *Mechanical properties*

As any soil, the mechanical behavior of WR and coarse-grained materials depends on state (pressure and density) and index properties (grading and particle shape). Moreover, coarse

materials are particularly prone to particle crushing due to size effects on rock particle strength. As a result of grain crushing, it is well known that dilatancy decreases and the material compressibility increases (Marachi et al., 1972; Marsal, 1967; Osses et al., 2024). Since the main topic of this thesis is related to the mechanical properties of WR and coarse-grained materials, a specific and more detailed review and analysis are given in Section 2.3, including large testing methodologies, critical state conditions, size effects, among other subjects.

2.1.2 Waste rock piles construction methods

Depending on the construction method, the internal structure of WRPs can be segregated (Anterrieu et al., 2010; Aubertin, Fala, et al., 2002; Qiu & Pabst, 2024; Raymond et al., 2021), creating heterogeneous piles with zones having varied grading. This might cause variations of hydraulic conductivity within the WRP (Aubertin, Fala, et al., 2002; Aubertin et al., 2005; Fala et al., 2006; Wilson et al., 2000) and the shear strength of the material, causing potential instabilities (Lahmira et al., 2016; Qiu & Pabst, 2023). The mechanical stability of WRPs is commonly assessed by 2D limit equilibrium analyses and other more advanced Finite element methods (e.g: (Majdanishabestari, 2023; Maknoon, 2016)). A factor of safety (FS) against slope sliding is obtained and compared with minimum requirements given by guidelines and regulations (e.g: Directive 019 (2021) and Guidelines for Preparing Mine Closure Plans in Québec, Canada (2016)). The construction method depends on numerous factors, such as the site topography, desired FS, WR lithologies, closure plan, and other geotechnical and environmental factors. The literature reports several methods, however, this manuscript mentions only three of the most common ones.

- **End-dumping**

The end-dumping method, often referred to as top-bottom construction, consists of pouring the WR material from the crest of the pile using a truck, as depicted in *Figure* 2.8a. It is commonly implemented in mountainous regions where the material is dumped into a valley and rests on its angle of repose, generally between $34 - 37°$ (Aubertin et al., 2021; Bard et al., 2011; Linero et al., 2007; Majdanishabestari et al., 2022; Zevgolis, 2018), as shown previously in *Figure* 2.2b for the Antamina mine in Peru. In terms of financial investment, this method represents the most convenient alternative, since it demands minimum earthworks and material hauling and spreading. However, it promotes significant particle segregation and maximizes the global slope of the pile, resulting in low FS against slope stability (Anterrieu et al., 2010; Aubertin, Bussière, & Bernier, 2002; McLemore et al., 2009; Raymond et al., 2021; Wilson et al., 2000). For instance, *Figure* 2.8b shows three distinct regions due to

particle segregation typically observed: (i) the upper region toward the pile crest with the prominent accumulation of fines; (ii) the coarser particles accumulated toward the toe of the pile due to enhanced momentum during deposition; and (iii) the intermediate region with evenly distributed fine and coarse particles. However, despite the segregation challenges, this technique is one of the most used due to the cost minimization benefits (Aubertin, Bussière, & Bernier, 2002; Hawley & Cunning, 2017; Martin, 2003; McLemore et al., 2009).

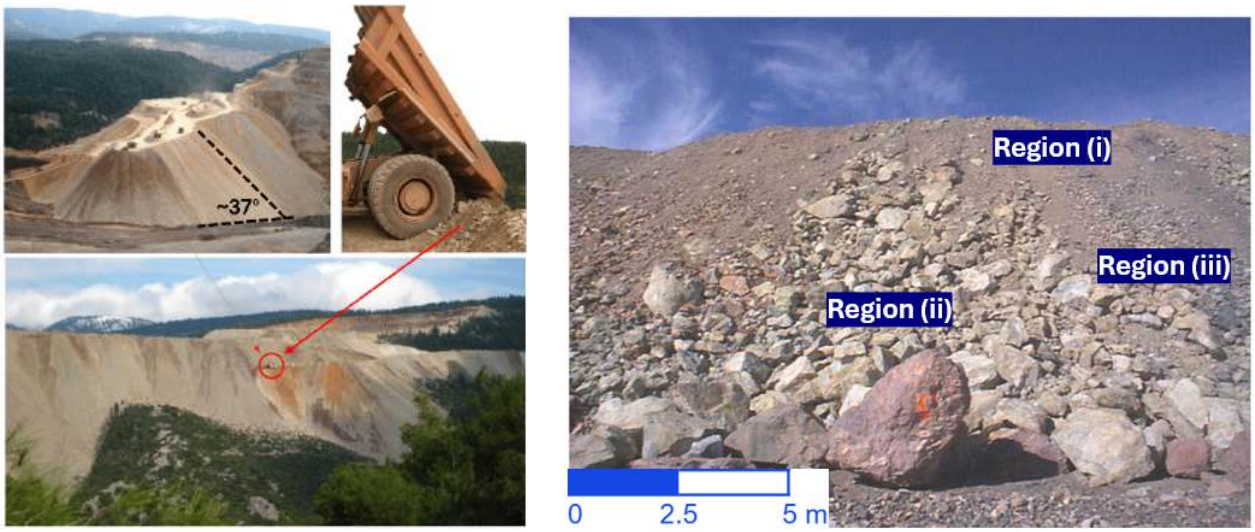

(a) (b)

Figure 2.8 End dumping photos : (a) haul truck pouring WRs from the crest, *modified from* Zevgolis (2018) ; (b) WRP showing segregated particles, *modified from* Martin (2003).

- **Push-dumping**

Push-dumping consists of depositing the material on the top platform of a WRP (i.e., away from the pile edge), and then spreading and pushing it by bulldozers. Pushed material pours along the slope of the pile and adopts its angle of repose. With this method, segregation is alleviated and the mechanical stability of the pile is enhanced compared to the end-dumping method, as heavy machines tend to densify the pile shallowly in subhorizontal layers (see *Figure* 2.9a), particularly during rainy seasons (Aubertin, Fala, et al., 2002; Raymond et al., 2021). As shown in *Figure* 2.9b, the distance from the crest at which the material is dumped by trucks also considers a safety distance to avoid potential sliding failures near the edge of the pile (Majdanishabestari, 2023). The push-dumping method is commonly used when the pile involves elevated heights, raising safety uncertainties to access the crest (Aubertin et al., 2021; Majdanishabestari, 2023; Raymond et al., 2021). Alternately, end-push dumping is often adopted in pit back-filling projects (Garcia-Torres et al., 2024; Ouellet et al., 2021), as depicted in *Figure* 2.10 for a pit (190 m deep) at the Canadian Malartic Mine in Canada.

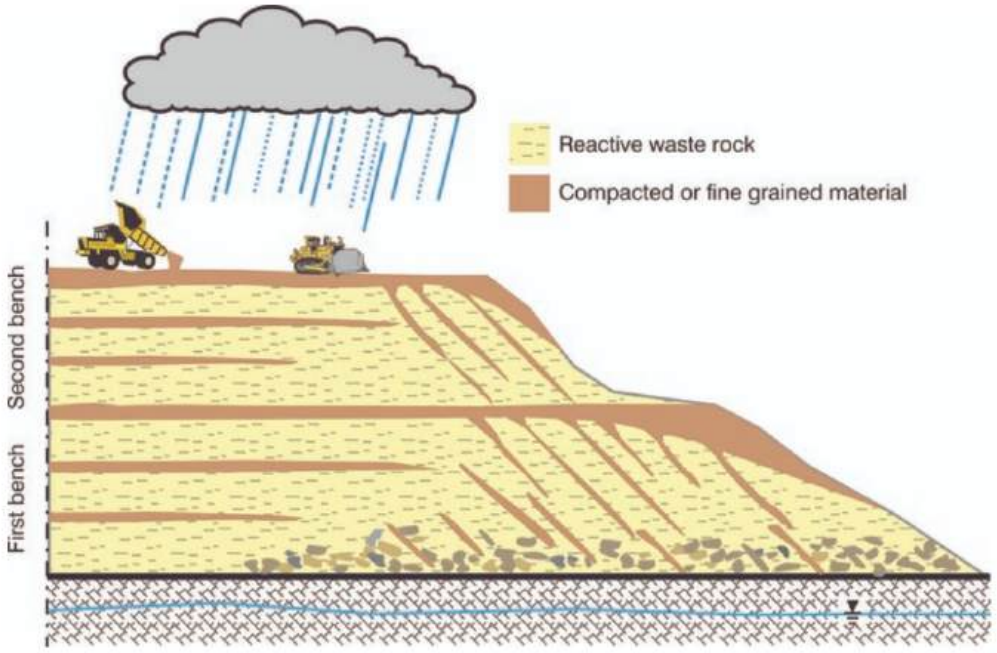

(a)

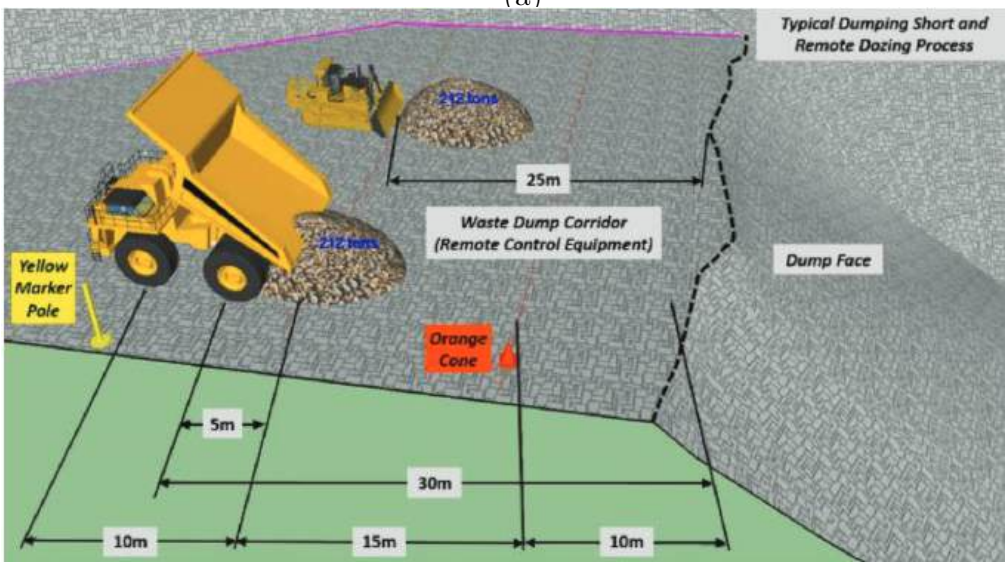

(b)

Figure 2.9 Push dumping: (a) conceptual illustration showing densified subhorizontal layers through heavy machine passing, after Bussière (2007) and Aubertin, Fala, et al. (2002); (b) conceptual sketch displaying delimitations considered as safety zone accessible by heavy equipment, after Bar et al. (2020) .

Figure 2.10 Real case scenario of end-push dumping during pit back-filling (Canada) after Garcia-Torres et al. (2024).

- **Construction with benches**

The minimum factor of safety (FS) against sliding recommended by most regulations for WRPs is FS$\geq$ 1.3 (MERN (2016)). However, end- and push-dumping in WRPs exceeding 150 m result in FS around 1.1 to 1.2 (Maknoon & Aubertin, 2021; Ouellet et al., 2021), necessitating intensive field monitoring to compensate for stability concerns (Garcia-Torres et al., 2024; Hawley & Cunning, 2017). To achieve a higher long-term FS $\geq$ 1.5, bottom-up construction with intermediate benches becomes essential (Aubertin et al., 2021; Hawley & Cunning, 2017; Maknoon & Aubertin, 2021). In this case, WR is discharged and spread by dozers, as shown in *Figure* 2.11a-b, forming benches with individual heights ranging from 6 to 50 m. The resulting WRP exhibits a gentle overall inclination around $\sim$26° with FS $\geq$ 1.5, depending on the WR properties. Individual bench angles of repose approach $\sim$37° (Barton & Kjærnsli, 1981; Blight, 2009; Linero et al., 2007; Maknoon & Aubertin, 2021; Zevgolis, 2018). This method has been widely implemented in Quebec (Aubertin et al., 2013, 2021). *Figure* 2.12 shows a real-case implementation of bench construction at the Canadian Malartic Mine, featuring individual berms of $\sim$25 m (Aubertin et al., 2021). Aubertin et al. (2013) recommends this method to alleviate pile depth and enhance physical stability. However, it is associated with higher costs compared to the end- and push-dumping methods.

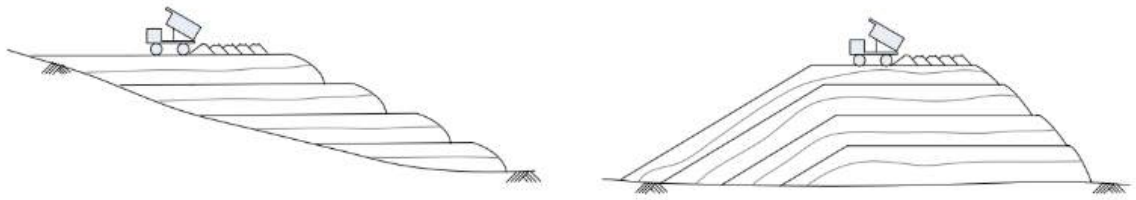

(a) (b)

Figure 2.11 Typical construction of WRP with benches after Zevgolis (2018): (a) on inclined topography; (b) on horizontal topography.

Figure 2.12 WRP constructed with benches at Canadian Malartic Mine after Aubertin et al. (2021).

2.1.3 Geotechnical stability assessment of waste rock piles

WRPs are exposed openly to the environment, implicating social responsibilities to be managed eco-responsibly (Aubertin et al., 2013, 2021). Therefore, designs require multidisciplinary efforts for geotechnical, hydrogeological and geochemical stability analyses. In terms

of mechanical stability, *Table* 2.2 presents the recommended minimum FS in the *Guidelines for Preparing Mine Closure Plans in Québec*, Canada by Ministère de l'Énergie et des Ressources naturelles (MERN) for WRP. According to these guidelines, the overall pile stability (i.e., global slope) should have a FS $\geq$ 1.3 and 1.5 for short- and long-term analyses, respectively. Also, the recommendation for individual benches are less restrictive, with a minimum FS between 1.0 to 1.2.

Table 2.2 Recommended minimum FS for the stability analysis of WRP after *Guidelines for Preparing Mine Closure Plans in Québec, Canada* (2016).

Condition	Factor of safety
Bearing capacity of the foundation (ground) beneath the pile*	1.5 to 2.0
Local pile stability (for each bench)	
Short-term static analysis*	1.0 to 1.1
Long-term static analysis	1.2
Overall pile stability, failures at depth or in the foundation (ground)	
Short-term static analysis*	1.3 to 1.5
Long-term static analysis	1.5
Pseudo-static analysis*	1.1 to 1.3

*Based on the risk and confidence level.

Several factors must be defined during the design of WRPs, such as the height and volume, material quality, pile slope, foundation type and construction method (Klohn Leonoff Ltd., 1991; Piteau Engineering Ltd., 1991). The accurate characterization of the mechanical properties of WR materials, particularly its shear strength, is crucial in WRP design projects. Furthermore, since WRs are dumped and piled in very loose conditions (Aubertin, Bussière, & Bernier, 2002; Aubertin et al., 1996, 2021; Bard et al., 2011; Barton & Kjærnsli, 1981; Linero et al., 2007; Ovalle et al., 2023; Valenzuela et al., 2008; Zevgolis, 2018), the material is not expected to present dilatancy or peak strength. Consequently, engineering designs must be carried out using the critical shear strength mobilized at large strains, which should correspond to the maximum strength of the material due to the loose configuration of WRs.

2.2 Mechanical characterization and testing of coarse granular materials

This thesis is motivated mainly by the challenges of the mechanical characterization of coarse mine WR. However, this topic shares the same fundamental challenges encountered in other

coarse granular materials, such as gravelly soils and quarry rockfill materials. Namely, developing experimental methods capable to handle materials containing overzised particles, and analyses considering the particular behavior of coarse-grained materials. Therefore, the following sections on mechanical testing and behavior covers not only WR, but any other coarse-grained materials involved in geotechnical engineering.

Different types of shear tests with distinct stress paths and strain field conditions are used to assess soil deformation and strength properties. The most common testing methods are the direct shear and the triaxial compression tests, which are also used for coarse soils. This section mainly focuses on large testing devices that can handle coarse granular materials.

A representative elementary volume (REV) specimen is typically defined after testing standards such as ASTM D3080 and D7181 for direct and triaxial shearing, respectively. Standards define a REV depending on the characteristic specimen size X (e.g., height, width or diameter) and the coarsest particle in the material (with grain size d_{max}). The most common practice is to use a minimum value for the aspect ratio of the specimen $\alpha = X/d_{max}$. Recent studies (Cantor & Ovalle, 2023; Quiroz-Rojo et al., 2024) discuss further other REV attributes by incorporating effects of α and microstructural behavior. This is particularly important when dealing with coarse-grained soils, as a REV aims to test a specimen as coarse as the device can handle, minimizing the effects of the specimen size and allowing an adequate assessment of soil behavior.

2.2.1 Direct shear testing

The direct shear test (DST) comprises two rectangular or circular specimen-containing boxes horizontally split by a gap, whereupon the shear plane surface is pre-located. This is illustrated in *Figure* 2.13, where the effective normal stress (σ'_n) and horizontal shear stress (τ) are applied to the specimen. Essentially, one half is stationary and the other is moved horizontally under τ, along the predefined horizontal plane between the two boxes. Since pore water pressure (PWP) is not monitored, the test is performed at a constant strain rate, low enough to avoid excess PWP if the specimen is saturated (ASTM D3080). The vertical settlement during consolidation and shearing, and horizontal displacement during shearing are recorded by strain transducers.

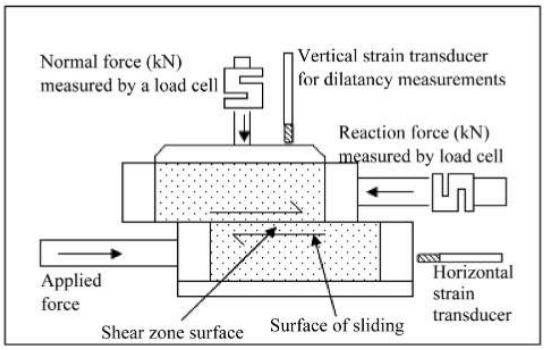

Figure 2.13 Schematic illustration of the forces applied in DST, after Wijeyesekera et al. (2013).

DST is adequate to test coarse-grained soils. *Table* 2.3 recapitulates large DST devices reported in the literature, showing tested materials having d_{max} as coarse as 85 mm. For example, a large box of 720×720 mm^2 is shown in *Figure* 2.14a, with the applied forces displayed in *Figure* 2.14b. The actuators apply vertical forces $F1, F2, F3$ for σ'_n, and F_s for τ, calculated from the shear cross-section area in the sliding zone along the predefined horizontal plane. Using this large device, Linero et al. (2020) have tested WR materials with aspect ratios $\alpha = W/d_{max} = 10$ (where W is the width of the specimen), which is the minimum α recommended for DST by the standard ASTM D3080. *Figure* 2.15 shows the test results displaying the variation of the ϕ' mobilized with horizontal shear displacement (*top-plot*). The *inset-plot* shows the repeatability of the friction angle at the largest displacement reached ($\phi'_{ds\ ld}$) at different σ'_n. The scatter is only $\pm 0.2°$, $1.3°$ and $0.9°$ for $\sigma'_n = 0.5,\ 1$ and 2 MPa, respectively. Furthermore, *bottom-plot* shows the variation of vertical settlement (δ_v) with shear displacement at different σ'_n. δ_v increases with σ'_n and stabilizes at larger shear displacements.

Table 2.3 Large DST devices reported

References	W (mm)	L (mm)	H (mm)	d_{max} (mm)
(Estaire & Santana, 2018)	1000	1000	1200	85
(Linero et al., 2020)	720	720	600	70
(Stark et al., 2014)	760	810	500	63
(TolouKian et al., 2018)	440	540	360	50
(Deiminiat et al., 2022)	300	300	150	5

DST is often criticized for its reliability in coarse materials due to the nonuniform distribu-

tion of stress at the edges, caused by the tilt of the loading plate (Castellanos & Brandon, 2013; Shibuya et al., 1997). Also, differential PWP in the specimen might occur, since the gap between the two halves might affect water drainage. The stress and strain fields are heterogeneous during shearing and cannot be used to assess the stiffness of the bulk material. However, DST is widely privileged because it is fast and simple to manipulate, and allows direct measurement of applied stresses (Fakhimi et al., 2008; Lini Dev et al., 2016; Matsuoka & Liu, 1998; Stark et al., 2014).

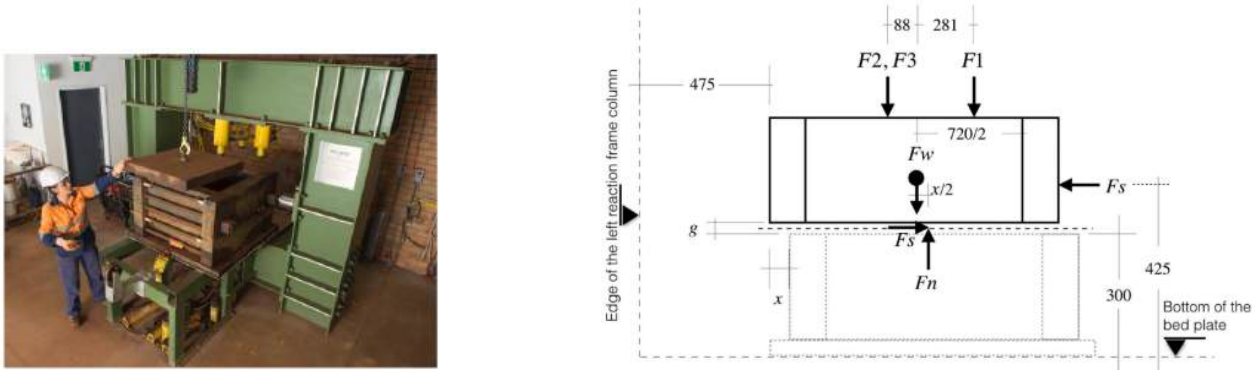

(a) (b)

Figure 2.14 A 720 × 720 mm squared DST box after Linero et al. (2020): (a) the loading frame and the shear box; (b) conceptual setup of the applied forces.

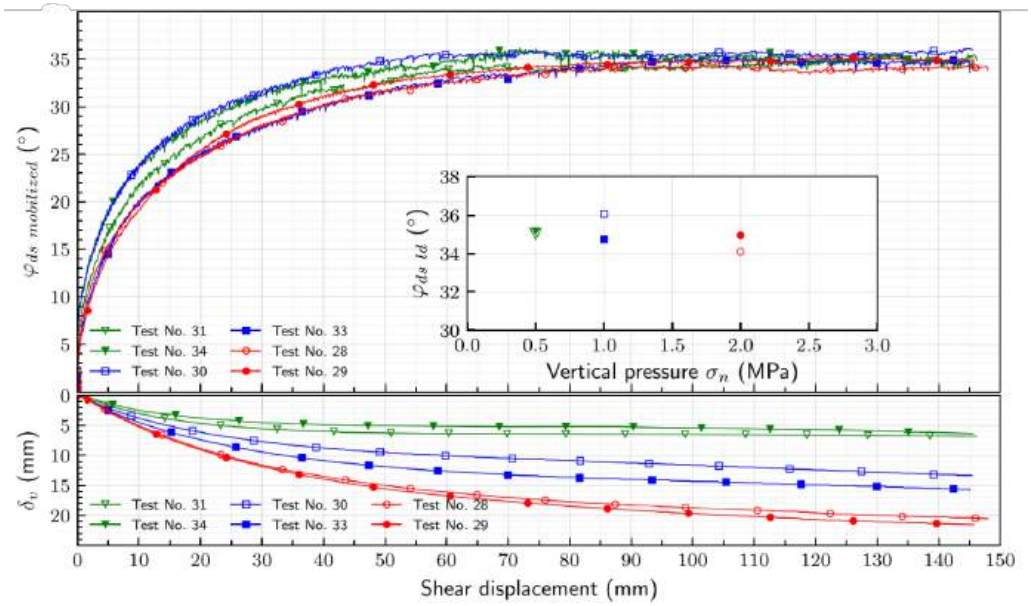

Figure 2.15 Test results from the 720 × 720 mm squared DST box after Linero et al. (2020): *top-plot* showing variation of ϕ' vs shear displacement (the *inset-plot* showing ϕ'_{max} repeatability at different σ'_n); and *bottom-plot* for vertical settlement variation.

2.2.2 Triaxial compression test

The conventional triaxial compression (CTC) test overcomes DST limitations by allowing relatively homogeneous strain fields and controlled stress paths (Lade & Duncan, 1976; Lambe, 1967). Conventionally, a cylindrical soil specimen in triaxial shearing, as shown in *Figure* 2.16, is loaded under axisymmetric conditions and controlled principal stresses ($\sigma_1, \sigma_2 = \sigma_3$). The specimen is covered by a waterproof membrane and includes a system to control soil saturation through the equilibrium of internal back pressure (σ_{cp}), PWP (u) and external confining pressure (σ_3). The Skempton coefficient ($B = \delta u/\delta\sigma_3$) is used to verify full saturation conditions once $B \geq$ 0.95. Once saturated, volume change is monitored through water drainage in the back pressure control line, while effective stresses are obtained as $\sigma'_3 = \sigma_3 - u$.

Three main kind of triaxial tests can be carried out: (i) Consolidation Drained (CD) test, with drained consolidation and shearing stages and continuous volume change monitoring; (ii) Consolidated Undrained (CU) test, with drained consolidation and undrained (i.e., constant volume) shearing, with PWP monitoring upon shear to obtain effective stresses; (iii) Unconsolidated Undrained (UU) test condition, where drainage is restricted during consolidation and shearing (i.e., constant specimen volume) and only total stresses are analyzed.

Unlike DST, where the failure plane is pre-defined, CTC test shearing allows "free" development of the failure surface throughout the specimen (Airey et al., 1985; Lade, 2016; Shibuya et al., 1997). Furthermore, CTC shearing enables accurate control and monitoring of PWP for saturated specimens, making it more versatile than DST. The measured specimen deformations in principal directions allow accurate estimation of the strain moduli (Lade, 2016). However, caution should be taken as end boundary effects (cap and base) can often induce nonuniform strain and stress distribution, leading to uncertainties in stress-strain behavior, volume change and PWP.

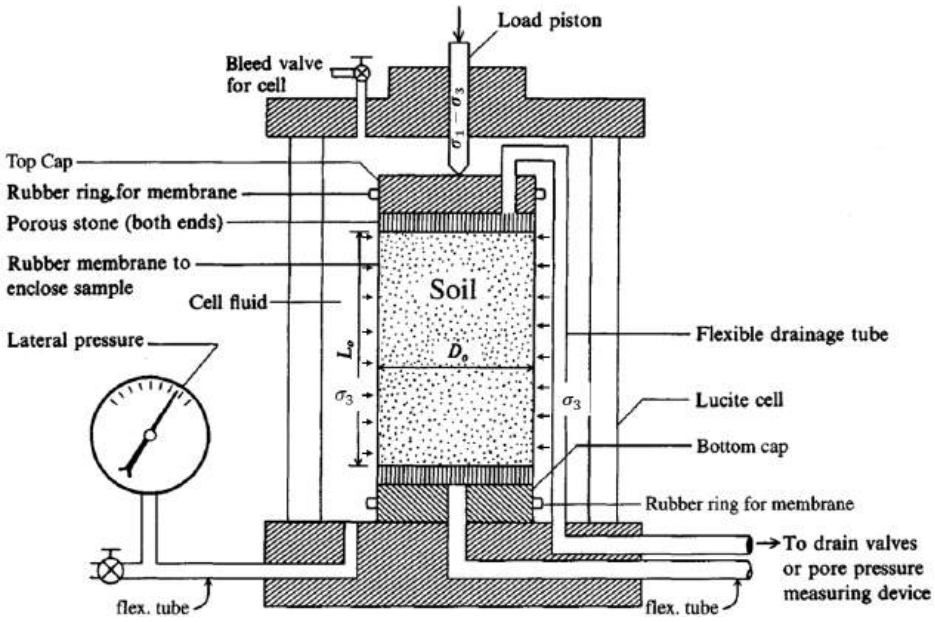

Figure 2.16 Schematic representation of a specimen in a triaxial shearing setup, after Bowles (1997).

Large-scale triaxial apparatuses are required to handle coarse soils. A typical example is shown in *Figure* 2.17, displaying a large CTC cell in École Centrale Nantes (France), allowing 1 m specimen diameter and 1.5 m high, where tests on materials having d_{max} up to 160 mm have been reported (Hu et al., 2011; Ovalle, 2013). This represents an aspect ratio $\alpha = D/d_{max} = 6$ (where D is the triaxial specimen diameter), which is the minimum α recommended by the standard (ASTM D7181, 2020) for CTC specimens. Typical stress-strain behavior is shown in *Figure* 2.18 depicting the response of the rockfill tested ($d_{max} =$ 160 mm) at $\sigma'_3 = 400$ kPa by Hu et al. (2011). The hardening of the strain is observed, while the volumetric change shows a contractive behavior. It is worth noting that $d_{max} = 160$ mm is still finer than the WR materials in the field, with d_{max} that can easily reach 1 m (see *Figure* 2.3). *Table* 2.4 lists some of the largest CTC cells ever reported worldwide, with maximum D of 1130 mm (Marsal, 1967).

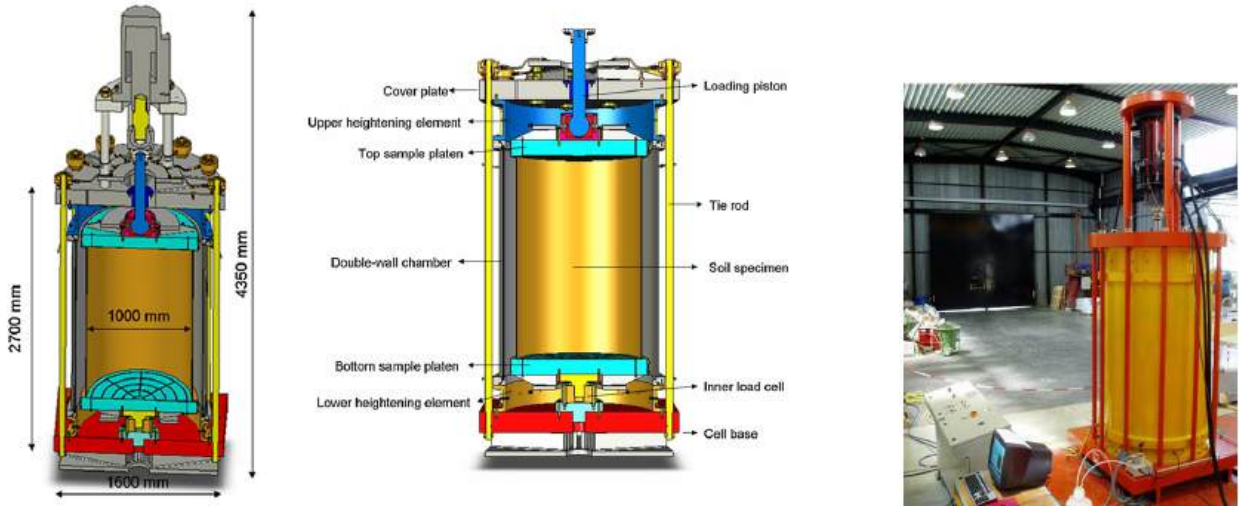

(a) (b)

Figure 2.17 Triaxial cell of 1000 mm diameter and 1500 mm height: (a) schematic setup after Hu et al. (2011); (b) the actual triaxial cell after Ovalle et al. (2014).

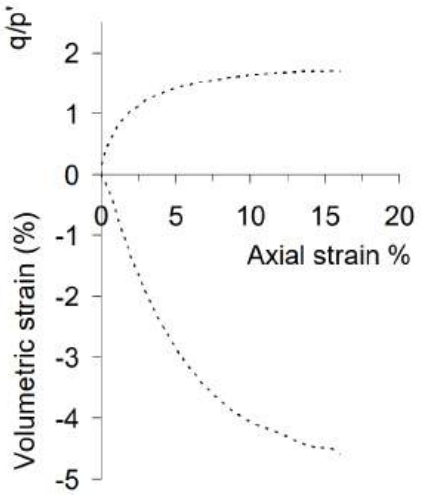

Figure 2.18 Stress-strain curve obtained at $\sigma_3' = 400$ kPa after Hu et al. (2011).

Table 2.4 Large CTC devices reported, *revised* from Hawley and Cunning (2017)

Laboratory	**D (mm)**	**Country**
CFE Rockfill laboratory*	1130	Mexico
State Key Laboratory of Coastal and Offshore Engineering*	1000	China
École Centrale Nantes	1000	France
University of Chile (Idiem Institute)	1000	Chile
Karlsruhe Institute of Technology	1000*	Germany
University of California - Berkeley	915	USA
Snowy Mountain Engineering Corporation, Cooma	570	Australia
Norwegian University of Science and Technology	500	Norway
Missouri Institute of Science and Technology	420	USA
Geodelft	400	Netherlands
University of Cataluña	300	Spain
University of Nottingham	300	UK
National Laboratory of Civil Engineering	300	Portugal
Building and Housing Research Center, Tehran	300	Iran
Polytechnique Montreal*	300	Canada

**added in this manuscript.*

2.2.3 Plate load tests on WR

Maknoon (2016) assessed the Young modulus (E) of WR using rigid plate loading both experimentally and numerically. The method used a large circular steel tank of 92 cm of diameter and 90 cm high shown in *Figure* 2.19a. WRs were mounted inside the tank, and rigid disks (weighing 8 kg each) positioned at the center for load application while recording subsequent settlements using gauges. Finite element simulations were also carried-out to replicate individual gauge measurements for comparison. The results are reported in *Figure* 2.19b showing good agreement between experimental and simulated analyzes. The estimates of E were between 0.5-40 MPa. On the other hand, the Poisson ratio (ν) of coarse-grained material is reported around $\nu = 0.3 \pm 0.05$ (e.g: (Das, 2019; Duncan & Bursey, 2013; Yang et al., 2018)). The variation is mainly due to the packing properties and mineralogy of the particles (Gercek, 2007).

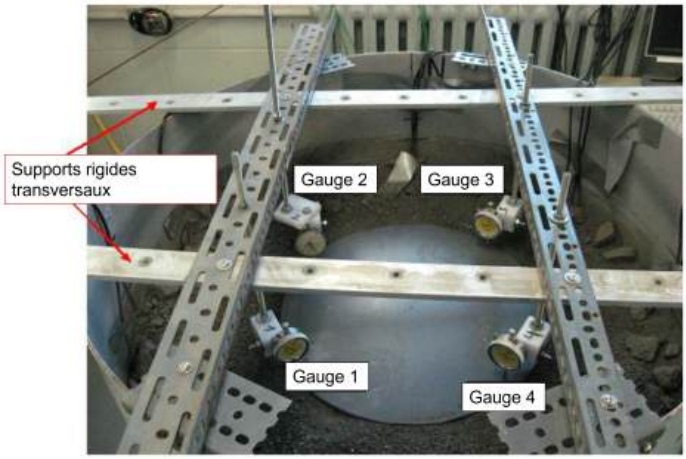

(a)

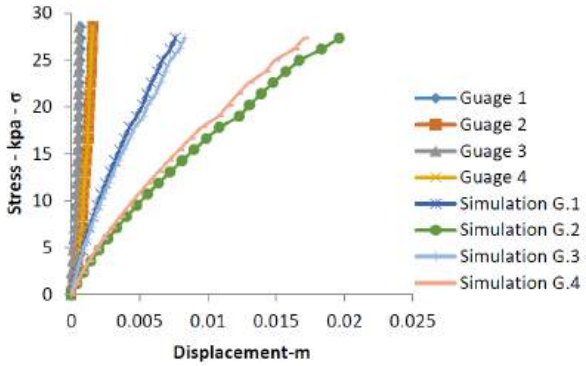

(b)

Figure 2.19 Assessment of Young's modulus E after Maknoon (2016): (a) experimental setup showing the settlement gauges and a large circular rigid steel tank of D= 92 cm and H=90 cm filled with WR; (b) test results comparing experimental gauge readings and simulated values.

2.2.4 Field (in-situ) testing

Most reported in-situ shearing tests are DST, due to their relative simplicity in execution and straightforward interpretation (Schultze, 1957). Jain and Gupta (1974) performed in-situ DST on a mixture of crushed sand rock and clay shales to study the shear strength for an embankment design (see *Figure* 2.20a). Boxes of different dimensions were used: $1.2 \times 1.2 \times 0.8$ m^3 (W×L×H) and a smaller one of $0.6 \times 0.6 \times 0.3$ m^3. The steel boxes with knife-like edges were buried in compacted rockfill having d_{max} up to 200 mm (8 in.) and 100 mm (4 in.) for larger and smaller boxes, respectively. As illustrated in *Figure* 2.20b, the setup uses sandbag dead weights to apply σ'_n and a bulldozer pulling the whole mass on rollers for shearing. The shear failure develops on the surface located at the bottom of the

box in contact with the surface of the platform. Horizontal shear displacement and vertical settlement were measured by dial gauges having 0.01 mm of sensitivity. *Figure* 2.20c shows the stress-strain curves of typical test results, where shear stress increases with horizontal shear displacement at a given σ_n. Visibly, the peak strength increases with increasing σ_n, which is consistent with the Mohr–Coulomb failure criterion. Furthermore, a ductile post-peak failure behavior is observed for all values of σ_n considered, possibly due to the presence of plastic clayey fines.

The study of Matsuoka et al. (2001) replicated this design, although it is entitled "a new in-situ DST box". However, as displayed in the conceptual sketch in *Figures* 2.21a, it is less laborious and extremely simplified compared to the original concept of Jain and Gupta (1974). The same shear cross section was maintained (1.2×1.2 m^2), and a bulldozer was used to apply horizontal forces with a chain. The setup in the field is shown in *Figures* 2.21b. Shear strength results presented in *Figure* 2.21c show good agreements between the boxes of different sizes used.

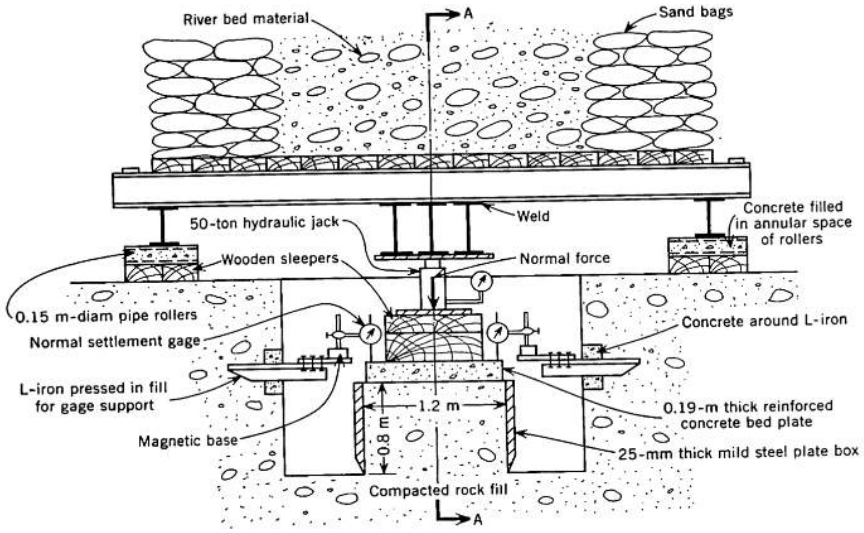

(a)

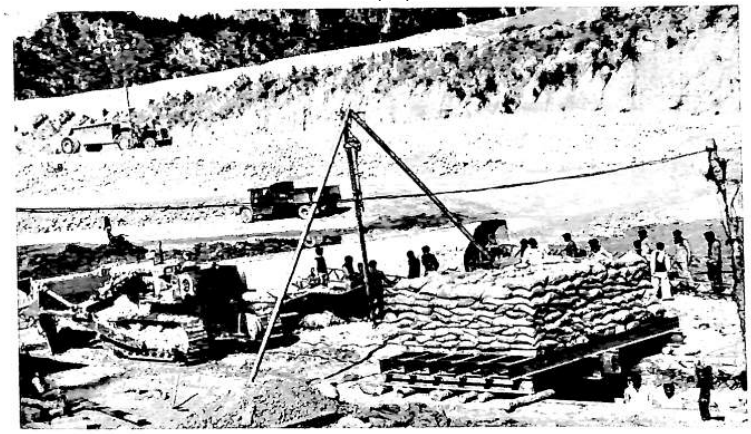

(b)

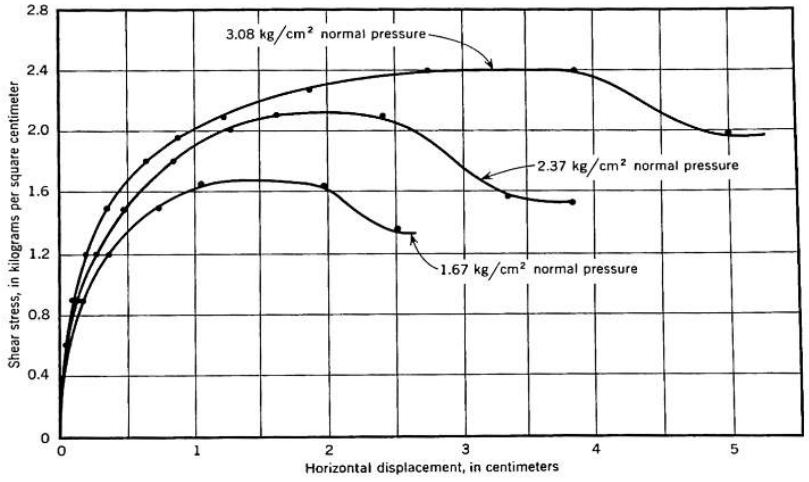

(c)

Figure 2.20 Large in-situ DST after Jain and Gupta (1974) with a shear surface of 1.2×1.2 m^2 for rockfill containing up to 200 mm particles: (a) schematic setup; (b) in-situ tests; (c) stress-strain results.

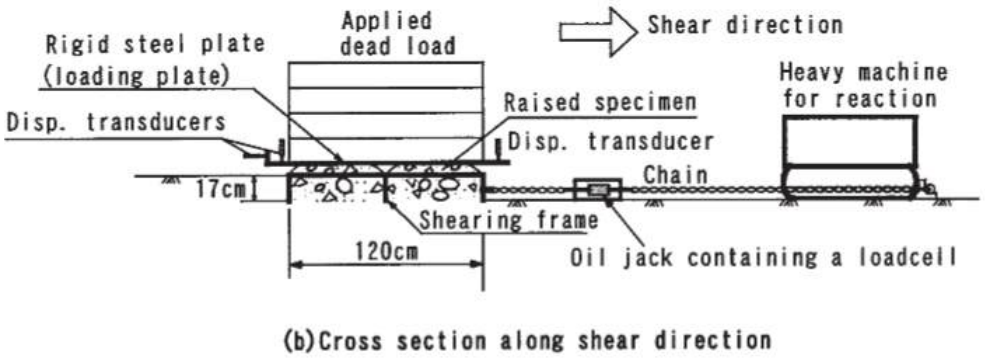

(a)

(b)

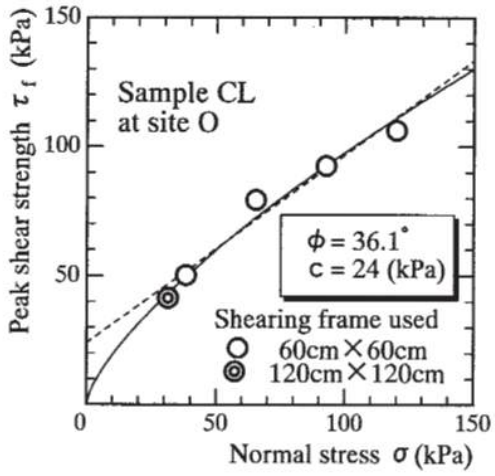

(c)

Figure 2.21 Large in-situ DST with a shear surface of 1.2×1.2 m^2 for rockfill containing d_{max} up to 150 mm after Matsuoka et al. (2001): (a) schematic setup; (b) in-situ test results after Liu (2009); (c) shear strength.

Barton and Kjærnsli (1981) proposed an in-situ tilting test to estimate rockfill shear strength at low stresses. The method involves using a large open rectangular box divided horizontally (see *Figure* 2.22a-1). The box is embedded in the ground (*Figure* 2.22a-2) and compacted by a machine passing "as in a regular pile construction". As displayed in *Figure* 2.22a-3, the surrounding rockfill is then removed to isolate the box. Subsequently, the middle belt is detached and the whole box is hydraulically raised at one end, as shown in *Figure* 2.22a-4. *Figure* 2.22b depicts a typical tilt-box of $5 \times 2 \times 2$ m^3 used in a rockfill dam in Italy (Barton, 2013). The tilt angle (α between $55 - 65°$) is the inclination tolerated before failure due to gravitationally induced shear and normal stresses (*Figure* 2.22a-5). As the authors claimed, $\alpha°$ mobilized corresponds to the material internal friction angle at extremely low stresses (Fannin et al., 2005; Iabichino et al., 2014; Leps, 1970; Ovalle et al., 2020; Seed & Goodman,

1964). Typical values are shown later in subsequent section on shear strength displaying material internal friction angle between $45 - 60^{\circ}$ at lower $\sigma'_n < 100$ kPa.

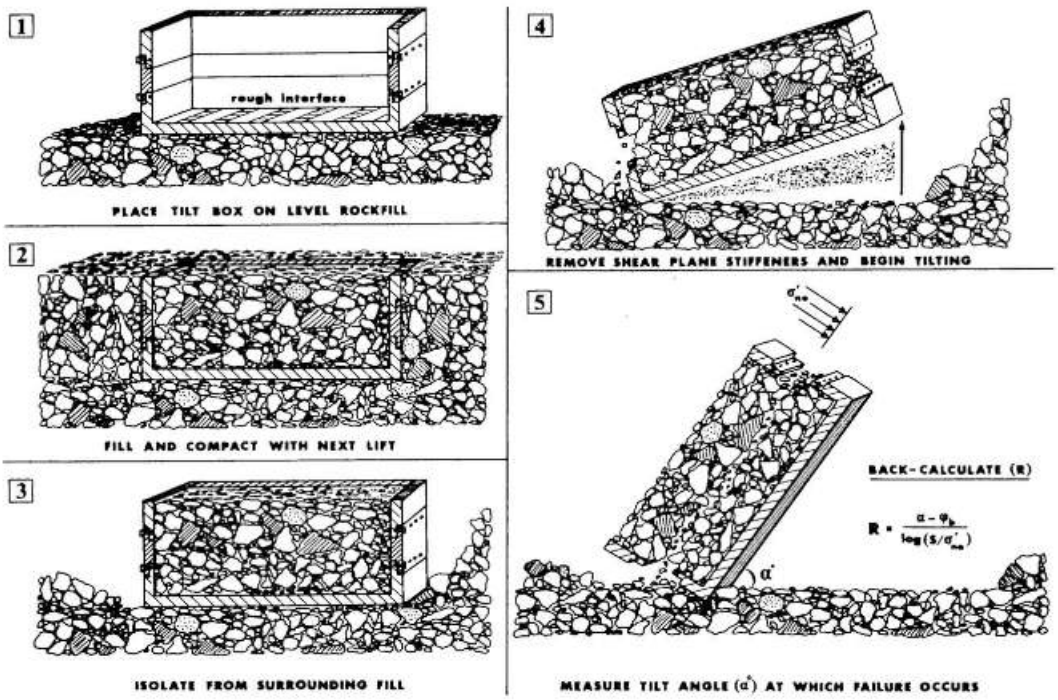

(a)

(b)

Figure 2.22 In-place tilt angle measurement after Barton and Kjærnsli (1981): (a) test procedures; (b) tilt-box of $5 \times 2 \times 2$ m^3 used at a rockfill dam in Italy after Barton (2013).

The reviewed in-situ designs have common limitations. Due to the difficulties of attaining high stresses, they can only provide information about the material at shallow depth behavior. The applied σ'_n must remain below the allowable bearing capacity of the platform on which the test is carried.

It is worth noting that, as discussed earlier, WRPs are in most cases above 100 m high, which approximately corresponds to a $\sigma'_n = 2$ MPa (Bard et al., 2011; Quezada & Villavicencio, 2024; Valenzuela et al., 2008). Therefore, low-level stresses attainable through the reviewed in-situ designs ($<$ 400 kPa) can only provide accurate information on the first $\approx$ 20 m. Nonetheless, it remains useful even for elevated piles, since in most cases failure occurs within shallow-depth surfaces (Arrieta & Zhang, 2024; Oyanguren et al., 2008; Seed & Goodman, 1964).

2.3 Mechanical behavior of coarse soils and rockfill materials

2.3.1 Critical state

The mechanical behavior of granular soils under shearing depends on it's initial state and loading conditions. Drained shearing of dense sand at a given σ'_n (*red* in *Figure* 2.23a) results in dilation due to particles overriding each other. As shown in *Figure* 2.23b, this mechanism implies increasing void ratio and mobilizes a peak shear strength. Upon continued shear strain, softening occurs towards a critical strength at the point A, which remains constant at indefinite shear deformation. In terms of volumetric strain, the soil reaches a critical void ratio (point *A'*) (Casagrande, 1936). On the other hand, loose materials under the same loading conditions (*blue* in *Figure* 2.23a) asymptotically reach the critical shear strength and contract toward the critical void ratio. This steady-state regime is known as the *critical state*, defined as the state in which the plastic shear strain continues indefinitely, without changes in soil volume or stress state. It has been widely shown experimentally that the critical state does not depend on the initial density or the stress path (Bolton, 1986; Casagrande, 1936; Kang et al., 2019; Mugele et al., 2024; Muir Wood & Maeda, 2008; Roscoe et al., 1958).

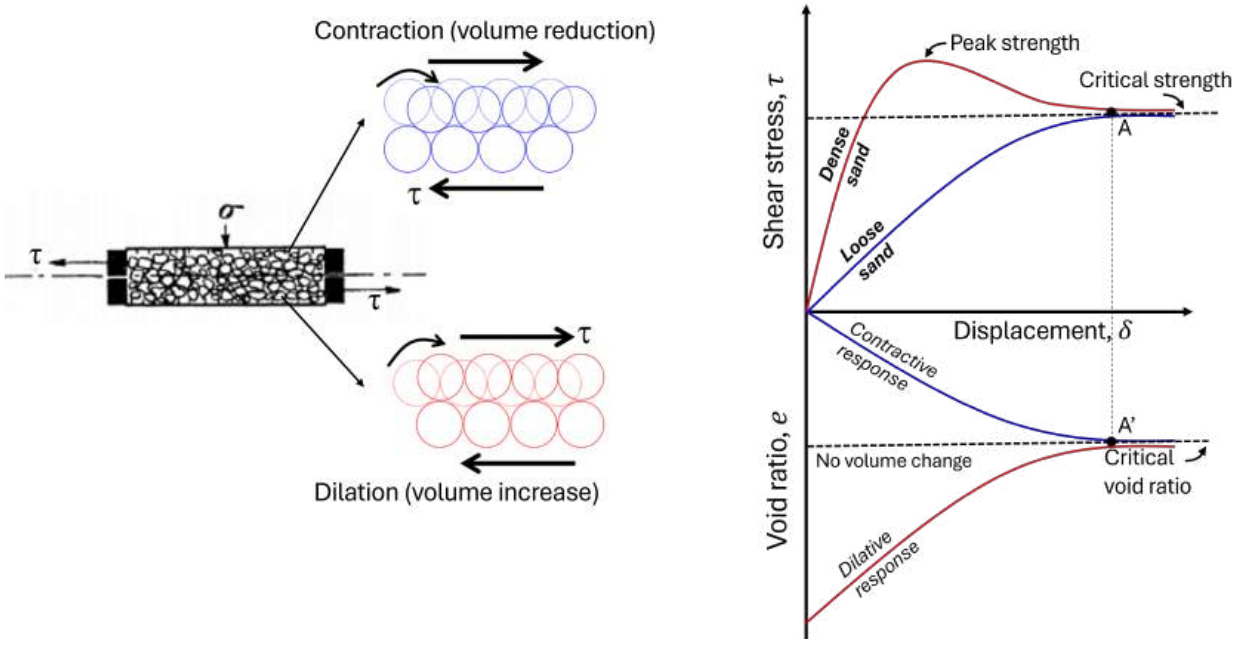

(a) (b)

Figure 2.23 Critical state of dense and loose cases: (a) representation of soil particles movement under direct shearing, *adapted* from Rowe (1962); (b) stress deformation relationships, *adapted* from Casagrande (1936).

Roscoe et al. (1958) tested saturated granular materials composed by steel balls in simple shearing under drained conditions. As previously stated, the loosely packed specimen in *Figure* 2.24a (point P) contracted toward a critical void ratio in state Q1. Point P' represents a subsequent shear test carried out at a denser state and higher σ'_n, and reaches its own critical point Q1'. The set of critical void ratios forms a line called the critical state line (CSL). *Figure* 2.24b displays the stress paths at constant σ'_n while τ increases. In granular soils, the shear strength can be interpreted using the Mohr-Coulomb failure criterion for cohesionless materials given by *Equation* 2.1, where ϕ'_{cr} is the critical effective friction angle. The projection of the tests in the Mohr-Coulomb stress plane shows that Q1 and Q1' lie on the same critical envelope inclined at a slope ϕ'_{cr}.

$$\tau = \sigma'_n \ \tan \phi'_{cr} \tag{2.1}$$

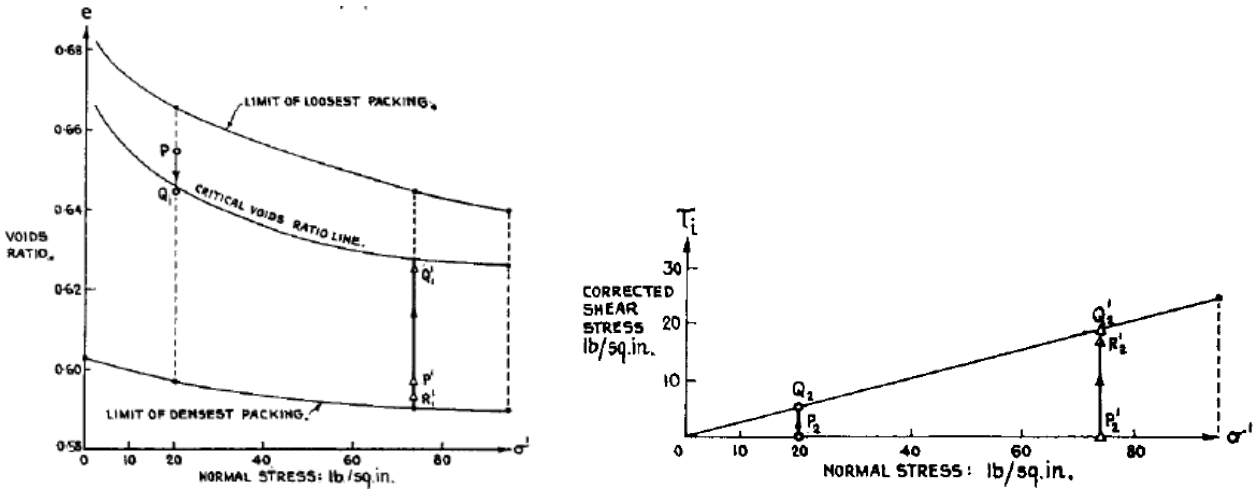

Figure 2.24 Critical state of steel balls after simple shear tests, from Roscoe et al. (1958).

Since the compaction properties depend on intrinsic material characteristics, such as PSD and grain shape, the density is usually expressed as the index density I_D (ASTM D4253, 2016) (also referred to as the relative density D_r in international literature outside Canada), related to the densest and loosest reference states. The definition of I_D is given by the following expression:

$$I_D = \frac{e_{max} - e}{e_{max} - e_{min}} \times 100 \tag{2.2}$$

where e_{min} and e_{max} are the void ratios at the loosest and densest states, respectively, obtained according to the standards ASTM D4253 and ASTM D4254 (2016). However, it is worth noting that the standards for e_{min} measurement are limited to particles finer than $d_{max} \leq 75$ mm. Therefore, I_D assessment of coarse soils remains challenging and/or inaccurate.

It has been shown that the CSL is unique for a given soil, regardless of the stress path and the initial density of the soil. If several other successive tests are performed on the same soil at different initial states (e, σ'_n), distinct critical state points will be aligned to form a unique CSL. For instance, Verdugo and Ishihara (1996) carried out a comprehensive experimental program on Toyoura sand, involving drained and undrained tests on dense and loose specimens, and showed a unique CSL on the $e - p'$ and $q - p'$ planes, as displayed in *Figures* 2.25a and 2.25b, where $p' = (\sigma'_1 + 2\sigma'_3)/3$ and $q = \sigma'_1 - \sigma'_3$ represent the effective mean stress and the deviatoric stress in CTC, respectively. Note that the relationship between ϕ'_{cr} and the ratio $M = q/p'$ at critical state is given by the following expression:

$$\sin \phi'_{cr} = \frac{3M}{6+M} \tag{2.3}$$

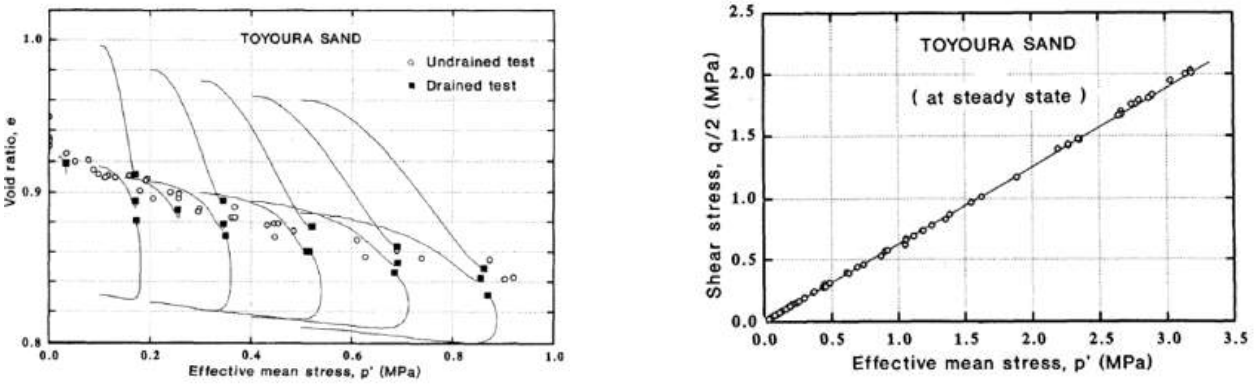

(a) (b)

Figure 2.25 Critical state of Toyoura sand after undrained and drained conditions on dense and loose specimens, on the (a) $e - p'$ plane and the (b) stress space $q - p'$, after Verdugo and Ishihara (1996).

The isometric view of the CSL in $e - p' - q$ space is shown in *Figure* 2.26. The CSL can be fitted to a logarithmic trend (*equation* 2.4) in $e - p'$ space and a straight line $q = Mp'$ in the stress space. Γ, λ, ξ and M are material constants, while p'_o is the reference pressure taken as 1 kPa.

$$e = \Gamma - \lambda log \left(\frac{p'}{p'_o} \right)^{\xi} \tag{2.4}$$

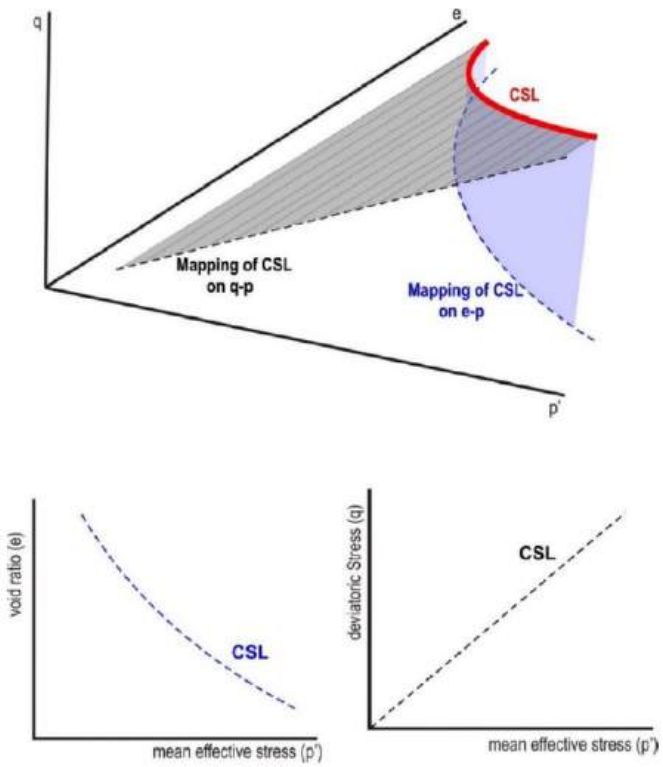

Figure 2.26 Isometric view of the CSL after Razavi (2023).

2.3.2 Representative elementary volume and specimen aspect ratio

International standards disagree on the minimum aspect ratio α that ensures a representative elementary volume (REV) of material to be tested under shearing (Quiroz-Rojo et al., 2024). *Table* 2.5 summarizes the α values recommended by testing standards worldwide. For CTC tests, the British BS 1377-8 (1990), American ASTM D7181 (2020) and DIN 18137 (2011)[2*] and Japanese JGS 0530 (2015) standards recommend minimum $\alpha = D/d_{max}$ of 5, 6 and 10, respectively. Concerning DST, the minimum values are $\alpha = W/d_{max}$ of 10, 6 and 23.5, respectively (where W is the width of the shear box). Also, the box height (H) must respect $W/H \geq 2$ and $W/d_{max} \geq 6$ for ASTM D3080 (2011), with relatively similar recommendations from other standards (Deiminiat & Li, 2022). These disagreements result in a significant scatter in published experimental results and might be at the source of the contradictory conclusions reported on size effects, as discussed later in this thesis.

[2*]similar as for the German DIN 18137

Table 2.5 Minimum α recommended by international testing standards after Cantor and Ovalle (2023).

Shearing Test	Standard	$d_{max} \leq$
Direct Shear	ASTM D3080	$\min\{H/6, D/10\}$
	BS 1377–7	$H/10$
	JGS 0561	$H/23.5$ '*... may be relaxed for soils that have a wide particle size range.*'
Triaxial	ASTM D7181	$D/6$
	BS 1377	$D/5$
	JGS 0520	$D/20$ for samples of $D = 35$ to 100 mm
	JGS 0530	$D/10$ for samples of $D = 300$ mm
	JGS 0520 and JGS 0530	$D/5$ '*... for soils having a wide range of particle sizes*'

Deiminiat et al. (2022) assessed the effects of $\alpha = W/d_{max}$ to ensure a REV specimen under DST, using three square boxes of width $W = 300$, 60 and 38 mm. A reference 'field' PSD was retained with a $d_{max} = 6$ mm on WR1 and WR2, as shown in *Figure* 2.27a-c. The results indicated that the friction angle decreased with W/d_{max} in both materials, converging toward a threshold value at which the results were deemed exempt from size influence (see *Figure* 2.28a-b). *Figure* 2.28c normalizes the obtained friction angle on every PSD, showing consistent results beyond $W/d_{max} \geq 60$, which is in agreement with other studies (Jacobson et al., 2007). Jewell and Wroth (1987) recommends a similar value, with aspect ratio calculated using the average diameter $W/d_{50} \geq 50$. However, if such a high α is required, DST may not be suitable for testing coarse materials, as the specimen would be significantly finer than the field material. Consequently, the properties of the fine fraction could differ substantially from those of the coarse fraction, potentially impacting the representativeness of the scaled specimen in terms of its mechanical behavior.

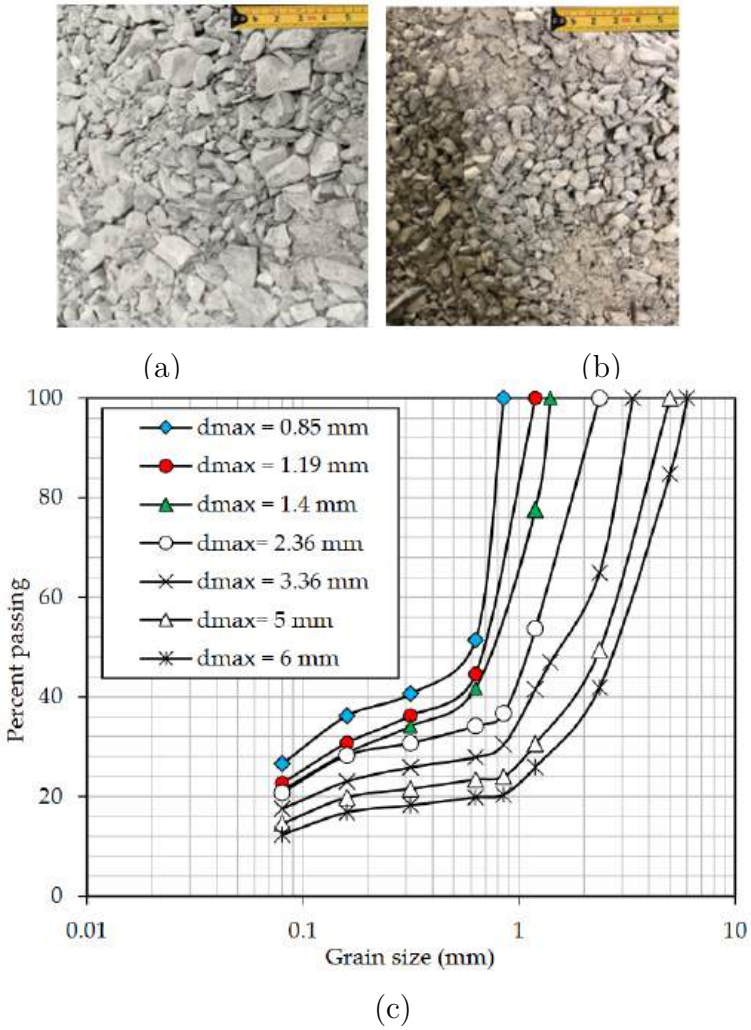

Figure 2.27 Tested WR material after Deiminiat et al. (2022): (a) WR1; (b) WR2; (c) PSDs of the scalped materials on both WRs.

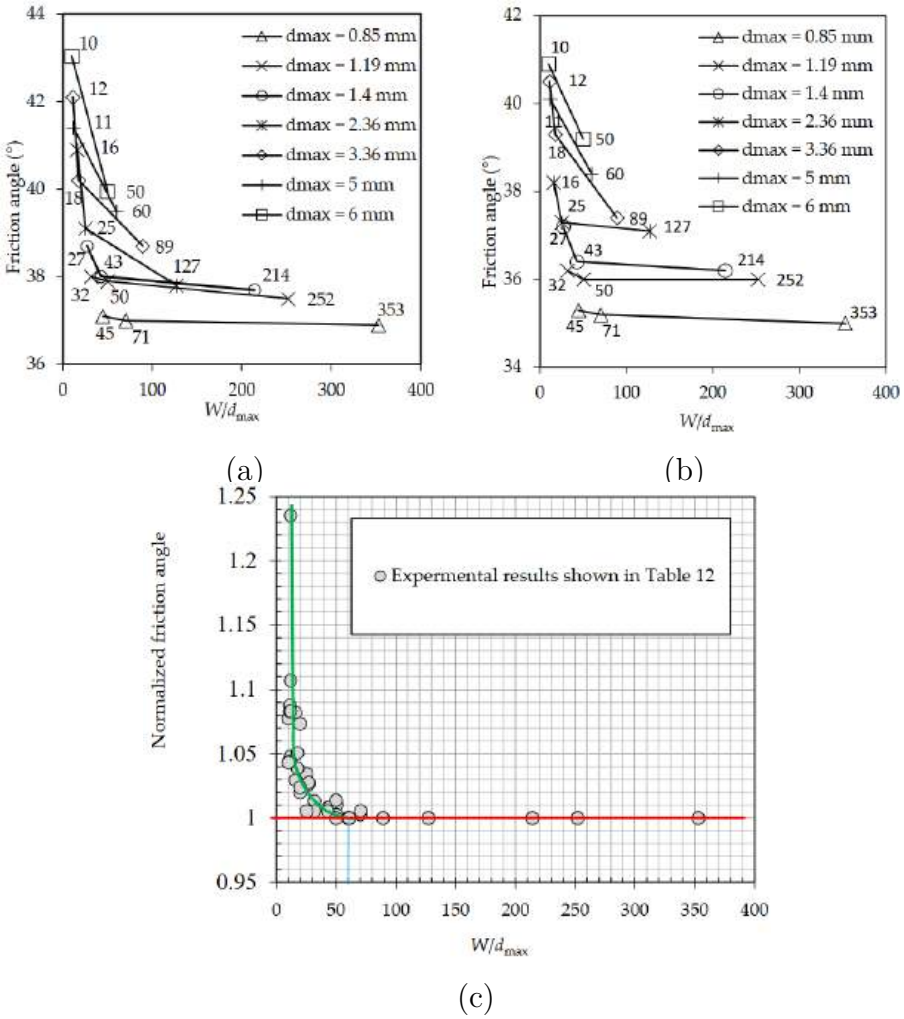

Figure 2.28 Results of the internal friction angle as a function of W/d_{max} after Deiminiat et al. (2022): (a) WR1; (b) WR2; (c) normalized friction angle.

Cantor and Ovalle (2023) evaluated $\alpha = H/d_{max}$ that allows a REV under virtual simple shearing tests using the Discrete Element Method (DEM). The setup is shown in *Figure* 2.29A for different α and grain size span ($S = [d_{max} - d_{min}]/[d_{max} + d_{min}]$) considered. *Figure* 2.29B shows the distributions of S studied. The results revealed that column-like structures (CLS) at the microstructural level enhance the macroscopic specimen size effect. *Figure* 2.30A shows that CLS fluctuates and crumbles at the specimen boundaries when low values of α are used (a-b), causing uncertainty and scattering in the shear strength. *Figure* 2.30A-(c and d) reveal that the CLS do not reach specimen boundaries for the showcased $\alpha = 43.2$. *Figure* 2.30B-a indicates that the threshold value at which CLS height ceases to reach the specimen boundaries is as early as $\alpha \geq 15$. This is further shown in *Figure* 2.30B-b where the mobilized ϕ_{cr} remains consistent beyond $\alpha \geq 15$, regardless of the size span S.

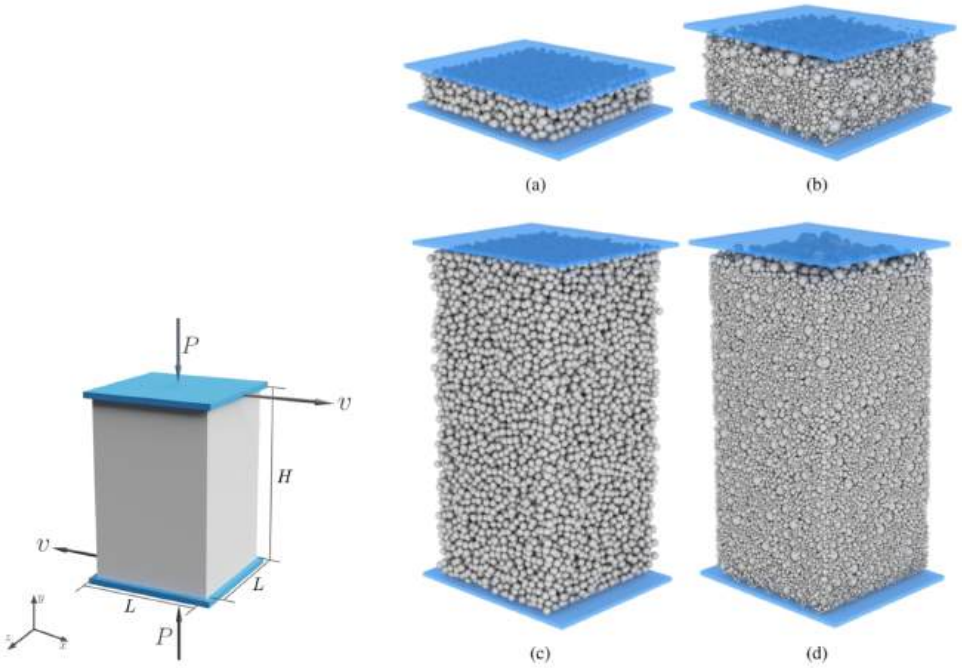

(A)

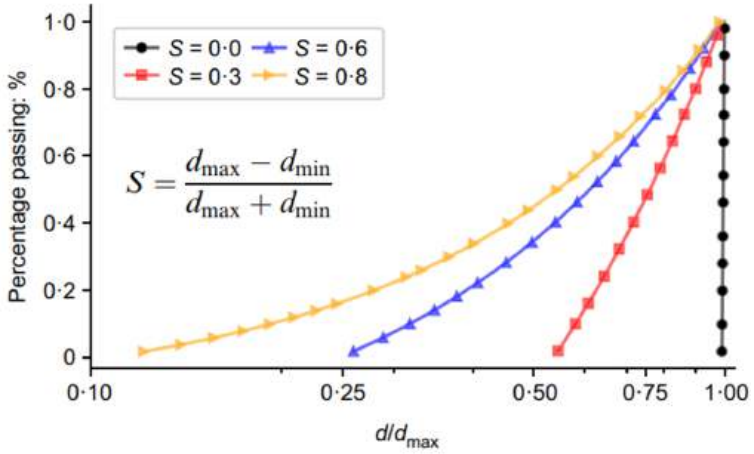

(B)

Figure 2.29 DEM simple shearing setup after Cantor and Ovalle (2023): (A) screenshots of specimens with grain size span $S = 0$ and $\alpha = 4.7$ (a) and 43.2 (c), and $S = 0.8$ with $\alpha = 4.8$ (b) and 43.2 (d), respectively; (B) PSDs tested, having $d_{max} = 20$ mm on all specimens and each grain size d contributes the same volume to the assembly.

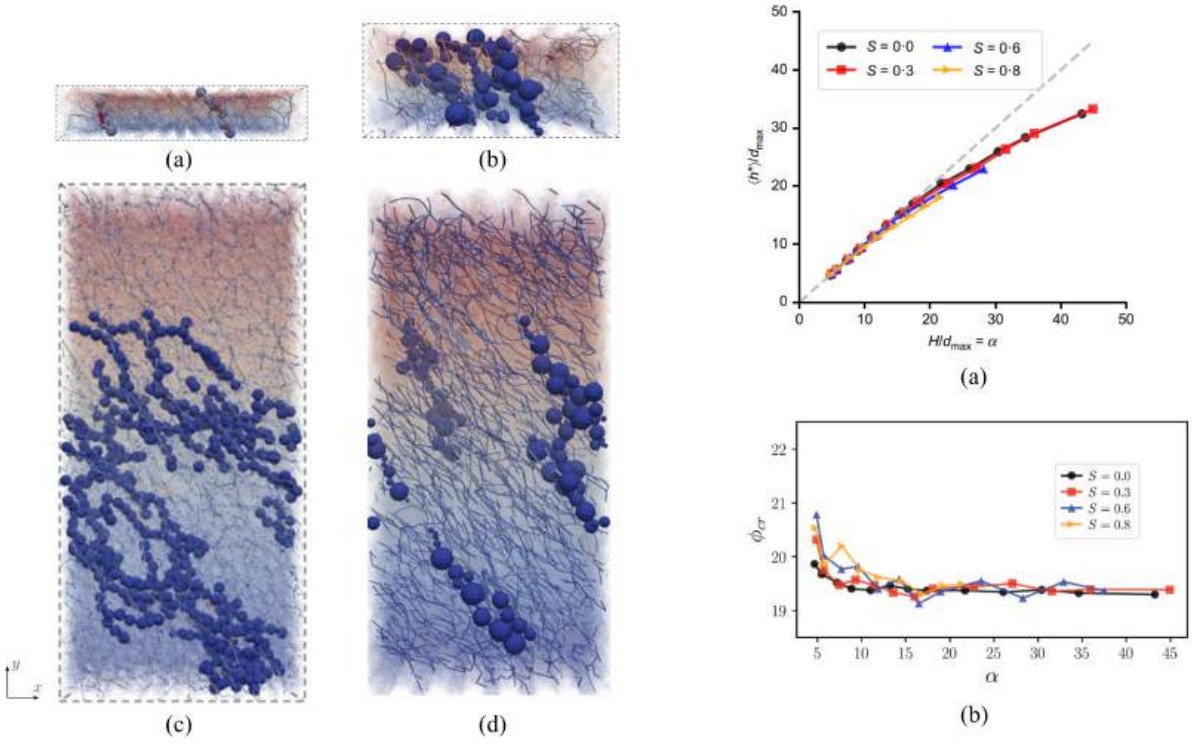

(A) (B)

Figure 2.30 Specimen size effects results after Cantor and Ovalle (2023): (A) column-like structures (CLS) of specimens with grain size span $S = 0$ and $\alpha = 4.7$ (a) and 43.2 (c), and $S = 0.8$ with $\alpha = 4.8$ (b) and 43.2 (d), respectively; (B) effects of α on CLS height (h^*/d_{max}) (a) and ϕ_{cr} (b).

2.3.3 Shear strength of coarse-grained soils

Significant natural variability of the shear strength is expected depending on soil type, PSD, mineralogy, void ratio, moisture content, and local heterogeneities (Mitchell & Soga, 2005; Phoon & Kulhawy, 1999; Terzaghi et al., 1996). In coarse granular soils, the shear response depends on the sizes, mineralogy, and shapes of the particles for a given σ'_3 (Holtz & Kovacs, 1981; Mitchell & Soga, 2005; Zhang et al., 2020). *Figure* 2.31a after Schmertmann (1978) illustrates the variability of the maximum effective internal friction angle (ϕ'_{max}) with relative density (D_r also known as index density I_D in Canada) and gradation. It can be seen that ϕ'_{max} increases with I_D on a given gradation, with coarser grains and well-graded PSDs mobilizing higher values than poorly and fine-grained ones. For $I_D = 0$, the influence of gradation shows scattering on ϕ'_{max}, between $28 - 38°$, which reduces between $42 - 46°$ for $I_D \geq 90$. This is because the prevalent void space in poor-graded (uniform) PSDs and lower I_D range causes more particle rearrangement upon shearing, thus mobilizing lower and

scattered ϕ'_{max} values. NAVFAC (1982) reported similar correlations in terms of void ratio, unit weight and USC soil classification (see *Figure* 2.31b). ϕ'_{max} increases with the material gradation as the void ratio decreases (unit weigth increasing); this trend increases with high I_D values. For a given USC soil class, a scatter of about 10° is observed for any slight variations of the void ratio (± 0.3). However, it is important to note that these charts do not disclose any information regarding the stress state, which, together with density, defines the state of the material. For instance, a specimen prepared at high I_D will certainly behave dilatant with high ϕ'_{max} at relatively low stresses; however, at a given elevated stress threshold the response will evolve towards contractancy, with a lower ϕ'_{max}; this is particularly relevant in crushable materials. Therefore, correlating the shear strength only with I_D results in a limited analysis, and the influence of the stress state should be also considered.

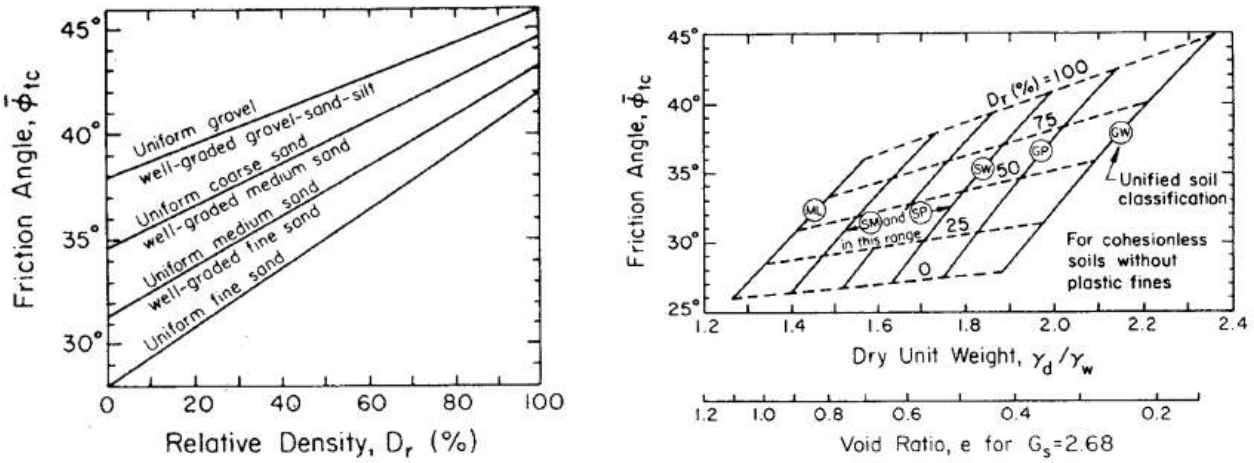

(a) (b)

Figure 2.31 Variation of ϕ'_{max} in cohesionless soils (accessed from Mitchell and Soga (2005)): (a) as function of D_r (also known as Index density I_D in Canada) and gradation after Schmertmann (1978) ; (b) as function of void ratio, unit weight and D_r after NAVFAC (1982).

Leps (1970) compiled the shear strength properties of rockfills using several results from large triaxial tests carried out in the 1960s in the Laboratories of El Infiernillo Dam (Mexico) (Marsal, 1968) and the University of Berkeley (USA) (Marachi et al., 1972), both with triaxial cells capable of testing specimens of $D = 1000$ mm. Later, this compilation has been updated by several authors by adding new results (Indraratna et al., 1993; Linero et al., 2007; Ovalle et al., 2020). *Figure* 2.32 presents the most recent compilation done by Ovalle et al. (2020) of 150 triaxial datasets of sands, WR and rockfills. As stated earlier in *Section 2.2.4*, ϕ'_{max} values between $45 - 55°$ at $\sigma'_n < 100$ kPa are reported. For a given σ'_n, the scatter on ϕ'_{max} depends on grading, mineralogy and shapes of the particles, USC classification, and

void ratio. In addition, ϕ'_{max} reduces significantly as σ'_n increases. For example, at $\sigma'_n = 5$ MPa (corresponding to a WRP of above 400 m high), ϕ'_{max} ranges around $30 - 42°$. This is explained by the mechanical degradation produced mainly by grain breakage. At high stresses (equivalent to elevated WRPs heights), interparticle contact forces might exceed the grain fragmentation strength and generate crushing within the granular soil (Bard et al., 2007; Barton & Kjærnsli, 1981; Linero et al., 2007). As a result, grading evolves and new fine fragments fill the voids between coarse grains, increasing volumetric contraction. This effect reduces dilatancy and the peak strength of dense materials, resulting in ϕ'_{max} reduction, as shown in *Figure* 2.32b. Alternatively, the shear strength envelope of crushable materials can be represented by a non-linear envelope in the $\tau - \sigma'_n$ stress plane. For instance, *Figure* 2.33 presents envelopes of WR materials from copper mines in Chile, tested in a large triaxial cell (D=1000 mm) at high σ'_n up to 4 MPa.

Barton and Kjærnsli (1981) proposed an empirical shear strength failure criterion given by *Equation* 2.5, which considers the non-linearity through σ'_n dependence.

$$\tau = \sigma'_n.tan\ (R.log\ (S/\sigma'_n) + \phi_b) \tag{2.5}$$

where R is the equivalent roughness, S is the equivalent compression strength and ϕ_b is the basic friction angle obtained from the tilt test seen earlier in *Figure* 2.22 from the same authors. The definitions of R and S are made empirically from abacuses shown in *Figures* 2.34a-b, respectively. R is estimated considering material origin, particle asperities (roundness/roughness) and porosity after compaction. S, on the other hand, incorporates the average particle size d_{50} and uniaxial compression strength (UCS) of the parent rock. For instance, the gradations A and B, showcased in *Figure* 2.34b, estimate $S \approx 150 \times 0.3 = 45$ MPa and $S \approx 150 \times 0.2 = 30$ MPa (for a UCS=150 MPa), respectively. The effects of the variation of R and S are shown in *Figure* 2.34c. For a constant R and σ'_n, the friction angle decreases with lower S values, and vice versa when S is constant.

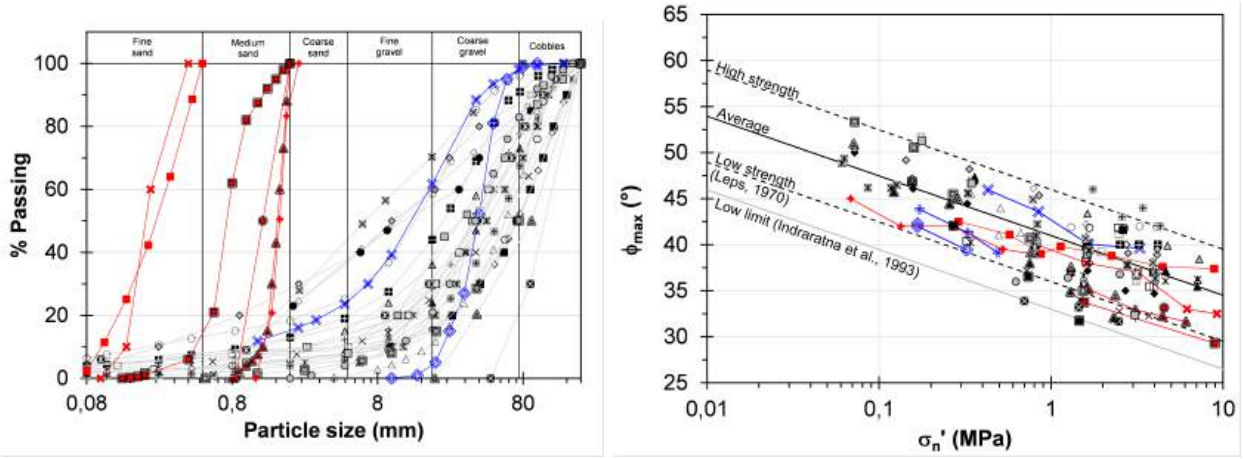

(a) (b)

(c)

Figure 2.32 Shear strength of coarse materials compiled after Ovalle et al. (2020): (a) PSDs of the compiled dataset; (b) ϕ'_{max} vs σ'_n.

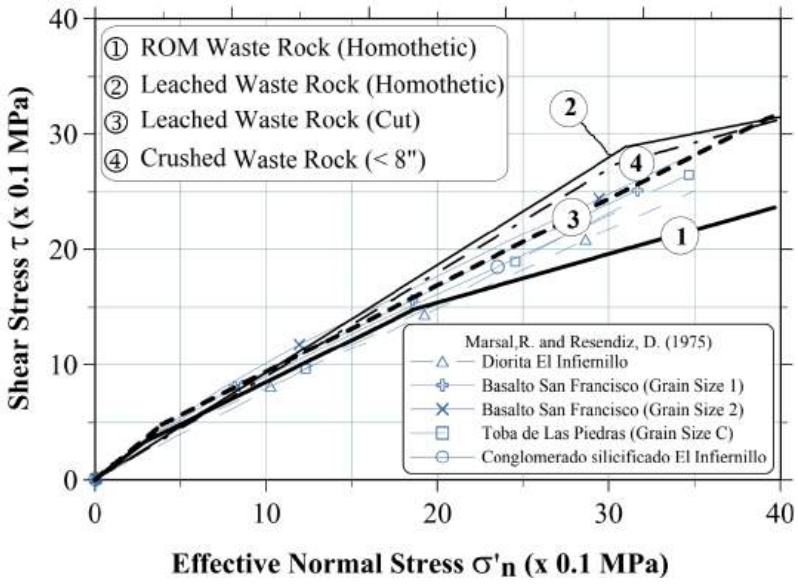

Figure 2.33 Failure envelopes of WR specimens showing non-linearity of the strength envelope at high stresses, after Bard et al. (2007).

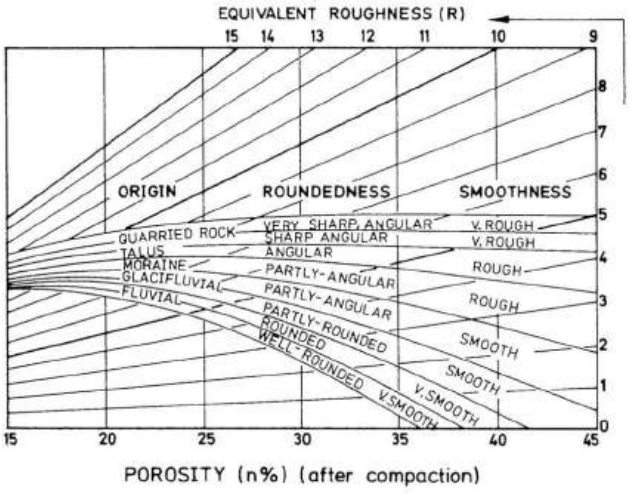

(a)

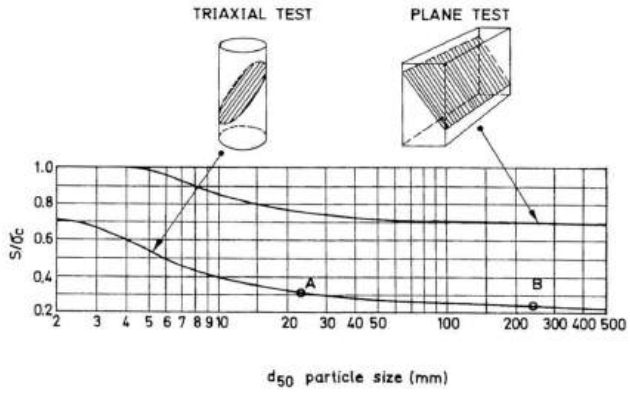

(b)

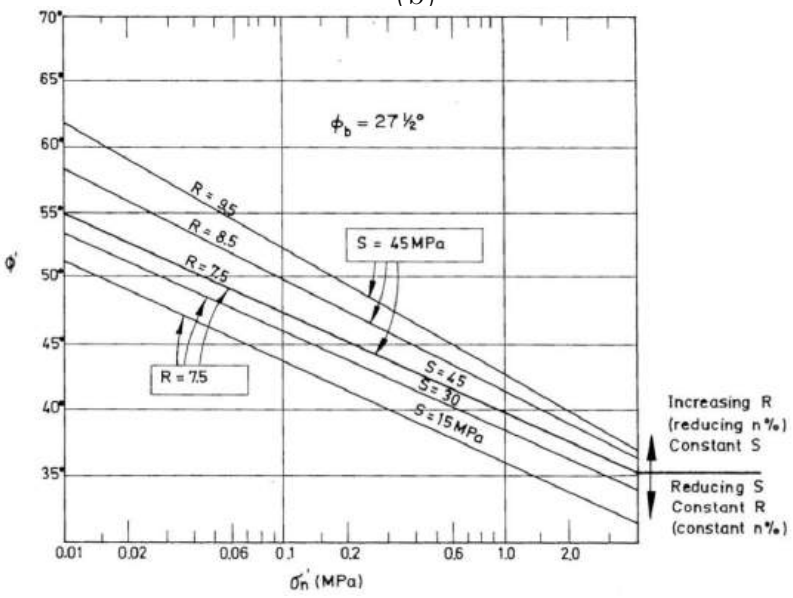

(c)

Figure 2.34 Estimation of the material paremeters from Barton-Kjaernsli shear strength criterion (Barton & Kjærnsli, 1981): (a) equivalent roughness R; (b) determination of the equivalent compression strength S; (c) effect of R and S on the estimated shear strength.

2.3.4 Effects of particle strength and particle crushing in coarse soils

Any granular material under relatively high stresses might experience grain crushing. However, coarse soils and rockfills are particularly vulnerable to this phenomenon, since larger grains have lower crushing strength. This is because, as stated by the classical theories of brittle solids mechanics (Griffith, 1921; Weibull, 1939), particle fragmentation occurs by the propagation of existing flaws in rock particles, and the probability of having weak flaws increases with the size of the particles (Marsal, 1967).

As shown in *Figure* 2.35, the mean characteristic crushing strength of particles from various rockfill materials decreases with increasing size (Ovalle et al., 2020). Each point represents a mean strength value after dozens of lump tests (compression between rigid platens until particle failure); for comparison purposes, the crushing strength is calculated as F/d^2, where F is the force at grain failure and d is the diameter of the rock particle. *Figure* 2.36 evidences that the higher the uniaxial compression strength (UCS) of the rock particles, the higher the shear strength of rockfill materials composed by those particles. Therefore, more resistant particles mobilize higher dilatancy and shear strength, while crushing becomes imminent in weaker particles, resulting in lower strength.

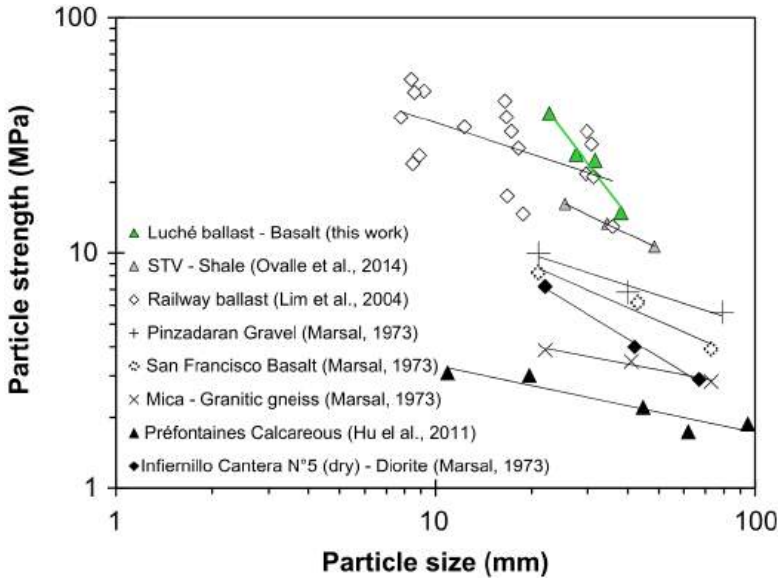

Figure 2.35 Variation of the average particle strength UCS with particle size after Ovalle et al. (2020).

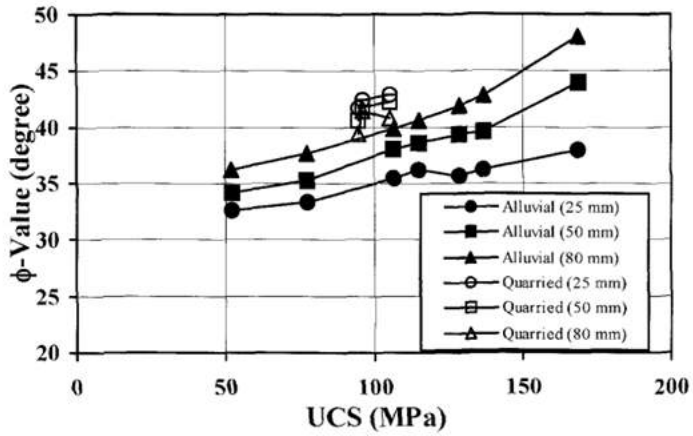

Figure 2.36 Particle strength correlation with the shear strength: ϕ' vs UCS in quarried and alluvial rockfills after Varadarajan et al. (2006).

The amount of grain crushing is typically quantified by a ratio between the initial PSD and the one after testing. Marsal (1967) defined a breakage ratio (B_g) as the positive sum of the percentages by weight differences before and after the test. For instance, for the same set of materials shown in *Figure* 2.32, *Figure* 2.37a exhibits increasing B_g with σ'_3, which results in decreasing shear strength in *Figure* 2.37b.

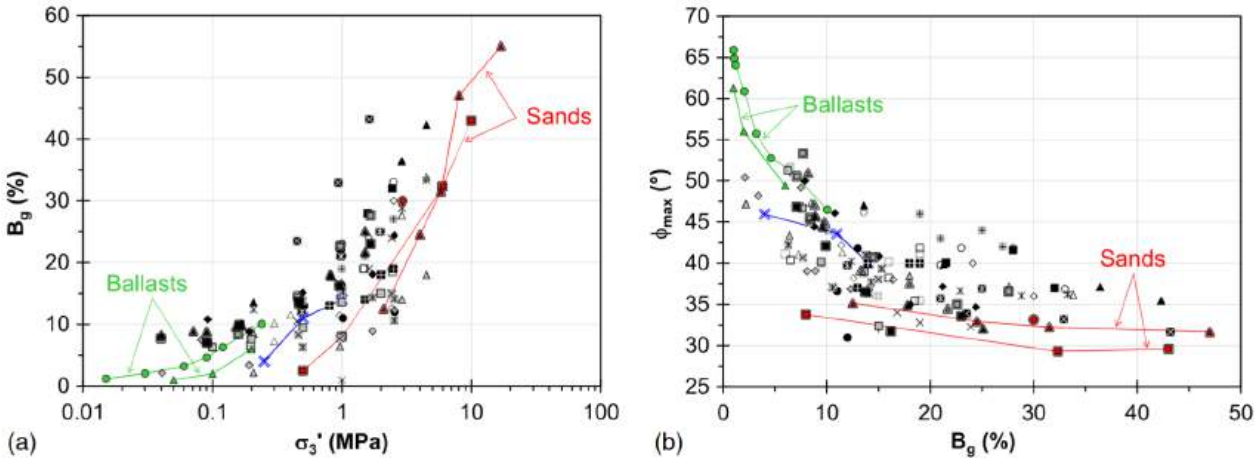

Figure 2.37 Variation of particle crushing with σ'_3 after Ovalle et al. (2020): (a) B_g vs σ'_3; (b) B_g vs ϕ_{max} (markers legend same as in Figure 2.32).

Particle strength is also sensitive to the presence of water (Oldecop & Alonso, 2003; Ovalle, 2018). In effect, humidity promotes corrosion of internal flaws (microcracks) in rock particles, decreasing individual particle crushing strength. As a result, B_g increases with the material

humidity (Osses et al., 2021; Ovalle et al., 2015). For instance *Figure* 2.38 presents the results of Osses et al. (2024) after oedometric compression tests on large specimens of 720 mm of diameter, using iron mining WR material and varying the material humidity through total suction (ψ); ψ=0 MPa are water saturated specimens and ψ >30 MPa are relatively dry specimens (water content less than 5 %). They used two specimens with parallel PSD: sandy fraction (S, d_{max} =2.5 mm) and gravelly fraction (G, d_{max} =50 mm). The results indicate that the coarser the material and the higher the humidity (i.e., lower ψ), the higher the compressibility. This is due to increasing particle crushing with both particle size (i.e., size effect in particle strength) and humidity (i.e., corrosion effect due to humidity).

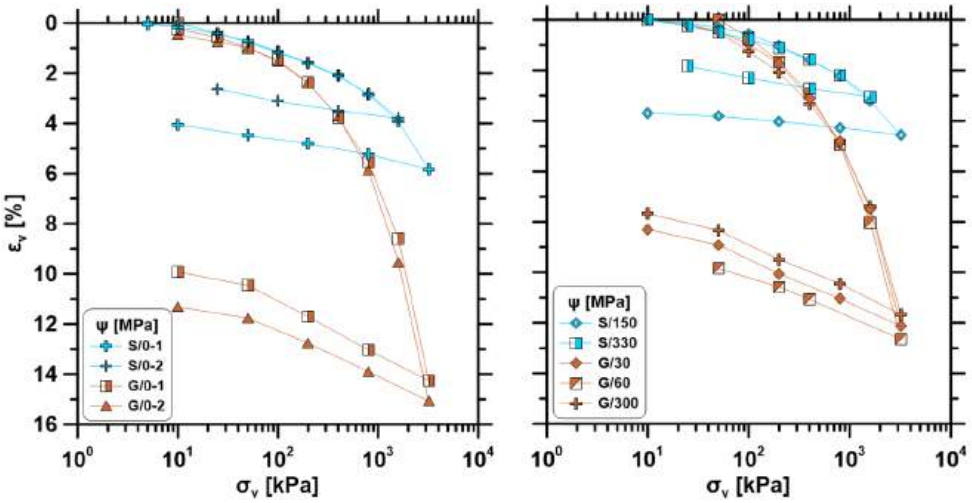

Figure 2.38 Compressibility curves of S and G material after Osses et al. (2024).

2.3.5 Effects of particle size distribution

Coarse granular materials can have PSDs that vary significantly from poor uniform grading to well-graded materials, as shown earlier in the case of WRs (refer to *Figure* 2.3). For a given density, the stress-strain behavior of a granular soil depends on its initial density, PSD (and its variation upon crushing) and characteristic particle shape. This is particularly the case for the volumetric response (dilatancy/contractancy) and the peak shear strength. Also, the location of the CSL in the $e - p'$ space is affected by the PSD.

Intending to study the effect of the PSD in granular materials, Li et al. (2015) presented the results of several drained triaxial compression tests on Hostun sand and Glass beads with varying grading ($C_u = 1.1 - 20$); *Figure* 2.39a shows the PSD of the tested materials. *Figure* 2.39b and 2.39c present the results on Glass beads and *Figure* 2.39d and 2.39e displays the results on Hostun sand. Overall, the CSLs of both materials shift down with

increasing C_u, which is equivalent to the effect of grading evolution during particle crushing (Muir Wood & Maeda, 2008; Ovalle & Hicher, 2020). Interestingly, *Figure* 2.39b and 2.39d indicate that the critical friction angle does not depend on the PSD. Indeed, provided that grain mineralogy, characteristic particle shape and grain surface roughness remain constant, substantial experimental evidence (Amirpour Harehdasht et al., 2018; Deng et al., 2021; Klinkmüller et al., 2016; Li et al., 2013; Yang & Luo, 2018) and numerical studies (Azéma et al., 2017; Cantor et al., 2018; Carrasco et al., 2025; Muir Wood & Maeda, 2008; Voivret et al., 2009; Wu et al., 2021) have indicated that gradation does not influence ϕ'_{cr} of granular materials.

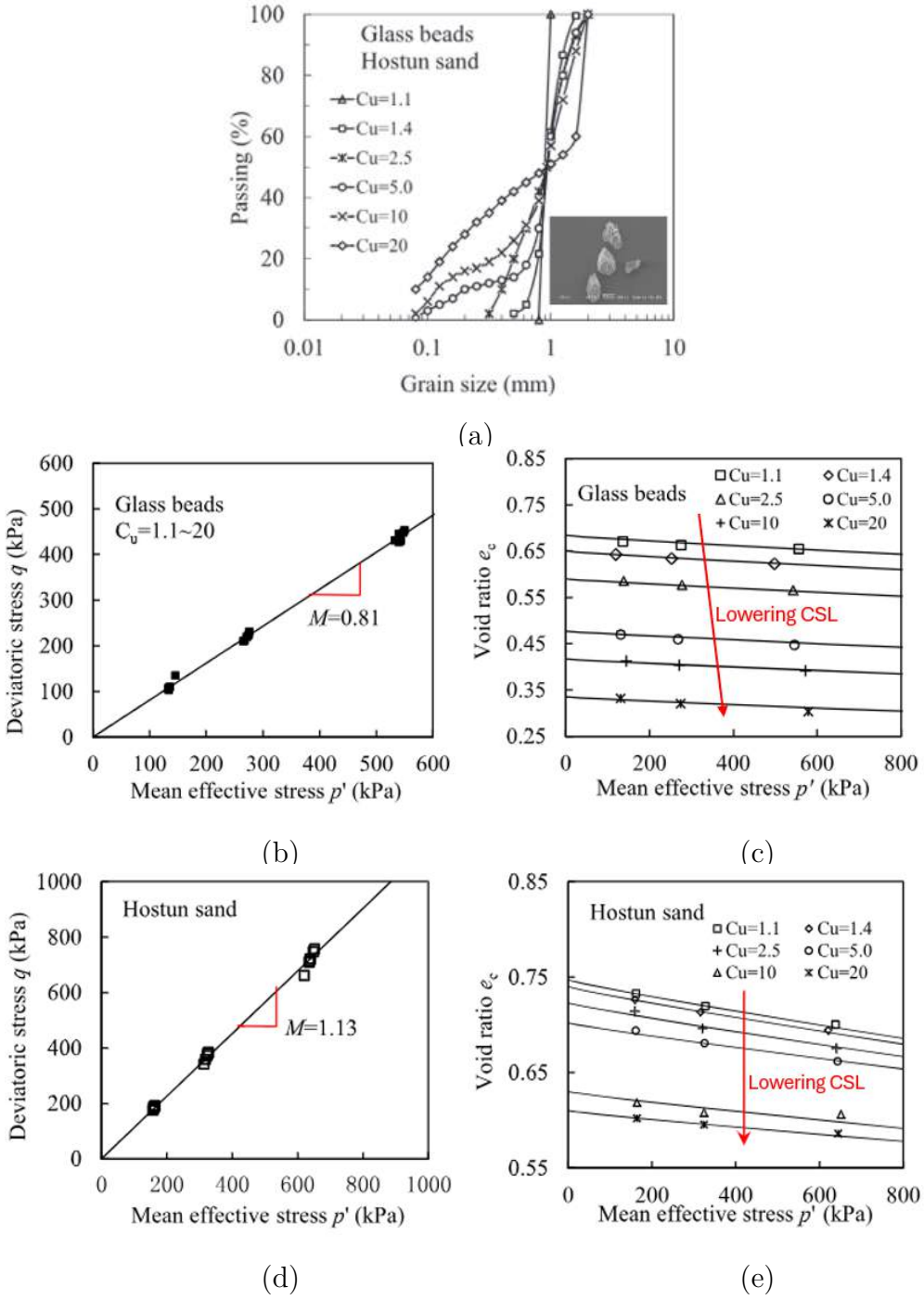

Figure 2.39 PSD effects on CSL, *modified* from Li et al. (2015): (a) PSDs investigated; (b-c) CSL in $q-p'$ and $e-p'$ on Glass beads, respectively; (d-e) CSL in $q-p'$ and $e-p'$ on Hostun sand, respectively .

Polanía et al. (2023) explored the effect of gradation using drained triaxial shearing experiments on spherical ceramic bead materials. 18 specimens were built using the grain size span

($\lambda = d_{max}/d_{min}$) varying from 2 to 200. *Figure* 2.40A shows (a) monodisperse, (b) bidisperse and (c-d) polydisperse specimens. The photos of the particles are shown in *Figure* 2.40B, respectively. The results in *Figure* 2.40C indicate that ϕ'_{cr} around 23.5±1° was mobilized for all specimens. Therefore, their study systematically confirms that PSD has no effect over ϕ'_{cr}.

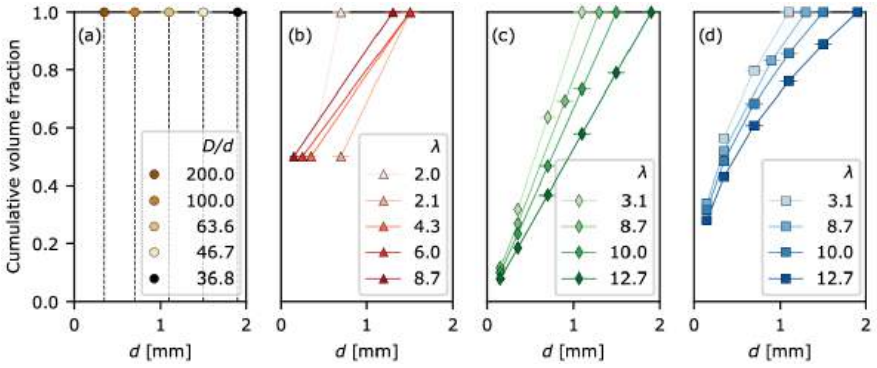

(A)

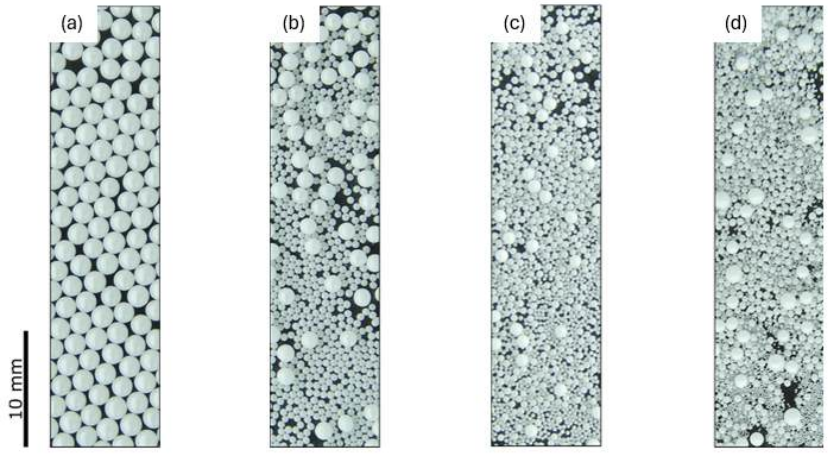

(B)

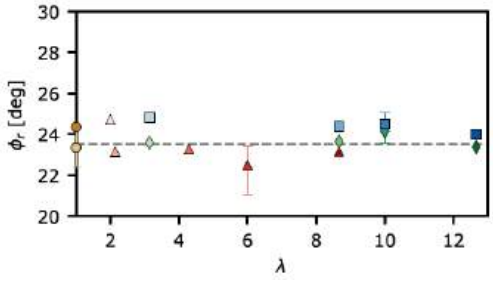

(C)

Figure 2.40 Systematic investigation of gradation effect on the critical effective friction angle after Polanía et al. (2023): (A) PSDs tested from monodisperse to polydisperse distributions (a-d); (B) photos corresponding to the PSDs, respectively (*adapted*); (C) results of ϕ'_{cr} vs size span λ (marker colors match those in a).

2.3.6 Effects of particle shape

Particle shape is an intrinsic soil parameter determined by the geological formation, erosion and transportation of the particles. In quarry materials, the shape of the grains is affected by blasting, excavation and grinding. Particle shape is usually measured using geometrical descriptors, which are given by grain dimensions and irregularities from a reference spherical shape. Wadell (1932) defines particle sphericity (S) as the global silhouette of the particle, and its roundness (R) to designate the sharpness and angularity, as shown in *Figure* 2.41a. However, the roughness asperities are often neglected. *Figure* 2.41b shows the shape chart for S and R of granular materials, initially proposed by Krumbein and Sloss (1963). The diagonal dashed lines represent the overall regularity, defined by Cho et al. (2006) as $\rho = (R + S)/2$.

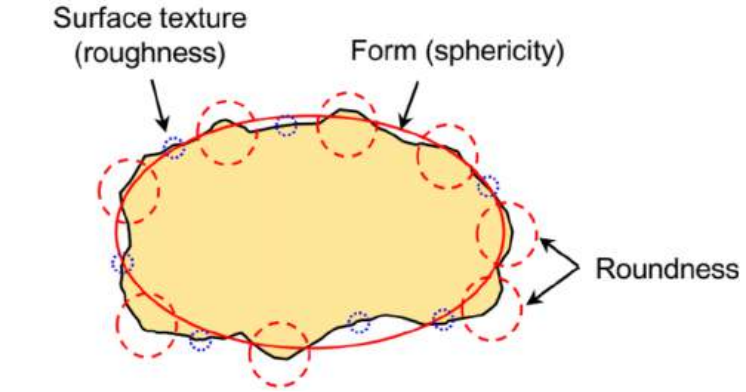

(a)

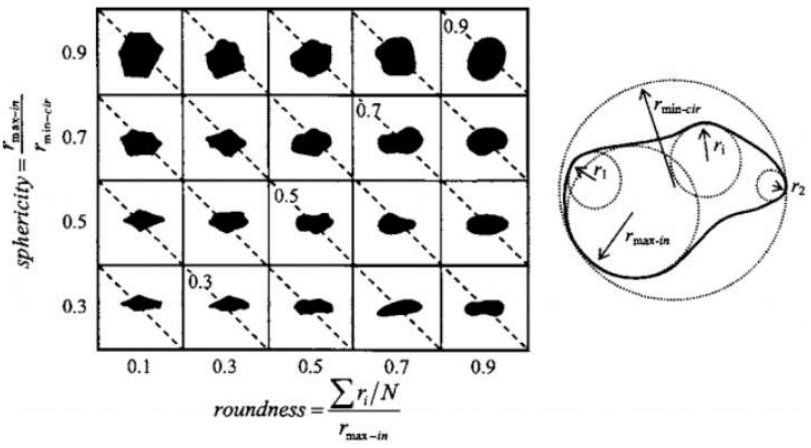

(b)

Figure 2.41 Characteristic particle shape: (a) geometrical descriptors of particle shape after Zheng and Hryciw (2015); (b) Roundness and Sphericity of granular materials (diagonal dashed lines correspond to constant particle regularity $\rho = (R + S)/2$) after Cho et al. (2006).

Zheng and Hryciw (2015) developed a computational algorithm allowing a more comprehensive definition of S and R. Among the S definitions reported (Mitchell & Soga, 2005; Rodriguez et al., 2012), Zheng and Hryciw proposed that the width-to-length sphericity (S_{WL} = particle width / particle length) replicates more accurately the traditional chart S. *Figure* 2.42 shows that S_{WL} displays a wide numerical range among the rests of the definitions of S (Zheng & Hryciw, 2016), in agreement with other studies (Cho et al., 2006; Zheng & Hryciw, 2015; Zheng & Hryciw, 2018).

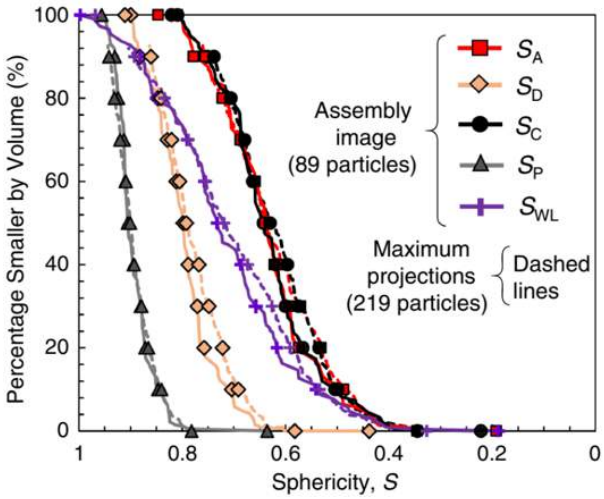

$$\text{Area Sphericity: } S_A = \frac{\text{Area of soil particle}}{\text{Area of minimum circumscribed circle}}$$

$$\text{Diameter Sphericity: } S_D = \frac{\text{Diamter of circle with same area of soil particle}}{\text{Diameter of minimum circumscribed circle}}$$

$$\text{Circle Ratio Sphericity: } S_C = \frac{\text{Diameter of maximum inscribed circle}}{\text{Diameter of minimum circum scribed circle}}$$

$$\text{Perimeter Sphericity: } S_P = \frac{\text{Perimeter of circle with same area of soil particle}}{\text{Perimeter of soil particle}}$$

$$\text{Width to Length Ratio Sphericity: } S_{WL} = \frac{\text{Width of soil particle}}{\text{Length of soil particle}}$$

Figure 2.42 Sphericity distributions after Zheng and Hryciw (2016)

The roundness, on the other hand, is computed as $R = \sum(r_i/N)/r_{in}$, where r_i represents the radius of circles fitted to concave corners of the particle, N is the number of the fitted circles and r_{in} is the radius of the largest inscribed circle (see elevation in *Figure* 2.41b). As shown in *Figure* 2.43, roundness and sphericity are measured using digital image analyses on photos of several particles, to ensure a statistically representative analysis. Other sophisticated methods also exist, which consider particle elongation, overall regularity and convexity to describe the irregularity of sand grains (Xiao et al., 2019; Yang & Luo, 2015).

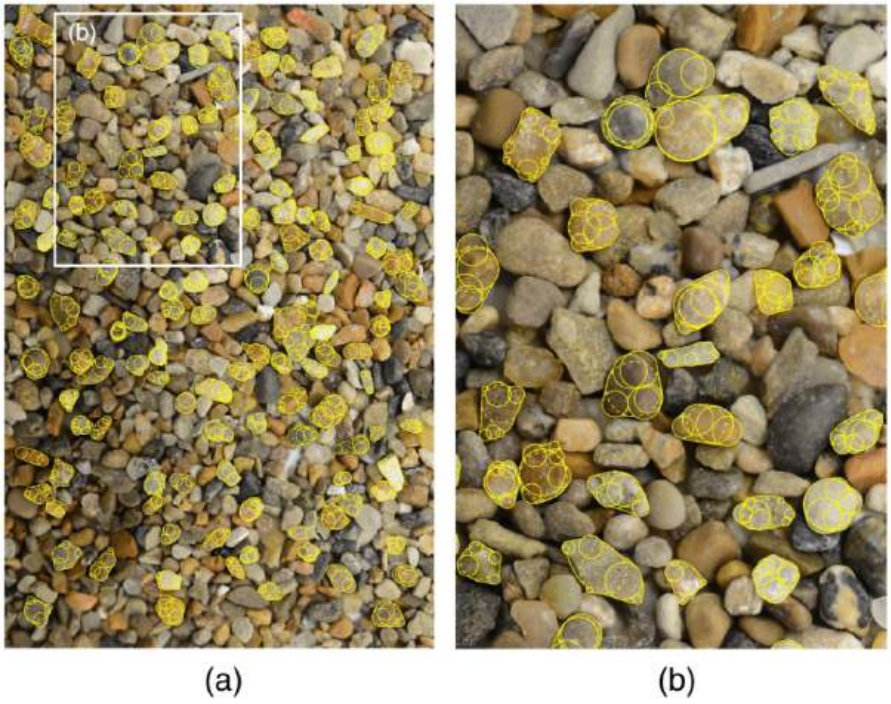

Figure 2.43 Digital image analysis from a grain assembly of sand particles after Zheng and Hryciw (2018).

Numerous works have shown that grain angularity strongly affects the shear strength of granular soils. Angular grains promote interlocking, which increases dilatancy and strength (Altuhafi et al., 2016; Cavarretta et al., 2010; Cho et al., 2006; Xiao et al., 2019). Thus, the higher S_{WL} and R, the lower the strength. *Figure* 2.44a displays the results of several shear test on 40 sands compiled by Cho et al. (2006), where ϕ'_{cr} clearly increases with grain angularity.

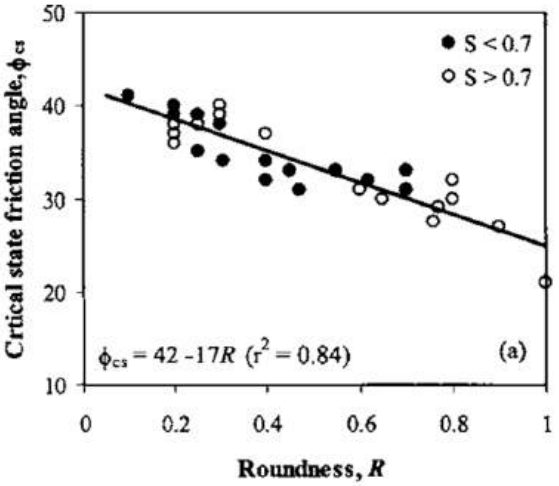

(a)

Figure 2.44 Effect of particle shape on ϕ'_{cr} after Cho et al. (2006).

Yang and Luo (2015) showed the effect of grain shape on the CSL in $q - p'$ space. Their results are summarized in *Figure* 2.45, presenting different mixtures used of uniformly graded clean angular sand (FS) with 20% and 40% of spherical glass beads (G) and angular crushed glass beads (C), respectively. It can be seen that the ratios q/p' of the strength envelope (i.e., critical strength) decrease from 1.23 to 1.13 and 1.09 when adding G, while they increase from 1.23 to 1.27 to 1.35 when adding C material.

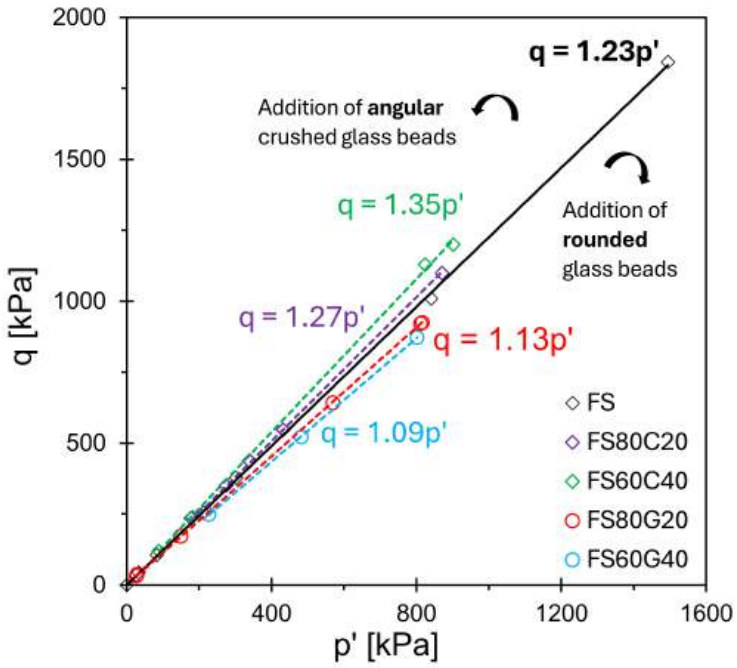

Figure 2.45 Influence of particle shape on critical shear strength; prepared using data from Yang and Luo (2015).

2.3.7 Boundary effects in triaxial testing

The triaxial test involves a cylindrical specimen between two loading plates (cap and base), which are not frictionless (Bishop & Green, 1965; Duncan & Dunlop, 1968). The cap and base have the same diameters as the specimen, restricting free dilation at large deformations because of friction at the boundaries. This results in a prevalent nonuniformity of stress and strain fields due to the inherent end restrictions imposed (Goto & Tatsuoka, 1988; Peri et al., 2019). *Figure* 2.46a shows that the dilation is confined in a narrow zone (Rowe & Barden, 1964); the volume expansion localizes and particles dilate more extensively than the rest of the specimen, resulting in sudden collapse of the shear strength. *Figure* 2.46b displays the stress-strain curves where the drop of σ'_1/σ'_3 is shown on end-restrained specimens (*continuous* lines). However, when lubrication is provided on the end plates (*free ends* in *Figure* 2.46b), the stress-strain behavior exhibits smooth volumetric and strength curves (*dashed* lines) and larger ε_a.

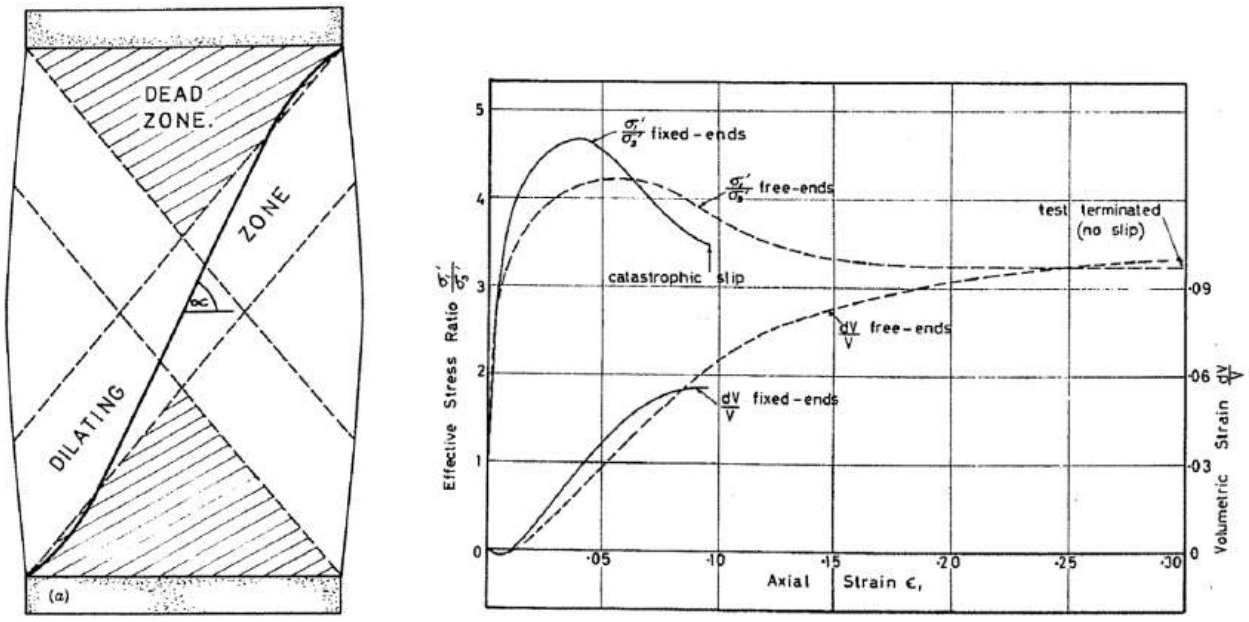

(a) (b)

Figure 2.46 Nonuniformity of specimen under triaxial compression due to end-restraints after Rowe and Barden (1964): (a) specimen sketch showing confined dilation due to end-restraints; (b) stress-strain curves displaying the difference on test with regular standard cap and bases (*continuous* lines) and free ends (*dashed* lines).

To remediate the heterogeneities of the specimen, Rowe and Barden (1964) proposed a low-friction experimental setup. The design involves enlarged platens enhanced with a lubricated sheet using vacuum grease to minimize friction, as shown in *Figure* 2.47a. However, evidence suggests that the effectiveness of lubricated platens depends on the specimen slenderness given by the height-to-diameter ratio (H:D), specimen preparation method and σ'_3 (Duncan & Dunlop, 1968; Mozaffari et al., 2022; Peri et al., 2019; Roy & Lo, 1971). As shown in *Figure* 2.47b for Fredericton sand specimens with lubricated ends at $\varepsilon_a = 30\%$, H:D=2 specimens still tend to bulge while H:D=1 allow for a more homogeneous strain field (Wightman et al., 2024). Hettler and Vardoulakis (1984) reported direct shearing results to quantify the friction (δ_o in degrees) existing at the contact of glass plate-lubricant-membrane and sand specimens. *Figure* 2.48a shows that δ_o is consistently below 0.75° for σ'_n considered (up to 2 MPa). Comparisons of the analytical friction angle of the sand with the measured value (ϕ'_M) using lubricated ends shows that, for $\delta_o \leq 1°$, the scatter is significant with H:D=0.36 (*Figure* 2.48b) and negligible with H:D=1 (*Figure* 2.48c). This may explain why significant scatter of ϕ' (between 1° to 6°) are reported for lower slenderness H:D< 1, even with lubricated ends (Goto & Tatsuoka, 1988; Hettler & Vardoulakis, 1984; Raju et al., 1972; Rowe & Barden, 1964). Consistently, Bishop and Green (1965) showed in sand specimens (with

D=4″) that proper lubrication is mandatory at H:D=1. The effect of H:D ratio and end platens is displayed in *Figure* 2.49a, showing that 4″ high specimens (H:D=1) with standard rough ends (non-lubricated) overestimate ϕ' for a given porosity. In harmony with the findings of Hettler and Vardoulakis (1984), lower slenderness (H:D=0.5) in 2″ high specimens exhibit higher ϕ' values despite lubrication. However, ϕ' appears unaffected by end friction with H:D=2 (8″ high specimens). *Figure* 2.49b asserts this observation, whereby H:D$\geq$ 1 ensures reliable results if adequate lubrication is provided. This finding is in agreement with other studies. For instance, Goto and Tatsuoka (1988) found that ϕ' of uniform Toyoura sand, tested using H:D between 2 to 2.5, was practically identical between the standard and lubricated ends (with less than 0.5° dispersion and up to 1° at low porosities).

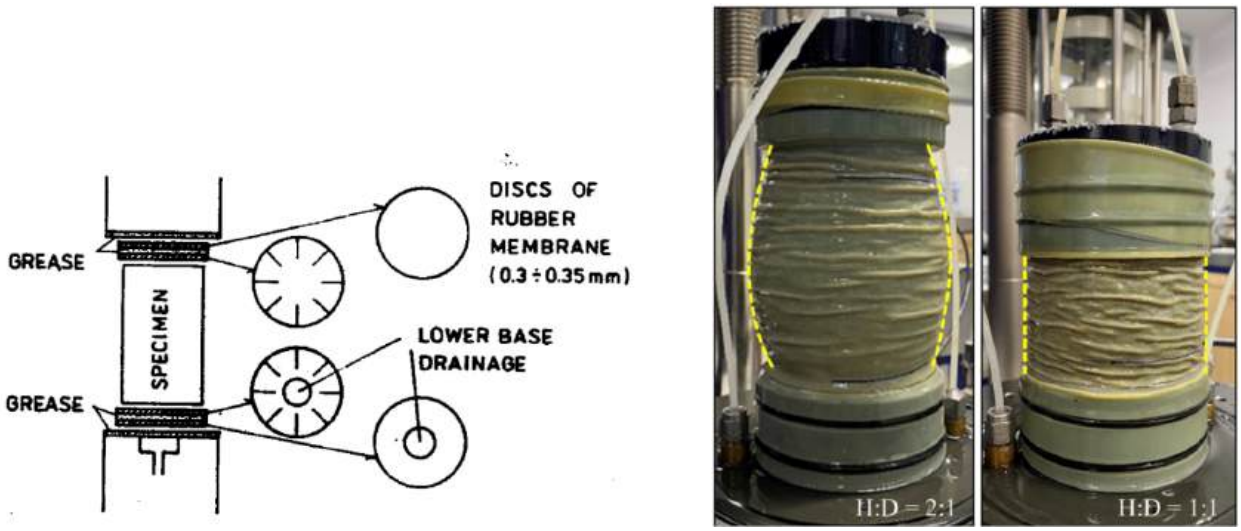

(a) (b)

Figure 2.47 Enlarged lubricated end platens in triaxial compression: (a) design setup after Feda et al. (1993); (b) photos of Fredericton sand specimens after Wightman et al. (2024) displaying slight bulging and improved strain distribution on H:D=2 and H:D=1 specimens at $\varepsilon_a = 30\%$, respectively.

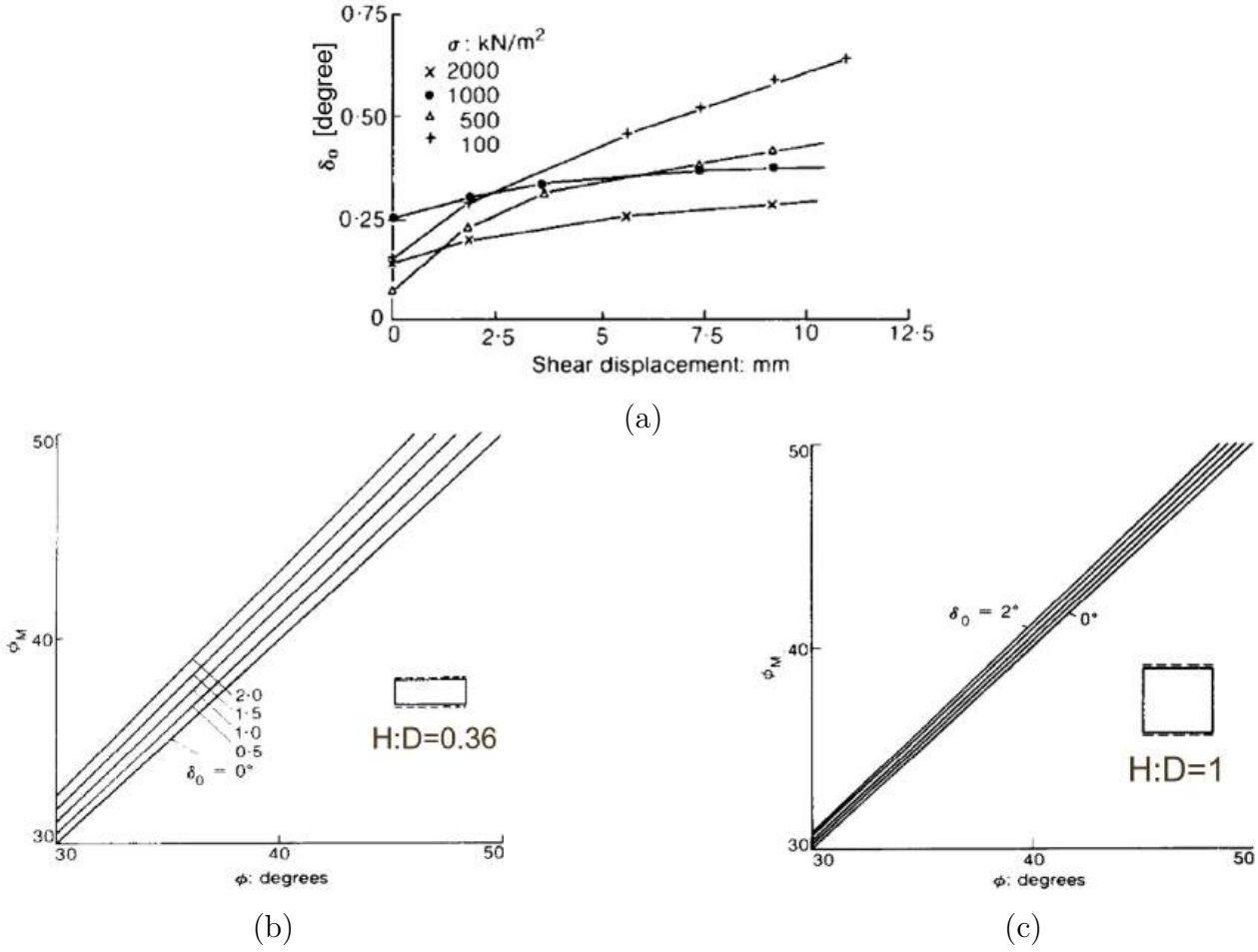

Figure 2.48 Measured friction angle at the contact of glass plate-lubricant-membrane and sand specimens after Hettler and Vardoulakis (1984): (a) direct shearing results; (b) comparison between measured ϕ_M and analytical ϕ with H:D=0.36 specimens; (c) with H:D=1 specimens.

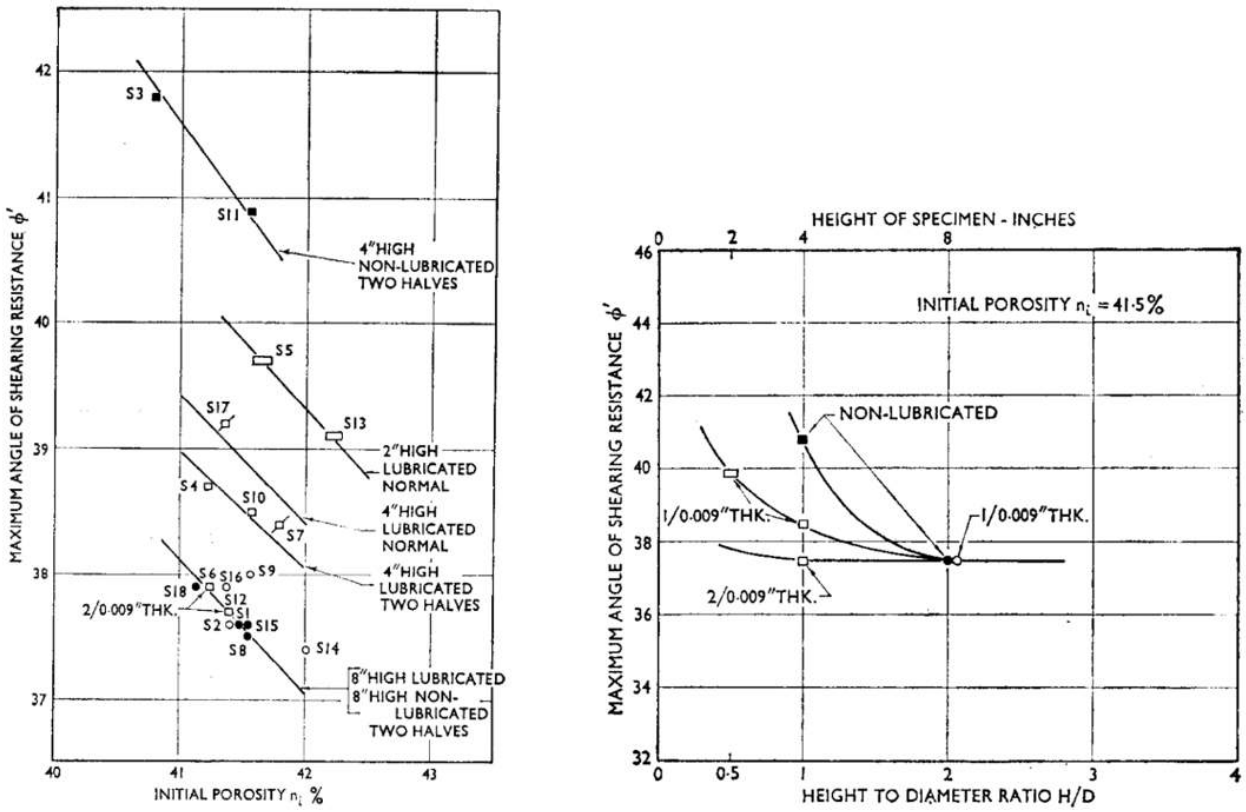

(a) (b)

Figure 2.49 Comparison between rough standard ends and lubricated platens on $D = 4''$ sand specimens after Bishop and Green (1965): (a) ϕ' vs initial porosity; (b) ϕ' vs slenderness H:D.

Figure 2.50 shows that the volumetric strain (ε_v) at failure is always underestimated when standard rough platens are employed, regardless of the slenderness of the specimen. Wightman et al. (2024) showed that the differences in the stress-strain relationships of lubricated Fredericton sand specimens with H:D=1 and 2 were significant at low $\sigma'_3 = 50$ kPa (see *Figure* 2.51a), but vanished at elevated $\sigma'_3 = 500$ kPa (see *Figure* 2.51b).

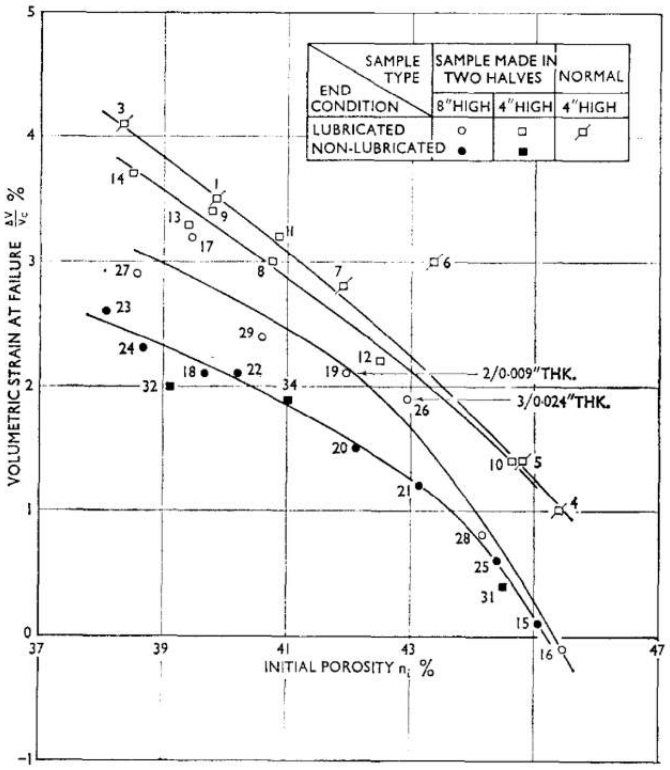

Figure 2.50 Variation of ε_v at failure vs initial porosity, comparing rough standard ends and lubricated platens with different H:D on $D = 4''$ sand specimens after Bishop and Green (1965).

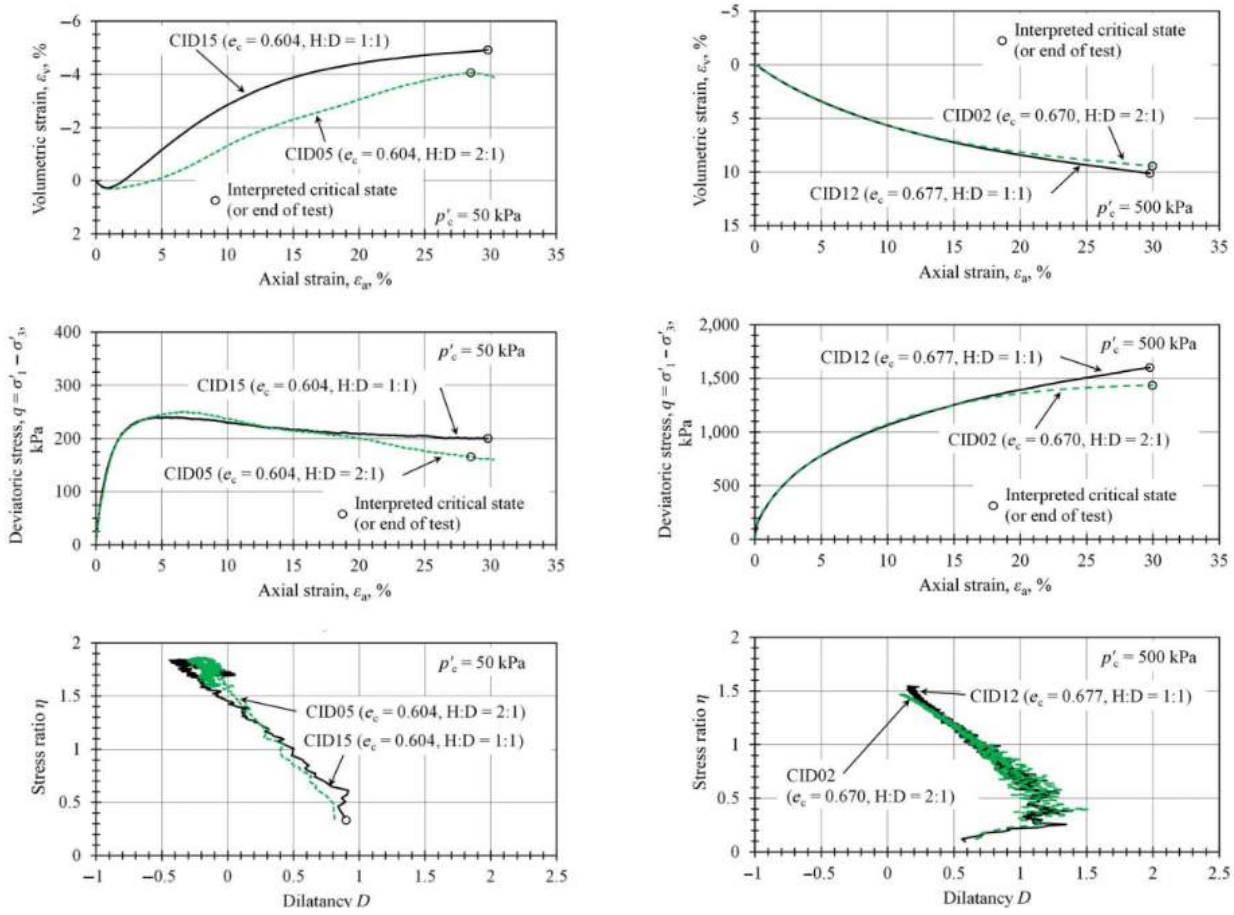

Figure 2.51 Stress-strain and dilatancy relationships on lubricated Fredericton sand specimens of H:D=1 and 2 after Wightman et al. (2024): (a) $\sigma'_3 = 50$ kPa; (b) $\sigma'_3 = 500$ kPa.

2.4 Small-scaling techniques for coarse granular soils

As stated previously, the shear strength and stress-strain properties of soils must be assessed to ensure adequate designs. However, oversized particle pose technical challenges in coarse soils and rockfills, such as mine WRs (Aubertin et al., 2021; Bard et al., 2011; Linero et al., 2007; Valenzuela et al., 2008), quarry rockfill (Leps, 1970; Marsal, 1967; Ovalle et al., 2020), ballasts (Al-Hussaini, 1983; Indraratna et al., 1993, 1998; Marachi et al., 1972) and fluvial coarse gravels (Holtz & Gibbs, 1956; Lowe, 1964; Wilson & Squier, 1969). As a result, physical tests on field materials become practically unfeasible, even when using the largest direct shear boxes (Barton & Kjærnsli, 1981; Estaire & Olalla, 2006; Linero et al., 2020; Matsuoka et al., 2001; Stark et al., 2014) or triaxial cells (Bard et al., 2011; Hu et al., 2011; Leussink, 1960; Marachi et al., 1972; Marsal, 1967; Ning et al., 2024) ever reported. The

tests must be performed on small-scale specimens where the PSD is modified to fit the test device, by respecting the minimum specimen aspect ratio α required by international testing standards. The literature provides various grading techniques for small-scaling; the most common methods are reviewed hereafter.

2.4.1 Scalping grading

Scalping grading is one of the most used scaling techniques in practice for shear strength assessment (Deiminiat et al., 2020, 2022; Hassan et al., 2022; Linero et al., 2007; Xu et al., 2018) and hydraulic conductivity (Deiminiat et al., 2023; Essayad, 2021; Peregoedova, 2012). After defining a d_{max} that can be handled in the available apparatus and ensures a REV, grading fractions of characteristic size $d > d_{max}$ are removed. Scalping consists of sieving the material below $d \leq d_{max}$ to generate the scaled PSD. Logically, the finest grains are conserved and the material becomes more uniformly graded.

Zeller and Wullimann (1957) used scalping to characterize the shear strength of the Göschenenalp dam shell material in Switzerland. The works of Parsons (1936), Bishop (1945), Hennes (1957) and Holtz and Gibbs (1956) advocated a minimum $\alpha \geq 5$ to ensure a REV specimen. Consequently, with their triaxial devices designed to test specimens up to D =505 mm (see *Table* 2.6), Zeller and Wullimann accommodated gravels with grain sizes finer than 100 mm. The scalped PSDs are shown in *Figure* 2.52. The characterization of particle shapes was reported to be consistent over the graded material. *Figure* 2.53 displays the stress-strain curves of 4 tests with d_{max} = 100 and 10 mm at varying porosity, showing negligible differences in loose specimens 2 and 4. However, dense specimens 1 and 3 exhibit noticeable scatter. This effect of porosity is exemplified in *Figure* 2.54, where a given d_{max} (corresponding to a distinct PSD) shows shear strength reduction with increasing porosity. *Figure* 2.54 also suggests that large d_{max} mobilizes lower strength in general, particularly in the low compactness range.

Table 2.6 Fractions tested and specimen sizes after Zeller and Wullimann (1957).

Fraction		*Diameter*		*Cross-section area*		*Height*	
mm	in.	mm	in.	cm²	sq. in.	mm	in.
< 100	4	505	$19\frac{7}{8}$	2000	310	900	$35\frac{7}{16}$
< 30	$1\frac{3}{16}$	252·5	$9\frac{15}{16}$	500	77·5	500	$19\frac{11}{16}$
< 10	$\frac{13}{32}$	160	$6\frac{5}{16}$	200	31	250	$9\frac{27}{32}$
< 1	0·04	80	$3\frac{5}{32}$	50	7·75	150	$5\frac{29}{32}$

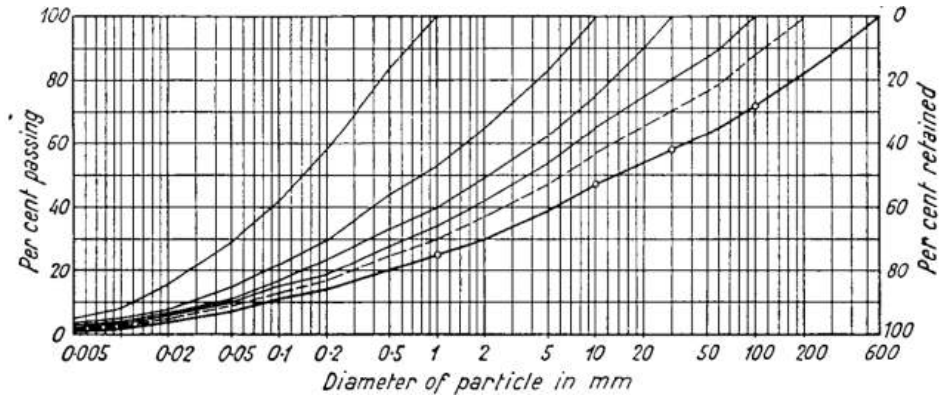

Figure 2.52 Scalped PSDs after Zeller and Wullimann (1957).

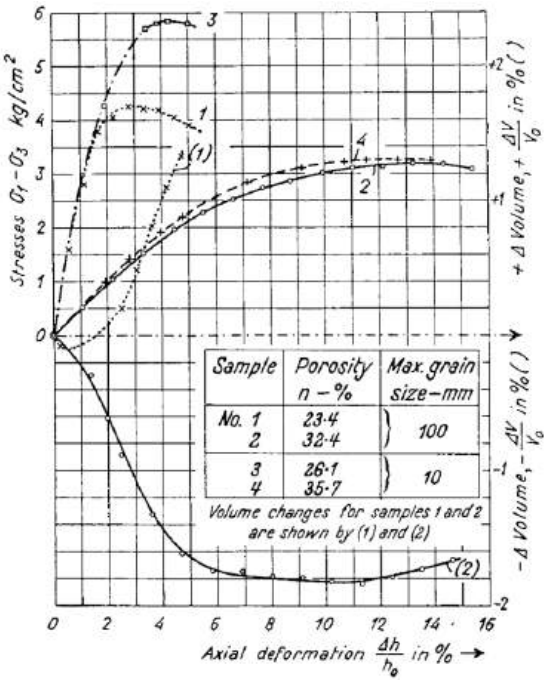

Figure 2.53 Scalping results after Zeller and Wullimann (1957): stress-strain curves for an example of 4 specimens.

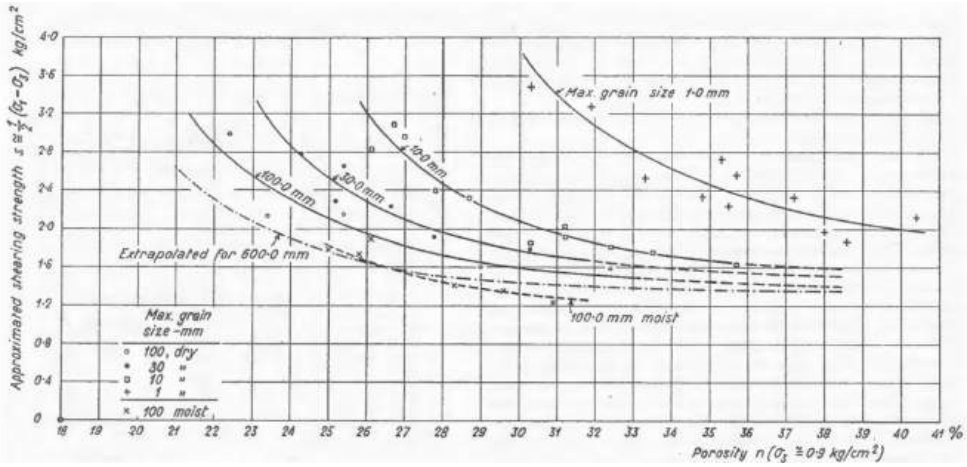

Figure 2.54 Scalping results after Zeller and Wullimann (1957): grading effect on shear strength with varying porosity.

Al-Hussaini (1983) evaluated scalping influence on crushed basalt having a PSD prototype ranging from $d_{max} = 76.2$ mm to a minimum size of 0.6 mm (see *Table* 2.7 and *Figure* 2.55). The tests were performed under conventional drained triaxial compression at two density indexes: $I_D = 75\%$ and 100% for medium-dense and dense specimens, respectively. *Figure* 2.56 shows significant size effects as ϕ increased with d_{max}, with consistently $\sim 7°$ difference between the coarsest and the finer materials, at any given σ_3. This trend contradicts the one previously reviewed from the study of Zeller and Wullimann (1957), showing shear strength reduction with d_{max}.

Table 2.7 Physical properties of crushed basalt tested by Al-Hussaini (1983).

Limits of particle gradation (mm)	Coefficient of uniformity	Void ratio	
		e_{max}	e_{min}
6.4–0.6	3.31	0.95	0.53
12.7–0.6	4.68	0.84	0.45
25.4–0.6	6.67	0.74	0.41
50.8–0.6	9.44	0.69	0.37
76.2–0.6	11.6	0.65	0.36

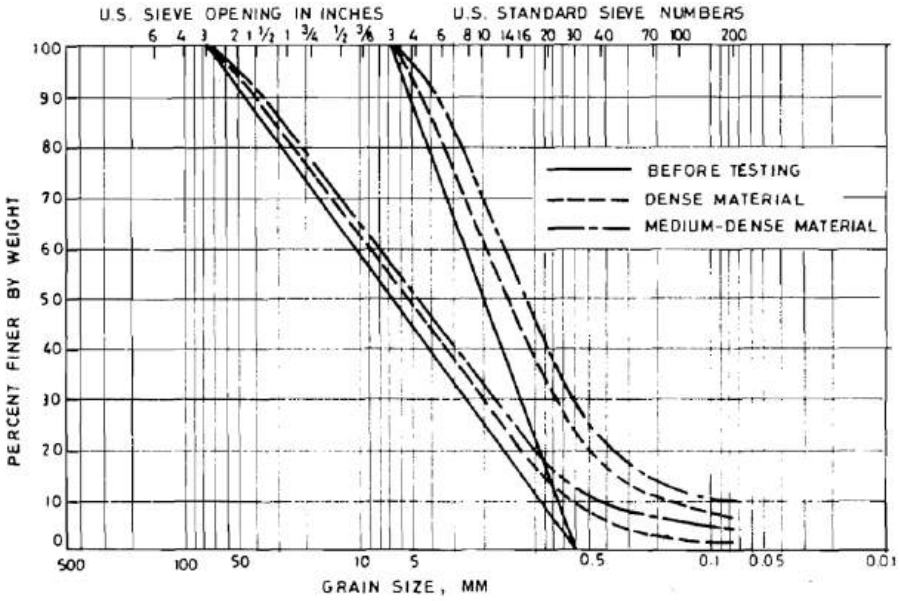

(a)

Figure 2.55 Scalped PSDs before and after test for $d_{max} = 76.2$ and 6.3 mm after Al-Hussaini (1983).

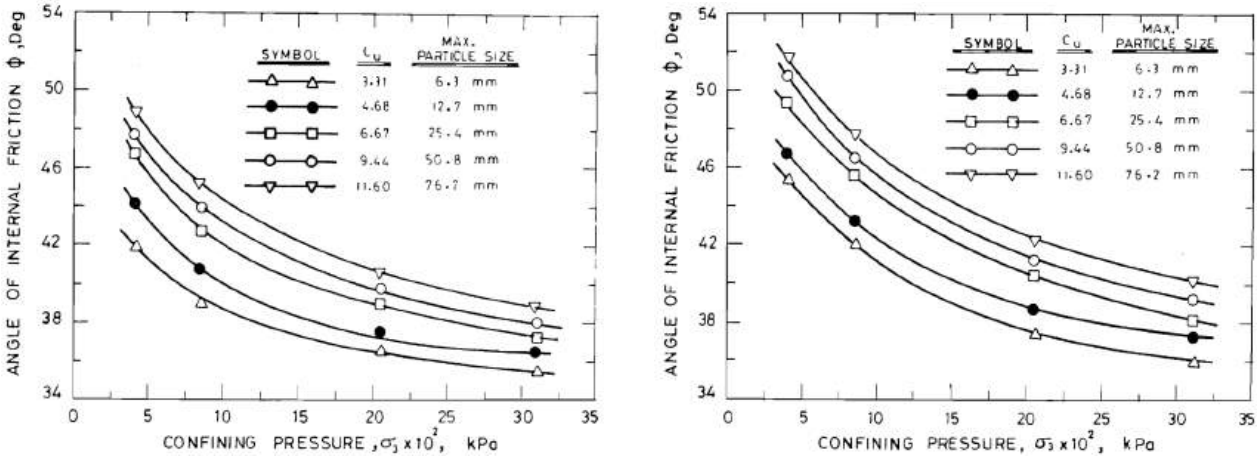

(a) (b)

Figure 2.56 Size effect on ϕ vs σ_3 in crushed basalt after Al-Hussaini (1983): (a) $I_D = 75\%$; and (b) $I_D = 100\%$.

Xu et al. (2018) tested dry loose crushed material using a large DST square box of 300 mm wide. The scalped PSDs are shown in *Figure* 2.57. The tests were carried out on different $\sigma_n = 250,\ 500$ and 1000 kPa. *Figure* 2.58 shows the typical stress-deformation curves at $\sigma_n = 250$ kPa. It can be noticed that the shear strength increases with d_{max}, contrasting

the trend seen previously from Zeller and Wullimann (1957). This is also seen on the shear strength envelopes in *Figure* 2.59, displaying higher strength with increasing d_{max}.

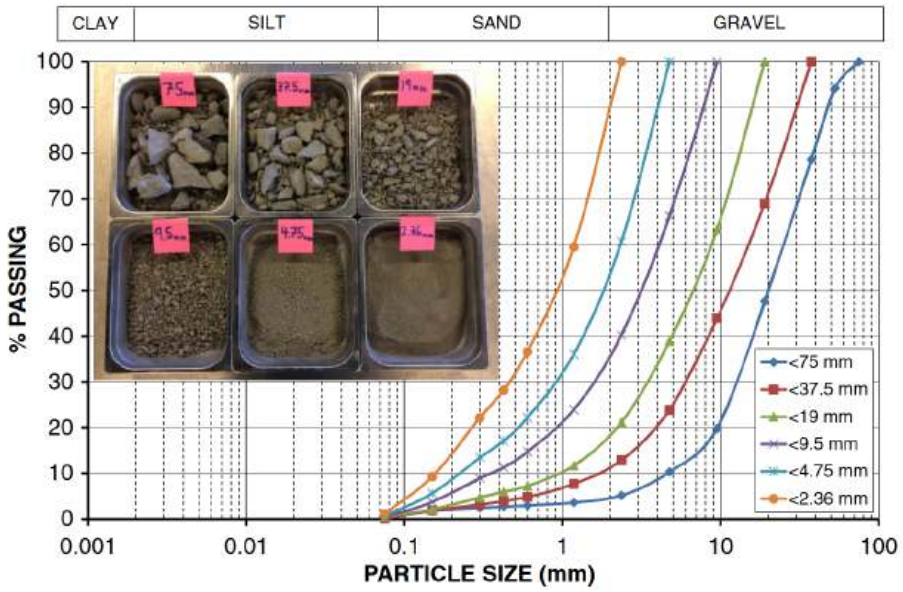

Figure 2.57 Scalped PSDs on crusher run materials after Xu et al. (2018).

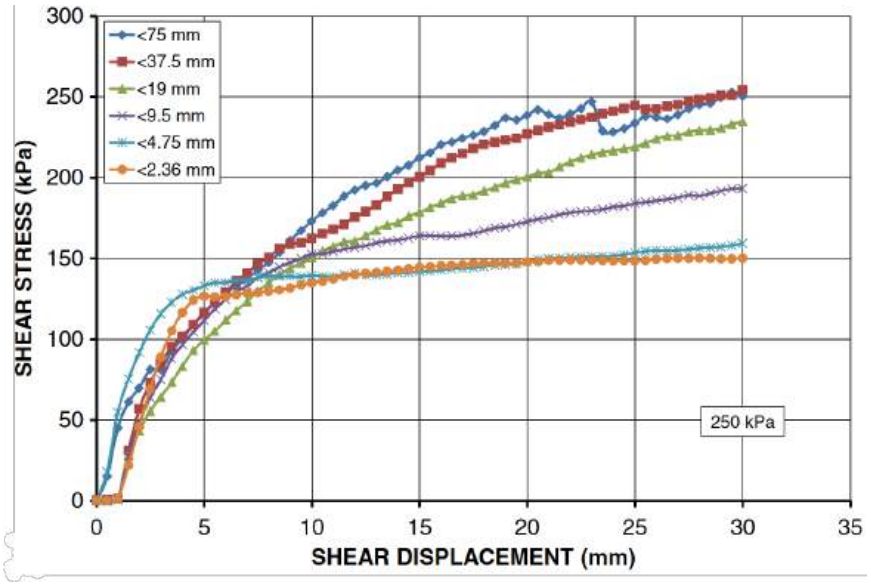

Figure 2.58 Effect of scalping on shear stress curves of crusher run specimens under $\sigma'_n = 250$ kPa, after Xu et al. (2018).

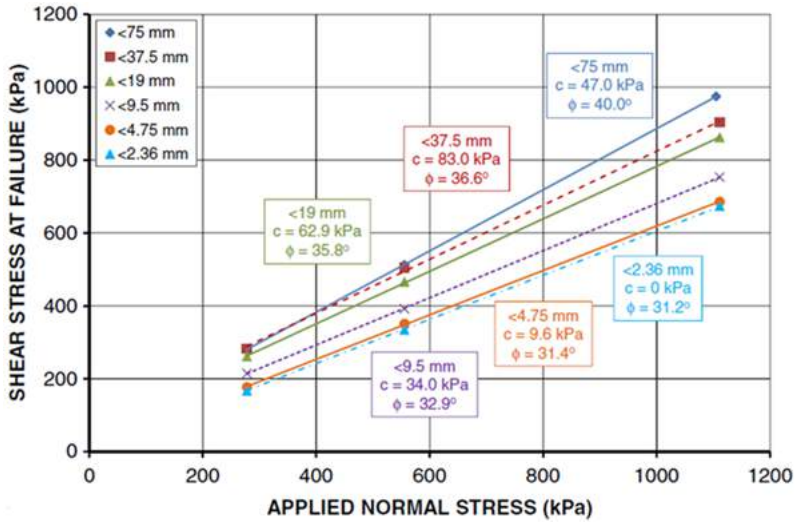

Figure 2.59 Shear strength envelop for different scalped d_{max} after Xu et al. (2018).

2.4.2 Parallel grading

Given a field coarse material of maximum grain size $d_{max-field}$, parallel gradation is defined by the following scaling factor (F):

$$F = d_{max-field}/d_{max} \tag{2.6}$$

After defining the coarsest particle that a specimen can have (d_{max}) to guarantee a REV, the subsequent grain size fractions ($d \leq d_{max}$) are then divided by F to obtain a parallel PSD, while the corresponding percents passing are conserved. It is noteworthy that parallelism is often not perfectly achievable below d_{20} (20% passing) due to generated nonexistent fines in the prototype field PSD (Deiminiat et al., 2020; Verdugo & de la Hoz, 2007). Therefore, several assumptions must be made to replace the fines from other materials or restrict the minimum particle diameter d_{min} (e.g: (Deiminiat & Li, 2022; Lowe, 1964; Marachi et al., 1972; Verdugo & de la Hoz, 2007). Regardless, parallel grading has been used extensively since 1964, when Lowe (1964) used it during the experimental characterization of the Shihmen dam shell material (in Taiwan) (Abbas et al., 2004; Dorador & Villalobos, 2020; Hu et al., 2011; Indraratna et al., 1993; Marachi et al., 1972; Ovalle et al., 2014; Varadarajan et al., 2003).

Marachi et al. (1972) modeled angular and alluvial rockfill materials having $d_{max} = 150$, 50 and 12 mm (i.e., $3 < F < 12$). *Figure* 2.60 shows the parallel PSDs used to evaluate the effects of specimen size. As stated, the parallelism was only attained above d_{20} and d_{min} was

restricted in all modeled PSDs. All materials respected $\alpha = 6$ in triaxial devices allowing D of 50, 300 and 916 mm (*Figure* 2.61). *Figure* 2.62 displays the stress-strain relationship of Pyramid dam material. The trend indicates that smaller specimens exhibit more dilation than intermediate and large specimens, across all used σ'_3 =30-650 psi (∼0.2-4.5 MPa). *Figure* 2.63 displays consistent ϕ' reduction with σ'_3; differences in ϕ' are between 3-4° and 0.5-1.5° for $F = 12$ and 3, respectively.

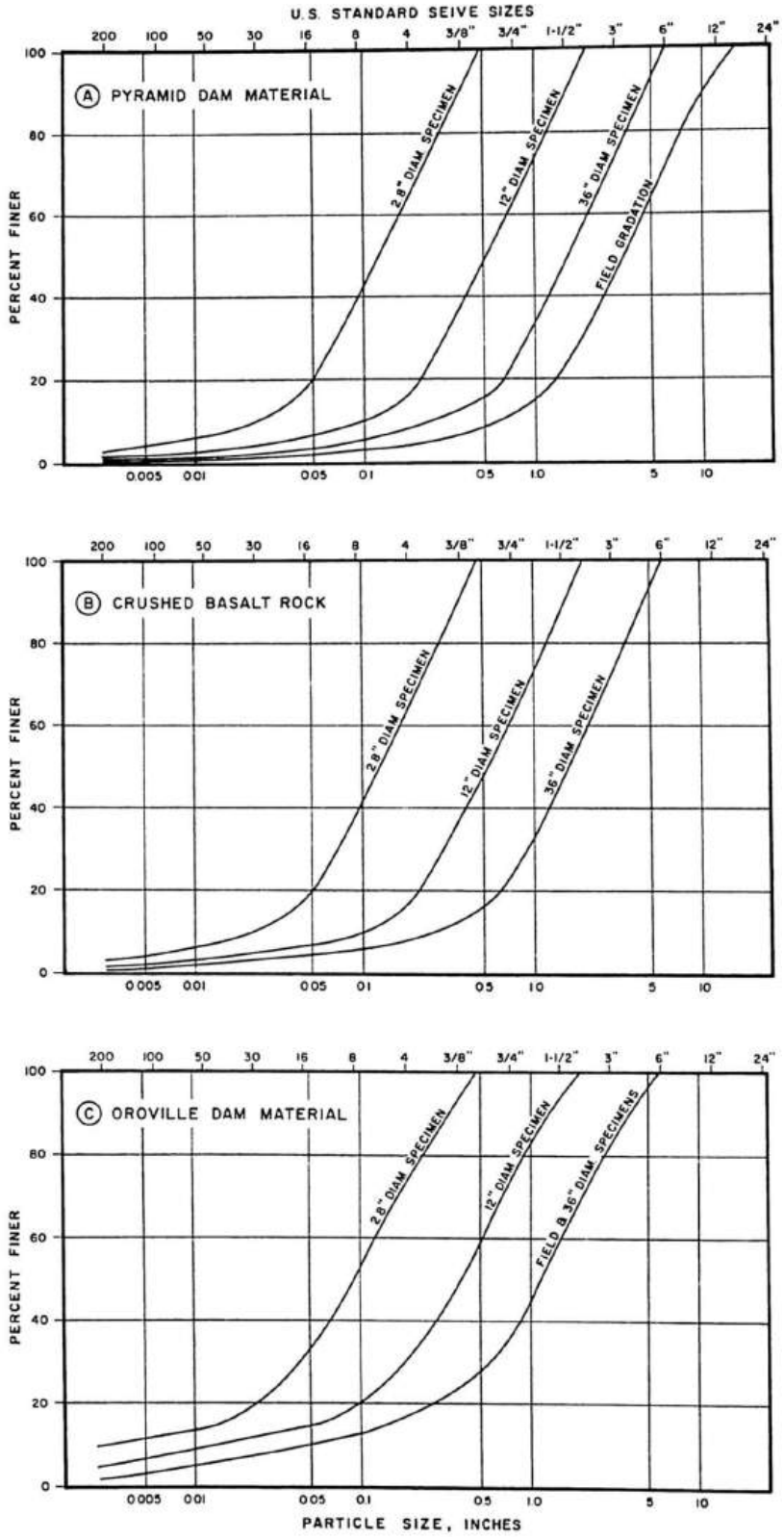

Figure 2.60 Parallel grading modeled after Marachi et al. (1972): (a) Pyramid dam rockfill material; (b) crushed basalt rockfills; (c) Oroville dam material.

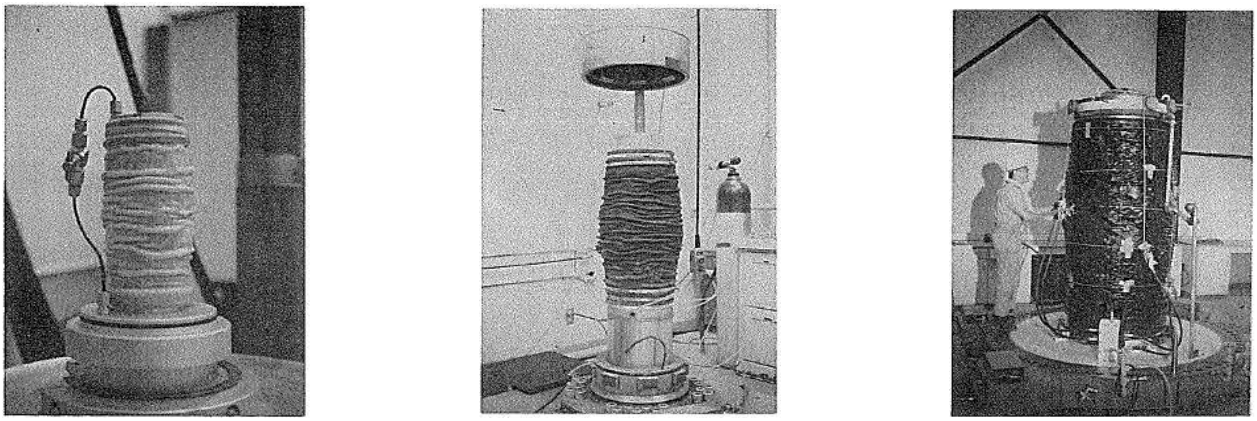

(a) (b) (c)

Figure 2.61 Specimen size tested after Marachi et al. (1972): (a) $D = 50$ mm (2.8 in.); (b) $D = 300$ mm (12 in.); (c) $D = 916$ mm (36 *in.*).

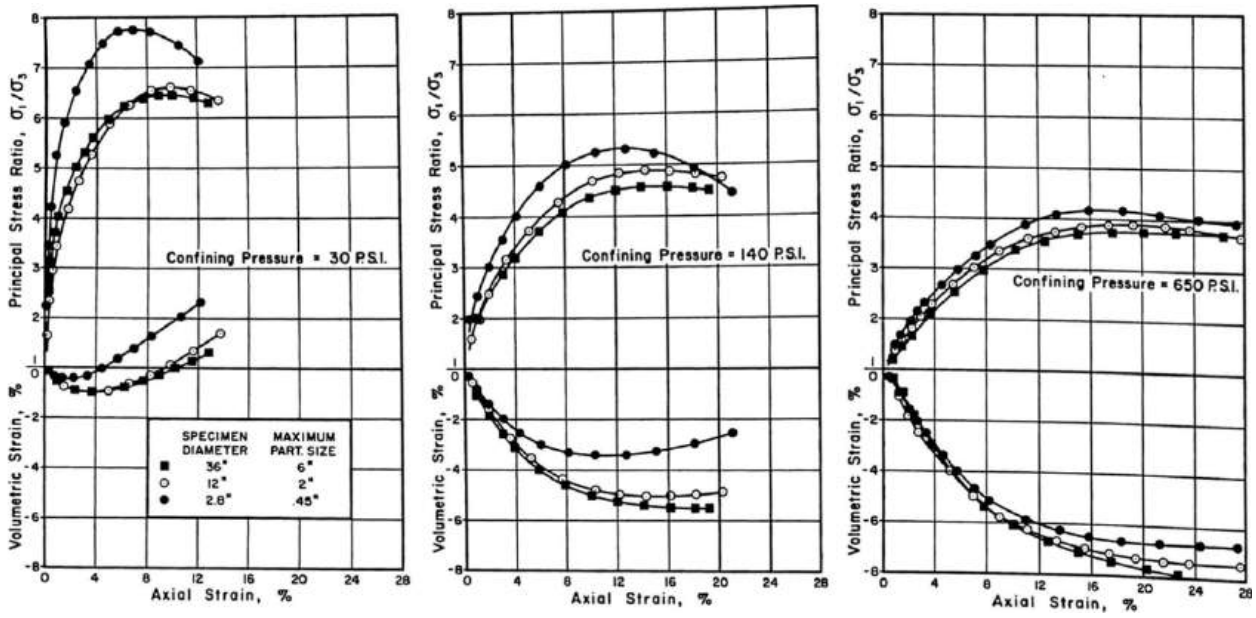

(a) (b) (c)

Figure 2.62 Stress-strain results of Pyramid dam material after Marachi et al. (1972): (a) σ_3' =30 psi; (b) σ_3' =140 psi; (c) σ_3' =650 psi.

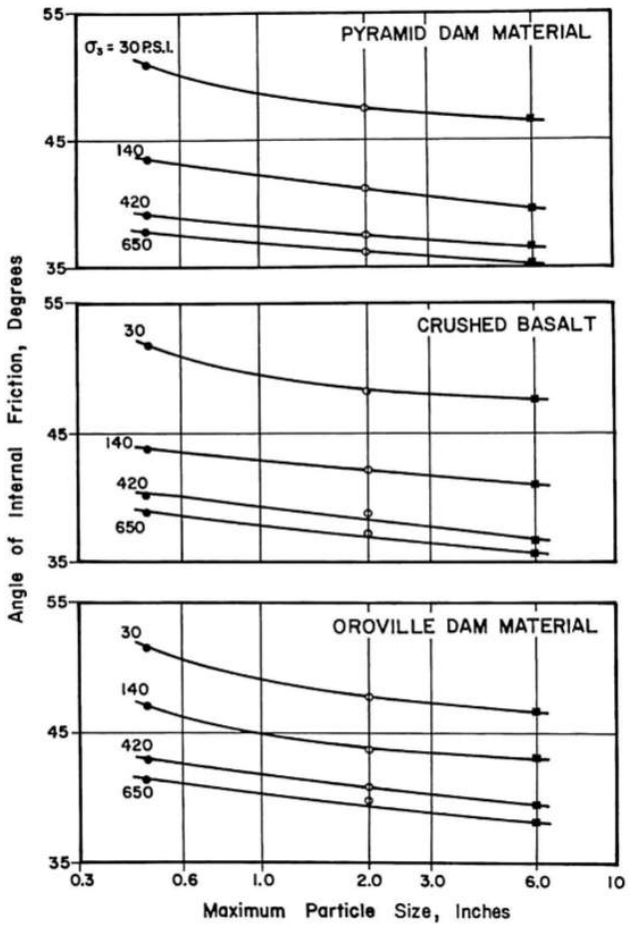

Figure 2.63 Variation of the internal friction angle with d_{max}, after Marachi et al. (1972).

Ovalle et al. (2014) used parallel grading on crushable calcareous rockfill (CP) and quartzite shale rockfill (STV) from the Préfontaines quarry and Trois Vallées (in France), respectively. *Figure* 2.64 shows the modeled PSDs for (a) CP and (b) STV rockfill materials. The specimens modeled were not small-scaled; rather, they were generated to be perfectly parallel. PSDs after tests at $\sigma'_3 = 400$ kPa are equally shown in the same figures. CP1 and STV1 (with d_{max} =40 mm) were tested in a triaxial device allowing $D = 250$ mm, and CP2 and STV2 (d_{max} =160 mm) with $D = 1000$ mm. All the specimens were deemed to ensure $\alpha = 6$. The stress-strain results are shown in *Figure* 2.65. In general, the modeled CP1 and STV1 materials reproduce the behavior of their parallel graded specimens CP2 and STV2, respectively. Thus, size effects are marginally noticeable. Dilatancy is noticed in both materials and vanishes at $\sigma'_3 \geq 200$ kPa, while contracting behavior prevails at larger confining σ'_3. This is mainly due to the significant particle crushing seen earlier in post-test PSDs (see *Figure* 2.64). Additionally, the mobilized maximum ϕ' is always higher in finer-grain speci-

mens (CP1 and STV1) compared to coarser ones (CP2 and STV2), as shown in *Figure* 2.66. Again, due to the increase in the crushing of particles in coarser materials.

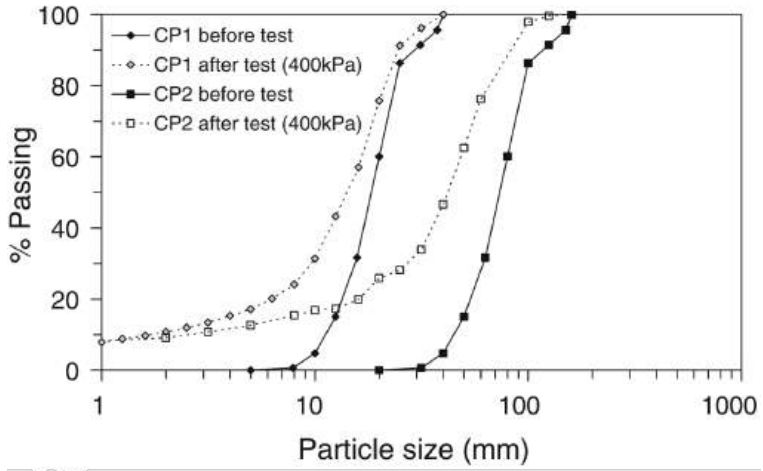

(a)

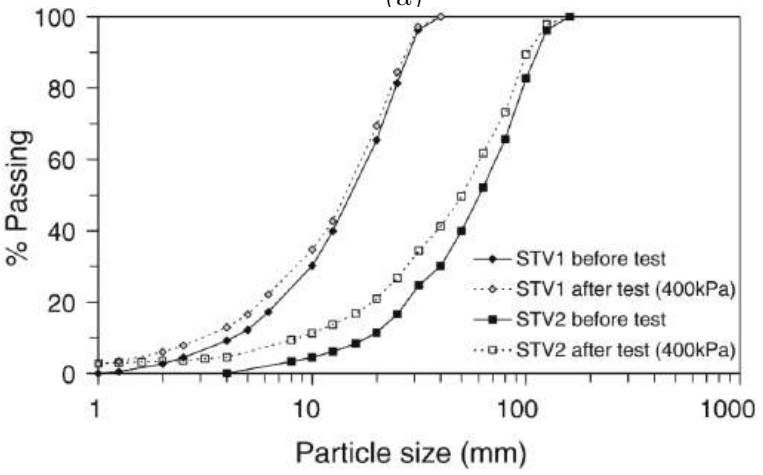

(b)

Figure 2.64 Parallel PSDs modeled after Ovalle et al. (2014): (a) CP rockfill material; (b) STV rockfill material.

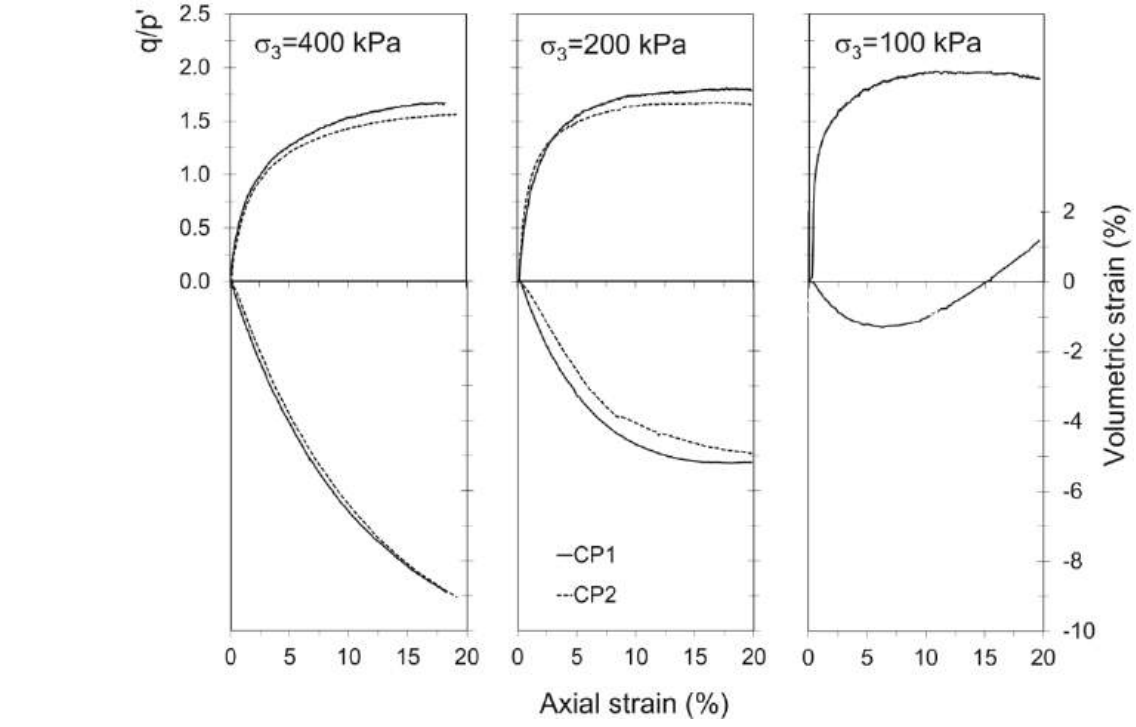

(a)

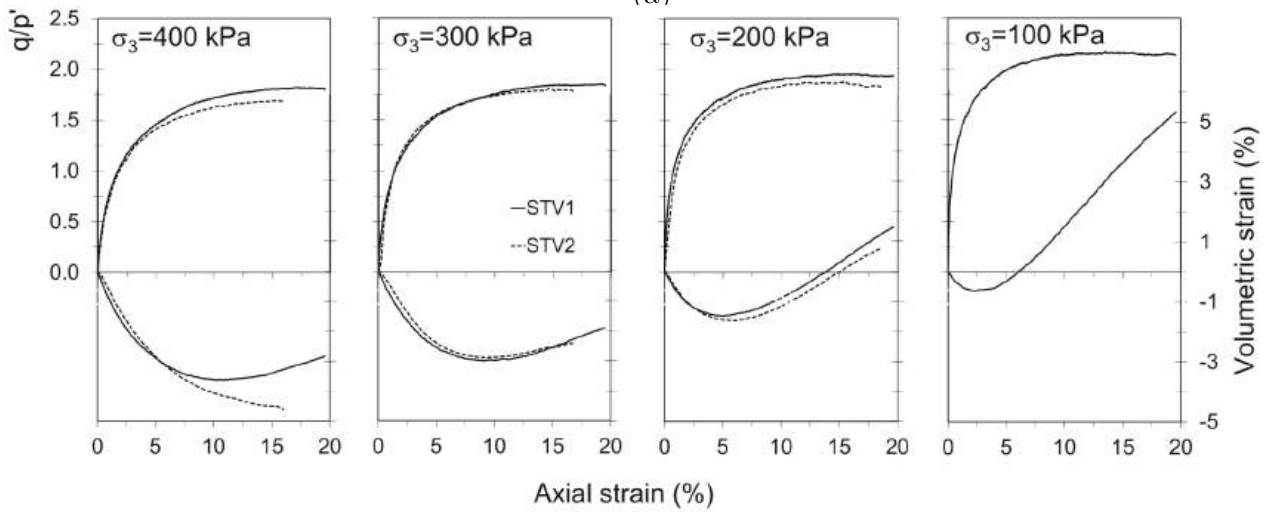

(b)

Figure 2.65 Stress-strain results at different σ_3 on parallel graded rockfill specimens after Ovalle et al. (2014): (a) CP material; (b) STV material.

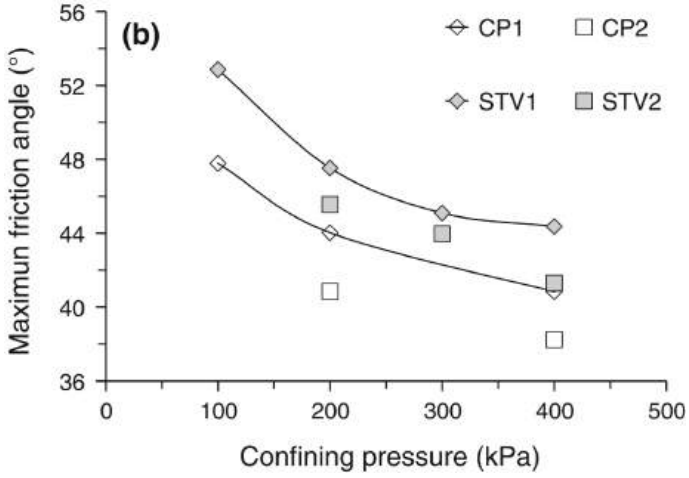

Figure 2.66 Friction angle vs σ_3 on the parallel PSDs modeled after Ovalle et al. (2014).

2.4.3 Scalp and replace

Early work of Holtz and Gibbs (1956) showed that ϕ' increases with gravel content $\geq 20\%$. Therefore, to anticipate the effect of removing oversized particles, Frost (1973) proposed the scalp and replacement method–often referred to as the truncation method (Deiminiat et al., 2020; Linero et al., 2007)– to characterize gravelly soils. This method was evaluated for shear strength characterization by Donaghe and Townsend (1976) and has proven to be consistent, giving similar results than scalping. However, it was recommended that if more than 10% coarse particles are removed to accommodate $\alpha = 6$, they should be replaced with an equal amount retained in the No.4 sieve.

Linero et al. (2007) compared CTC tests on truncated and parallel WR specimens in a 1 m diameter cell. The PSDs modeled are shown in *Figure* 2.68 with a $d_{max} = 200$ mm (i.e. specimen aspect ratio $\alpha = 5$). The initial void ratio of the dry specimens was $e = 0.46$, corresponding to loose state conditions. *Figure* 2.68a and b show results for truncated specimens, displaying stress-strain behavior and void ratio variation, respectively. For a given σ'_3, strain hardening toward the peak values at large strains is observed and specimens display contractive behavior. The steeper void ratio curves in (b) suggest significant particle rearrangement due to more void spaces and particle crushing at high stress levels tested ($\sigma'_3 \geq 1$ MPa). On the other hand, parallel-graded specimens shown with $\sigma'_3 = 0.1$ MPa exhibit dilatancy (*Figure* 2.69a). Similar stress-strain behavior as for the truncated specimen is noticed, suggesting that both techniques can be used to assess coarser-grained material behavior. However, *Figure* 2.70a suggests that higher ϕ' values are reached with truncated specimens for a given σ'_3 due to more coarser particles. Yet, this is somewhat counter-intuitive

due to visible significant particle crushing (see *Figure* 2.70b).

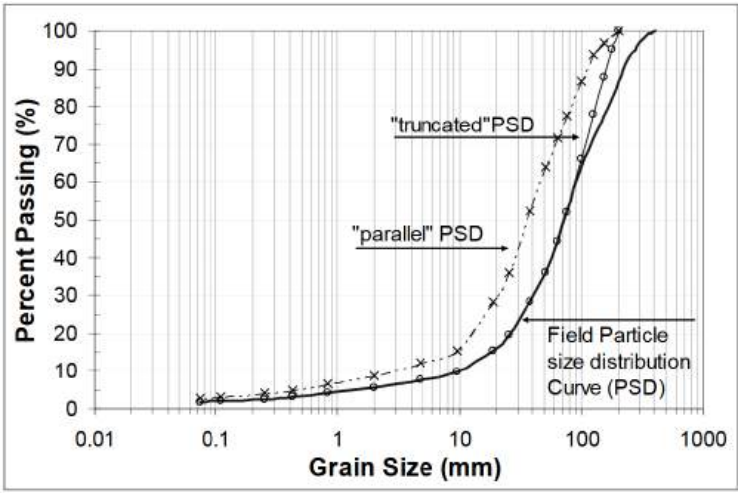

Figure 2.67 Truncated and parallel PSDs modeled after Linero et al. (2007).

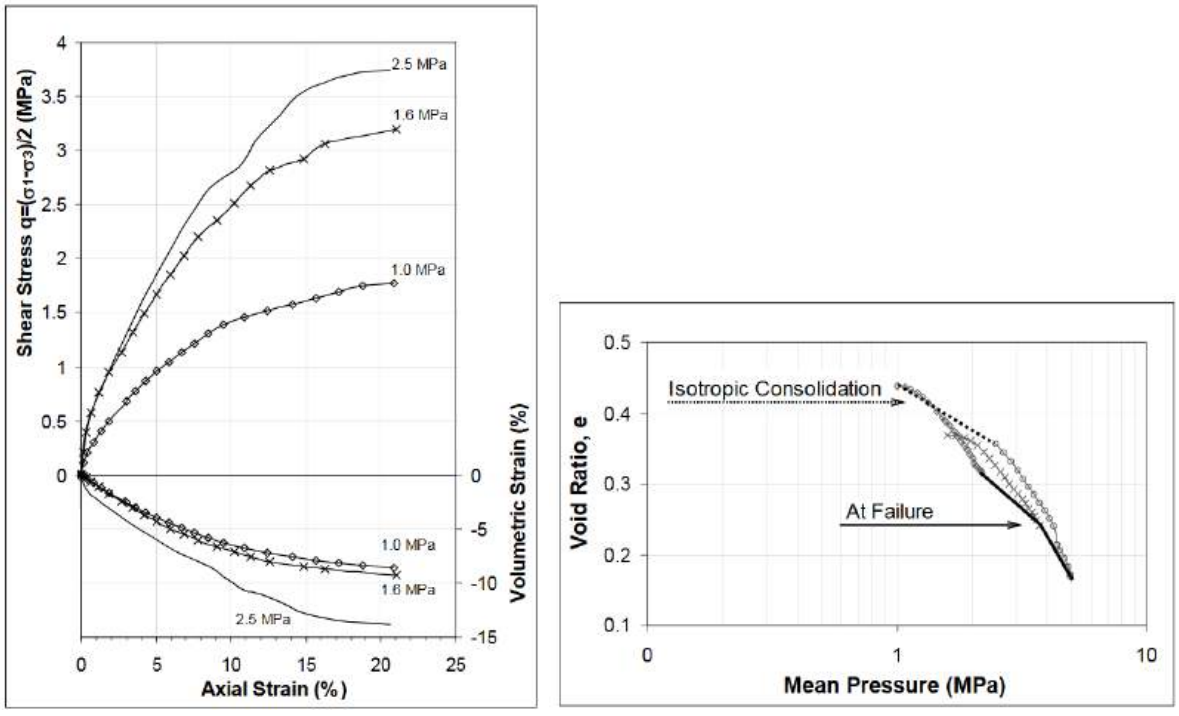

(a) (b)

Figure 2.68 Tests results on truncated specimens after Linero et al. (2007): (a) stress-strain curves; (b) void ratio vs mean stress.

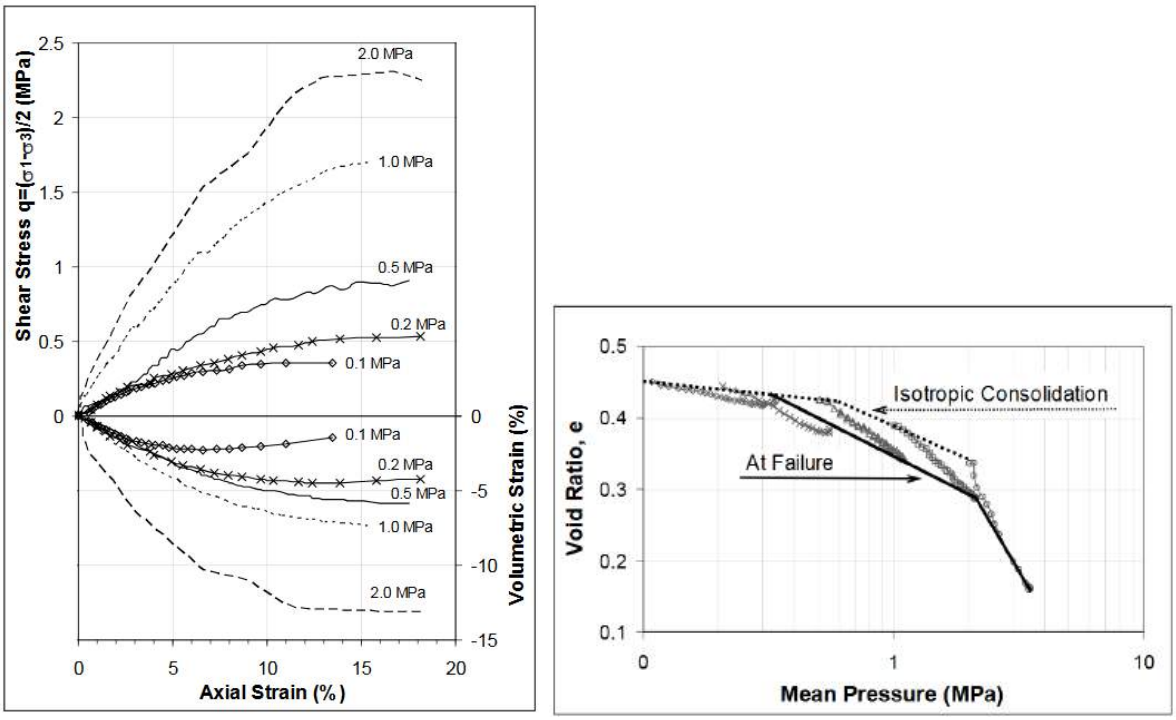

(a) (b)

Figure 2.69 Tests results on parallel-graded specimens after Linero et al. (2007): (a) stress-strain curves; (b) void ratio vs mean stress.

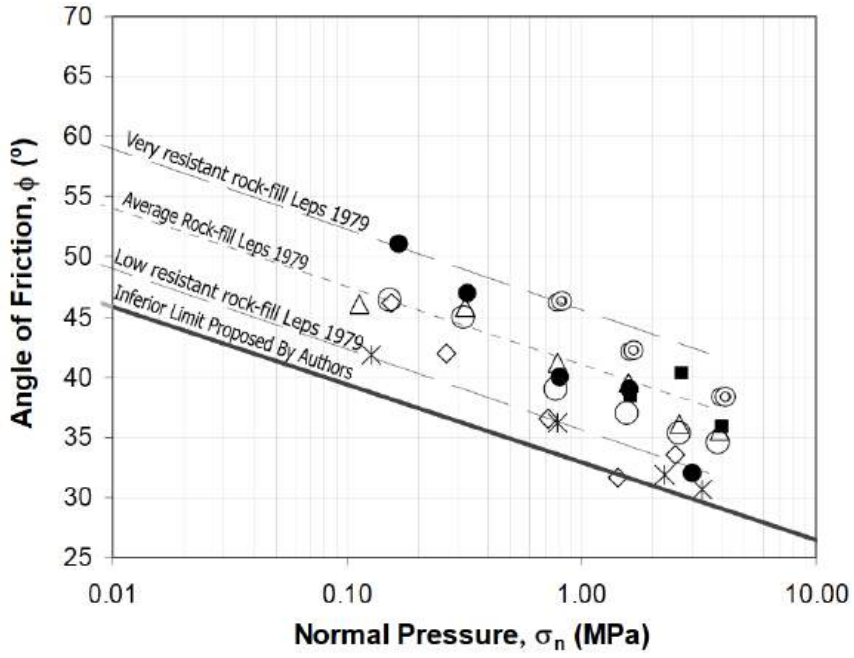

(a)

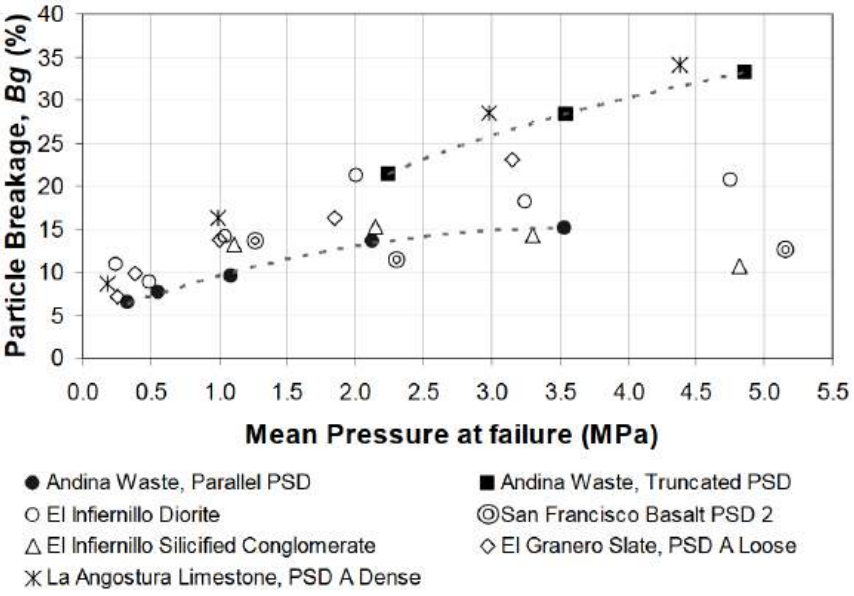

(b)

Figure 2.70 Comparison of truncated and parallel-graded specimens after Linero et al. (2007): (a) friction angle; (b) particle breakage.

2.5 Concluding remarks and research motivation

The mechanical behavior of waste rock, rockfills, and coarse soils, is governed by many factors, including the intrinsic properties of the granular material, specimen state and testing conditions. In addition, since experimental methods have size limitations, coarse soils are often scaled-down to fit the material into available devices. This introduces significant challenges in ensuring that the mechanical characterization remains representative of field conditions, which is essential for reliable engineering design.

A thorough literature review revealed that shear strength obtained using small-scale specimens of coarse materials is often inconsistent, even when the largest testing equipment is used. Namely, several authors show that the effective mobilized friction angle (ϕ') increases with the characteristic size of the particles, while many others conclude the contrary. *Figure* 2.71 presents a summary of various studies certifying this statement.

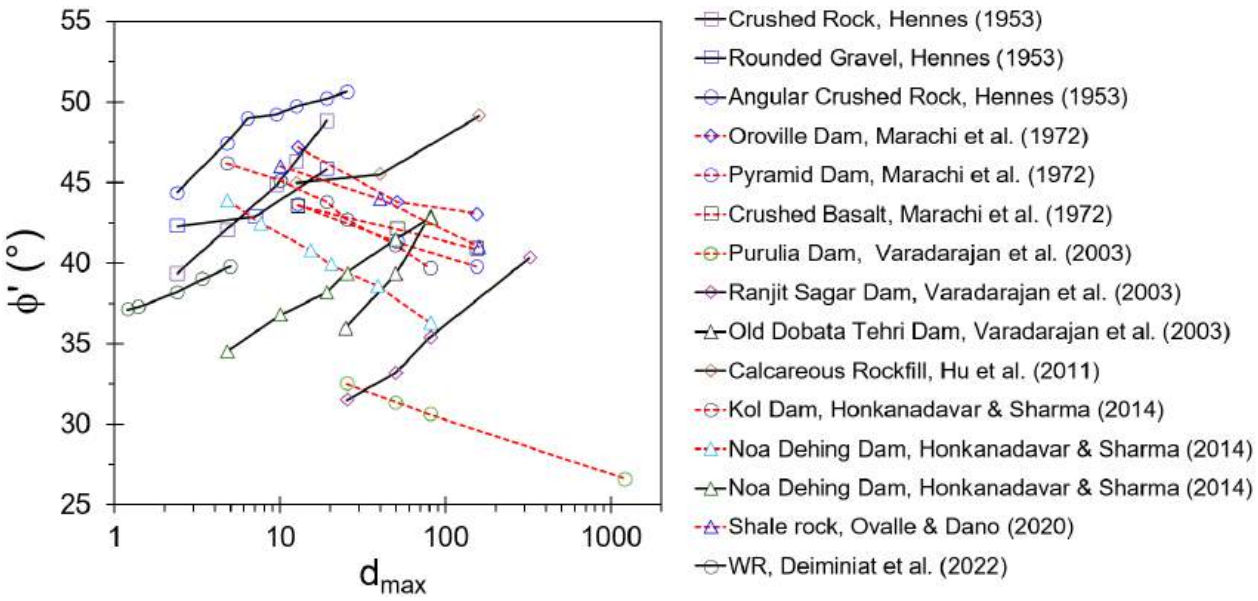

Figure 2.71 Summary of the contradicting trends reported in the literature on size effects of shear strength.

A number of factors might explain these apparent contradictions:

- the requirements to guarantee a REV specimen are different between well-known international standards, leading engineers and researchers to use different particle size scaling factors (i.e., aspect ratios α) and to make comparisons between specimens that are not large enough to be representative of the field material, or having significant experimental scattering;

- due to technical challenges to to accurately assess the density index of coarser-grained materials, tests do not always reach the critical state (particularly in dense specimens). Therefore, the comparisons at different scales might be between shear strength measured at different characteristic states (peak, critical, hardening, etc.);
- although under specific conditions the effective critical friction angle does not depend on PSD, the maximum strength does. Thus, changing the PSD to obtain more uniform small-scale specimens could result in lower maximum shear strength. This is clearly a grading effect that could be confused in the literature with size effects;
- the treatment of end restraint effects in triaxial specimens differs greatly between authors, resulting in a dispersion that is likely to be confounded with size effects;
- since small-scale requires altering the PSD, the characteristic particle shape of the material could also change, and this aspect is often neglected.

The main motivation of this thesis lies in the apparent contradictions about the effects of small-scale in coarse granular materials. This topic requires further investigation to improve the reliability of the mechanical characterization of coarse granular materials. It is presumed that most previous works have tried to cover small-scale effects under the umbrella of *particle size effects*. However, a critical review shows that different parameters, other than size, hide behind the effects of small-scaling, such as elementary volumes, grain shape, density and boundary conditions.

CHAPTER 3 METHODOLOGY

This section presents the experimental methods used in this thesis for investigating the effects of small-scaling and grading in coarse soils and rockfill materials. The approach followed to address the objectives proposed in *Chapter* 1 encompasses a series of experimental tests to evaluate the characteristic mechanical behavior of coarse soils in small, medium and large-sized laboratory and field tests. Tests were carried out on coarse soils of different origins: blasted waste rocks (WR) from mining operations, quarry rockfill and alluvial gravel materials.

3.1 Material sampling and geotechnical characterizations

3.1.1 Mine Waste Rocks

These materials were used for the experimental program presented in *Chapter* 4. Around 1 tonne of WR materials containing two lithologies, Sediments (Sed1) and Porphry (PO), were collected from the Canadian Malartic Mine in Québec, Canada, and transported to the Laboratory of Mining Environment of Polytechnique Montreal. Upon reception, the material was sieved in the laboratory and the PSDs are displayed in *Figure* 3.1. The characteristic grading properties show $d_{max} = 75$ mm and $C_u = 200$ and 17 for Sed1 and PO, respectively. The curvature coefficients for Sed1 and PO are $C_c = (d_{30})^2/(d_{10} \times d_{60}) = 5.5$ and 1.9, respectively. Furthermore, according to the mine, Sed1 and PO had the specifications shown in *Table* 3.1.

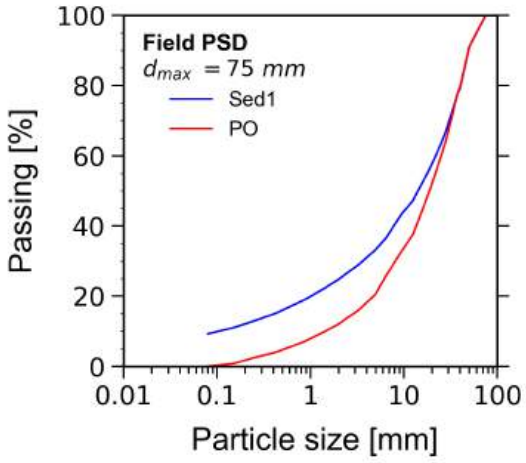

Figure 3.1 PSDs of the tested WR materials: Sed1 and PO.

Table 3.1 specimend WR material characteristics

Lithology	**specimen mass (kg)**	**UCS (MPa)**	G_s
Sediments, Sed1	520	128	2.75
Porphyry, PO	475	250	2.69

Characterization of fines

The material finer than 80μm was first characterized to identify its mineralogical composition. The Scanned Electronic Microscopic (SEM) analyses in *Figure* 3.2a-b reveal that the fine fraction of Sed1 contains flat laminated particles, whereas PO comprises angular particle shapes. On the other hand, the X-ray Diffraction (XRD) analyses in *Figure* 3.3 show similar mineralogical phases in both materials, including silicates (quartz and albite), carbonates, micas and chlorites.

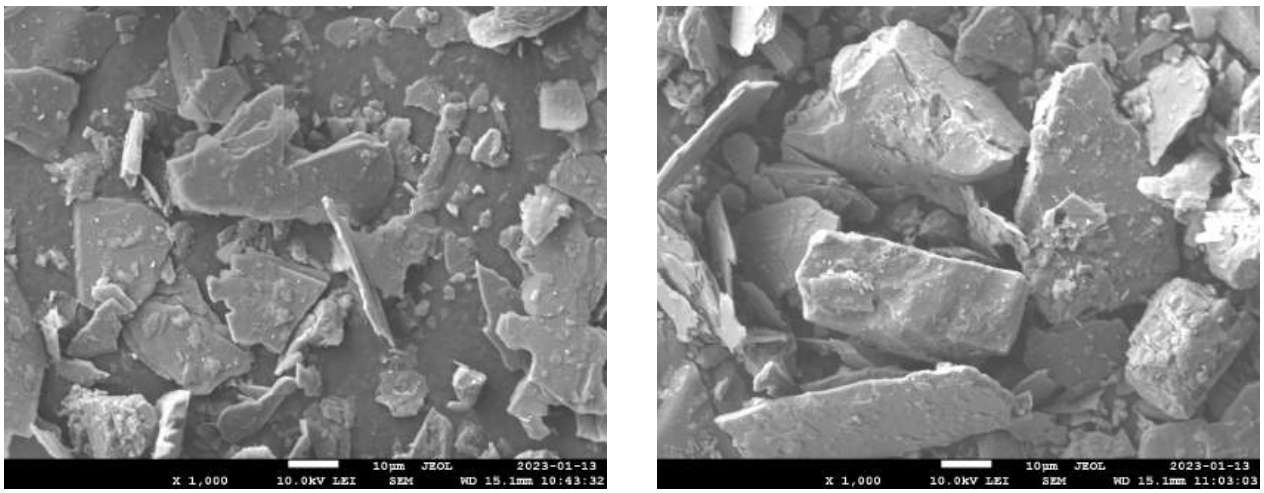

(a) (b)

Figure 3.2 SEM characterization of fines $d < 80\mu m$: (a) Sed1 material; (b) PO material.

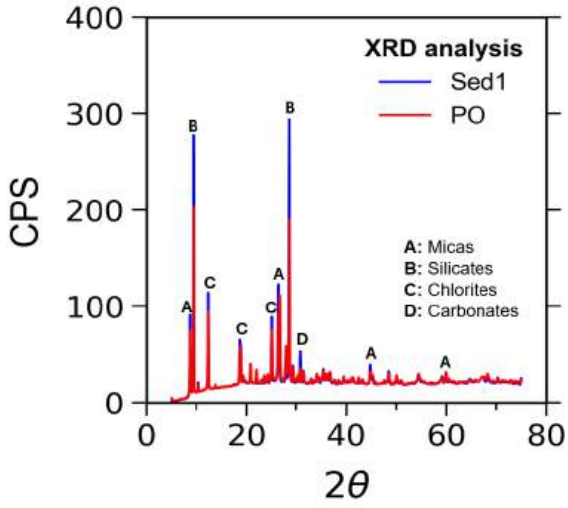

Figure 3.3 XRD analyses on both materials.

The Plasticity Index (PI) of the fine fraction of Sed1 (10%) was determined. Following ASTM D4318 (2017), the fraction passing 0.425μm sieve was used to determine the Plastic Limit (w_P) and the Liquid Limit (w_L). The results of 6 tests showed an average value around $w_P \approx 23\%$ and $w_L \approx 27\%$; $PI = w_L - w_P \leq 5\%$, classifying as low plastic fines. Therefore, Sed1 classifies as well-graded gravel with silt and sand (GW-GM) (ASTM D2487, 2017). Conversely, PO material does not contain fines and classifies as well-graded gravel with sand (GW).

Particle shape characterization

The roundness (R) and particle width-to-length sphericity (S_{WL}) were determined on the size fractions above $d > 1\ mm$. For this end, the computational algorithm proposed by Zheng and Hryciw (2015) and Zheng and Hryciw (2016) was used and the details are outlined hereafter.

Algorthim to compute particle shapes

Figure 3.4 outlines the procedures followed for the S_{WL} computation on a given particle. First, the particle photo is imported and binarized in Matlab. After which the following steps proceed:

- discretization of particle silhouette (a);
- definition of a minimum loop from outer points which allows englobing all discretized points (b);

- the distance between 2 far points (1 and 5 in this illustrative case), is defined as the diameter of the trial circle, which becomes the minimum circumscribing circle (c);

- if there is any point outside the trial circle, it is added to the first two points to obtain a new diameter and therefore a new minimum trial circle (d);

- the particle is circumscribed by a rectangular bounding box ranging over 180° orientation from which the largest dimensions are defined: the length and the width of the particle [e-h].

In parallel, the roundness R is determined from the binarized photo in 3 steps:

1. *Maximum inscribed circle radius (r_{in})* (*Figure* 3.5a-d): from the particle silhouette defined earlier (*Figure* 3.4), an Euclidean distance map (D in pixels) is delimited for each point inside the particle to the outline perimeter. Then a maximum inscribed circle with center C_{in} and maximum D is obtained with radius r_{in}.

2. *Identification of particle corners*: a random segment AB is defined (*Figure* 3.6a) with a critical distance between the approximated chord and the original segment (δ_o) (*Figure* 3.6b-c). The corner points are then identified by all key points, for instance, point E in *Figure* 3.6d. A particle centroid O is detected and a straight-line OE is drawn. Logically, point E should be between two adjacent key points C and D. Another straight line CD is drawn, and an intersection F is identified when OE is prolonged. If $OE > OF$ then E is considered a corner point. Otherwise, the point is omitted. This process is repeated on all points to identify all 'concave' corners (*Figure* 3.6e).

3. *Circle fitting in concave corners* (*Figure* 3.7): a large circle of center C and radius r is fitted to englobe all the key points identified previously (1 to 43), and the minimum distance d is defined from C to any particle contour point. If $d \approx r$, a circle tangent to the concave contour is fitted (*Figure* 3.7b) and the key points fitted are excluded for the subsequent iterations. If $d < r$ (*Figure* 3.7c), the point is also excluded and the new iteration follows in other remaining points, or until only 3 key points remain. *Figure* 3.7d shows the final fitted circles of radius r_i.

At the end of iterations, R is automatically calculated by *Equation* 3.1 proposed by Wadell (1932), where N is the number of the fitted circles.

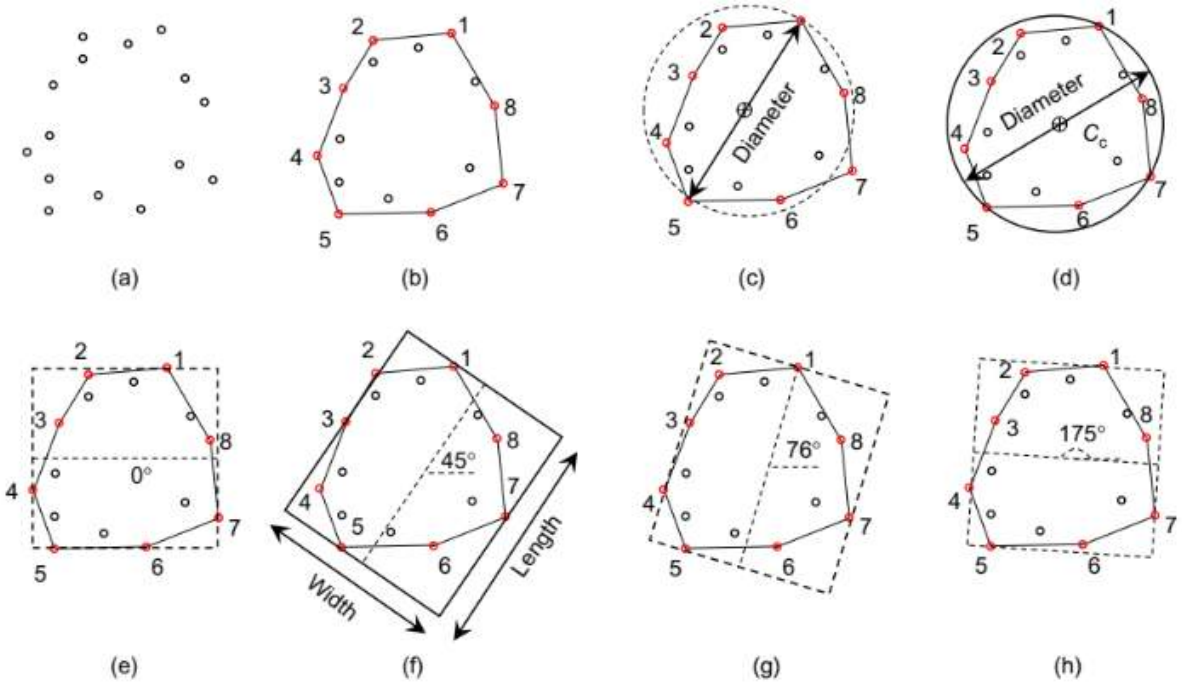

Figure 3.4 Determination of the largest particle dimensions (Zheng & Hryciw, 2015).

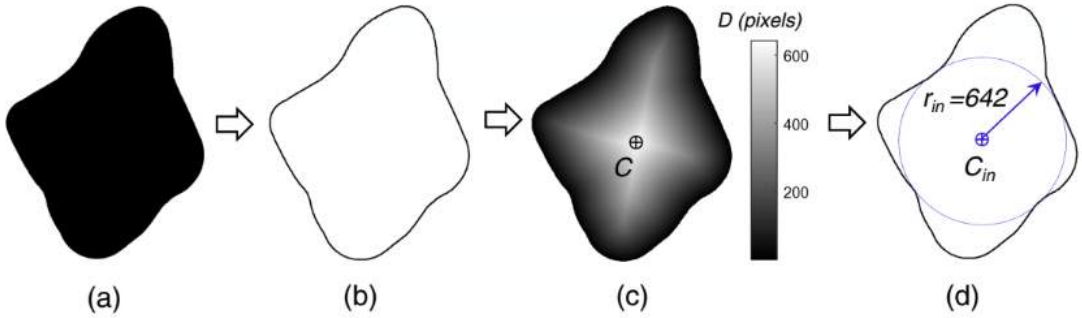

Figure 3.5 Determination of the maximum inscribed circle radius r_{in} after Zheng and Hryciw (2016): (a) input binary image; (b) extracted particle outline; (c) Euclidean distance map; (d) computed r_{in}.

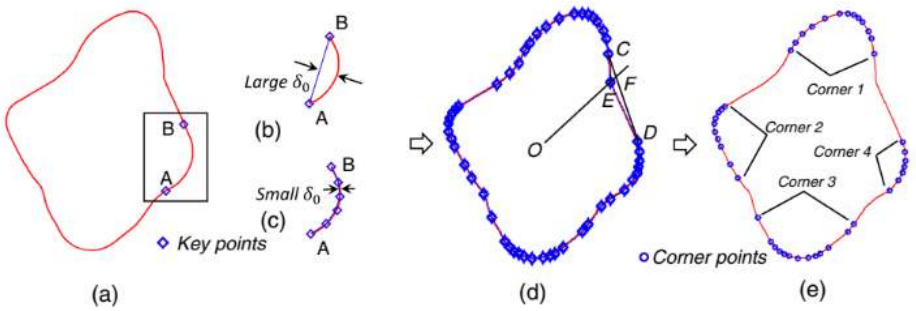

Figure 3.6 Identification of particle corners (Zheng & Hryciw, 2016): (a) random segment between 2 key points; (b-c) various δ_o between chords and original segments; (d) determination of a corner point; (e) identified particle corners.

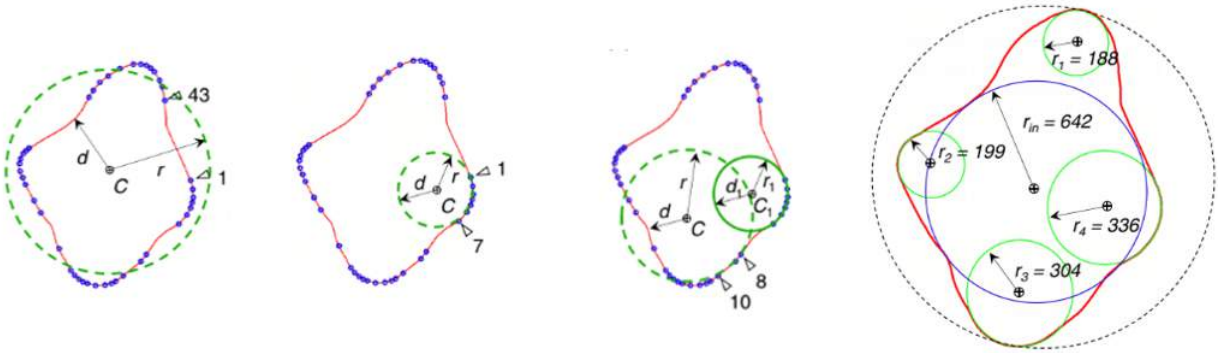

(a) (b) (c) (d)

Figure 3.7 Corner fitting procedures: (a) first attempt fitting key points 1 to 43; (b) a concave corner accepted when $r \leq d$; (c) circle rejected when $r > d$ and only 3 key points are remaining; (d) final result fitting all concave corners.

$$R = \sum \frac{r_i/N}{r_{in}} \tag{3.1}$$

Results on Sed1 and PO materials

As shown in *Figure* 3.8, the previously detailed procedure is followed, where Sed1 particles binarization is presented (*Figure* 3.8a). The results in *Figure* 3.8b indicate that Sed1 and PO material have $R = 0.3 - 0.4$ and $S_{WL} = 0.7$, classifying as subangular particles with low sphericity.

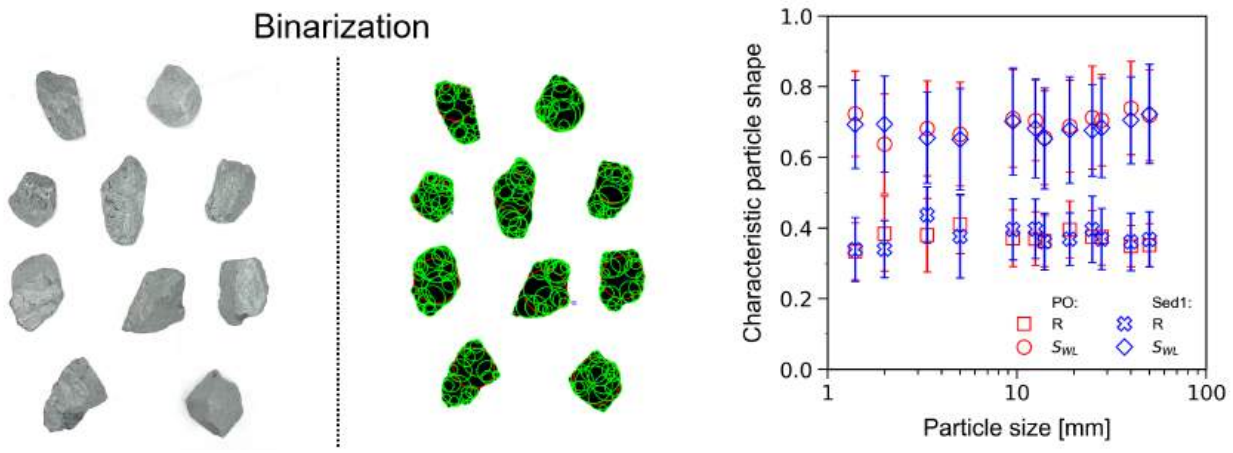

(a) (b)

Figure 3.8 Results on particle shape characterization: (a) binarization of Sed1 particles $d = 50$ mm; (b) computed R and S_{WL} on Sed1 and PO.

In order to study size effects and REV conditions in mine waste rock materials, several specimens were prepared using the scalping grading technique. Varied d_{max} and C_u were generated from the field PSDs shown previously in *Figure* 3.1. The resulting PSDs are explained and presented in *Chapter* 4. The materials were tested in triaxial specimens of different diameter $D = 150$ and 300 mm.

3.1.2 Quarry Rockfills

These materials were used for the experimental program presented in *Chapter* 5. The quarry rockfills were specimend from a quarry in St-Eustache (Québec), and consist of blasted and crushed dolomite rock. 1 tonne was received and sieved at the Laboratory of Mining Environment of Polytechnique Montreal (*Figure* 3.9a). The characteristic grading properties presented in *Figure* 3.9b show $d_{max} = 90$ mm, $C_u = 9$ and $C_c = 1.6$. Therefore, the material classifies as GW (ASTM D2487, 2017). *Figure* 3.9c reveals that both R and S_{WL} were consistent across sizes, denoting subangular to subrounded particles ($R = 0.3 - 0.4$) with medium to high sphericity ($S_{WL} = 0.5 - 0.8$).

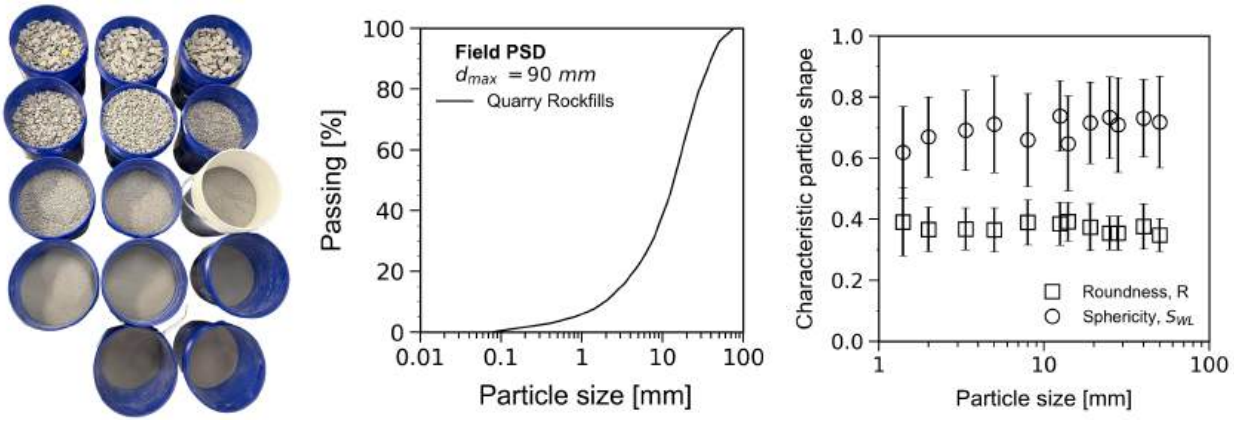

(a) (b) (c)

Figure 3.9 Quarry Rockfills: (a) buckets received; (b) PSD of the in-situ material; (c) particle shapes.

Specific gravity G_s

According to ASTM D854 (2014), *Figure* 3.10 displays two PSD fractions used to characterize the G_s of the material: a scalped PSD $d \leq 4.75$ mm and a coarse PSD retained at $d = 4.75$ mm. The passing percentage of a characteristic size d ($\%_d$) was obtained after *Equation* 3.2 (ASTM C127, 2024).

First, the material was oven-dried for 24 hours and placed in a calibrated 500 ml pycnometer of mass (M_a). M_b is then recorded, comprising the solid material and the pycnometer. The distilled water is filled in the pycnometer up to the 500 ml marker, and the whole is placed on a shaking de-airing device for 30 minutes to evacuate the entrapped air. This results in the water level dropping below the 500 mL point. Hence, the pycnometer is refilled to the marker, to record the mass with solid and water (M_c). Subsequently, the pycnometer is emptied, cleaned and refilled with only distilled water up to the marker, to record M_d. The G_s is calculated after *Equation* 3.4, and the results on the fraction $d \leq 4.75$ mm from the three tests indicate average $G_s = 2.79$, and $G_s = 2.74$ in coarse aggregate $d > 4.75$ mm.

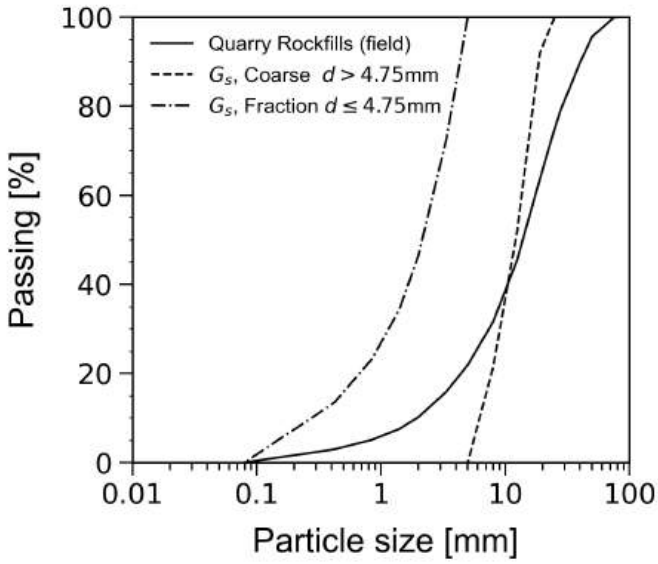

Figure 3.10 PSDs for G_s determination.

$$\text{coarse PSD } (>4.75 \text{ mm}) = \frac{\%_d - \%_{4.75}}{100 - \%_{4.75}} \times 100 \tag{3.2}$$

$$G_{(s,t)} = \frac{M_s}{M_W} = \frac{(M_b - M_a)}{(M_b - M_a) - (M_c - M_d)} \tag{3.3}$$

$$G_{(s,calibrated)} = K \times G_{(s,t)} \tag{3.4}$$

with,

$G_{(s,t)}$: Specific gravity at room temperature;

$G_{(s,calibrated)}$: Calibrated specific gravity of material;

M_s: Mass of solid;

M_W: Mass of water;

K: Temperature coefficient given in ASTM.

In order to account for the effects of grading and evaluate the impact of boundary effect on triaxial compression behavior, the quarry rockfill material was scaled down at $d_{max} =$ 25, 12.5, 8, 6.3 and 5 mm using scalping grading and parallel techniques. The resulting PSDs

are explained and presented in *Chapter* 5. The materials were tested in triaxial specimens of diameter D = 150 mm.

3.1.3 Alluvial Gravels

These materials were used for the experimental program presented in *Chapter* 6, carried out at the *Institut für Bodenmechanik und Felsmechanik* (IBF) (Institute of Soil Mechanics and Rock Mechanics) at the Karlsruhe Institute of Technology, in Germany. 15 tons of terrace alluvial material (Terrassenschotter) were sampled (*Figure* 3.11a). Due to the large quantity, the material was first sieved using a large machine shown in *Figure*3.11(b) for aggregates $d \geq 11$ mm, and then in a medium-sized machine (*Figure* 3.11c) for the portion below $d < 11$ mm. The PSD in *Figure* 3.12a indicates that the material classifies as GW, with $C_u = 59.7$, $C_c = 1.5$ and $d_{max} = 125$ mm. G_s of 2.67 was obtained. The characteristic particle shapes in *Figure* 3.12b indicate variations in $R = 0.3 - 0.8$, showing subrounded to well-rounded particles. However, S_{WL} remains systematically stable from medium to high sphericity, with $S_{WL} = 0.6 - 0.8$.

(a) (b) (c)

Figure 3.11 Specimen alluvial gravels sampled: (a) unsieved material in the bag; (b) large-scale sieving on $d \geq 11$ mm; (c) sieving machine used for the portion $d < 11$ mm.

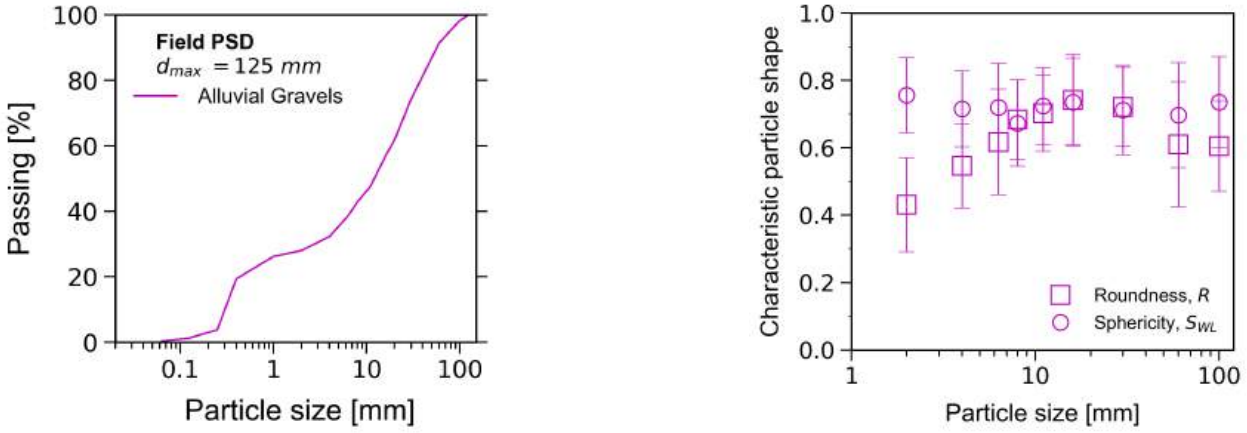

(a) (b)

Figure 3.12 Tested alluvial gravels: (a) PSD of the field material; (b) particle shapes.

In order to account for the effects of specimen size and grading on characteristic mechanical properties, the alluvial gravel material was scaled down at d_{max} = 100, 60, 30, 20, 11 and 6.3 mm using scalping grading and truncation techniques. The materials were tested in triaxial specimens of diameter D = 100, 150 and 800 mm, as further detailed in *Chapter* 6.

3.2 Experimental devices and setups

This section describes the experimental devices used in this research for small, medium sized and large mechanical testing. The study was developed in two laboratories and one mine site, as explained hereafter.

3.2.1 Laboratory of Mining Environment at Polytechnique Montreal

The laboratory of Mining Environment at Polytechnique Montreal is equipped with VJTech triaxial devices allowing specimens of D = 150 and 300 mm. *Figure* 3.13 shows these apparatuses, with M1 for specimens of D = 150 mm and height H=300 mm, and L1 for D = 300 and H=600 mm. Data acquisition (DAQ) comprises hydraulic pressure controllers and loadcells that store data automatically in the Clisp Studio software from VJTech. The loadcell capacity for M1 is 50 kN and 200 kN for L1. The M1 and L1 triaxial devices have the standard rough caps and bases and can withstand maximum confining pressures of σ_3 = 1700 and 2000 kPa, respectively. The typical photos of M1 and L1 specimens after tests are shown in *Figure* 3.14.

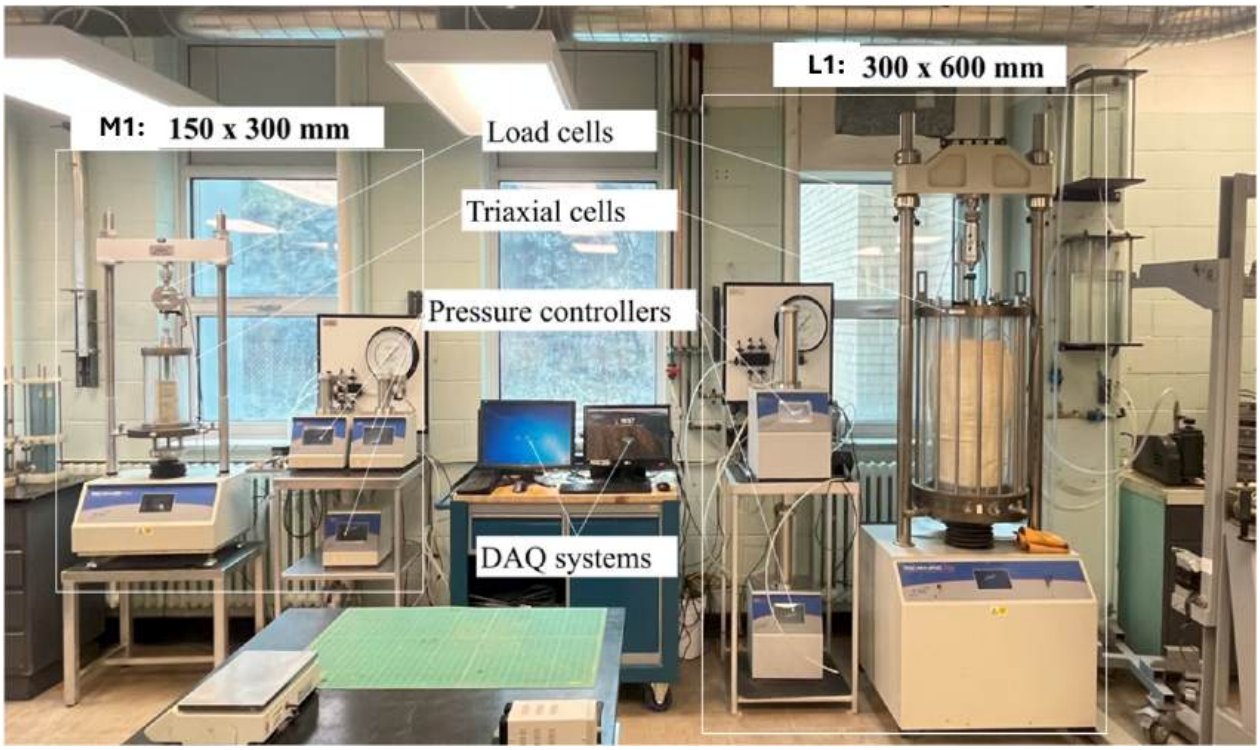

Figure 3.13 Triaxial test setup at Polytechnique, for medium- and large-sized specimens, M1 and L1, respectively.

Figure 3.14 Photos displaying M1 (D=150mm) and L1 (D=300mm) specimens after test.

In this thesis, the boundary conditions of M1 specimens were modified to avoid end-restraint effects. The cap and base were enlarged to 170 mm and lubricated, to allow end dilation of D=150 mm specimens. The enlarged caps were made of 3 cm thick lucite material. A sheet of latex membrane (1 mm thick) was placed between the cap and the specimen, and the contact between the membrane and the cap was lubricated with silicone grease. *Figure* 3.15a-b presents M1 specimens with different end configurations: (a) regular standard rough platens and (b) enlarged-lubricated platens. These end configurations were used in the study presented *Chapter* 5, to assess the end-restraint effects in triaxial tests on H:D=2:1 specimens of quarry rockfill.

(a) (b)

Figure 3.15 Photos of M1 specimens before testing: (a) with standard cap and base; (b) with enlarged-lubricated cap and base.

3.2.2 In-situ tests at Canadian Malartic Mine

A non-standard large-scale in-situ direct shear test (DST) box was developed to characterize Sed1 material at the Canadian Malartic Mine in Quebec, Canada. As shown in *Figure* 3.16, a square lattice shear frame of $120 \times 120 \times 38$ cm^3 was designed following the approach of Matsuoka et al. (2001), to accommodate WR material with $d_{max} = 75$ mm and a maximum horizontal pulling force ($F_h = 50t$). F_h is measured by the two loadcells placed by the front side of the box (*Figure* 3.16a). The maximum capacity of each loadcell shown in *Figure* 3.16b is $100t$, the sensitivity is 2.85mV/Volt, and the excitation voltage is 5V. This allows calculating the conversion factor to transform the measured volts into tonnes. The large steel box is made of high-strength C-shaped steel sections $C15 \times 40 - 50$ (i.e., the thickness that varies between 13.2-18.2 mm). Additionally, a pressing kit acting as the loading plate, was adopted to accommodate the counterweights ($10t$ each) used to apply the

normal force (F_v).

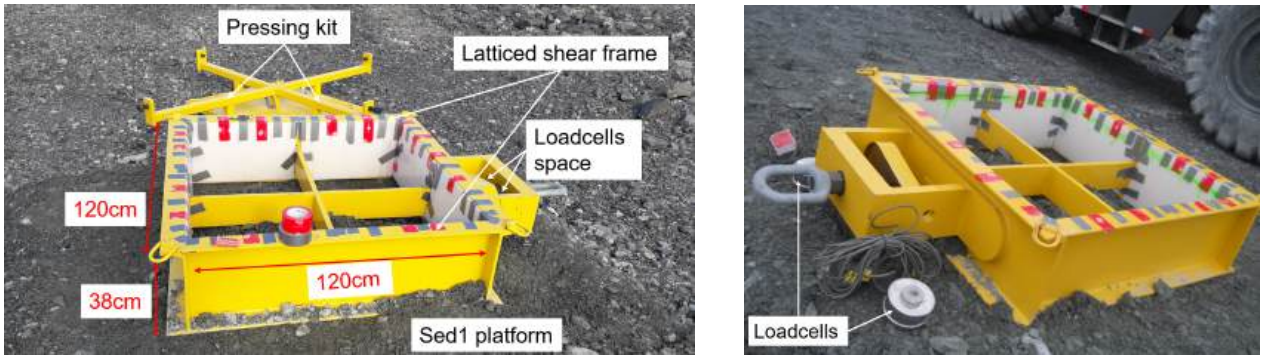

(a) (b)

Figure 3.16 In-situ latticed DST frame: (a) details of the box components; (b) sideview showing loadcells.

The principle is that the box is pulled over the platform made of the same material that fills it, and shear failure develops on the surface between the box bottom and the surface of the platform. Two SP2-50 model potentiometers attached to the pressing kit and an external referral point record the settlement and horizontal displacement (h) of the specimen under loading. The potentiometers were acquired from DigiKey and have the following specifications: full stock (fs) range distance of 101.6–1270 mm, accuracy ±0.25% of fs and repeatability of 0.02% of fs.

The full-scale setup of the test is depicted in *Figure* 3.17, showing an excavator used to apply F_h via a pulling chain attached to the box, and a crane for F_v manipulations. The setup also shows a data acquisition system (DAQ) to record all the data. *Figure* 3.18 shows (a) the used potentiometer series, (b) USB-2408-500 (16-channel input), and (c) a Walz7000 scale readout to display digital loadcell readings. In addition, the DAQ consists of TracerDAQ Pro software from Measurement Computing and a PE Portable Enclosure from Waltz Scale for easy and safe handling.

This design allows direct measurement of the applied σ'_n and τ as the shear cross-section area is assumed constant upon shearing. *Figure* 3.19a shows an example of a shearing test pulling $F_v = 30t$ (i.e., 3 crane counterweights); the correction of the chain inclination in (b) is done using an online protractor tool for accurate result interpretation. As displayed in *Figure* 3.20a-b, shear strength at large strain beyond $h \geq 40$ cm can be achieved. This in-situ configuration was used in the study presented *Chapter* 4, to assess the shear strength of coarse WR materials at Canadian Malartic Mine.

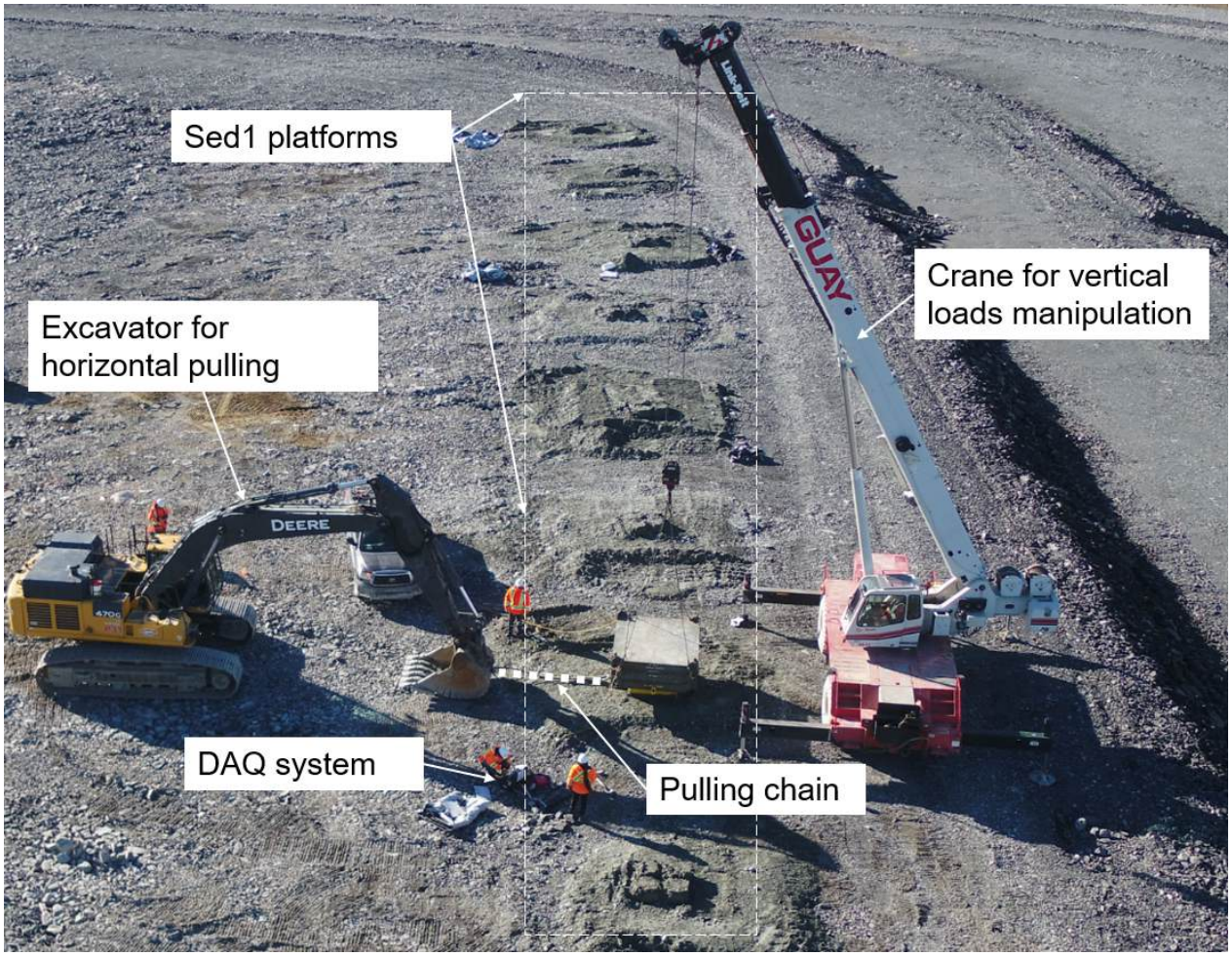

Figure 3.17 In-situ full-scale setup view.

(a) (b) (c)

Figure 3.18 DAQ components: (a) SP2-50 model potentiometer; (b) USB-2408-500 (16-channel input); (c) Waltz7000 scale display.

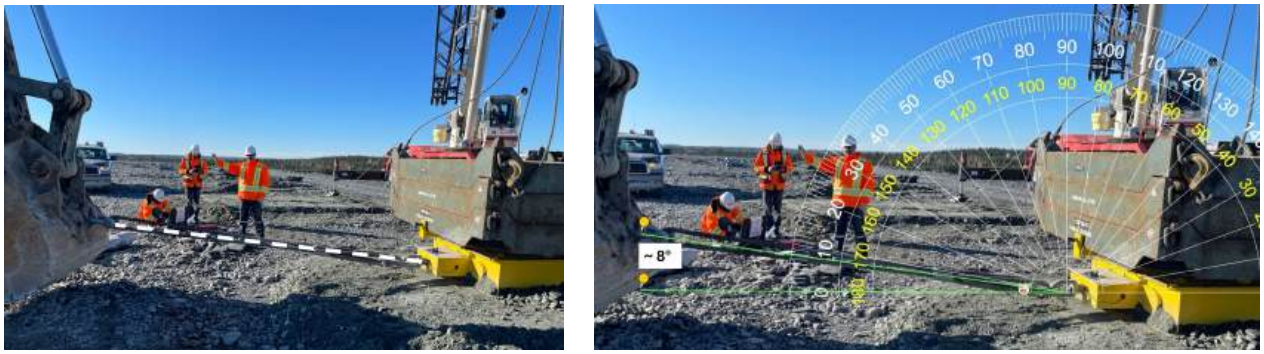

(a) (b)

Figure 3.19 In-situ DST shearing: (a) showcase of the test under $F_v = 30t$; (b) online measurement of the inclination angle for data correction.

(a) (b)

Figure 3.20 Large shear strain attained beyond $h \geq 40$ *cm*: (a) back view; (b) side view.

3.2.3 IBF laboratory at KIT

The IBF laboratory disposes of triaxial devices allowing $D = 100$, 150, and 800 mm. Unlike the equipment at Polytechnique Montreal, the devices handle specimens with the same heights as the diameters: H:D=1. In order to make a distinction with M1 and L1 in *Section 3.2.1*, here $D = 100$, 150, and 800 mm are referred to as S2, M2 and L2, for small, medium and large specimens, respectively.

Figure 3.21a shows the device pedestal for L2 specimens, displaying also the burette and pressure control systems. The view of the cell installation is shown in *Figure* 3.21b. The DAQ system and hydraulic steer wheels view are shown in *Figure* 3.22. Furthermore, *Figure* 3.23 shows the final stage of the L2 specimen ready for testing. It should be noted that the preparation of an L2 specimen (∼900 kg) took around 6 working days, including 2-3 for sieving and specimen preparation, 1 for saturation and consolidation, and 2 for shearing and

dismantling. Typical photos after the tests are shown in *Figure* 3.23a-b, showcasing the membrane removal and close-up view of the alluvial gravels in the specimen.

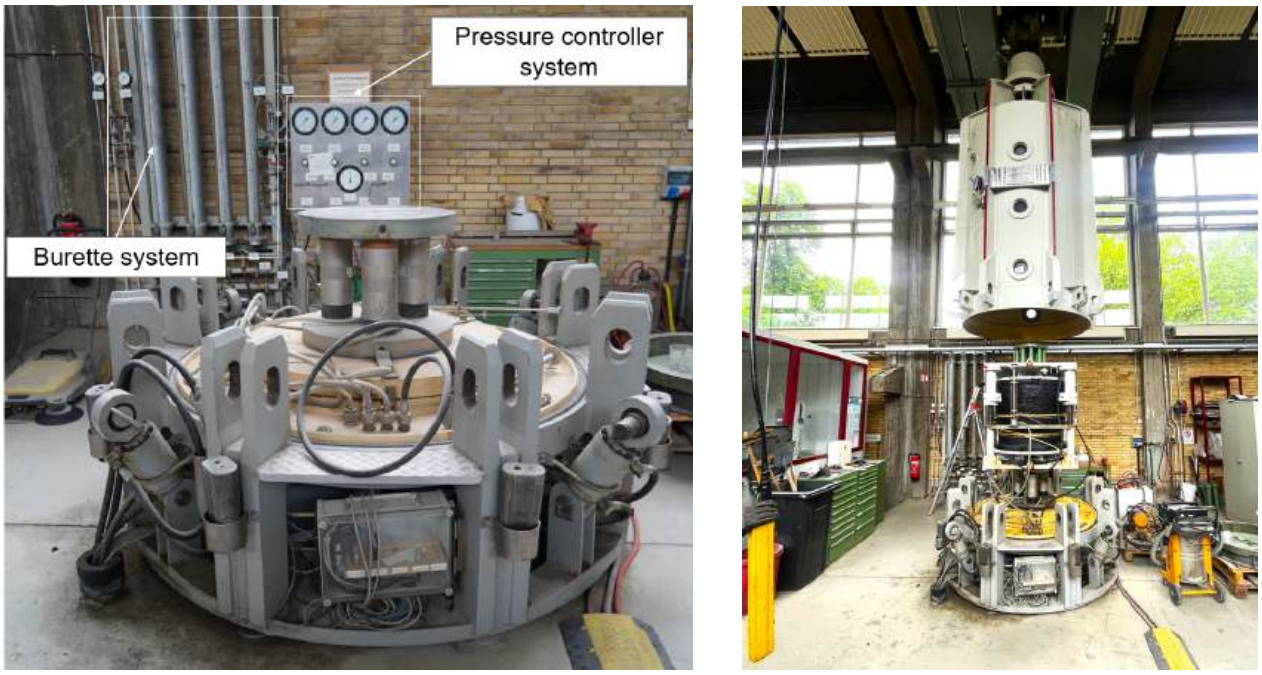

(a) (b)

Figure 3.21 L2 ($D = 800$ mm) test setup: (a) device pedestal; (b) placing the cell cover.

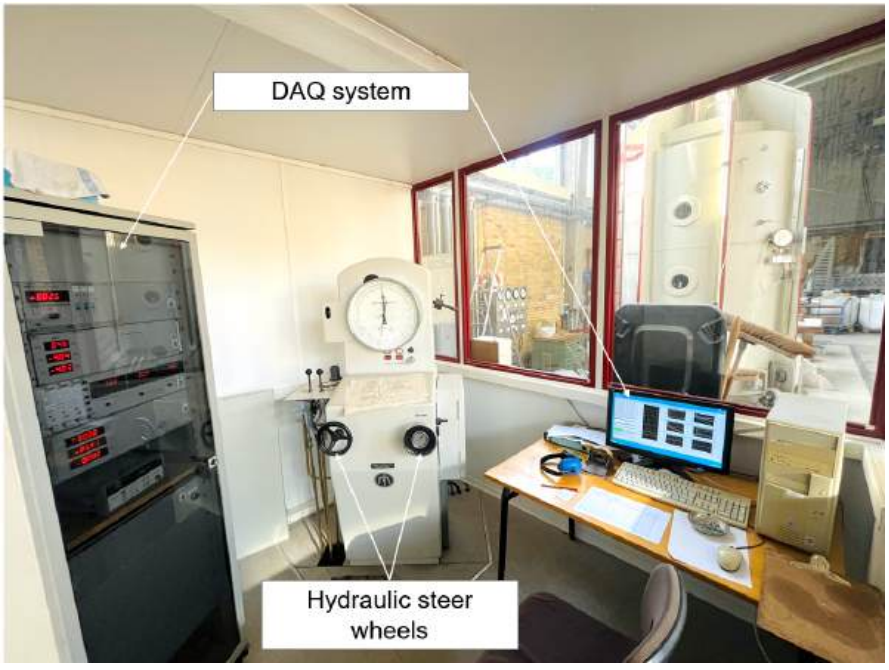

Figure 3.22 DAQ system for L2 specimens at IBF.

Figure 3.23 L2 ($D = 800$ mm) test setup, device ready for testing.

(a)

(b)

Figure 3.24 L2 ($D = 800$ mm) specimens after testing: (a) removing the membrane; (b) view of alluvial gravels in the specimen.

3.3 Overview of the experimental work

In this thesis, around 170 tests were carried out on a wide range of coarse granular materials (mine WR, quarry rockfill and alluvial gravels), using several triaxial laboratory devices of varied sizes (D=100 to 800 mm). The packing properties and characteristic particle shapes of all tested materials were characterized to establish a comparable basis ranging from loose to dense specimens, as well as subangular to rounded coarse particles. The stress levels varying from $\sigma'_3 = 45 - 600\ kPa$ were considered to the characteristic mechanical property behaviors, considering grading effects.

In addition, a large in-situ DST was performed using one of the world's largest direct shear boxes $1200 \times 1200 \times 380\ mm^3$ ever reported. The results presented in the following Chapters allowed a comprehensive assessment of the effect of small-scaling methodologies in coarse soils across varying scales.

CHAPTER 4 ARTICLE 1 – Grading Scalping and Sample Size Effects on Critical Shear Strength of Mine Waste Rock Through Laboratory and In-Situ Testing

Journal: International Journal of Rock Mechanics and Mining Sciences.
Published: September 21, 2024.
DOI: doi.org/10.1016/j.ijrmms.2024.105915

Authors: Gilbert Girumugisha[a,b], Carlos Ovalle[a,b,*], and Serge Ouellet[c]

[a]Dep. of Civil, Geological and Mining Engineering, Polytechnique Montréal, Québec, Canada.

[b]Research Institute of Mining and Environment (RIME UQAT-Polytechnique), Canada

[c]Agnico Eagles Mines, Partenariat Malartic.

[*]Corresponding Author, ✉ carlos.ovalle@polymtl.ca.

ABSTRACT Geotechnical stability analyses of mine waste rock (WR) piles require the critical friction angle (ϕ_{cr}) of the coarse blasted rock. However, due to the presence of oversized rock clasts, shear strength can only be characterized on small samples prepared using grading scaling techniques, such as scalping. Thus, considering a testing device able to handle samples of characteristic size D, the material should be scaled down to a maximum particle size d_{max} given by the minimum sample aspect ratio: $\alpha = D/d_{max}$. However, a practical concern about how far the size scale can be reduced while keeping representative results remains a matter of debate in the geotechnical community. International standards do not agree on the minimum recommended α, and its effects on the mechanical behavior remain poorly understood. This paper aims to investigate the grading effects and sample size effects on ϕ_{cr} of WR materials using the scalping technique, to provide insights on the minimum recommended α. Triaxial tests were conducted on loose and dense samples of diameters $D = 150$ and 300 mm. Samples were scalped from field material having $d_{max} = 75$ mm, to allow a range of α from 4 to 30. Additionally, one of the world largest in-situ direct shear boxes ($120 \times 120 \times 38$ cm^3) was developed to test the same WR material. The results show that scalping is an appropriate technique to assess the critical shear strength of WR. The minimum α for ϕ_{cr} assessment in triaxial testing is not sensitive to grading nor sample size, but it is affected by sample density. The aspect ratio was found to be $\alpha \geq 12$ and $\alpha \geq 16$

for loose and dense samples, respectively. This finding advocates that α values recommended by worldwide standards, such as ASTM D7181-20, might be too low and should be revisited after comprehensive testing.

4.1 Introduction

Significant amount of waste rock (WR) material must be blasted and excavated to access ore in hard rock mining operations. In open pit mines, the stripping ratio (defined as WR/ore in weight) is about 2 to 3, implying millions of tons of WR produced yearly (SME, 2011). In addition, with the price increase of minerals in recent years, the tendency to have lower grades and deeper pits has become economically feasible. This scenario suggests that WR volume production is expected to grow significantly in the future (USGS, 2022). Large amounts of loose dumped WR are stored in piles that can reach hundreds of meters in height. To analyze their physical stability, the critical shear strength of the loose WR material is required. Blasting typically results in WR having well graded particle size distribution (PSD). The material can have coarse rock clasts that can easily reach around 1 m in diameter, as well as gravelly and sandy fractions, and a limited amount of fine content (FC) of about FC= 5 to 20% (finer than 80 microns, i.e. passing sieve #200) (Bard et al., 2011; Hawley & Cunning, 2017; Linero et al., 2007; McLemore et al., 2009; Valenzuela et al., 2008). However, mechanical characterization of such coarse materials is not possible in standard laboratory devices, neither using the largest apparatuses ever reported (Barton, 2013; Barton & Kjærnsli, 1981; Hu et al., 2011; Indraratna et al., 1998; Lee et al., 2009; Li et al., 2020; Linero et al., 2020; Marachi et al., 1972; Marsal, 1967; Ovalle et al., 2020; Verdugo & de la Hoz, 2007; Zhang et al., 2016). The most common approach is to modify the PSD through grading scaling techniques, such as scalping and parallel grading. The aim being to reduce the maximum particle size (d_{max}) to handle a small-scaled sample that can be tested in standard direct shear boxes or triaxial cells.

Grading scaling is usually done through the aspect ratio, defined as $\alpha = D/d_{max}$ for triaxial samples of diameter D, or $\alpha = L/d_{max}$ for direct shear boxes of width L. Note that the height (H) of the sample should also be large enough to avoid boundary effects; for instance, $2D \leq H \leq 2.5D$ for triaxial tests (ASTM D7181, 2020) and $L/H \geq 2$ for direct shear tests (ASTM D3080, 2011). The value of α should be high enough to test a representative sample avoiding size effects on its mechanical behavior. Also, the smallest recommended α is aimed to prepare samples having d_{max} as coarse as possible as the field material. However, international testing standards disagree on the minimum α required. For triaxial tests, ASTM D7181 and JGS 0530 recommend $\alpha \geq 6$ and 10, respectively. Concerning direct shear tests (DST),

ASTM D3080 and JGS 0561 recommend $\alpha \geq 10$ and 70, respectively. At the same time, experimental evidence on this issue is scarce and the effects of α on the mechanical behavior of granular soils remain a topic of debate in the geotechnical community. For instance, recent studies on DST propose that a representative sample should have a value of $\alpha = 40$ to 60 (Amirpour Harehdasht et al., 2018; Bauer & Ebrahimian, 2021; Cerato & Lutenegger, 2006; Deiminiat et al., 2022; Jacobson et al., 2007; Jewell & Wroth, 1987; Wu et al., 2008; Ziaie Moayed et al., 2016). However, if such a high α is needed, DST could be unsuitable to test coarse materials since the sample would be considerably finer than the field material. Eventually, the properties of the fine fraction could greatly differ from the coarse fraction, affecting the scaled sample representativity in terms of its mechanical behavior. On the other hand, according to the standards, triaxial testing could allow a coarser representative than DST, when comparing devices of the same characteristic size. However, there are only few reported works of α effects on triaxial tests and the standards are mainly based on pioneering works of Holtz and Gibbs (1956), Zeller and Wullimann (1957) Lowe (1964), and Fumagalli (1969), among others. Thus, with the aim of ensuring proper mechanical characterization of « as coarse as possible » scaled granular materials, it is important to further explore and understand both sample size and particle size effects.

As a condition for all the existing grading scaling techniques, the characteristic particle shape of the scaled material must remain the same as the original sample. Otherwise, particle shape could significantly affect the mechanical behavior and it would be impossible to isolate particle shape effects from sample size and particle size effects (Carrasco et al., 2022, 2023; Linero et al., 2019; Ovalle & Dano, 2020). The most common scaling down techniques used are parallel and scalping grading. Parallel grading consists in creating a scaled PSD from a coarse reference or field material, using a constant geometrical reduction factor over every particle size fraction. Given the maximum particle size in the field ($d_{max-field}$), the reduction factor is defined for a target d_{max} in the laboratory sample as $F = d_{max-field}/d_{max}$. Then, every size fraction in the field material is reduced to a size $d = d_{field}/F$, creating a parallel PSD (Marachi et al., 1972; Ovalle et al., 2014; Varadarajan et al., 2003). Thus, the uniformity coefficient ($C_u = d_{60}/d_{10}$) is maintained on scaled samples. The main limitation of this technique is that if the reduction factor is high enough, the scaled material could result in excessive amount of fines, which could significantly affect its mechanical behavior (Williams & Walker, 1983). Verdugo and de la Hoz (2007) proposed that parallel gradation could be valid only if the modeled PSD has FC $< 10\%$.

On the other hand, for a target d_{max} in the laboratory sample, the scalping technique consists in keeping unchanged the finest particle size and removing oversized particles within the field sample (Al-Hussaini, 1983; Deiminiat et al., 2022; Linero et al., 2007; Zeller & Wullimann,

1957). In other words, particles coarser than d_{max} are simply excluded and the PSD changes to a more uniform distribution compared to the field material. The main constraint of the scalping technique is that the stress/strain behavior at relatively low strains, which depends on the PSD (Muir Wood & Maeda, 2008), could differ from the original material. However, provided that characteristic grain shape remains unchanged along particle sizes, several experimental (Amirpour Harehdasht et al., 2018; Deng et al., 2021; Klinkmüller et al., 2016; Li et al., 2013; Liu et al., 2013; Polanía et al., 2023; Yang & Luo, 2018) and numerical (Azéma et al., 2017; Cantor et al., 2018; Cantor & Ovalle, 2023; Muir Wood & Maeda, 2008; Voivret et al., 2009; Wu et al., 2021) evidence have shown that the critical friction angle (ϕ_{cr}) does not depend on grading. Therefore, the scalping technique should give representative results in terms of the critical shear strength, which is the condition needed to characterize loose WR materials. Nonetheless, only a limited number of research works have been reported on the effect of scalping on ϕ_{cr} of coarse granular materials, and their conclusions are often contradictory. Namely, some authors have stated that the friction angle decreases with d_{max} (Linero et al., 2007; Ovalle et al., 2014; Zeller & Wullimann, 1957), while others have concluded the opposite (Al-Hussaini, 1983; Cao et al., 2020; Deiminiat et al., 2022; Hao & Pabst, 2023; Hennes, 1957; Xu et al., 2018). The sources of this disagreement are probably in sample properties and testing conditions. For instance, none of these studies have verified if characteristic particle shape was maintained in small-scaled samples compared to the original material. Or else, samples were prepared under different density configurations, therefore, the reported values do not always represent critical strength. In other words, most of these studies intend to correlate d_{max} with ϕ_{cr}, missing more comprehensive analyses based also on different sample size (D), aspect ratio (α), and initial densities.

In this paper, we intend to fill the gaps by focusing on these aspects, with the aim of characterizing the critical shear strength of WR material. Several samples were prepared having aspect ratios from $\alpha = 4$ to 30, corresponding to $d_{max} = 5$ to 50 mm. Moreover, in order to study sample size effects on a given material, two triaxial sample sizes were used: D =150 and 300 mm in diameter. Drained triaxial shearing on loose and dense dry material are presented. In addition, large in-situ DST were performed on the same WR material using one of the world largest direct shear boxes for samples of $120 \times 120 \times 38$ cm^3. The results are analyzed in terms of critical shear strength depending on aspect ratio, grading, sample size, and density.

4.2 Waste rock materials

Two WR materials were collected from a hard rock mine in Canada: Sediments (Sed1) and Porphyry (PO). Sed1 and PO rocks have specific gravity (G_S) and uniaxial compression strength (UCS) values of G_S = 2.75 and 2.69, and UCS = 128 and 250 MPa, respectively. XRD analyses indicate that the main mineralogical phases of both materials are silicates (quartz and albite), and other minerals can also be identified such as carbonates, micas and chlorites. *Figure* 4.1 presents the PSD of both materials after field sampling, with a common maximum particle size of $d_{max-field}$ = 75 mm. The uniformity coefficients ($C_u = d_{60}/d_{10}$) are 200 and 17 for Sed1 and PO, respectively. PO contains no fines, while Sed1 has 9% of low plasticity fines (Plasticity Index of 5%). According to ASTM D2487, Sed1 classifies as well-graded gravel with silt and sand (GW-GM) and PO classifies as well graded gravel with sand (GW).

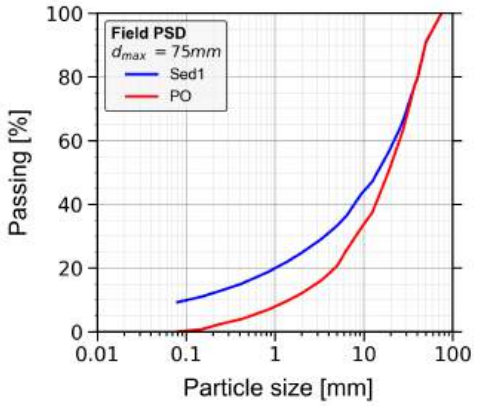

Figure 4.1 PSD of field waste rock materials Sed1 and PO.

4.2.1 Grading scalping

Additionally, a third material called Sed2 was prepared from Sed1 after removing all the fines (FC=0%) and particles coarser than 25 mm. The scalping technique was applied to prepare small-scaled samples from Sed1, Sed2 and PO. *Figure* 4.2 presents the scalped grading for several d_{max} down to 5 mm, resulting in PSD of scalped samples having variable C_u of 60 to 200 for Sed1, C_u = 10 to 28 for Sed2, and C_u = 10 to 17 for PO. *Table* 4.1 1 summarizes the resulting values of d_{max} and C_u for 57 samples prepared by grading scalping. Each sample was deemed to be tested on triaxial specimens of given diameter D = 150 or 300 mm, which allowed to accommodate different aspect ratio α from 4 to 30 (see *Table* 4.1). These values were selected to cover a range larger than the recommended α in testing standards.

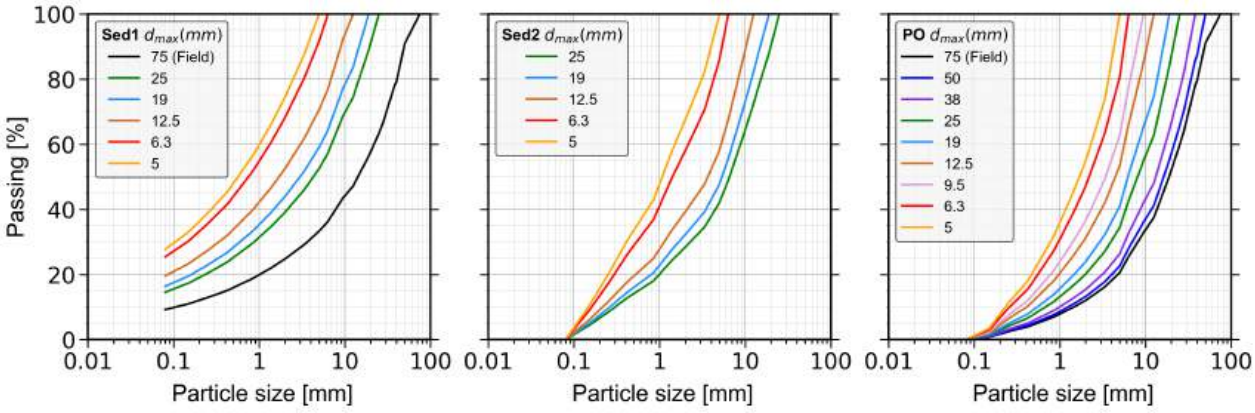

Figure 4.2 PSD after grading scalping: (a) Sed1; (b) Sed2 and (c) PO.

4.2.2 Particle shape analysis

Characteristic particle shape analysis was performed prior to testing, in order to verify if they remained the same along particle sizes. Following Wadell (1932), two characteristic particles shape descriptors were used: width to length sphericity (S_{WL} = particle width/particle length) and roundness ($R = \sum(r_i/N)/r_{in}$; where r_i is the radius of circles fitting particle concave corners, N the number of the fitted circles, and r_{in} the radius of the largest inscribed circle). Photos of each size fraction above 1 mm were taken (see an example in *Figure* 4.3). To ensure statistical representativity, more than 45 particles for each size fraction were considered for each computation (Cavarretta et al., 2010; Cho et al., 2006; Yang & Wei, 2012; Zheng & Hryciw, 2015; Zheng & Hryciw, 2016). Images were imported in Matlab for digital image particle shape computation using the algorithm proposed by Zheng and Hryciw (2015). As shown in *Figure* 4.3a, the method consists in binarizing the images and fitting the particle silhouette in a quadrilateral polygon from which the width and length are estimated. Then, a largest circle whose radius r_{in} equals the maximum distance from the center to the outline perimeter, is inscribed for R computation. *Figure* 4.3b displays the results in terms of S_{WL} and R. The characterization shows that characteristic particle shapes are almost the same throughout all particle sizes for both materials Sed1 and PO, with ranges of $R = 0.3$ - 0.4 and $S_{WL} = 0.7$. Accordingly, the materials classify as subangular particles with low sphericity (Powers, 1953; Zheng & Hryciw, 2016).

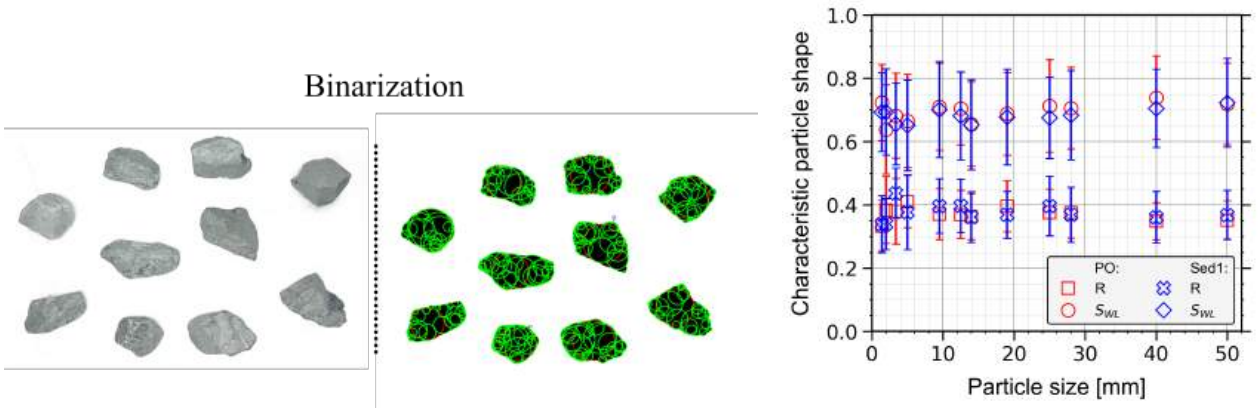

(a) (b)

Figure 4.3 Particle shape description method: (a) image binarization and shape fitting of Sed1 particles of $d = 50$ mm; (b) particle shape descriptors (sphericity S_{WL} and roundness R).

4.3 Shear testing

4.3.1 Laboratory triaxial tests

Table 4.1 lists 57 monotonic triaxial tests under consolidated drained conditions performed on cylindrical dry specimens. As shown in *Figure* 4.4, tests were carried out in two triaxial cells allowing samples of D = 150 mm and 300 mm, referred respectively as medium (M) and large (L) samples. M samples are used for evaluating the effects of α and grading scalping on the three WR materials tested. Among the 57 triaxial tests presented, only 6 were carried out on L samples: 1 test on Sed1, 2 on Sed2 and 3 on PO. L tests are used for sample size effect assessment through comparisons with M samples on the same WR and PSD, thus having different α. Loose samples were mounted without compaction by simply pouring the material in 10 distinct layers of homogeneous materials. Approximately 1.0 kg per layer was used for M samples, and 7.8 kg per layer for L samples. As listed in *Table* 4.1, dry densities (γ_d) obtained were different since the PSD varied between scalped samples. Densities of Sed1, Sed2 and PO varied between γ_d = 17.83 – 18.95 kN/m^3, 18.57 – 18.95 kN/m^3, and 18.05 – 18.90 kN/m^3, respectively. Only for PO material, dense samples were also prepared through 25 Standard Proctor hammer blows uniformly distributed over the surface of each layer. For dense samples, about 1.4 kg and 10.2 kg of material was used per layer for M and L samples, respectively. Dense PO samples reached γ_d from 21.45 to 25.62 kN/m^3, depending on the PSD (see *Table* 4.1).

Isotropic consolidation stage was performed by maintaining a desired confinement stress (σ_3)

until volumetric strain (ε_v) stabilization. As indicated in *Table* 4.1, Sed 1 and Sed2 were tested at σ_3 varying between 45 to 210 kPa. On the other hand, in order to isolate the effects of density and α, all PO samples were tested at $\sigma_3 = 150$ kPa. Depending on the value of σ_3, density, and sample size, ε_v stabilization took between 2 to 10 min for different samples. Since all the samples were dry, ε_v was estimated through volume changes of the confinement cell. Finally, vertical strain rates of 1 mm/min on M samples and 2 mm/min on L samples were applied, while recording the deviatoric stress ($q = \sigma_1 - \sigma_3$) up to 15 % of axial strain (ε_1).

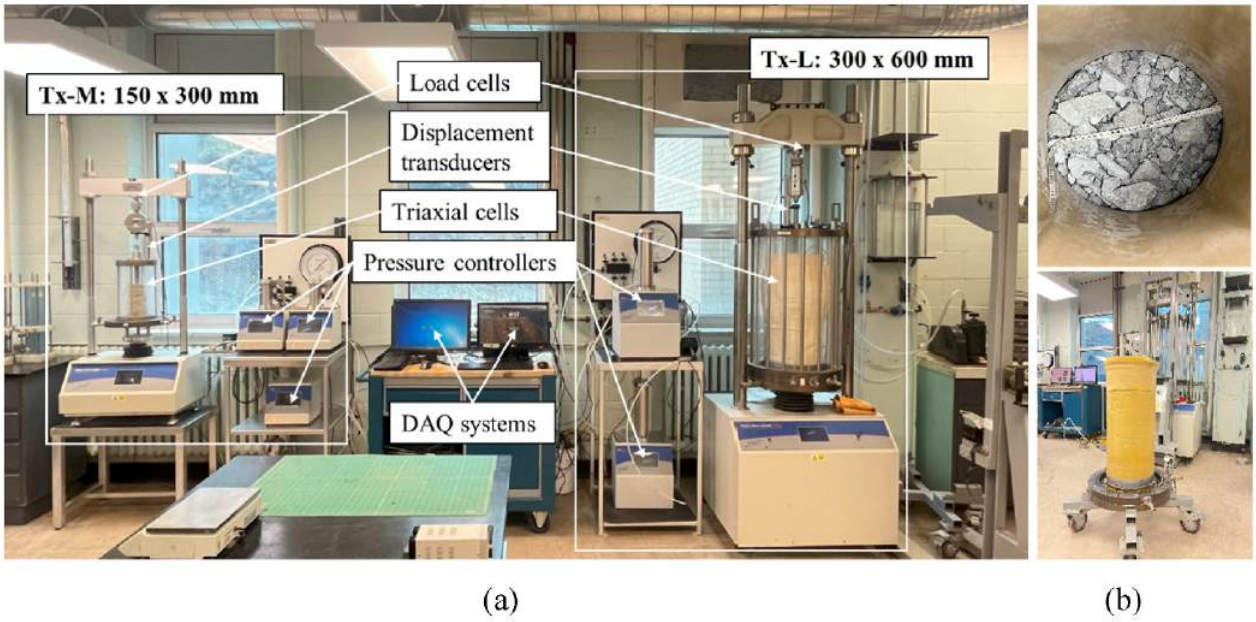

Figure 4.4 Laboratory setup: (a) triaxial (Tx) devices M and L and (b) typical sample of D = 300 mm.

Table 4.1 Summary of triaxial laboratory tests.

Test ID	Material & sample size (M or L)[1]	d_{max} (mm)	C_u	FC (%)	D (mm)	α	γ_d kN/m^3	σ_3 (kPa)	ϕ_p (°)	ϕ_{cr} (°)
T01	Sed1-L	12.5	80	20	300	24	18.58	210	-	37.3
T02	Sed1-M	5	100	29	150	30	18.31	150	-	36
T03	Sed1-M	12.5	80	20	150	12	18.95	150	-	35.5
T04	Sed1-M	25	120	17	150	6	18.95	150	-	36.3
T05	Sed1-M	12.5	80	20	150	12	18.95	80	-	37.3
T06	Sed1-M	25	120	17	150	6	18.95	80	-	40.7

Table 4.1 Summary of triaxial laboratory tests. (continued)

Test ID	Material & sample size (M or L)[1]	d_{max} (mm)	C_u	FC (%)	D (mm)	α	γ_d kN/m^3	σ_3 (kPa)	ϕ_p (°)	ϕ_{cr} (°)
T07	Sed1-M	6.3	60	26	150	24	18.95	150	-	36
T08	Sed1-M	25	120	17	150	6	18.95	210	-	37
T09	Sed1-M	5	100	29	150	30	18.86	210	-	35.8
T10	Sed1-M	12.5	80	20	150	12	18.95	210	-	36.1
T11	Sed1-M	6.3	60	26	150	24	18.95	210	-	36.2
T12	Sed1-M	25	120	17	150	6	18.95	80	-	37.5
T13	Sed1-M	6.3	60	26	150	24	18.95	80	-	37.5
T14	Sed1-M	25	120	17	150	6	18.95	210	-	37.3
T15	Sed1-M	25	120	17	150	6	18.95	80	-	39.2
T16	Sed1-M	12.5	80	20	150	12	18.95	45	-	38.7
T17	Sed1-M	6.3	60	26	150	24	18.95	45	-	39
T18	Sed1-M	19	84	16	150	8	18.9	80	-	38.2
T19	Sed1-M	19	84	16	150	8	18.95	210	-	34.8
T20	Sed2-L	12.5	24	0	300	24	18.67	210	-	38.8
T21	Sed2-L	12.5	24	0	300	24	18.57	150	-	39.9
T22	Sed2-M	25	28	0	150	6	18.86	150	-	37.6
T23	Sed2-M	12.5	24	0	150	12	18.95	150	-	38
T24	Sed2-M	25	28	0	150	6	18.86	210	-	34.2
T25	Sed2-M	12.5	24	0	150	12	18.88	210	-	37.9
T26	Sed2-M	12.5	24	0	150	12	18.93	210	-	37.1
T27	Sed2-M	5	10	0	150	30	18.95	210	-	37.5
T28	Sed2-M	25	28	0	150	6	18.74	210	-	36.7
T29	Sed2-M	6.3	13	0	150	24	18.95	150	-	38.9
T30	Sed2-M	6.3	13	0	150	24	18.95	210	-	37.5
T31	Sed2-M	6.3	13	0	150	24	18.95	150	-	38.6
T32	Sed2-M	25	28	0	150	6	18.86	210	-	36.4
T33	Sed2-M	12.5	24	0	150	12	18.95	210	-	37.4
T34	Sed2-M	5	10	0	150	30	18.95	210	-	37.6
T35	Sed2-M	19	27	0	150	8	18.85	150	-	37.2
T36	Sed2-M	19	27	0	150	8	18.95	210	-	38.2
T37	PO-loose-M	6.3	12	0	150	24	18.9	150	-	39.5
T38	PO-loose-M	12.5	14	0	150	12	18.9	150	-	40.3
T39	PO-loose-M	25	16	0	150	6	18.9	150	-	40

Table 4.1 Summary of triaxial laboratory tests. (continued)

Test ID	Material & sample size (M or L)[1]	d_{max} (mm)	C_u	FC (%)	D (mm)	α	γ_d kN/m^3	σ_3 (kPa)	ϕ_p (°)	ϕ_{cr} (°)
T40	PO-loose-M	5	10	0	150	30	18.86	150	-	40
T41	PO-loose-M	6.3	12	0	150	24	18.9	150	-	40.1
T42	PO-loose-M	38	17	0	150	4	18.05	150	-	40.1
T43	PO-loose-M	9.5	16	0	150	16	18.2	150	-	39.6
T44	PO-dense-M	6.3	12	0	150	24	22.29	150	48.6	41.5
T45	PO-dense-M	12.5	14	0	150	12	22.31	150	47.9	42.1
T46	PO-dense-M	25	16	0	150	6	21.65	150	46.5	40.7
T47	PO-dense-M	5	10	0	150	30	21.6	150	47.4	41.3
T48	PO-dense-M	25	16	0	150	6	21.47	150	46.7	-
T49	PO-dense-M	25	16	0	150	6	22.14	150	48.5	44.7
T50	PO-dense-M	12.5	14	0	150	12	22.49	150	47.5	42.8
T51	PO-dense-M	12.5	14	0	150	12	22.6	150	48	42
T52	PO-dense-M	38	17	0	150	4	21.45	150	47.4	44.4
T53	PO-dense-M	38	17	0	150	4	22.02	150	47.8	42.4
T54	PO-dense-M	9.5	16	0	150	16	21.5	150	46.2	41.7
T55	PO-dense-L	25	16	0	300	12	25.62	150	49.5	43.8
T56	PO-dense-L	50	17	0	300	6	23.4	150	49	42.6
T57	PO-dense-L	12.5	14	0	300	24	23.79	150	46.5	41

[1] All Sed1 and Sed2 samples were prepared at a loose state;
for PO samples, the initial density is indicated as loose or dense.

4.3.2 In-situ DST

As shown in *Figure* 4.5a, a large direct shear squared box of side L =120 cm and height H = 38 cm (sample of 120 × 120 × 38 cm^3) was designed following the approach of Matsuoka et al. (2001). The large in-situ DST used in this study consists in a box that can be slid over a platform made of the same material that fills the box. Therefore, the shear failure is developed on the surface between the bottom part of the box and the surface of the platform. The large steel shear box was designed to accommodate horizontal pulling loads up to 50 tonnes. The box was made of high strength C-shaped steels of sections C15×40-50 (i.e., thickness varying between 13.2-18.2 mm). A pressing kit acting as loading plate over the WR sample into the box was adopted to allow safe accommodation of vertical dead loads (F_v) (see *Figure* 4.5a-c). Loads were provided by 10 tonnes crane counterweights, and the

system was designed to apply up to 30 tonnes per test (see *Figure* 4.5d). Considering the dimensions of the box and the weight of the pressing kit, normal stresses (σ_n) of 76, 142 and 208 kPa can be applied using counterweights of F_v = 10, 20 and 30 tonnes, respectively. As shown in *Figure* 4.5a-b, the shear box includes two load cells of 100 tonnes maximum capacity installed on the front-side of the box to record the horizontal force (F_h). The load cells are placed in a horizontal frame welded on the side of the box and are connected to a shackle where a chain can be attached for horizontal pulling. Also, a potentiometer extending up to 1.5 m and referred to an external fixed point was placed on the box to record the horizontal displacements h (see *Figure* 4.5c). Finally, a chain was attached to the shear box via the shackle and linked to an excavator arm to be pulled horizontally for shearing. *Figure* 4.5e shows the data acquisition (DAQ) system that is installed at a safe distance from the test setup to record all the measurements (F_h and h over time). Several distinct platforms of Sed1 WR (d_{max} = 75mm, PSD in *Figure* 4.1) were constructed using uncompacted homogeneous loose material. Each platform had a surface of 8 m × 4 m, and 0.5 m of thickness.

Note that the aspect ratio of the in-situ DST is α=L/d_{max} ∼16, which is lower than recommended values reported in the literature of about α ∼50 (Amirpour Harehdasht et al., 2018; Bauer & Ebrahimian, 2021; Cerato & Lutenegger, 2006; Deiminiat et al., 2022; Jacobson et al., 2007; Jewell & Wroth, 1987; Wu et al., 2008; Ziaie Moayed et al., 2016). It should also be noted that it was not feasible to investigate higher values of α due to the limitations in machinery availability and the costs involved in field testing. In-situ DST test preparation and running consisted in the following steps:

- place the box on top of a platform and ensure horizontally;
- tape Teflon linings inside the box walls to minimize lateral friction;
- inside the box, scratch the surface of the platform using a manual shovel to allow a better mixing and homogeneity between the sample and the platform material;
- fill the box with homogeneous Sed1 material in the loosest condition (i.e., no compaction was provided); dry densities reached varied between 16.4 and 17.5 kN/m^3;
- install the pressing kit and ensure horizontally;
- install the potentiometer on the box;
- attach the chain to the box and the excavator arm;
- run the data acquisition system and start recording;

- install the crane counterweights for normal stress on the sample;
- pull horizontally at constant displacement rate using the excavator to slide the box over the platform up to at least 40% of the box side (0.5 m), while recording F_h from the load cells and h from the potentiometer; horizontal displacement that could be controlled by the excavator varied depending on σ_n: the displacement rate was of 4 cm/s for normal stress of σ_n= 76 kPa, 2 cm/s for σ_n= 142 kPa, and 1.5 cm/s for σ_n= 208 kPa, thus always lower than 3%/s of the box dimension L = 120 cm;
- deconstruct the whole system, move the box to another platform and restart a new test.

As summarized in *Table* 4.2, 15 in-situ DST were carried out.

Table 4.2 Summary of in-situ tests.

Test ID	Material	d_{max} (mm)	H (cm)	L (cm)	α	σ_n (kPa)	τ (kPa)	τ/σ_n	ϕ_{cr} (°)
T01	Sed1	75	38	120	16	76	71.8	0.94	43.4
T02	Sed1	75	38	120	16	142	98.5	0.69	34.7
T03	Sed1	75	38	120	16	208	139.5	0.67	33.8
T04	Sed1	75	38	120	16	76	58.4	0.77	37.6
T05	Sed1	75	38	120	16	142	102.7	0.72	35.8
T06	Sed1	75	38	120	16	208	148	0.71	35.4
T07	Sed1	75	38	120	16	76	58.4	0.77	37.6
T08	Sed1	75	38	120	16	142	95.4	0.67	33.9
T09	Sed1	75	38	120	16	208	137.8	0.66	33.5
T10	Sed1	75	38	120	16	76	60.5	0.8	38.6
T11	Sed1	75	38	120	16	142	97.4	0.69	34.4
T12	Sed1	75	38	120	16	208	113.1	0.54	38.5
T13	Sed1	75	38	120	16	208	142.3	0.68	34.3
T14	Sed1	75	38	120	16	208	157.2	0.76	37
T15	Sed1	75	38	120	16	208	150.6	0.72	35.8

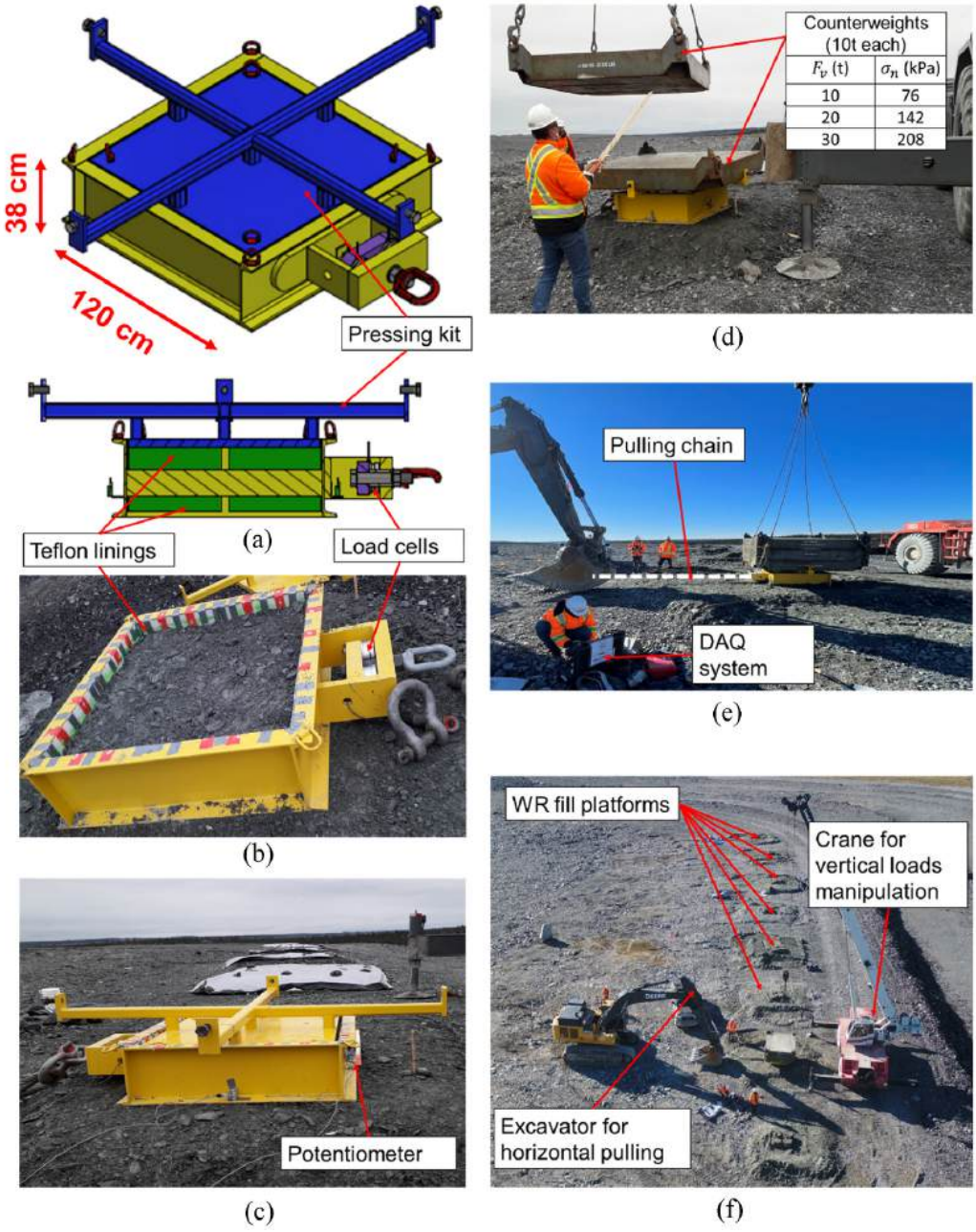

Figure 4.5 In-situ DST setup: (a) large DST box design; (b) DST box filled with WR material; (c) pressing kit and potentiometer installations; (d) installation of vertical loads; (e) pulling chain and DAQ system and (f) general view of the test setup.

4.4 Results and discussions

4.4.1 Triaxial tests

First, it is worth noting that, at the level of confining stresses used in this study, the amount of particle breakage remains low. For instance, *Figure* 4.6 illustrates initial and final PSD for tests T04, T22 and T56 (all at $\sigma_3 = 150$ kPa), where Marsal's breakage ratio B_g is 5%, 2%, and 5% for Sed1, Sed2, and PO, respectively; B_g is defined as the sum of positive differences between the percentage of the total sample retained in each size fraction before and after the test (Marsal, 1967).

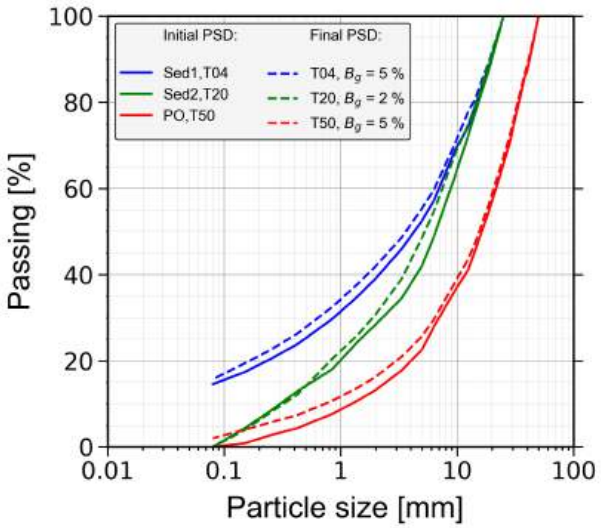

Figure 4.6 PSD before and after triaxial testing for Sed1, Sed2 and PO materials ($\sigma_3 = 150$ kPa).

In order to isolate α effects from sample size effects on scalped samples, *Figures* 4.7-4.9 show the stress ratios q/p (where $p = (\sigma_1 + 2\sigma_3)/3$ is the mean stress) against ε_1 only for the triaxial tests on M samples (size D = 150 mm). For each material, tests are grouped by σ_3. Additionally, PO tests are also classed by initial density (dense and loose) on *Figure* 4.9. Additional figures detailing individual test stress-strain curves are included in *Appendix* A. It can be observed that all tests on loose samples exhibit hardening and reached their maximum strengths around ε_1=10%, which remain almost constant up to ε_1=15 %. Loose samples of Sed1 present slight dilation at low σ_3 of 45 and 80 kPa, which vanishes to fully contractive behavior for $\sigma_3 \geq 150$ kPa (see *Figure* 4.7). Maximum volumetric contraction at σ_3= 210 kPa varies between $\varepsilon_v \sim 4$ to 5% for Sed1 (*Figure* 4.7), and from $\varepsilon_v \sim 2$ to 4% for Sed2 (*Figure* 4.8) ($\varepsilon_v > 0$ is defined as contraction). Dense M samples of PO material shown

on *Figure* 4.9, which were tested only at σ_3= 150 kPa, attain their peak strength values at ε_1 ∼3 %, followed by post-peak strength softening toward critical strength at large strains. At ε_1=15 %, dense dilatant PO samples reach ε_v ∼ -3 to -5%, while loose contractive samples exhibit ε_v ∼ 1 to 2%.

It is well known that contractive or dilatant behaviors of a sample depend on the material, the PSD, the initial density and σ_3. However, for a given material all q/p values reached at large vertical strain in *Figures* 4.7-4.9 tend to similar values, which is consistent with several reported experimental results indicating that critical strength does not depend on PSD. However, the effect of sample aspect ratio can not be clearly recognized in these figures. In order to do so, *Figure* 4.10a presents the critical friction angle for all tests on M samples as a function of α, where dashed lines represent the mean ϕ_{cr} of each σ_3. For comparison, ϕ_{cr} is assumed to be the mobilized shear strength at ε_1=15 %, and calculated according to the Mohr-Coulomb failure criterion for non-cohesive materials (i.e., $\sin\phi_{cr}$ = 3M/(6+M); where M=q/p at ε_1 = 15%). Loose M samples tested at σ_3 = 150 kPa exhibit mean ϕ_{cr} of 36°, 38° and 40° for Sed1, Sed2 and PO, respectively. For PO material, ϕ_{cr} is remarkably stable between α = 4 to 30. Concerning Sed1 and Sed2, it can be observed that, for a given σ_3, ϕ_{cr} is stable for α between 12 and 30 but presents dispersion (of about 3°) at $\alpha < 12$.

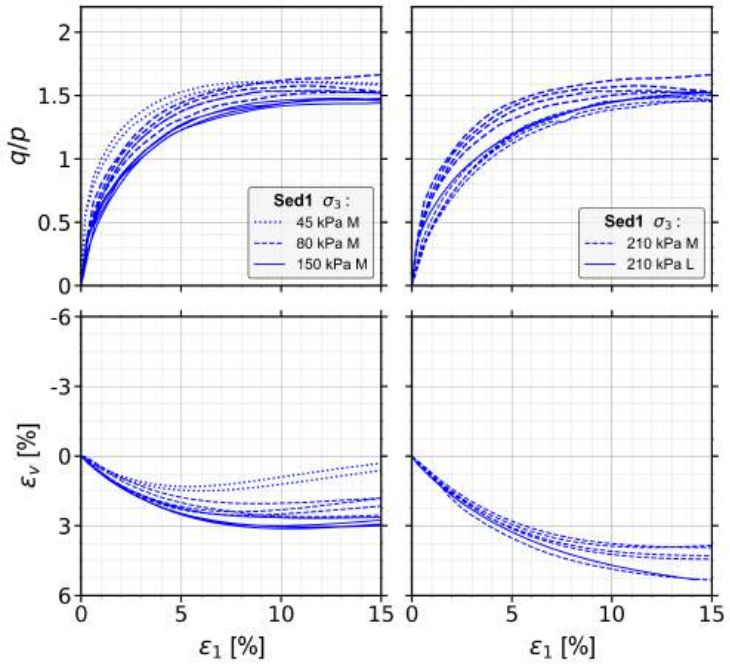

Figure 4.7 Stress-strain curves after triaxial tests for Sed1 samples: (a) q/p vs ε_1 and (b) ε_v vs ε_1.

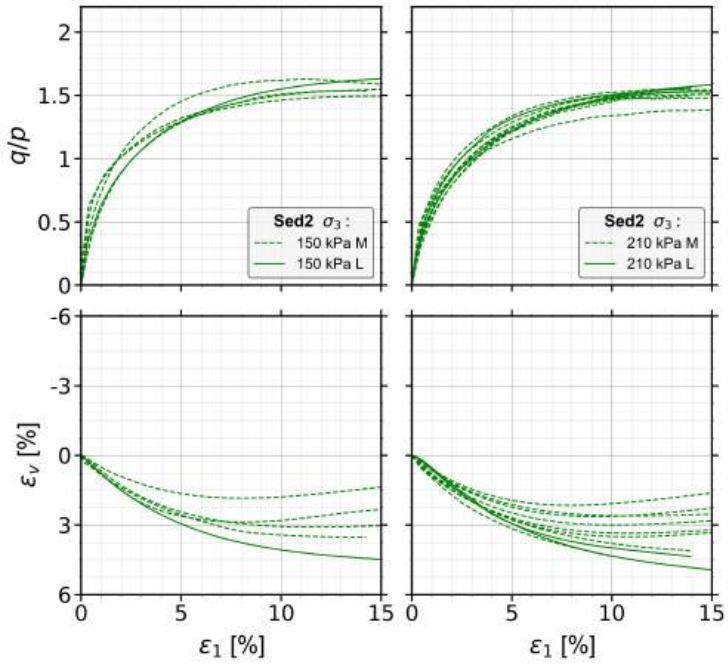

Figure 4.8 Stress-strain curves after triaxial tests for Sed2 samples: (a) q/p vs ε_1 and (b) ε_v vs ε_1.

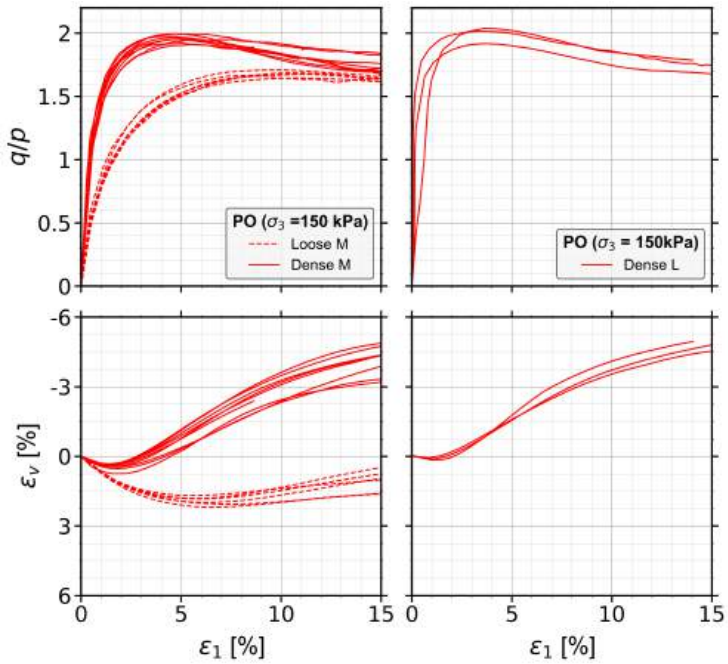

Figure 4.9 Stress-strain curves after triaxial tests for PO samples: (a) q/p vs ε_1 and (b) ε_v vs ε_1.

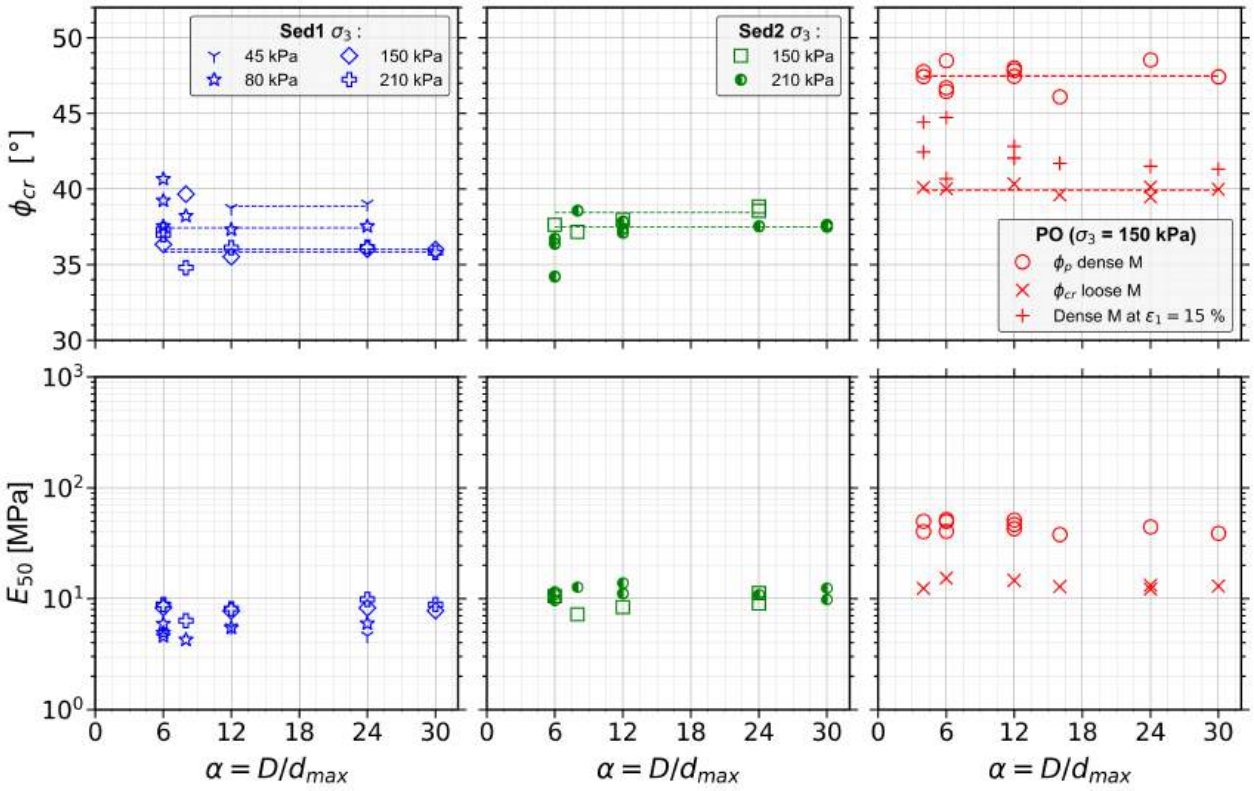

Figure 4.10 Sample aspect ratio effects on M samples for Sed1 (i), Sed2 (ii), and PO (iii) samples: (a) ϕ_{cr} vs α (dashed lines represent the mean ϕ_{cr} for $\alpha \geq 12$ values) and (b) E_{50} vs α.

Several studies have found that a scatter of more than 2° on ϕ_{cr} is non-negligible. For instance, the pioneering work by Zeller and Wullimann (1957) considered scalping grading to be representative of the loose field material when scatter was $\leq 2°$. Lowe (1964) also reported differences around 2° between modeled samples using parallel grading. Holtz and Gibbs (1956) investigated samples of different α and considered the results 'practically identical' only when the scatter was less than 1.1°, whereas a dispersion of 3° was considered a 'marked difference'. Bareither et al. (2007, 2008) investigated the repeatability and reproducibility of the shear strength on 30 different sands in small- and large-scale DST devices, and concluded that less than 2° is a typical experimental scatter on ϕ_{cr}. Therefore, in this study it has been assumed that a scatter of 3° (or more observed at $\alpha = 6$) is not negligible. To highlight the variability of ϕ_{cr} on all M samples, *Figure* 4.11 illustrates the ratio $\phi_{cr}/\phi_{(\alpha=12)}$, where $\phi_{(\alpha=12)}$ is the ϕ_{cr} at $\alpha = 12$, with both values obtained at the same σ_3. It can readily be noticed that the dispersion of ϕ_{cr} attain 10% at $\alpha < 12$, and continually vanishes to <4% beyond this threshold value.

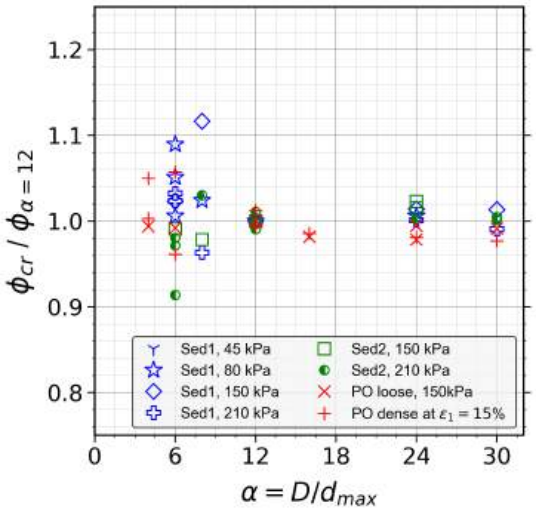

Figure 4.11 Ratio $\phi_{cr}/\phi_{(\alpha=12)}$ vs α for all loose M samples, including PO dense M samples at ε_1 = 15 %.

On the other hand, dense M samples exhibit higher ϕ_{cr} than loose samples and data scatter is not negligible, presumably because the critical state was not fully reached at ε_1=15 % due to heterogeneous strain localization within the samples (see *Figure* 4.10a (iii)). Still, the values on dense samples seem stable for $\alpha \geq$16 with a mean value of ϕ_{cr}=41.3°, while it varies from 40.7° to 44.7° when $\alpha \leq$12. Finally, *Figure* 4.10a displays also the peak strengths of dense M samples of PO material in terms of the peak friction angle (ϕ_p); dashed lines represent the mean values of each set of data: ϕ_{cr} for loose and ϕ_p for dense. Peak friction angle of dense samples varies from 46.5° to 49.5°, with an average of ϕ_p=48°. This scattering is expected since it is well known that slight differences in the PSD and initial densities affect ϕ_p.

It is well known that the PSD has an effect on the deformation moduli of granular materials. However, since the differences in C_u are not significant for the scalped materials shown in *Figure* 4.2 (see values in *Table* 4.1), an analysis of α effects on the material strain modulus is worth discussing. *Figure* 4.10b presents the secant modulus E_{50} of loose M samples against α, for tests with varying σ_3 from 45 to 210 kPa. E_{50} is defined as the modulus associated with the half of the peak deviatoric stress: E_{50}=0.5$q_{(peak)}/\varepsilon_{50}$, where ε_{50} is the axial deformation at a mobilized deviatoric stress of 0.5$q_{(peak)}$. For a given σ_3, E_{50} of M loose samples does not vary significantly. Including tests at all σ_3, the values are between E_{50}= 5-10, 7-14, and 12-15 MPa for loose Sed1, Sed2, and PO, and E_{50}= 40-55 MPa, for PO dense, respectively, and are in the range compiled by Ovalle et al. (2020) for several rockfills and WR materials. In addition, there is no clear effect of α observed. Therefore, a reasonable estimation of E_{50} can be achieved using the scalping technique, provided that the changes in d_{max} are limited

(from 75 to 5mm in this study) and eventually depending on the characteristics of the fine content.

Finally, in order to isolate sample size effects, it is worth comparing tests on the same material and at the same σ_3 , but tested in different cells M and L. Note that the same WR material (i.e., having the same PSD) has different α when tested on samples M and L. For instance, the same material and PSD (Sed1, d_{max}= 12.5 mm, C_u = 80 and FC = 20 %) was used in tests T10 (size M and α =12) and T01 (size L and α =24). The same case is met for all the M-L pairs plotted in *Figure* 4.12, in terms of critical and peak friction angles. Overall, M and L samples on all considered materials exhibited comparable ϕ_{cr} for $\alpha \geq$12, the differences being less than 2°. However, for the samples with $\alpha \leq$6 (pairs plotted with half-filled markers), differences between ϕ_p and ϕ_{cr} could reach up to 3° relating M and L. Therefore, no significant size effect is observed only if $\alpha \geq$12, which is consistent with α effect observed in *Figure* 4.11. Still, test T56 on a dense PO sample of size L, d_{max}= 50 mm (the coarsest material in *Table* 4.1) and α =6, exhibited a ϕ_{cr} = 42.6°, which is remarkably similar to the mean value of all PO M samples (ϕ_{cr}=42.4°).

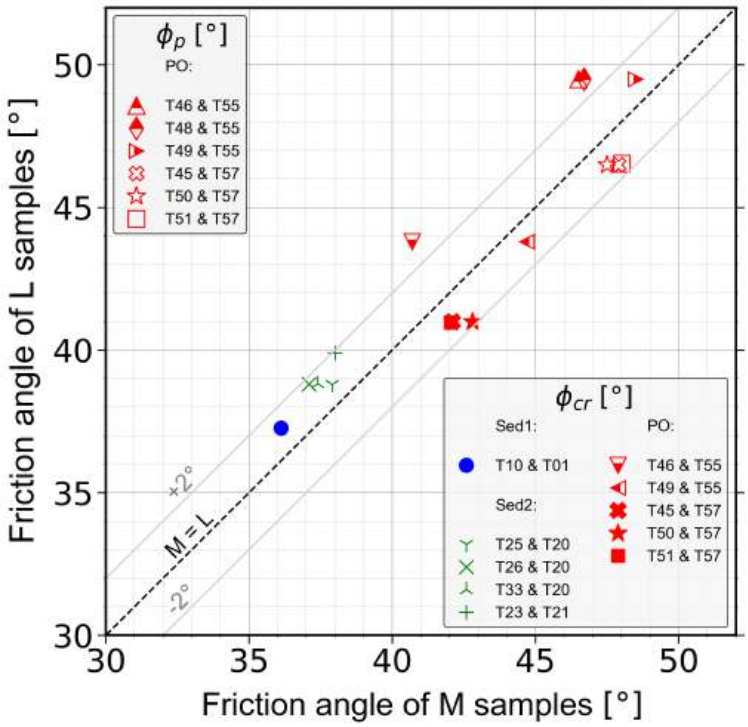

Figure 4.12 Correlation of critical and peak friction angles obtained in the same materials in M and L samples (half-filled markers indicate tests at $\alpha \leq 6$).

4.4.2 In-situ DST

Figure 4.13 presents the shear stress ratio τ/σ_n plotted against normalized horizontal shear displacement (h/L) for all conducted in-situ DST, where $\sigma_n = F_v/A$, $\tau = F_h/A$, and A is the section of the sheared surface (120×120 cm^2). Additional figures detailing individual test are included in *Appendix* B. Unlike triaxial testing conditions, in-situ DST allows large displacement and steady shearing under critical strength condition. Loose samples exhibit hardening and attain critical strength around h/L=20%, which remains almost constant up to h/L=40 % and more.

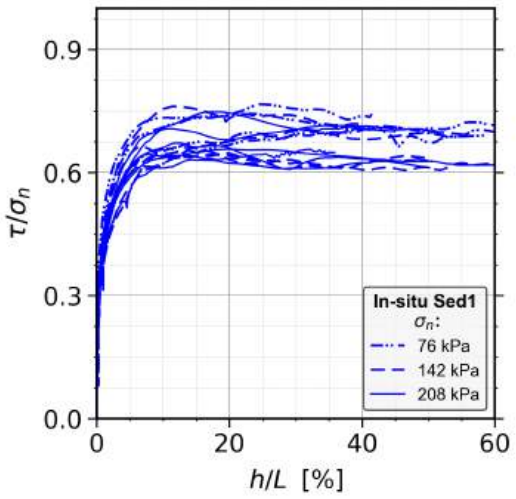

Figure 4.13 In-situ DST results: Stress ratio-normalized deformation curves.

Figure 4.14 illustrates the average in-situ ϕ_{cr} for each σ_n tested (ϕ_{cr} values for each individual test can be retrieved in *Table* 4.2). ϕ_{cr} is calculated according to the Mohr-Coulomb failure criterion for non-cohesive materials (i.e., tan $\phi_{cr} = \tau/\sigma_n$; where τ/σ_n is taken at h/L=40 %). *Figure* 4.14 also displays the values obtained after triaxial tests on M and L samples of Sed1 material, and the dashed line represents the mean ϕ_{cr} of all triaxial tests with $\alpha \geq 12$ at a given σ_n. Expectedly, ϕ_{cr} decreases with increasing σ_n. In-situ DST results have mean values of ϕ_{cr}= 39°, 35°, and 35° under σ_n= 76, 142, and 208 kPa, respectively. For a given σ_n, these averages are very similar to the ones obtained in the laboratory triaxial tests. For instance, tests T16 and T17 at σ_3= 45 kPa, corresponding to σ_n ∼75 kPa, exhibit the same ϕ_{cr}= 39° as the mean value from in-situ tests at σ_n= 76 kPa. Likewise, the average ϕ_{cr} at σ_n= 235 kPa in triaxial tests (tests T02, T03, T04 and T07, all at σ_3= 150 kPa) is 36°, while mean in-situ value at σ_n= 208 kPa is ϕ_{cr}=35°.

As previously mentioned, triaxial tests on samples having $\alpha \leq 6$ (circle markers in *Figure*

4.14) present non-negligible scatter with respect to triaxial samples of $\alpha \geq 12$. Furthermore, *Figure* 4.14 also includes the triaxial test T01 on an L sample and $\alpha = 24$ having practically the same ϕ_{cr} compared to M samples of $\alpha \geq 12$ (at the same σ_n). However, it is clear that data scatter after in-situ tests is non-negligible, presumably because the aspect ratio $\alpha \sim 16$ is too low to ensure a representative sample in a DST test.

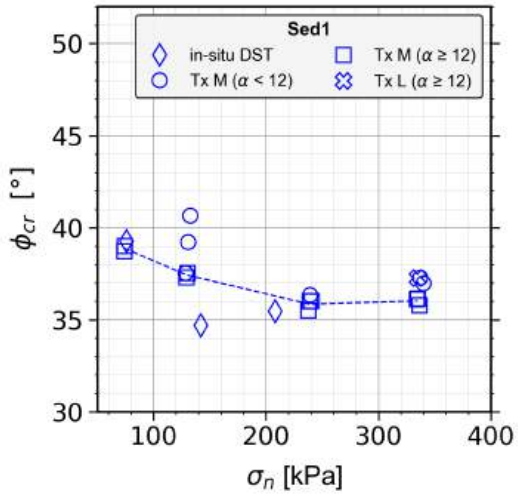

Figure 4.14 Comparison between laboratory triaxial (Tx) and in-situ results in terms of ϕ_{cr} vs σ_n (the dashed line represents the mean ϕ_{cr} of all triaxial tests with $\alpha \geq 12$).

4.5 Conclusions

Grading effects and sample size effects on shear strength of mine waste rocks (WR) were experimentally investigated using the scalping technique. The objective was to provide insights on the minimum recommended sample aspect ratio α. Laboratory triaxial and large in-situ direct shear tests (DST) were carried out on samples having d_{max} ranging from 5 to 75 mm. Triaxial tests were conducted on three distinct WR materials, Sed1, Sed2, and PO, on medium and large cylindrical samples of diameters D = 150 mm (M) and D = 300 mm (L), respectively. Additionally, one of the world largest in-situ DST boxes (120 x 120 x 38 cm^3) was developed to test the same WR material as in the laboratory.

Using the scalping technique, several samples were prepared having α from 4 to 30, to cover a range larger than α recommended by international engineering standards. The results were analyzed in terms of critical shear strength depending on aspect ratio, density, and sample size. The following conclusions can be drawn:

- For a given material, triaxial laboratory results on loose M samples showed stable mean

critical friction angle (ϕ_{cr}) along α from 4 to 30, which was consistent with several reported experimental evidence stating that ϕ_{cr} does not depend on grading. However, in two of the three materials tested, namely Sed1 and Sed2, ϕ_{cr} of loose samples having $\alpha \leq 6$ presented non negligible dispersion of about 3°.

- Results of ϕ_{cr} on dense samples displayed significant scattering and were stable only beyond $\alpha \geq 16$.

- Sample size effects on shear strength were evaluated comparing the results of M and L samples having the same grading. The analysis showed that both peak friction angle (ϕ_p) and ϕ_{cr} did not present size effect when $\alpha \geq 12$, with scattering of less than 2°. However, when $\alpha \leq 6$ the differences between M and L could reach up to 3°, which could be attributed to a low α value and not necessarily to size effects.

- Results of the large in-situ DST presented very similar mean ϕ_{cr} as laboratory triaxial results on loose samples tested at comparable normal stresses. However, in-situ data were significantly scattered at the tested $\alpha \sim 16$, suggesting that this aspect ratio for direct shear testing might still be too low compared to triaxial conditions.

In summary, the findings of this study indicate that critical strength after triaxial tests on scalped WR samples present significant scattering when $\alpha \leq 6$. Triaxial tests on loose samples gave consistent ϕ_{cr} only for $\alpha \geq 12$, while dense samples reached stable ϕ_{cr} only for $\alpha \geq 16$. Beyond these minimum values, small-scaling of coarse materials using the scalping technique is a reliable approach to assess ϕ_{cr}, provided that the characteristic shape of the particles remains the same on scalped samples. For both cases (loose and dense), the α values found for stable ϕ_{cr} are higher than the recommendations of some worldwide geotechnical standards, such as ASTM D7181-20, which proposes $\alpha = 6$ for triaxial tests. Moreover, the study allows to conclude that the minimum α for ϕ_{cr} assessment in triaxial testing is not sensitive to grading nor sample size, but it is affected by the density of the sample. Further comprehensive investigations on different WR materials are needed to confirm these results and to determine a precise minimum value of α which guarantees a representative sample. Meanwhile, it seems clear that the recommendations of widely used standards should be revisited.

Acknowledgements

This research work benefited from the financial support of the Natural Sciences and Engineering Research Council of Canada (NSERC) [reference RGPIN-2019-06118], the Fonds de

recherche du Québec Nature et technologies (FRQNT) through « Programme de recherche en partenariat sur le développement durable du secteur minier-II » [reference 2020-MN-281267] and the industrial partners of the Research Institute on Mines and the Environment (RIME) UQAT-Polytechnique (http://www.irme.ca/en). The authors extend the acknowledgements to Mitacs and Agnico Eagle Mines for the financial support of the in-situ experiments through the Business Strategy Scholarship.

Bibliography

Al-Hussaini, M. M. (1983). Effect of particle size and strain conditions on the strength of crushed basalt. *Canadian Geotechnical Journal*, *20*(4), 706–717.

Amirpour Harehdasht, S., Hussien, M. N., Karray, M., Roubtsova, V., & Chekired, M. (2018). Influence of particle size and gradation on shear strength–dilation relation of granular materials. *Canadian Geotechnical Journal*, *56*(2), 208–227.

ASTM D2487. (2017). *Standard practice for classification of soils for engineering purposes (unified soil classification system)*. ASTM International.

ASTM D3080. (2011). *Standard test method for direct shear test of soils under consolidated drained conditions*. ASTM International.

ASTM D7181. (2020). *Standard test method for consolidated drained triaxial compression test for soils*. ASTM International.

Azéma, E., Linero, S., Estrada, N., & Lizcano, A. (2017). Shear strength and microstructure of polydisperse packings: the effect of size span and shape of particle size distribution. *Physical Review E*, *96*(2), 022902.

Bard, E., Anabalón, M. E., & Campaña, J. (2011). Waste rock behavior at high pressures. In *Multiscale geomechanics* (pp. 83–112).

Bareither, C. A., Benson, C. H., & Edil, B. (2008). Comparison of shear strength of sand backfills measured in small-scale and large-scale direct shear tests. *Canadian Geotechnical Journal*, *45*(9), 1224–1236.

Bareither, C. A., Benson, C. H., & Edil, T. B. (2007). Reproducibility of direct shear tests conducted on granular backfill materials. *Geotechnical Testing Journal*, *31*(1), 84–94.

Barton, N. (2013). Shear strength criteria for rock, rock joints, rockfill and rock masses: problems and some solutions. *Journal of Rock Mechanics and Geotechnical Engineering*, *5*(4), 249–261.

Barton, N., & Kjærnsli, B. (1981). Shear strength of rockfill. *Journal of the Geotechnical Engineering Division*, *107*(7), 873–891.

Bauer, E., & Ebrahimian, B. (2021). Investigations of granular specimen size effect in interface shear box test using a micro-polar continuum description. *International Journal for Numerical and Analytical Methods in Geomechanics*, *45*(17), 2467–2489.

Cantor, D., Azema, E., Radjai, F., & Sornay, P. (2018). Rheology and structure of polydisperse three-dimensional packings of spheres. *Physical Review E*, *98*(5).

Cantor, D., & Ovalle, C. (2023). Sample size effects on the critical state shear strength of granular materials with varied gradation and the role of column- like local structures. *Géotechnique*, *75*(1), 29–40.

Cao, P., Jiang, M.-j., & Ding, Z.-j. (2020). Effects of particle size on mechanical behaviors of calcareous sand under triaxial conditions. *Japanese Geotechnical Society Special Publication*, *8*(5), 182–187.

Carrasco, S., Cantor, D., & Ovalle, C. (2022). Effects of particle size-shape correlations on steady shear strength of granular materials: the case of particle elongation. *International Journal for Numerical and Analytical Methods in Geomechanics*, *46*(5), 979–1000.

Carrasco, S., Cantor, D., Ovalle, C., & Quiroz, P. (2023). Shear strength of angular granular materials with size and shape polydispersity. *Open Geomechanics*, *4*.

Cavarretta, I., Coop, M., & O'Sullivan, C. (2010). The influence of particle characteristics on the behaviour of coarse grained soils. *Géotechnique*, *60*(6), 413–423.

Cerato, A., & Lutenegger, A. (2006). Specimen size and scale effects of direct shear box tests of sands. *Geotechnical Testing Journal*, *29*(6), 507–516.

Cho, G.-C., Dodds, J., & Santamarina, J. C. (2006). Particle shape effects on packing density, stiffness, and strength: natural and crushed sands. *Journal of Geotechnical and Geoenvironmental Engineering*, *132*(5), 591–602.

Deiminiat, A., Li, L., & Zeng, F. (2022). Experimental study on the minimum required specimen width to maximum particle size ratio in direct shear tests. *CivilEng*, *3*(1), 66–84.

Deng, N., Wautier, A., Thiery, Y., Yin, Z.-Y., Hicher, P.-Y., & Nicot, F. (2021). On the attraction power of critical state in granular materials. *Journal of the Mechanics and Physics of Solids*, *149*, 104300.

Fumagalli, E. (1969). Tests on cohesionless materials for rockfill dams. *Journal of the Soil Mechanics and Foundations Division*, *95*(1), 313–332.

Hao, S., & Pabst, T. (2023). Mechanical characterization of coarse-grained waste rocks using large-scale triaxial tests and neuroevolution of augmenting topologies. *Journal of Geotechnical and Geoenvironmental Engineering*, *149*(6).

Hawley, M., & Cunning, J. (2017). *Guidelines for mine waste dump and stockpile design*. CSIRO Publishing.

Hennes, R. G. (1957). The strength of gravel in direct shear. In G. P. Tschebotarioff (Ed.). ASTM International.

Holtz, W. G., & Gibbs, H. J. (1956). Triaxial shear tests on pervious gravelly soils. *Journal of the Soil Mechanics and Foundations Division*, *82*(1), 867–1–867–22.

Hu, W., Dano, C., Hicher, P.-Y., Le Touzo, J.-Y., Derkx, F., & Merliot, E. (2011). Effect of sample size on the behavior of granular materials. *Geotechnical Testing Journal*, *34*(3), 186–197.

Indraratna, B., Ionescu, D., & Christie, H. D. (1998). Shear behavior of railway ballast based on large-scale triaxial tests. *Journal of Geotechnical and Geoenvironmental Engineering*, *124*(5), 439–449.

Jacobson, D. E., Valdes, J. R., & Evans, T. M. (2007). A numerical view into direct shear specimen size effects. *Geotechnical Testing Journal*, *30*(6), 512–516.

Jewell, R. A., & Wroth, C. P. (1987). Direct shear tests on reinforced sand. *37*(1), 53–68.

JGS 0530. (2015). *Preparation of specimens of coarse granular materials for triaxial tests*. Japanese Geotechnical Society (JGS).

JGS 0561. (2015). *Method for consolidated constant pressure direct box shear test on soils*. Japanese Geotechnical Society (JGS).

Klinkmüller, M., Schreurs, G., Rosenau, M., & Kemnitz, H. (2016). Properties of granular analogue model materials: a community wide survey. *Tectonophysics*, *684*, 23–38.

Lee, D.-S., Kim, K.-Y., Oh, G.-D., & Jeong, S.-S. (2009). Shear characteristics of coarse aggregates sourced from quarries. *International Journal of Rock Mechanics and Mining Sciences*, *46*(1), 210–218.

Li, G., Ovalle, C., Dano, C., & Hicher, P.-Y. (2013). Influence of grain size distribution on critical state of granular materials. In Q. Yang, J.-M. Zhang, H. Zheng, & Y. Yao (Eds.), *Constitutive modeling of geomaterials* (pp. 207–210). Springer Berlin Heidelberg.

Li, M., Zhang, J., Meng, G., Gao, Y., & Li, A. (2020). Testing and modelling creep compression of waste rocks for backfill with different lithologies. *International Journal of Rock Mechanics and Mining Sciences*, *125*, 104170.

Linero, S., Bradfield, L., Fityus, S. G., Simmons, J. V., & Lizcano, A. (2020). Design of a 720-mm square direct shear box and investigation of the impact of boundary conditions on large-scale measured strength. *Geotechnical Testing Journal*, *43*(6).

Linero, S., Palma, C., & Apablaza, R. (2007). Geotechnical characterisation of waste material in very high dumps with large scale triaxial testing. In Y. Potvin (Ed.), *Slope stability 2007: proceedings of the 2007 international symposium on rock slope stability in open pit mining and civil engineering* (pp. 59–75). Australian Centre for Geomechanics.

Linero, S., Azema, E., Estrada, N., Fityus, S., Simmons, J., & Lizcano, A. (2019). Impact of grading on steady-state strength. *Géotechnique Letters*, *9*(4), 328–333.

Liu, Y.-J., Li, G., Yin, Z.-Y., Dano, C., Hicher, P.-Y., Xia, X.-H., & Wang, J.-H. (2013). Influence of grading on the undrained behavior of granular materials. *Comptes Rendus. Mécanique*, *342*(2), 85–95.

Lowe, J. (1964). Shear strength of coarse embankment dam materials. *Proc., 8th Int. Congress on Large Dams*, *3*, 745–761.

Marachi, N. D., Chan, C. K., & Seed, H. B. (1972). Evaluation of properties of rockfill materials. *Journal of the Soil Mechanics and Foundations Division*, *98*(1), 95–114.

Marsal, R. J. (1967). Large scale testing of rockfill materials. *Journal of the Soil Mechanics and Foundations Division*, *93*(2), 27–43.

Matsuoka, H., Liu, S., Sun, D., & Nishikata, U. (2001). Development of a new in-situ direct shear test. *Geotechnical Testing Journal*, *24*(1), 92–102.

McLemore, V. T., Fakhimi, A., van Zyl, D., Ayakwah, G. F., Anim, K., Boakye, K., Ennin, F., Felli, P., Fredlund, D., & Gutierrez, L. A. (2009). Literature review of other rock piles: characterization, weathering, and stability. *J Questa Rock Pile Weathering Stability Project. New Mexico Bureau of Geology and Mineral Resources. New Mexico Tech, USA*.

Muir Wood, D., & Maeda, K. (2008). Changing grading of soil: effect on critical states. *Acta Geotechnica*, *3*(1), 3–14.

Ovalle, C., & Dano, C. (2020). Effects of particle size–strength and size–shape correlations on parallel grading scaling. *Géotechnique Letters*, *10*(2), 191–197.

Ovalle, C., Frossard, E., Dano, C., Hu, W., Maiolino, S., & Hicher, P.-Y. (2014). The effect of size on the strength of coarse rock aggregates and large rockfill samples through experimental data. *Acta Mechanica*, *225*(8), 2199–2216.

Ovalle, C., Linero, S., Dano, C., Bard, E., Hicher, P.-Y., & Osses, R. (2020). Data compilation from large drained compression triaxial tests on coarse crushable rockfill materials. *Journal of Geotechnical and Geoenvironmental Engineering*, *146*(9), 06020013.

Polanía, O., Cabrera, M., Renouf, M., Azéma, E., & Estrada, N. (2023). Grain size distribution does not affect the residual shear strength of granular materials: an experimental proof. *Physical Review E*, *107*(5), L052901.

Powers, M. C. (1953). A new roundness scale for sedimentary particles. *Journal of Sedimentary Petrology*, *23*(2), 117–119.

SME. (2011). *SME mining engineering handbook* (P. Darling, Ed.; 3rd).

USGS (Ed.). (2022). *Mineral commodity summaries* (3rd). U.S. Geological Survey (USGS).

Valenzuela, L., Bard, E., Campaña, J., & Anabalón, M. (2008). High Waste Rock Dumps — Challenges and Developments [Place: Perth]. In A. Fourie (Ed.), *Rock Dumps 2008: Proceedings of the First International Seminar on the Management of Rock Dumps, Stockpiles and Heap Leach Pads* (pp. 65–78). Australian Centre for Geomechanics.

Varadarajan, A., Sharma, K. G., Venkatachalam, K., & Gupta, A. K. (2003). Testing and modeling two rockfill materials. *Journal of Geotechnical and Geoenvironmental Engineering*, *129*(3), 206–218.

Verdugo, R., & de la Hoz, K. (2007). Strength and stiffness of coarse granular soils. In H. I. Ling, L. Callisto, D. Leshchinsky, & J. Koseki (Eds.), *Soil stress-strain behavior: measurement, modeling and analysis* (pp. 243–252). Springer Netherlands.

Voivret, C., Radjaï, F., Delenne, J. Y., & El Youssoufi, M. S. (2009). Multiscale force networks in highly polydisperse granular media. *Physical Review Letters*, *102*(17), 178001.

Wadell, H. (1932). Volume, shape, and roundness of rock particles. *The Journal of Geology*, *40*(5), 443–451.

Williams, D. J., & Walker, L. (1983). Laboratory and field strength of mine waste rock. *Civil Eng Tran*, *27*(3), 299–304.

Wu, M., Wang, J., Russell, A., & Cheng, Z. (2021). DEM modelling of mini-triaxial test based on one-to-one mapping of sand particles. *Géotechnique*, *71*(8), 714–727.

Wu, P.-K., Matsushima, K., & Tatsuoka, F. (2008). Effects of specimen size and some other factors on the strength and deformation of granular soil in direct shear tests. *Geotechnical Testing Journal*, *31*(1), 45–64.

Xu, Y., Williams David, J., Serati, M., & Vangsness, T. (2018). Effects of scalping on direct shear strength of crusher run and crusher run/geogrid interface. *Journal of Materials in Civil Engineering*, *30*(9), 04018206.

Yang, J., & Luo, X. D. (2018). The critical state friction angle of granular materials: does it depend on grading? *Acta Geotechnica*, *13*(3), 535–547.

Yang, J., & Wei, L. (2012). Collapse of loose sand with the addition of fines: the role of particle shape. *Géotechnique*, *62*(12), 1111–1125.

Zeller, J., & Wullimann, R. (1957). The shear strength of the shell materials for the goschenenalp dam, switzerland. *4th International Conference on Soil Mechanics and Foundation Engineering*, *2*, 399–415.

Zhang, Z.-L., Xu, W.-J., Xia, W., & Zhang, H.-Y. (2016). Large-scale in-situ test for mechanical characterization of soil–rock mixture used in an embankment dam. *International Journal of Rock Mechanics and Mining Sciences*, *86*, 317–322.

Zheng, J., & Hryciw, R. D. (2015). Traditional soil particle sphericity, roundness and surface roughness by computational geometry. *Géotechnique*, *65*(6), 494–506.

Zheng, J., & Hryciw, R. (2016). Roundness and sphericity of soil particles in assemblies by computational geometry. *Journal of Computing in Civil Engineering*, *30*(6), 04016021.

Ziaie Moayed, R., Alibolandi, M., & Alizadeh, A. (2016). Specimen size effects on direct shear test of silty sands. *International Journal of Geotechnical Engineering*, 1–8.

CHAPTER 5 ARTICLE 2 – End-restraint Effects in Triaxial Tests on H:D=2:1 Samples of Rockfill Material

Journal: Geotechnique Letters.
Submitted: January 28, 2025.

Authors: Gilbert Girumugisha[a,b], Carlos Ovalle[a,b,*]

[a]Dep. of Civil, Geological and Mining Engineering, Polytechnique Montréal, Québec, Canada.

[b]Research Institute of Mining and Environment (RIME UQAT-Polytechnique), Canada

[*]Corresponding Author, ✉ carlos.ovalle@polymtl.ca.

ABSTRACT Several authors have shown that end-restraint effects in triaxial tests are negligible in samples with a height-to-diameter ratio of H:D≥2. However, these works are mainly based on fine soils and sands, and few studies have focused on coarse angular soils, which typically mobilize high frictional stresses that could boost boundary effects. The aim of this study is to assess end-restraint effects in triaxial tests on H:D=2:1 samples of rockfill material, through a comprehensive set of drained tests on loose dry samples of 150 mm in diameter. The results show that end-restraint effects in coarse angular soil are not overcome in samples having H:D=2:1. Standard rough end platens induce higher secant strain modulus, dilatancy and shear strength. Thus, lubrication should be systematically used in these materials. The letter also gives practical recommendations on lubrication setup to avoid buckling.

5.1 Introduction

The mechanical characterization of coarse soils is usually carried out based on tests in small-scaled samples, which may be affected by size effects (Al-Hussaini, 1983; Hu et al., 2011; Marachi et al., 1972). Recent research has shown that the sources of size effects are mainly related to differences in grading (Girumugisha et al., 2024; Muir Wood & Maeda, 2008), particle shape (Carrasco et al., 2025; Linero et al., 2017; Ovalle & Dano, 2020), particle crushing (Frossard et al., 2012; Ovalle et al., 2014) and sample size (Cantor & Ovalle, 2023; Quiroz-Rojo et al., 2024). However, test conditions can differ greatly between experimental

setups, particularly end-restraint effects in triaxial samples. This topic was early reported in the literature for fine soils and sands (Bishop & Green, 1965; Duncan & Dunlop, 1968; Rowe & Barden, 1964; Taylor, 1941), but has rarely been studied for coarse soils.

In standard triaxial devices, the interface between the soil and the top and bottom end platens is a rough porous stone, restricting free dilation. Such inherent constraints induce heterogeneous strain fields, shear strain localization and bulging deformation (Frost & Yang, 2003; Liu et al., 2013; Peri et al., 2019; Raju et al., 1972; Sheng et al., 1997), leading to poor testing reproducibility (Colliat-Dangus et al., 1988; Mozaffari et al., 2022) and uncertainty in the critical state parameters (Lee & Vernese, 1978; Reid et al., 2021; Wightman et al., 2024).

Taylor (1941) suggested a minimum sample slenderness to avoid end friction effects, defined as a height-to-diameter ratio H:D$\geq$2. While systematic studies performed in fine soils (Asaoka et al., 1994; Duncan & Dunlop, 1968; Kodaka et al., 2007; Muraro & Jommi, 2019; Olson et al., 1964; Shockley & Ahlvin, 1960) and sands (Bishop & Green, 1965; Colliat-Dangus et al., 1988; Olson et al., 1964; Raju et al., 1972; Rowe & Barden, 1964; Roy & Lo, 1971) have shown consistent shear strength, non-homogeneous strain fields are not fully overcome with H:D$\geq$2 (Mozaffari et al., 2022; Muraro & Jommi, 2019; Yeh et al., 2024). Rowe and Barden (1964) proposed enlarged end platens covered with a greased latex rubber sheet on the contact surface. However, slender lubricated samples often slide sideways and buckle at large strains (Duncan & Dunlop, 1968; Olson et al., 1964; Rowe & Barden, 1964), which can be avoided using H:D$\sim$1 (Feda et al., 1993; Goto & Tatsuoka, 1988; Hettler & Vardoulakis, 1984). As far as the authors are aware, the only study on the effects of triaxial end-restraint in rockfill was reported by Al-Hussaini (1970). His results indicated that rough end platens significantly enhance the stiffness and dilatancy, while having a minor effect on shear strength. Although most testing standards have been drawn based on test results in fine soils and sands with critical ϕ' lower than $\sim$35°, data in coarse soils are scarce. Provided that coarse angular soils typically exhibit high values of $\phi'\sim$40° or more (Leps, 1970; Ovalle et al., 2020), it can be expected that frictional components at the sample boundaries might have a great impact on the material response.

The main objective of this letter is to assess end-restraint effects in triaxial tests on H:D=2:1 samples of coarse angular soil. Monotonic triaxial tests were performed on dry samples of $D = 150$ mm in diameter, under consolidated drained conditions at confining stresses of $\sigma_3 = 100$ and 400 kPa. The results with rough and enlarged lubricated platens are compared in terms of shear strength and deformation properties. Additionally, the effects of grading were studied on scaled samples prepared by scalping and parallel grading techniques.

5.2 Methodology

5.2.1 Materials tested

Well-graded rockfill material was sampled from a quarry in St-Eustache, Canada. The material consists of blasted and crushed dolomite rock, with specific gravity $G_s = 2.75$ and subangular grain shapes. Field PSD shown in *Figure* 5.1 indicates well-graded gravel without fines (GW according to ASTM D2487). Maximum particle size is $d_{max} = 90$ mm, $d_{50} = 13.9$ mm and uniformity and curvature coefficients are given by $C_u = d_{60}/d_{10}$=9 and $C_c = (d_{30})^2/(d_{10} \times d_{60})$=1.6, respectively.

Several samples were prepared using scalping (S) (*Figure* 5.1a) and parallel grading (P) (*Figure* 5.1b) techniques; d_{max} of different scaled materials was set to 5, 6, 8, 12 and 25 mm. For S samples, particles coarser than a chosen d_{max} were simply removed and a new PSD was generated. P samples were prepared by creating a parallel PSD curve between percents passing of 100% to 10%; for size fractions finer than d_{10}, the PSD curves were simply extended until the finest particle in the field material ($d_{min} = 0.08$ mm). The detailed information of all the materials is given in *Table* 5.1[1], included as supplementary information.

[1]Since *Géotechnique Letters* only accepts short papers of less than 2000 words, *Table* 5.1 is included as supplementary information at the end of this paper.

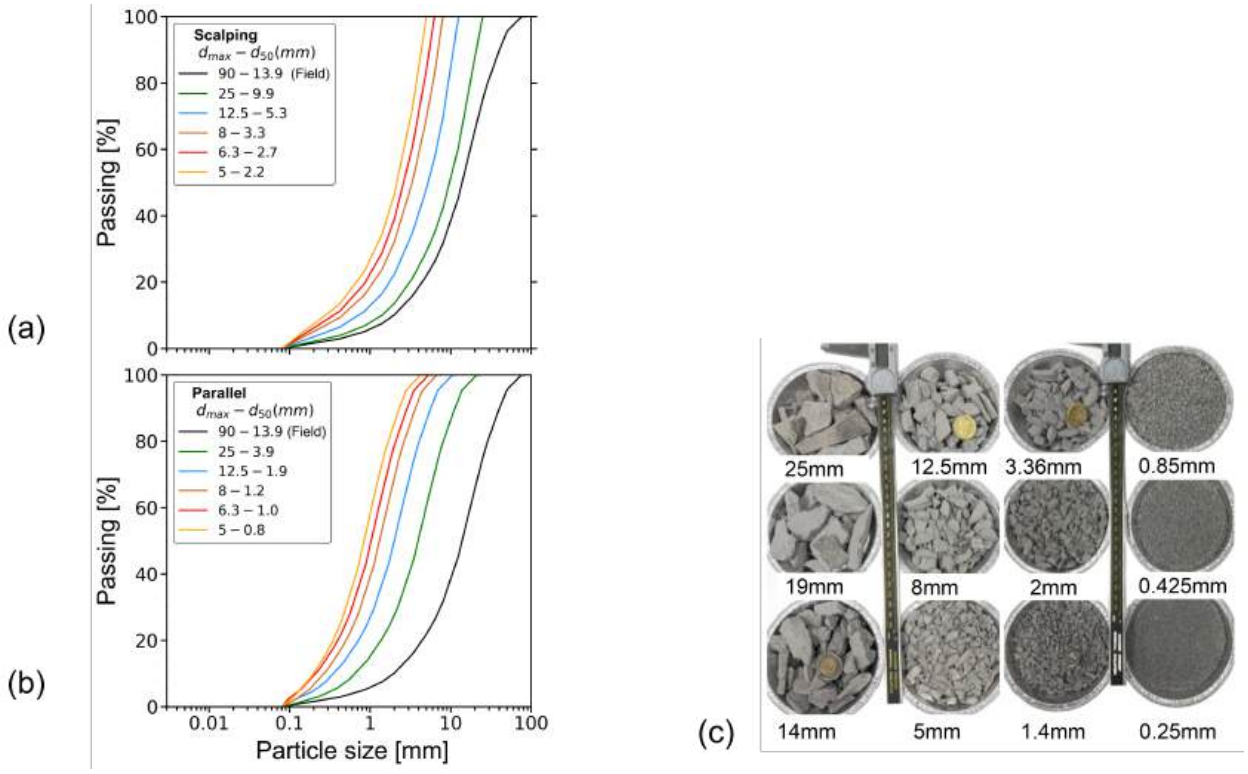

Figure 5.1 Field and scaled samples of quarried rockfill, scaling with d_{max} between 5 to 25 mm using (a) scalping grading and (b) parallel grading techniques; (c) characteristic photos of the subangular particles.

5.2.2 Triaxial samples preparation

Samples were prepared in a mold of 300 mm in height and 150 mm in diameter (H:D=2:1), covered by a 2 mm thick latex membrane. To minimize strain localization promoted in dense soils, all the samples were prepared in the loosest possible configuration, by pouring the material in layers without any compaction. Ten distinct layers of homogeneous dry material ($\sim 950g$ each) were gently placed in the mold. Due to different grading between samples, the attained dry densities varied slightly from $\gamma_d = 16.14 - 17.64\ kN/m^3$ in S and $\gamma_d = 16.40 - 18.12\ kN/m^3$ in P samples (see *Table* 5.1, included as supplementary information), respectively.

Two lubricated end configurations were evaluated, both with enlarged caps of 170 mm in diameter and made of 3 cm thick lucite material (see *Figure* 5.2). The aim was to evaluate the best approach that avoids buckling (Raju et al., 1972; Sheng et al., 1997). The first configuration consists of a thin film of silicone grease applied to the entire section of the enlarged caps, covered by a continuous sheet of latex membrane (1 mm thick). For the

second lubricated configuration, a cross-shaped cut was induced in the center of the sheet (*Figure* 5.2b).

5.2.3 Triaxial testing

Samples were isotropically consolidated until volume stabilization (∼45 minutes). Two effective confining pressures of $\sigma'_3 = 100\ kPa$ and 400 kPa were used. The volumetric strain (ε_v) was estimated from the cell water volume. Shearing was carried out at constant axial strain rate of 1 mm/min. The deviatoric stress $q = \sigma'_1 - \sigma'_3$ and the mean effective stress $p' = (\sigma'_1 + 2\sigma'_3)/3$ were monitored until reaching an axial strain of $\varepsilon_a = 15\%$.

The following tests were carried out: (i) 30 tests on samples with standard rough ends and (ii) 49 tests with enlarged platens and lubricated sheets (*Figure* 5.2).

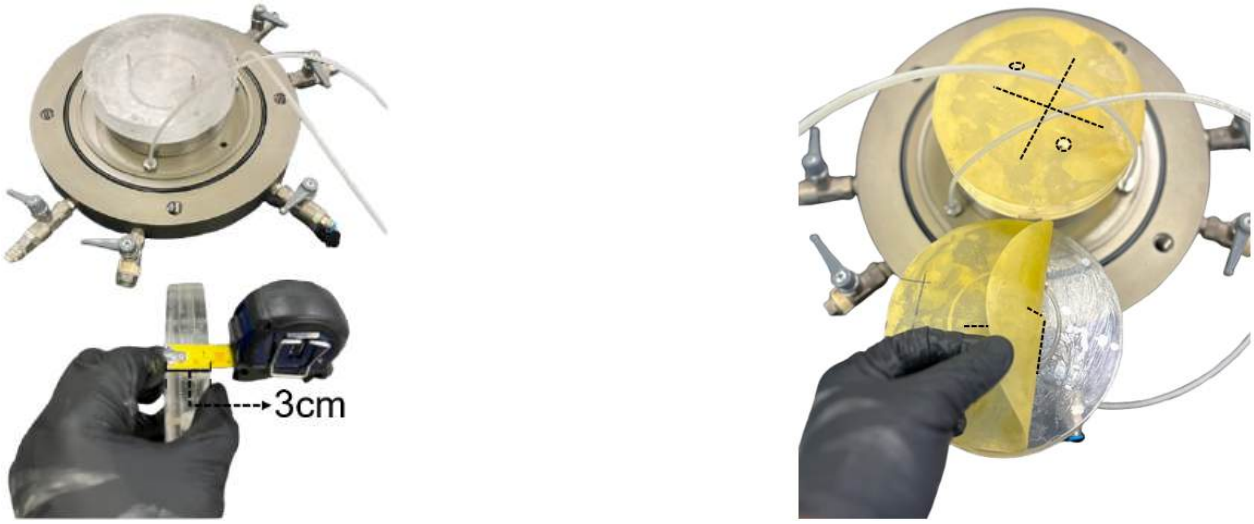

(a) (b)

Figure 5.2 Enlarged cap setup (D = 170 mm): (a) lubricated cap; (b) positioning cross-cut greased rubber sheets.

5.3 Experimental Results

Figure 5.3 displays photos of the samples after testing. Regarding samples with rough ends (*Figure* 5.3a), shear bands and sample bulging are systematically observed. This is an unexpected result in such loose materials, and evidence suggests that end-restraint effects might be amplified in highly frictional soils, such as coarse crushed rock. Most of the cases with a continuous lubricated sheet exhibited buckling, as shown in *Figure* 5.3b. On the other hand, cross-cutting the sheets helps to maintain the verticality of the samples (see *Figure* 5.3c),

certainly because this setup allows for the free movement of the particles in contact with the caps. Given these results, all tests with continuous sheets were repeated using cross-cut sheets, and the following analyses consider only the latter configuration.

(a) Standard rough ends.

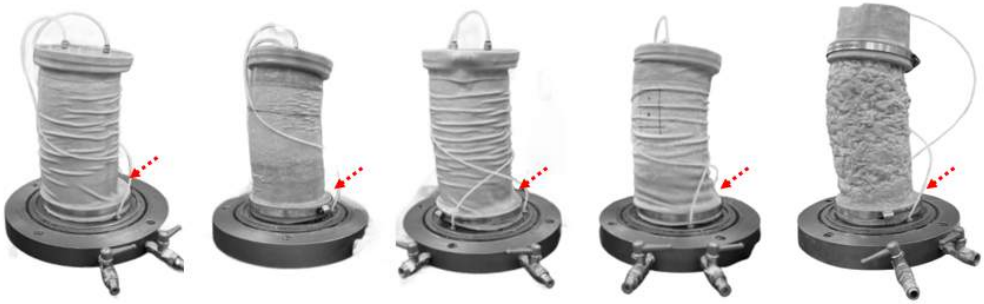

(b) Lubricated with *continuous* greased latex rubber sheets; *Red* arrows designate sliding movement.

(c) Lubricated with *cross-cut* greased latex rubber sheets.

Figure 5.3 Pictures across tested d_{max} showing samples deformation after testing.

Figure 5.4 presents typical stress-strain responses for selected S and P materials (d_{max} =12.5 mm), tested with rough platens (R) and lubricated platens (L), where the stress ratio q/p' and ε_v are plotted against ε_a. The first letter in the legend indicates the PSD scaling method (S or P), while the second one designates the platen configuration (R or L); the number that follows is $\sigma'_3 = 100$ or 400 kPa. For instance, SR100 and SL100 nominate scalped materials tested at $\sigma'_3 = 100$ kPa with rough and lubricated platens, respectively.

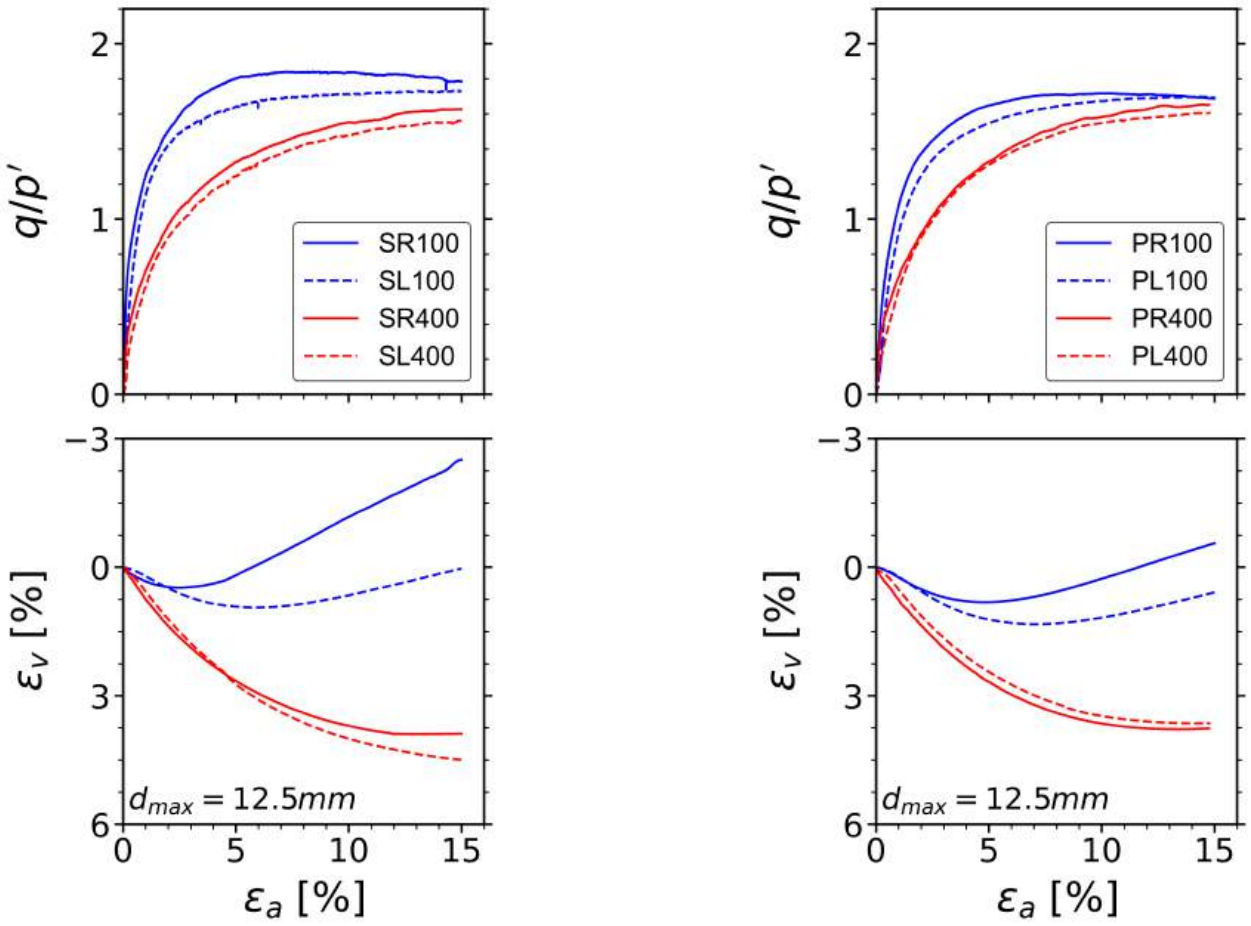

Figure 5.4 Stress-strain behaviour of samples of d_{max} =12.5 mm, with standard rough (continuous lines) and lubricated ends (dashed lines) at 100 (*blue*) and 400 kPa (*red*), respectively: (a) S and (b) P materials.

Following the same trend of the samples with d_{max} =12.5 mm shown in *Figure* 5.4, all the tests exhibited stress hardening towards maximum q/p' reached around $\varepsilon_a = 15\%$. The stress-strain plots of the 79 tests are included as supplementary information[2], shown in *Figures* 5.9 and 5.10 for S and P samples, respectively. Additional figures detailing individual test stress-strain curves are shown in *Appendix* C.

As an expected general trend, tests with standard rough ends overestimate q/p' values and dilation in both sets of materials (S and P) and confining stresses used. However, these differences are greatly reduced at higher σ'_3. To highlight these observations, *Figure* 5.5 presents the evolution of ϕ' in all the tests, obtained according to the Mohr-Coulomb failure

[2]Since *Géotechnique Letters* only accepts short papers of less than 2000 words, *Figures* 5.9 and 5.10 are included as supplementary information at the end of this paper.

criterion for cohesionless materials: $sin\phi' = 3(q/p')_{max}/(6+(q/p')_{max})$; the results are plotted against d_{50}, displaying all the tests carried out on every PSD shown in *Figure* 5.1 (detailed data is included in *Table* 5.1). Since the critical strength does not depend on PSD (Cantor & Ovalle, 2023; Li et al., 2013; Muir Wood & Maeda, 2008; Yang & Luo, 2018), ϕ' should be a stable value among all the samples tested, provided that boundary effects are negligible. For all tests with rough ends, ϕ' is scattered between 39.6−46.4° at $\sigma'_3 = 100$ kPa, and 38.8−41.7° at 400 kPa, without a clear distinction between the SR and PR tests. On the other hand, lubricated tests exhibited slightly lower strength between ϕ' =39.2−43.5° at $\sigma'_3 = 100$ kPa and 37.3−40.7° at 400 kPa, with lower scattering compared to the cases with rough ends. These relatively high values of ϕ' —compared with sands and fine soils— are consistent with enhanced end-restraint effects, as hypothesized in the first section of this letter.

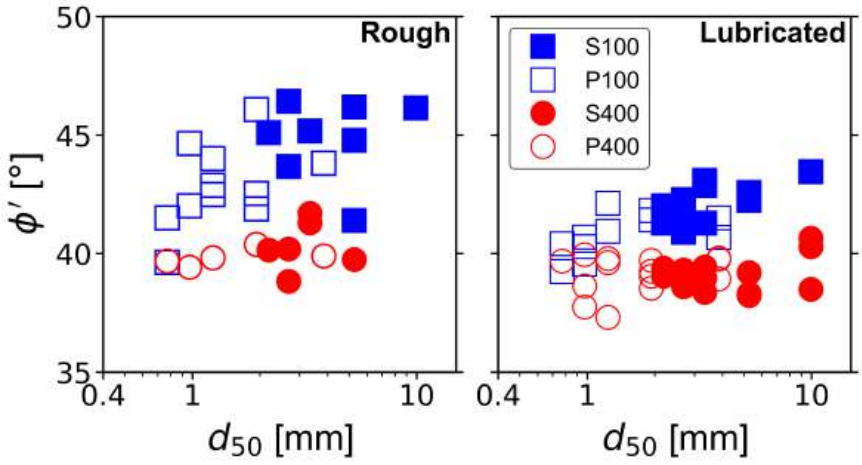

Figure 5.5 The evolution of the mobilized ϕ' with d_{50}: *blue* square and *red* circle filled and empty markers for S and P samples, respectively.

Figure 5.6 displays the maximum dilatancy rate ($(d\varepsilon_v/d\varepsilon_a)_{max}$; negative values designate dilation) for all tests. As expected, the results reflect that rough boundaries promote dilatancy and increase dispersion of the data. The main source of scattering in R cases is probably related to strain localization, as shown in *Figure* 5.3a. In such heterogeneous strain fields, ε_v does not necessarily represent the sample strain, but a mean value between volume change during shear sliding within the shear band, and a relatively constant volume in the rest of the sample.

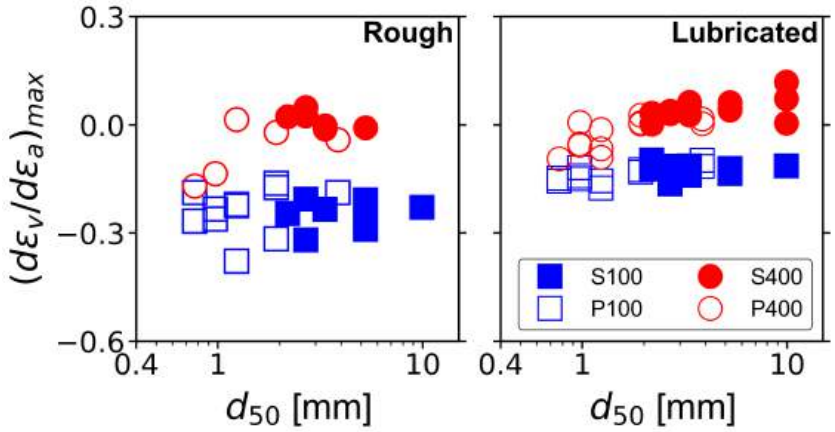

Figure 5.6 The evolution of $(d\varepsilon_v/d\varepsilon_a)_{max}$ with d_{50}: *blue* square and *red* circle filled and empty markers for S and P samples.

Figure 5.7 presents the characteristic secant strain modulus (E_{50}) evolution across d_{50} for all tests; E_{50} is defined as the ratio of the 50% of the maximum deviatoric stress and the corresponding ε_a. In SR and PR cases, E_{50} exhibits great scattering without a noticeable trend. Moreover, the values appear to increase with the particle size in tests at σ'_3 = 100 kPa (from ∼8-19 MPa), while the inverse trend is observed at 400 kPa (from ∼23-17 MPa). Comparatively, E_{50} of samples with lubricated platens exhibit more stable results in all materials S and P.

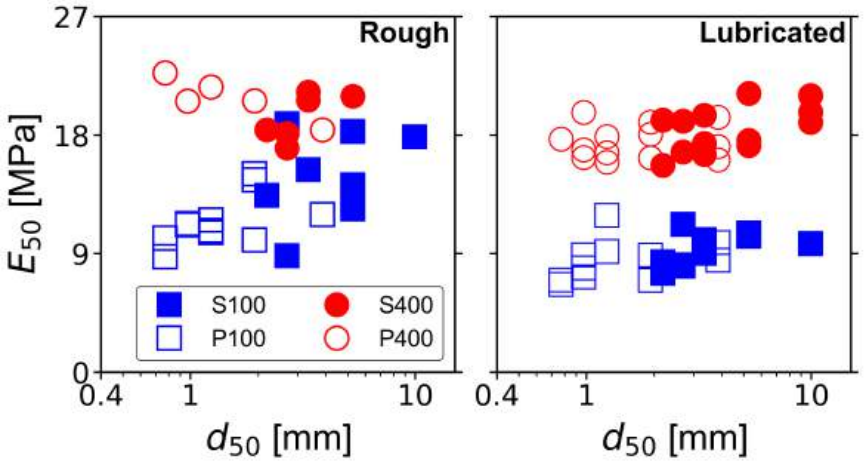

Figure 5.7 The evolution of E_{50} with d_{50}: *blue* square and *red* circle filled and empty markers for S and P samples, respectively.

In order to assess the representativeness of small-scaling methods, *Figure* 5.8 summarizes the results by displaying the mean values and their standard deviation for each testing condition

(R and L) and scaling technique (S and P). In terms of shear strength (*Figure* 5.8a), rough ends clearly give higher mean ϕ', particularly at the lower level of confining pressure. The difference in ϕ' between 100 and 400 kPa is remarkably reduced in PL tests, indicating that lubrication and better graded materials give more stable results. Regarding dilatancy in both S and P samples (*Figure* 5.8b), the differences due to end friction effects are noticeable only at $\sigma'_3 = 100$ kPa, with enhanced $(d\varepsilon_v/d\varepsilon_a)_{max}$ in R samples. However, the effect seems negligible at $\sigma'_3 = 400$ kPa. On the other hand, mean E_{50} values increase with rough ends, and this effect is strongly enhanced in S samples (see *Figure* 5.8c). Again, at $\sigma'_3 = 400$ kPa the results are more stable.

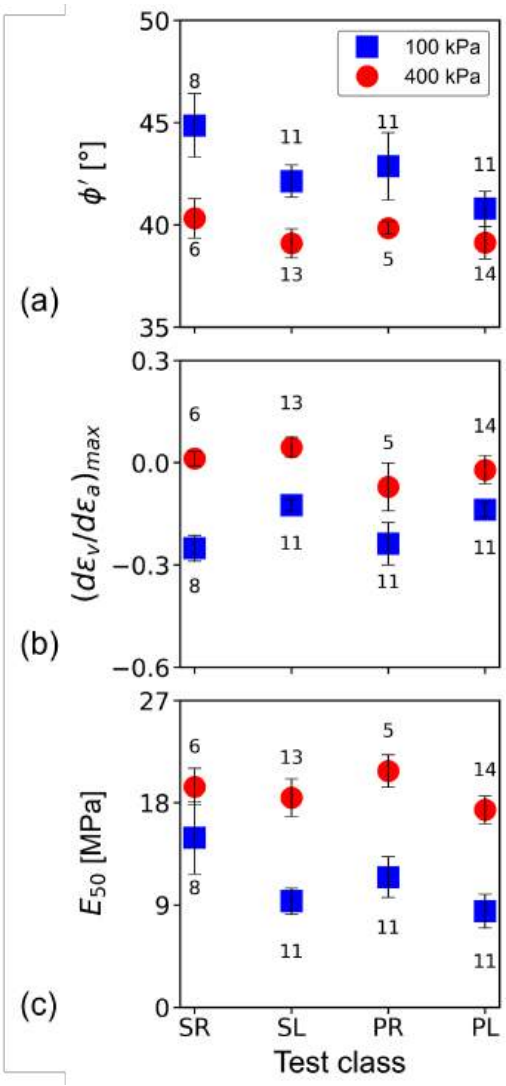

Figure 5.8 Summary of mean values and standard deviations of (a) ϕ', (b) $(d\varepsilon_v/d\varepsilon_a)_{max}$ and (c) E_{50}, for all tests; marks represent mean values, bars are the standard deviations and numbers next to each mark indicate the number of tests carried out.

5.4 Conclusions

This letter presented a comprehensive study on end-restraint effects in triaxial tests on loose quarry rockfill dry samples with 150 mm in diameter and slenderness H:D = 2:1. Standard rough platens caps were compared with enlarged and lubricated platens. Materials tested had varied PSD, generated by scaling using scalping and parallel grading. The following conclusions are drawn:

- End-restraint effects in scaled rockfill samples are not fully overcome with slenderness H:D = 2:1; standard rough ends induce strain localization, while lubricated ends allow for homogeneous strain fields.
- End-restraint effects appear as higher and scattered shear strength, dilatancy and secant stiffness.
- Samples prepared by scalping and tested with standard rough platens revealed the strongest end friction effects, with higher values of ϕ' and E_{50} compared with parallel graded materials under the same testing conditions.
- In general, parallel graded samples with lubricated caps displayed relatively consistent strain-strain curves in the whole set of tests, particularly at high confining pressure.

The results indicate that end lubrication should be systematically used in triaxial tests on coarse rockfill materials, even in H:D = 2:1 samples. Also, it is highly recommended to use shredded sheets on lubricated caps. This method allows radial movement of the particles in contact with the ends, avoiding a single sliding surface that can cause buckling of the sample.

Acknowledgements

This study was funded by the Natural Sciences and Engineering Research Council of Canada (NSERC) [reference RGPIN-2019-06118] and the industrial partners of the Research Institute on Mines and the Environment (RIME) (http://www.irme.ca/en). The authors also thank Lafarge Canada for providing rockfill material and Patrick Bernèche for his support in the extensive experimental work.

Bibliography

Al-Hussaini, M. M. (1970). *The influence of end restraint and method of consolidation on the drained triaxial compressive strength of crushed napa basalt* (Miscellaneous Paper No. S-70-18). U.S. Army Engineer Waterways Experiment Station. Vicksburg, Mississippi, USA.

Al-Hussaini, M. M. (1983). Effect of particle size and strain conditions on the strength of crushed basalt. *Canadian Geotechnical Journal*, *20*(4), 706–717.

Asaoka, A., Nakano, M., & Noda, T. (1994). Soil-water coupled behaviour of saturated clay near/at critical state. *Soils and foundations*, *34*(1), 91–105.

ASTM D2487. (2017). *Standard practice for classification of soils for engineering purposes (unified soil classification system)*. ASTM International.

Bishop, A. W., & Green, G. E. (1965). The influence of end restraint on the compression strength of a cohesionless soil. *Géotechnique*, *15*(3), 243–266.

Cantor, D., & Ovalle, C. (2023). Sample size effects on the critical state shear strength of granular materials with varied gradation and the role of column- like local structures. *Géotechnique*, *75*(1), 29–40.

Carrasco, S., Cantor, D., Ovalle, C., & Dubois, F. (2025). Particle shape distribution effects on the critical strength of granular materials. *Computers and Geotechnics*, *177*, 106896.

Colliat-Dangus, J., Desrues, J., & Foray, P. (1988, January). Triaxial testing of granular soil under elevated cell pressure. In *Advanced triaxial testing of soil and rock* (p. 21). ASTM International.

Duncan, J. M., & Dunlop, P. (1968). The significance of cap and base restraint. *Journal of the Soil Mechanics and Foundations Division*, *94*(1), 271–290.

Feda, J., Bohac, J., & Herle, I. (1993). End restraint in triaxial testing of soils. *Acta Technica CSAV*, *38*, 197–197.

Frossard, E., Hu, W., Dano, C., & Hicher, P.-Y. (2012). Rockfill shear strength evaluation: a rational method based on size effects. *Géotechnique*, *62*(5), 415–427.

Frost, J. D., & Yang, C.-T. (2003). Effect of end platens on microstructure evolution in dilatant specimens. *Soils and Foundations*, *43*(4), 1–11.

Girumugisha, G., Ovalle, C., & Ouellet, S. (2024). Grading scalping and sample size effects on critical shear strength of mine waste rock through laboratory and in-situ testing. *International Journal of Rock Mechanics and Mining Sciences*, *183*, 105915.

Goto, S., & Tatsuoka, F. (1988, January). Effects of end conditions on triaxial compressive strength for cohesionless soil. In *Advanced triaxial testing of soil and rock* (p. 14). ASTM International.

Hettler, A., & Vardoulakis, I. (1984). Behaviour of dry sand tested in a large triaxial apparatus. *Géotechnique*, *34*(2), 183–197.

Hu, W., Dano, C., Hicher, P.-Y., Le Touzo, J.-Y., Derkx, F., & Merliot, E. (2011). Effect of sample size on the behavior of granular materials. *Geotechnical Testing Journal*, *34*(3), 186–197.

Kodaka, T., Higo, Y., Kimoto, S., & Oka, F. (2007). Effects of sample shape on the strain localization of water-saturated clay. *International journal for numerical and analytical methods in geomechanics*, *31*(3), 483–521.

Lee, K. L., & Vernese, F. J. (1978). End restraint effects on cyclic triaxial strength of sand. *Journal of the Geotechnical Engineering Division*, *104*(6), 705–719.

Leps, T. M. (1970). Review of shearing strength of rockfill. *Journal of the Soil Mechanics and Foundations Division*, *96*(4), 1159–1170.

Li, G., Ovalle, C., Dano, C., & Hicher, P.-Y. (2013). Influence of grain size distribution on critical state of granular materials. In Q. Yang, J.-M. Zhang, H. Zheng, & Y. Yao (Eds.), *Constitutive modeling of geomaterials* (pp. 207–210). Springer Berlin Heidelberg.

Linero, S., Fityus, S., Simmons, J., Lizcano, A., & Cassidy, J. (2017). Trends in the evolution of particle morphology with size in colluvial deposits overlying channel iron deposits. *EPJ Web Conf.*, *140*, 14005.

Liu, X., Shao, L., & Guo, X. (2013). Local data analysis for eliminating end restraint of triaxial specimen. *Transactions of Tianjin University*, *19*(5), 372–380.

Marachi, N. D., Chan, C. K., & Seed, H. B. (1972). Evaluation of properties of rockfill materials. *Journal of the Soil Mechanics and Foundations Division*, *98*(1), 95–114.

Mozaffari, M., Liu, W., & Ghafghazi, M. (2022). Influence of specimen nonuniformity and end restraint conditions on drained triaxial compression test results in sand. *Canadian Geotechnical Journal*, *59*(8), 1414–1426.

Muir Wood, D., & Maeda, K. (2008). Changing grading of soil: effect on critical states. *Acta Geotechnica*, *3*(1), 3–14.

Muraro, S., & Jommi, C. (2019). Implication of end restraint in triaxial tests on the derivation of stress–dilatancy rule for soils having high compressibility. *Canadian Geotechnical Journal*, *56*(6), 840–851.

Olson, R. E., Campbell, L. M., Lee, K., Seed, H. B., Turnbull, J. M., & Poulos, S. (1964). Discussion of "importance of free ends in triaxial testing". *Journal of the Soil Mechanics and Foundations Division*, *90*(6), 167–179.

Ovalle, C., & Dano, C. (2020). Effects of particle size–strength and size–shape correlations on parallel grading scaling. *Géotechnique Letters*, *10*(2), 191–197.

Ovalle, C., Frossard, E., Dano, C., Hu, W., Maiolino, S., & Hicher, P.-Y. (2014). The effect of size on the strength of coarse rock aggregates and large rockfill samples through experimental data. *Acta Mechanica*, *225*(8), 2199–2216.

Ovalle, C., Linero, S., Dano, C., Bard, E., Hicher, P.-Y., & Osses, R. (2020). Data compilation from large drained compression triaxial tests on coarse crushable rockfill materials. *Journal of Geotechnical and Geoenvironmental Engineering*, *146*(9), 06020013.

Peri, E., Ibsen, L. B., & Nordahl Nielsen, B. (2019). Influence of sample slenderness and boundary conditions in triaxial test - a review. *E3S Web Conf.*, *92*, 02009.

Quiroz-Rojo, P., Cantor, D., Renouf, M., Ovalle, C., & Azéma, E. (2024). REV assessment of granular materials with varied grading based on macro- and micro-mechanical statistical data. *Acta Geotechnica*.

Raju, V., Sadasivan, S., & Venkataraman, M. (1972). Use of lubricated and conventional end platens in triaxial tests on sands. *Soils and Foundations*, *12*(4), 35–43.

Reid, D., Fourie, A., Ayala, J. L., Dickinson, S., Ochoa-Cornejo, F., Fanni, R., Garfias, J., da Fonseca, A. V., Ghafghazi, M., Ovalle, C., Riemer, M., Rismanchian, A., Olivera, R., & Suazo, G. (2021). Results of a critical state line testing round robin programme. *Geotechnique*, *71*(7), 616–630.

Rowe, P. W., & Barden, L. (1964). Importance of free ends in triaxial testing. *Journal of the Soil Mechanics and Foundations Division*, *90*(1), 1–27.

Roy, M., & Lo, K. (1971). Effect of end restraint on high pressure tests of granular materials. *Canadian Geotechnical Journal*, *8*(4), 579–588.

Sheng, D., Westerberg, B., Mattsson, H., & Axelsson, K. (1997). Effects of end restraint and strain rate in triaxial tests. *Computers and Geotechnics*, *21*(3), 163–182.

Shockley, W. G., & Ahlvin, R. G. (1960). Nonuniform conditions in triaxial test specimens. *Research conference on shear strength of cohesive soils*, 341–357.

Taylor, D. (1941). Cylindrical compression research program on stress-deformation and strength characteristics of soils. *MIT 7th Progress Report to Water Experiments Station*.

Wightman, A., Dickinson, S., Jeong, C.-G., Shanmugarajah, T., & Billings, M. (2024). Importance of sample height–diameter ratio in triaxial testing with free ends for determination of the critical state of sands. *Geotechnical Testing Journal*, *48*(2).

Yang, J., & Luo, X. D. (2018). The critical state friction angle of granular materials: does it depend on grading? *Acta Geotechnica*, *13*(3), 535–547.

Yeh, F.-H., Ge, L., Jhuo, Y.-S., & Chen, L.-C. (2024). Re-examining the influence of end restraint on mechanical behaviors of dense quartz sands. *KSCE Journal of Civil Engineering*, *28*(6), 2201–2209.

5.5 Supplementary information

Table 5.1 Summary of all tests

Test ID	d_{max} (mm)	d_{50} (mm)	C_u	C_c	Test class	γ_d (kN/m^3)	E_{50} (MPa)	ϕ' (°)	$(d\varepsilon_v/d\varepsilon_a)_{max}$ (-)
T01	25	9.9	8.8	1.6	SR100	17.07	18	46.1	-0.23
T02	12.5	5.3	9.0	1.6		17.00	14	46.2	-0.28
T03	12.5	5.3	9.0	1.6		17.37	12	41.4	-0.21
T04	12.5	5.3	9.0	1.6		17.56	18	44.8	-0.29
T05	8	3.3	9.0	1.8		17.14	15	45.2	-0.23
T06	6.3	2.7	9.2	1.8		17.31	19	46.4	-0.32
T07	6.3	2.7	9.2	1.8		17.06	9	43.7	-0.21
T08	5	2.2	9.5	1.8		17.14	13	45.1	-0.25
T09	25	9.9	8.8	1.6	SL100	17.64	10	43.5	-0.11
T10	12.5	5.3	9.0	1.6		17.47	10	42.2	-0.13
T11	12.5	5.3	9.0	1.6		17.48	11	42.6	-0.12
T12	8	3.3	9.0	1.8		16.67	10	41.3	-0.14
T13	8	3.3	9.0	1.8		17.29	9	43.1	-0.13
T14	8	3.3	9.0	1.8		16.50	10	42.9	-0.11
T15	6.3	2.7	9.2	1.8		17.10	11	40.9	-0.16
T16	6.3	2.7	9.2	1.8		17.53	8	42.3	-0.12
T17	6.3	2.7	9.2	1.8		17.30	8	41.5	-0.11
T18	5	2.2	9.5	1.8		16.89	7	41.3	-0.10
T19	5	2.2	9.5	1.8		17.39	8	42.0	-0.12
T20	12.5	5.3	9.0	1.6	SR400	16.49	21	39.8	-0.01
T21	8	3.3	9.0	1.8		17.10	21	41.3	-0.01
T22	8	3.3	9.0	1.8		16.89	21	41.7	0.00
T23	6.3	2.7	9.2	1.8		16.53	17	38.8	0.05
T24	6.3	2.7	9.2	1.8		16.87	18	40.2	0.02
T25	5	2.2	9.5	1.8		16.93	18	40.2	0.02
T26	25	9.9	8.8	1.6	SL400	16.98	19	38.5	0.07
T27	25	9.9	8.8	1.6		16.85	21	40.3	0.00
T28	25	9.9	8.8	1.6		16.83	20	40.7	0.12
T29	12.5	5.3	9.0	1.6		16.14	18	38.3	0.06
T30	12.5	5.3	9.0	1.6		16.51	21	38.2	0.04

Table 5.1 Summary of all tests. (continued)

Test ID	d_{max} (mm)	d_{50} (mm)	C_u	C_c	Test class	γ_d (kN/m^3)	E_{50} (MPa)	ϕ' (°)	$(d\varepsilon_v/d\varepsilon_a)_{max}$ (-)
T31	12.5	5.3	9.0	1.6		16.97	17	39.2	0.04
T32	8	3.3	9.0	1.8		16.87	17	39.4	0.05
T33	8	3.3	9.0	1.8		16.30	17	39.0	0.06
T34	8	3.3	9.0	1.8		16.61	20	38.4	0.03
T35	6.3	2.7	9.2	1.8		16.94	17	38.6	0.04
T36	6.3	2.7	9.2	1.8		16.94	19	39.3	0.03
T37	5	2.2	9.5	1.8		16.76	19	39.4	0.00
T38	5	2.2	9.5	1.8		16.71	16	39.0	0.03
T39	25	3.9	9.0	1.6		16.93	12	43.8	-0.19
T40	12.5	1.9	9.0	1.6		18.00	15	46.1	-0.32
T41	12.5	1.9	9.0	1.6		17.12	10	41.9	-0.17
T42	12.5	1.9	9.0	1.6		17.56	15	42.5	-0.16
T43	8	1.2	9.0	1.6		17.61	11	42.5	-0.22
T44	8	1.2	9.0	1.6	PR100	17.40	12	44.0	-0.38
T45	8	1.2	9.0	1.6		17.50	11	42.9	-0.22
T46	6.3	1.0	9.0	1.6		17.45	11	44.7	-0.23
T47	6.3	1.0	9.0	1.6		17.92	11	42.0	-0.26
T48	5	0.8	9.0	1.6		17.77	9	39.6	-0.19
T49	5	0.8	9.0	1.6		17.78	10	41.5	-0.27
T50	25	3.9	9.0	1.6		16.89	8	40.7	-0.10
T51	25	3.9	9.0	1.6		17.38	10	41.5	-0.12
T52	12.5	1.9	9.0	1.6		17.00	7	41.4	-0.13
T53	12.5	1.9	9.0	1.6		17.21	9	41.8	-0.13
T54	8	1.2	9.0	1.6		17.16	9	40.9	-0.16
T55	8	1.2	9.0	1.6	PL100	17.73	12	42.1	-0.18
T56	6.3	1.0	9.0	1.6		17.71	7	39.6	-0.14
T57	6.3	1.0	9.0	1.6		18.06	8	40.7	-0.15
T58	6.3	1.0	9.0	1.6		17.67	9	40.3	-0.12
T59	5	0.8	9.0	1.6		18.08	7	39.2	-0.16
T60	5	0.8	9.0	1.6		18.12	7	40.4	-0.15
T61	25	3.9	9.0	1.6		16.51	18	39.9	-0.04
T62	12.5	1.9	9.0	1.6		16.40	21	40.4	-0.02
T63	8	1.2	9.0	1.6	PR400	17.71	22	39.8	0.01

Table 5.1 Summary of all tests. (continued)

Test ID	d_{max} (mm)	d_{50} (mm)	C_u	C_c	Test class	γ_d (kN/m^3)	E_{50} (MPa)	ϕ' (°)	$(d\varepsilon_v/d\varepsilon_a)_{max}$ (-)
T64	6.3	1.0	9.0	1.6		18.03	21	39.4	-0.14
T65	5	0.8	9.0	1.6		17.65	23	39.7	-0.17
T66	25	3.9	9.0	1.6	PL400	17.13	19	38.9	0.02
T67	25	3.9	9.0	1.6		17.50	16	39.8	0.00
T68	25	3.9	9.0	1.6		17.23	17	39.8	0.02
T69	12.5	1.9	9.0	1.6		17.50	19	38.5	0.00
T70	12.5	1.9	9.0	1.6		17.50	16	39.3	0.01
T71	12.5	1.9	9.0	1.6		17.23	18	39.0	0.00
T72	12.5	1.9	9.0	1.6		17.49	16	39.7	0.03
T73	8	1.2	9.0	1.6		16.78	16	37.3	-0.01
T74	8	1.2	9.0	1.6		17.59	18	39.8	-0.09
T75	8	1.2	9.0	1.6		17.59	17	39.6	-0.07
T76	6.3	1.0	9.0	1.6		17.59	20	37.7	0.01
T77	6.3	1.0	9.0	1.6		17.97	16	40.0	-0.06
T78	6.3	1.0	9.0	1.6		17.97	17	38.6	-0.05
T79	5	0.8	9.0	1.6		17.50	18	39.7	-0.09

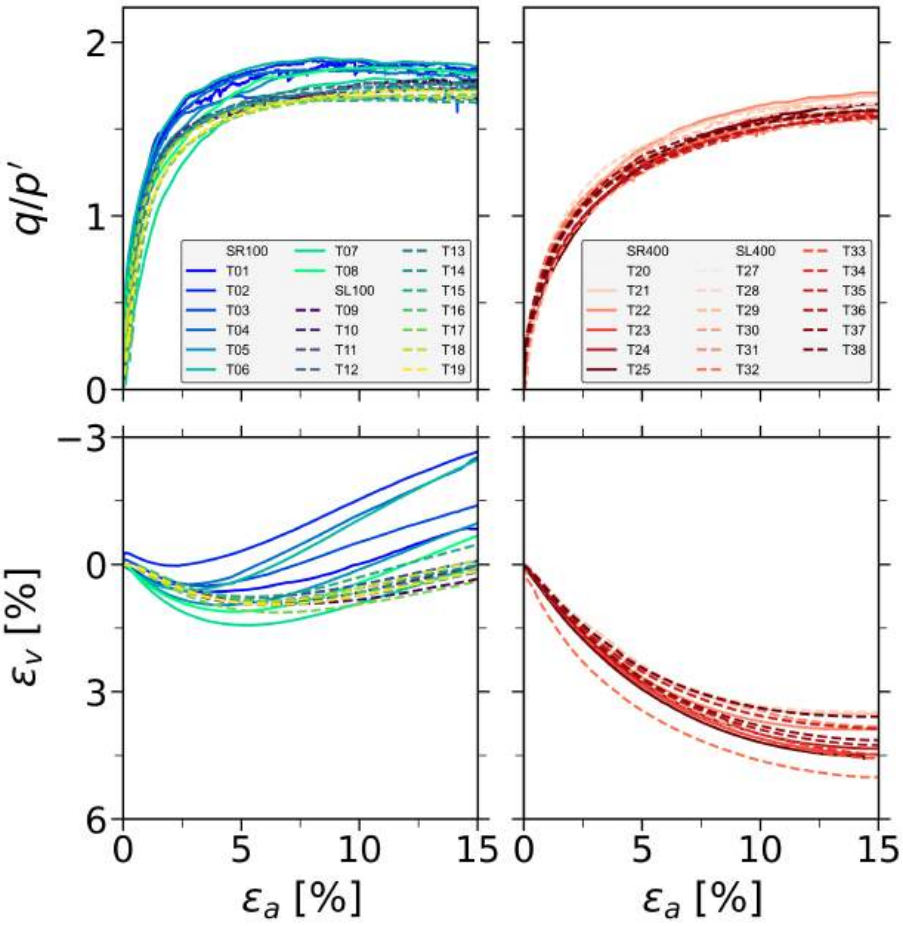

Figure 5.9 Stress-strain curves of scalping graded samples with both rough (continuous lines) and lubricated ends (dashed lines) at $\sigma'_3 = 100$ (*left*) and 400 kPa (*right*), respectively.

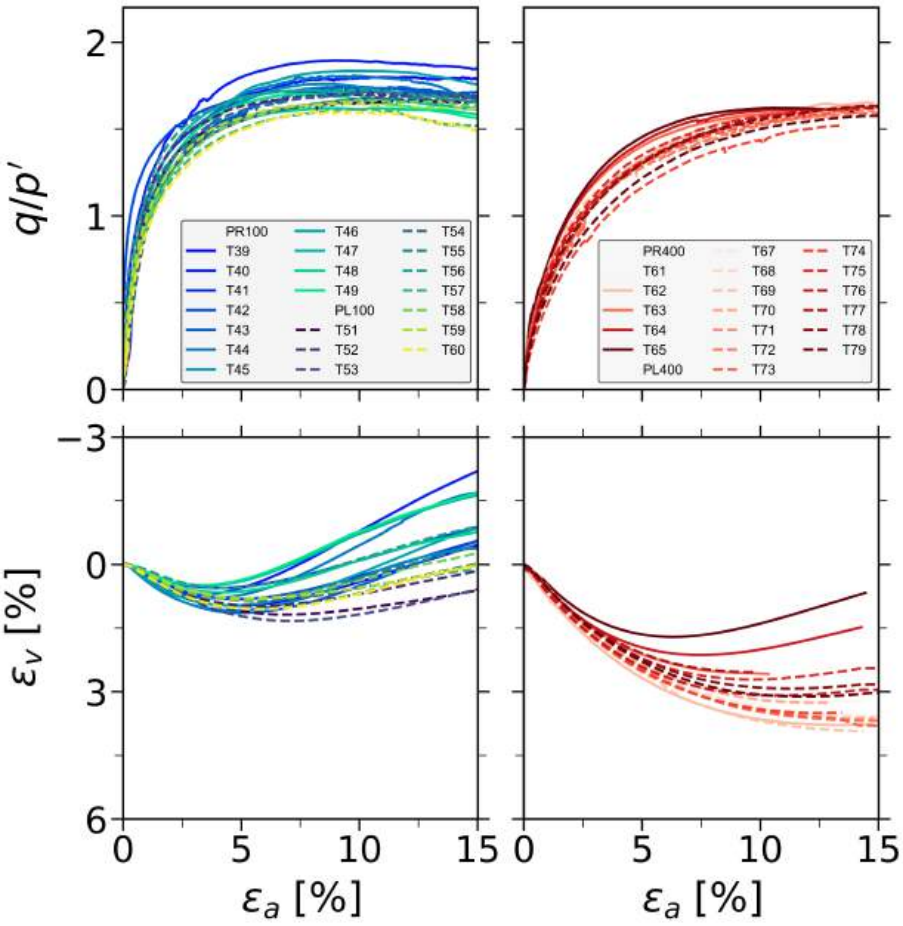

Figure 5.10 Stress-strain curves of parallel graded samples with both rough (continuous lines) and lubricated ends (dashed lines) at $\sigma'_3 = 100$ (*left*) and 400 kPa (*right*), respectively.

CHAPTER 6 ARTICLE 3 – Effects of Triaxial Sample Scaling on the Mechanical Behavior of Alluvial Gravels

Journal: Journal of Geotechnical and Geoenvironmental Engineering.
Submitted: January 28, 2025.

Authors: Gilbert Girumugisha[a,b], Carlos Ovalle[a,b,*], Holger Reith[c], and Hans Henning Stutz[c]

[a]Dep. of Civil, Geological and Mining Engineering, Polytechnique Montréal, Québec, Canada.

[b]Research Institute of Mining and Environment (RIME UQAT-Polytechnique), Canada

[c]Institute of Soil Mechanics and Rock Mechanics (IBF), Karlsruhe Institute of Technology (KIT), Karlsruhe, Germany

[*]Corresponding Author, ✉ carlos.ovalle@polymtl.ca.

ABSTRACT In practical engineering, mechanical characterization of coarse gravels is usually performed on small-scale samples, where the maximum particle size is limited to fit the material in standard testing devices. This implies altering the original particle size distribution, which is known to influence the stress-strain behavior. However, most research on grading effects has been done after comprehensive testing on sands, and the impact of small-scaling on gravelly soils is still poorly understood. This paper presents an experimental study on the shearing response of coarse soil at different sample scales. The main objective is to assess the impact of small-scaling methods on the stress-strain behavior of coarse alluvial soils. Scalping grading and truncation techniques were used to prepare scaled samples. Several tests were performed using triaxial cells with samples of 100, 150 and 800 mm in diameter. The analyses indicate that volumetric dilatancy strongly decreases with sample size, while the secant strain modulus and peak shear strength slightly increase in larger samples. Differences are mainly related to particle size distributions and packing properties. The article discusses practical insights into the effects of small-scaling variations and their implications for characterizing gravelly materials.

6.1 Introduction

Large-scale testing of coarse soils remains challenging for geotechnical engineers, mainly due to the scarcity of large devices worldwide. Thus, mechanical characterization for civil engineering applications, including foundations, embankments, dams, railway ballasts, and slope stability assessments of gravelly soils, is often based on small-scale samples. Scaling methods involve altering the particle size distribution (PSD), by removing the coarse fraction that cannot be fitted in a representative elementary volume (REV) of material, even when using the largest triaxial (Hettler & Vardoulakis, 1984; Hu et al., 2011; Leussink, 1960; Marachi et al., 1972; Marsal, 1967; Ning et al., 2024; Ovalle et al., 2014; Verdugo & de la Hoz, 2007) or direct shear (Barton & Kjærnsli, 1981; Girumugisha et al., 2024; Linero et al., 2020; Matsuoka et al., 2001) devices available. However, uncertainties persist regarding the representativeness of scaling methods in capturing the behavior of oversized materials.

The most common scaling techniques used in practice are scalping grading (Al-Hussaini, 1970; Deiminiat et al., 2022; Girumugisha et al., 2024; Zeller & Wullimann, 1957), parallel grading (Lowe, 1964; Marachi et al., 1972; Osses et al., 2024; Varadarajan et al., 2003; Verdugo & de la Hoz, 2007) and truncation method (also known as scalp-and-replace method) (Hassan et al., 2022; Linero et al., 2007). First, the maximum particle size (d_{max}) that can be used in a laboratory sample should be defined based on testing standards or specific requirements for the REV (Girumugisha et al., 2024; Quiroz-Rojo et al., 2024). Then, the size fractions having a characteristic size $d > d_{max}$ are removed to form a finer PSD. In scalping, all the material presenting $d \leq d_{max}$ is sieved to generate a new PSD. Thus, the coefficient of uniformity ($C_u = d_{60}/d_{10}$) of the small-scale sample decreases. Parallel grading, on the contrary, keeps the same C_u defining a scaling factor as $F = d_{max-field}/d_{max}$, where $d_{max-field}$ is the coarsest particle in the original soil. Then, all the size fractions are simply reduced in size by F, generating a PSD parallel to the field material. However, the scaled PSD is not always parallel in the finer fractions, since it might require grain sizes that are not available in the original soil (i.e., finer than the finest fraction in the field soil). Since scalping and parallel grading methodologies require imperatively proper sieving to create the scaled PSDs, practitioners often use the truncation method. This method considers replacing particles exceeding d_{max} by the corresponding mass of grains having $d = d_{max}$. Therefore, the shape of the field PSD within the fractions finer than d_{max} is maintained, thus avoiding sieving of the scaled sample.

It is well known that PSD impacts the stress-strain behavior of granular soils. Under particular states (e.g., stress and relative density), well-graded soils exhibit lower void ratios

than uniform ones, due to more efficient packing provided by fine grains fitting into coarse pores. Along drained shearing, more uniformly graded soils exhibit higher volumetric strains, yet lower peak shear strength than well-graded materials (Ahmed et al., 2023; Yang & Luo, 2018). Also, when C_u increases, the critical state line shifts towards lower void ratios in the mean effective stress space (Biarez & Hicher, 1994, 1997; Daouadji et al., 2001; Muir Wood & Maeda, 2008). This behavior has been implemented in constitutive models for crushable soils upon grading evolution (Daouadji et al., 2001; Kikumoto et al., 2010; Ovalle & Hicher, 2020). It has also been widely reported that the critical friction angle does not depend on the PSD (Cantor et al., 2018; Li et al., 2013; Polanía et al., 2023; Yang & Luo, 2018). Still, this is only verified if the characteristic particle shape is consistent across grain size fractions (Carrasco et al., 2023, 2025; Linero et al., 2019; Ovalle & Dano, 2020). Given these empirical observations, it can be expected that changing grading after small-scaling affects the stress-strain behavior. However, most studies on grading effects have been conducted on sands and fine soils, and the impacts of small-scaling coarse gravels are still poorly understood. Indeed, some authors have claimed that the shear strength decreases in larger and coarser samples (Linero et al., 2007; Marachi et al., 1972; Ovalle et al., 2014; Zeller & Wullimann, 1957), mainly due to the amount of particle crushing increasing with grain size. Conversely, several other studies have concluded that strength increases when the material becomes coarser (Al-Hussaini, 1983; Deiminiat et al., 2022; Hao & Pabst, 2023; Varadarajan et al., 2003). This apparent discrepancy could be explained by a lack of proper material characterization ensuring fair comparisons at different scales, namely in terms of particle shapes at different grain sizes (Linero et al., 2017), minimum sample REV required (Cantor & Ovalle, 2023) and compaction properties. Therefore, the constraints of small-scaling methods are often ignored by practitioners, and the impacts on geotechnical designs are typically neglected or covered by conservative factors of safety.

The main objective of this paper is to assess the impact of small-scaling methods on the stress-strain behavior of coarse gravelly soil. In this context, monotonic triaxial tests were conducted on dense alluvial gravel materials under consolidated drained conditions, to explore the effects of sample size and grading on deformation and strength characteristics. Scalping grading and truncation techniques were employed at different targeted triaxial sample sizes, with diameters of 100, 150, and 800 mm. Packing properties and characteristic particle shapes of all tested grain sizes were characterized to establish a comparable basis. The analyses focus on dilatancy, secant stiffness, and peak and critical state friction angles. The discussion addresses practical insights into the effects of small-scaling and its implications for the characterization of gravelly materials.

6.2 Experimental methods

6.2.1 Alluvial soil characterization

Approximately 15 tons of terrace alluvial gravel material were collected from a field site. The soil has a maximum particle size $d_{max-field} = 125\ mm$ and less than 2 % fines (finer than 80 μm). *Figure* 6.1a illustrates the PSD of the sampled material, while *Figure* 6.1b presents the characteristic rounded grain shapes of different size fractions. The specific gravity is $G_s = 2.67$ and, according to ASTM D2487, the field material classifies as well-graded gravel with sand (GW).

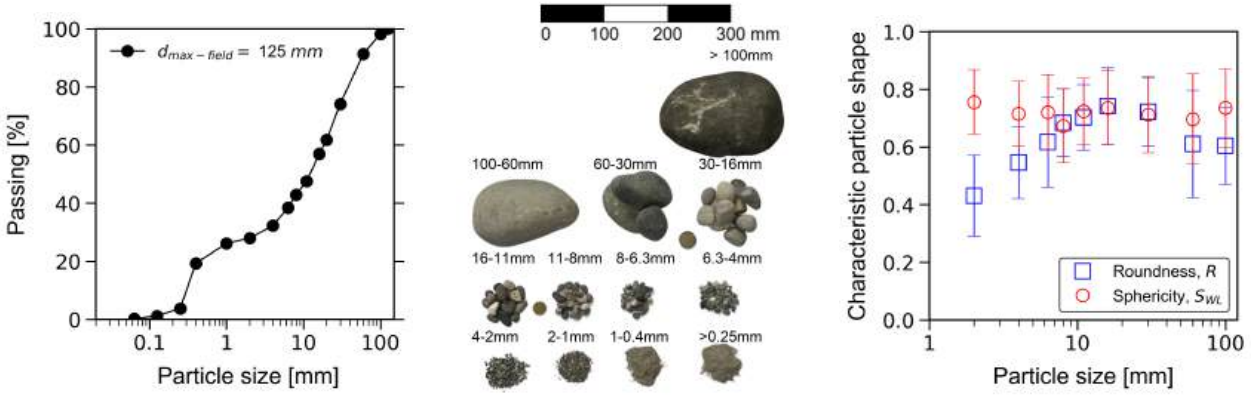

(a) (b) (c)

Figure 6.1 Alluvial soil characterization: (a) PSD of the field soil; (b) photo of the particles; (c) particle shapes over size fractions > 1 mm.

Particle shapes were measured in size fractions between 2 and 100 mm. Two characteristic shape descriptors were used: width-to-length sphericity (S_{WL} = particle width / particle length) and roundness ($R = \sum(r_i/N)/r_{in}$); where r_i represents the radius of circles fitted to concave corners of the particle, N is the number of the fitted circles and r_{in} is the radius of the largest inscribed circle. Digital shape analyses were carried out on photos comprising more than 40 particles for each size fraction to ensure statistical representation. The detailed methodology followed for shape computations is found in the work of Zheng and Hryciw (2015). As shown in *Figure* 6.1c, R varies with particle size, covering a range from subrounded to well-rounded particles ($R = 0.3{-}0.8$). In contrast, S_{WL} remains relatively consistent across sizes, indicating medium to high sphericity ($S_{WL} = 0.6 - 0.8$).

6.2.2 Small-scale grading

Ten distinct PSDs were prepared from the original alluvial gravel: 7 PSDs using the scalping grading method (*Figure* 6.2a) and 3 PSDs using the truncation technique (*Figure* 6.2b). Grading was set based on the triaxial sample diameter (D), in order to get a minimum sample aspect ratio D/d_{max} of 8. Three triaxial devices were used, each accommodating different sizes: small samples for $D = 100\ mm$ (hereafter referred to as S samples), medium samples with $D = 150\ mm$ (M samples) and large samples with $D = 800\ mm$ (L samples); the apparatuses are available at the IBF laboratory of the Karlsruhe Institute of Technology (Brauns & Kast, 2007; Brauns & Reith, 2000). The materials having $d_{max} = 11$, 6.3 and 4 mm were tested as S samples, $d_{max} = 20$, 11 and 6.3 mm as M samples, and L samples for the coarsest materials having $d_{max} = 100$, 60 and 30 mm. The evolution of C_u ranging from 1.8-57.3 is plotted in *Figure* 6.2c, displaying a common trend of all the scalped materials, and higher values for the truncated PSDs.

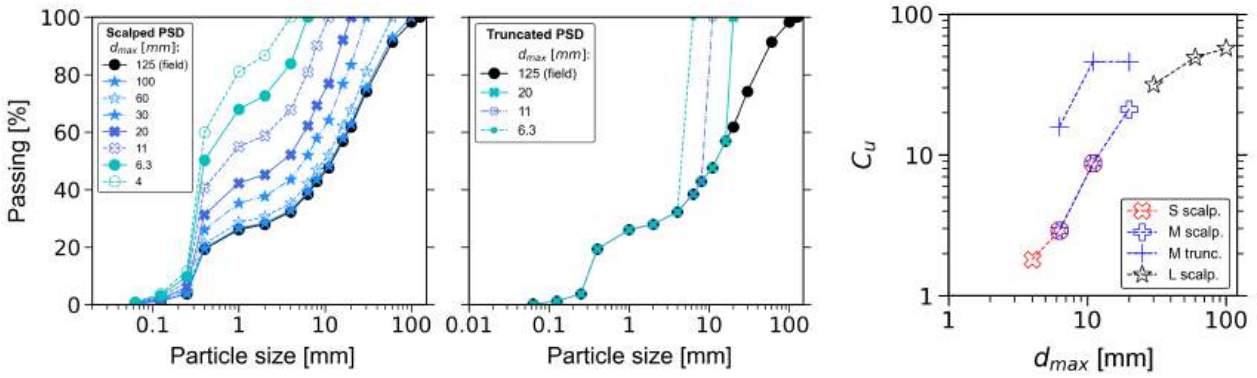

(a) (b) (c)

Figure 6.2 Particle size distributions of the scaled materials from alluvial sandy gravel: (a) scalping grading; (b) truncation technique; (c) evolution of C_u with d_{max} across all scaled samples.

The determination of maximum ($\gamma_{d_{max}}$) and minimum ($\gamma_{d_{min}}$) dry densities was conducted according to DIN 18126 standard for all the scalped PSDs having $d_{max} \leq$ 60 mm. Three mold diameters of $\varnothing$ =250, 150 and 100 mm were used based on the corresponding d_{max} of 60 & 30, 20 & 11 and 6.3 & 4 mm, respectively. To obtain $\gamma_{d_{max}}$, dry samples were placed in the molds with a scoop, gently enough to minimize particle rearrangement and densification. The mold was then fixed on the shaking table shown in *Figure* 6.3a, and a vertical spring load was applied to the sample (see *Figure* 6.3b). The densest state was attained by vibrating the table at a frequency of 1.66 ± 0.1 Hz for 5 minutes. Each PSD was tested three times using

virgin material. After each trial, three separate settlement values were recorded, cumulating nine distinct measurements for each PSD. Finally, the mean values were used to obtain $\gamma_{d_{max}}$.

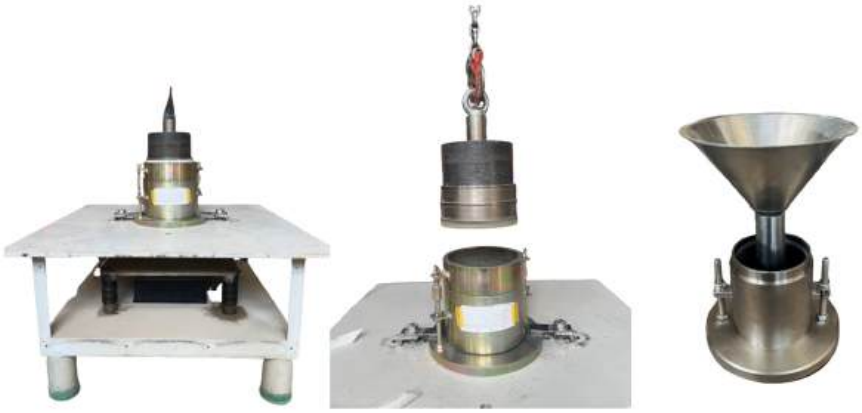

(a) (b) (c)

Figure 6.3 Experimental setup for maximum and minimum densities: (a) shaking table for $\gamma_{d_{max}}$ determination; (b) spring load showcase for $\varnothing = 150\ mm$ mold; (c) $\gamma_{d_{min}}$ determination setup for samples with $d_{max} \leq 6.3\ mm$.

The materials used for $\gamma_{d_{max}}$ determination were subsequently reused to obtain $\gamma_{d_{min}}$, in order to account for any potential degradation of the particles. For samples tested with $\varnothing = 250$ and 150 mm molds, the loosest configuration was achieved by gently placing dry material into the mold using a scoop. For samples tested with the $\varnothing$ =100 mm mold, a funnel was used instead of the scoop (see Figure 6.3c). The funnel was positioned by the bottom of the mold and the material was gradually poured. Six separate trials were repeated for each PSD sample. $\gamma_{d_{min}}$ was then calculated using the mean values. The values of $\gamma_{d_{max}}$ and $\gamma_{d_{min}}$ of each PSD are plotted in *Figure* 6.4a. The results show increasing density with d_{max}, with coarser samples (better graded) reaching denser packings. The corresponding maximum (e_{max}) and minimum (e_{min}) void ratios were subsequently calculated, and the Density Index (I_D) was obtained as

$$I_D = \frac{e_{max} - e}{e_{max} - e_{min}}$$

As proposed by Biarez and Hicher (1997) and displayed in *Figure* 6.4b, e_{max} and e_{min} correlate with particle roundness, showing relatively stable values beyond $C_u \geq 10$.

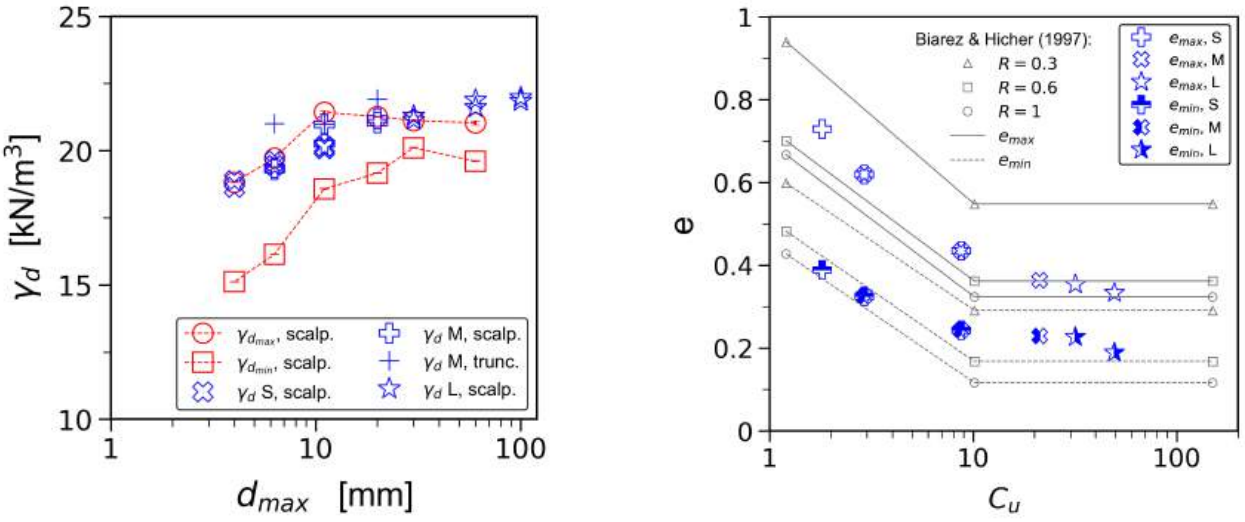

(a) (b)

Figure 6.4 Packing properties for all scaled materials: (a) $\gamma_{d_{max}}$ and $\gamma_{d_{min}}$ (mean from 9 distinct values for $\gamma_{d_{max}}$ and 6 values for $\gamma_{d_{min}}$); (b) comparison with the correlations of Biarez and Hicher (1997).

6.2.3 Triaxial testing program

A detailed summary of 21 tests is listed in *Table* 6.1, showing 6 S samples, 9 M samples and 6 L samples. All samples have a height-to-diameter ratio of H/D=1 and lubricated end platens to minimize heterogeneous strain fields. The tests involved monotonic triaxials on saturated dense samples, under consolidated drained conditions.

Table 6.1 Summary of the triaxial tests performed

Sample ID	**D** (mm)	**Scaling**	d_{max} (mm)	C_u	γ_d (kN/m^3)	e (-)	σ'_3 (kPa)	E_{50} (MPa)	ϕ'_p (°)	ϕ'_{cr} (*) (°)	ψ_{max} (°)	e_{cr}(*) (-)
S1	100	Scalping	4	1.8	18.64	0.43	100	56.2	47.0	39.2	21.0	0.57
S2			6.3	2.9	19.45	0.37	100	60.2	46.5	38.5	21.4	0.50
S3			11	8.7	20.15	0.32	100	61.9	48.6	40.3	21.1	0.42
S4			4	1.8	18.88	0.41	600	199.2	42.9	37.1	12.6	0.48
S5			6.3	2.9	19.61	0.36	600	180.7	42.8	38.0	11.9	0.41
S6			11	8.7	20.17	0.32	600	149.0	44.1	40.0	10.7	0.35
M1	150		6.3	2.9	19.31	0.38	100	63.7	48.5	40.6	20.0	0.48
M2			11	8.7	20.26	0.32	100	56.8	48.8	41.7	19.8	0.36
M3			20	21.2	21.18	0.26	100	83.7	49.6	40.1	21.1	0.33
M4			6.3	2.9	19.37	0.38	600	163.1	42.6	36.8	12.2	0.43
M5			11	8.7	20.98	0.27	600	187.1	43.5	38.4	11.6	0.30
M6			20	21.2	21.05	0.27	600	191.0	44.0	38.9	11.1	0.29
M7		Truncation	6.3	46.0	21.00	0.27	100	45.9	47.3	42.9	19.7	0.33
M8			11	46.0	20.98	0.27	100	68.0	49.0	42.0	18.1	0.34
M9			20	15.9	21.91	0.22	100	77.5	50.4	42.6	16.2	0.26
L1	800	Scalping	30	31.7	21.29	0.25	100	80.4	50.0	44.9	14.2	0.28
L2			60	49.3	21.62	0.23	100	92.8	47.6	44.9	11.9	0.24
L3			100	57.3	21.98	0.21	100	58.3	49.4	46.6	13.2	0.23
L4			30	31.7	21.15	0.26	600	263.1	45.5	42.4	8.4	0.27
L5			60	49.3	21.89	0.22	600	206.6	46.3	41.8	8.8	0.23
L6			100	57.3	21.85	0.22	600	228.0	44.6	42.1	9.9	0.22

(*) estimated critical state values.

- **S samples, D =100 mm**

As indicated in *Table* 6.1, all S samples were prepared using scalped materials. End platens were lubricated using silicon grease, as displayed in Figure 6.5a. Samples were prepared at a dense state by mounting six distinct layers of homogeneous dry material, each one with a mass around $\sim 285g$, and compacted using standard Proctor hammer blows to attain a targeted thickness. Due to the different PSDs, γ_d for each sample varied slightly between 18.64 and 20.15 kN/m^3, as displayed in *Figure* 6.4a and *Table* 6.1. However, I_D remained above 0.9 for all samples.

After flushing the sample for a minimum of one hour, saturation started by gradually raising the back pressure (σ_{cp}). After 24 hours, the Skempton coefficient ($B = \delta u/\delta\sigma_3$, where u is pore pressure) was checked and a sample was deemed fully saturated when $B \geq$ 0.95.

Isotropic consolidation started by maintaining a desired effective confining stress ($\sigma'_3 = \sigma_3 - \sigma_{cp}$), until the volumetric strain (ε_v) was stabilized. Two σ'_3 of 100 and 600 kPa were

considered in this study. Lastly, the shear stage was performed at constant vertical strain rate of 0.10 mm/min, and deviatoric stress ($q = \sigma'_1 - \sigma'_3$) was monitored until an axial deformation (ε_a) of 24%.

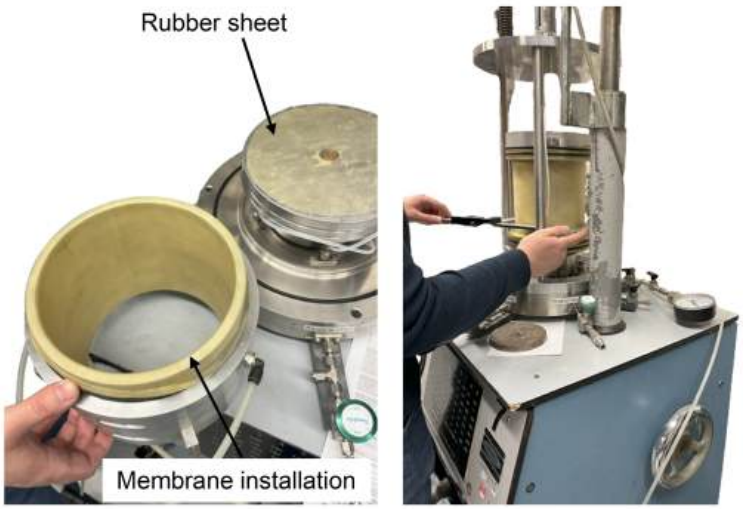

(a) (b)

Figure 6.5 S & M tests setup: (a) test base preparation; (b) sample dimension measurements.

- **M samples, D =150 mm**

A similar protocol described previously for S samples was followed for M samples. For comparison, 6 tests were accommodated using materials prepared with the scalping grading method, and three by the truncation technique (see *Table* 6.1); $\sigma'_3 = 100$ and 600 kPa were used for scalped samples ($C_u = 2.9-21$), and only $\sigma'_3 = 100$ kPa was considered on truncated samples having $C_u = 15.9 - 46$. Dense M samples were mounted in eight dry homogeneous layers and compacted using a standard Proctor hammer. Each layer had a mass of $\sim 675g$ and $\sim 725g$ for scalped and truncated samples, respectively. Due to diverse C_u values of the tested materials, the attained γ_d varied between 19.31 and 21.18 kN/m^3 for scalping, and 20.98 and 21.91 kN/m^3 for truncation (see *Figure* 6.4a); $I_D \geq 0.9$ was also achieved in all M cases. The saturation stage proceeded and samples were deemed fully saturated when $B \geq 0.95$, usually after 48 to 72 hours. samples were then consolidated at a targeted σ'_3, and sheared at a constant rate of ~ 0.14 mm/min up to $\varepsilon_a = 24\%$.

- **L samples, D =800 mm**

Figure 6.6 illustrates the triaxial test setup for L samples. 6 materials with C_u between 32 and 57 were scalped and tested at σ'_3 =100 and 600 kPa. The total mass of L samples was approximately 900 kg. The base was lubricated with silicon grease and a rubber sheet was added (see *Figure* 6.6a). A $5mm$ thick membrane was then installed in the mold (*Figure* 6.6b), as well as metal plates to protect it from puncturing during compaction (*Figure* 6.6c). A thin sand layer was added to improve the saturation through the porous stone (*Figure* 6.6c). Dense samples were prepared using 8 homogeneous layers of dry material, each weighing around $\sim 110kg$. Compaction was done for each layer using a vibrating tamper (see *Figure* 6.6d) until a thickness of 10 cm was reached. Before adding subsequent layers, the top surface was scratched to ensure contact homogeneity. At the mid-height (before adding the 5^{th} layer), density was checked to verify if the sample respected the targeted γ_d. In case of non-compliance, the mold containing the 5 layers was transported to the triaxial device pedestal to apply static compaction using the built-in hydraulic jack. Then, it was returned for the completion of the remaining layers. After the material was filled, the metal plates were removed from the mold.

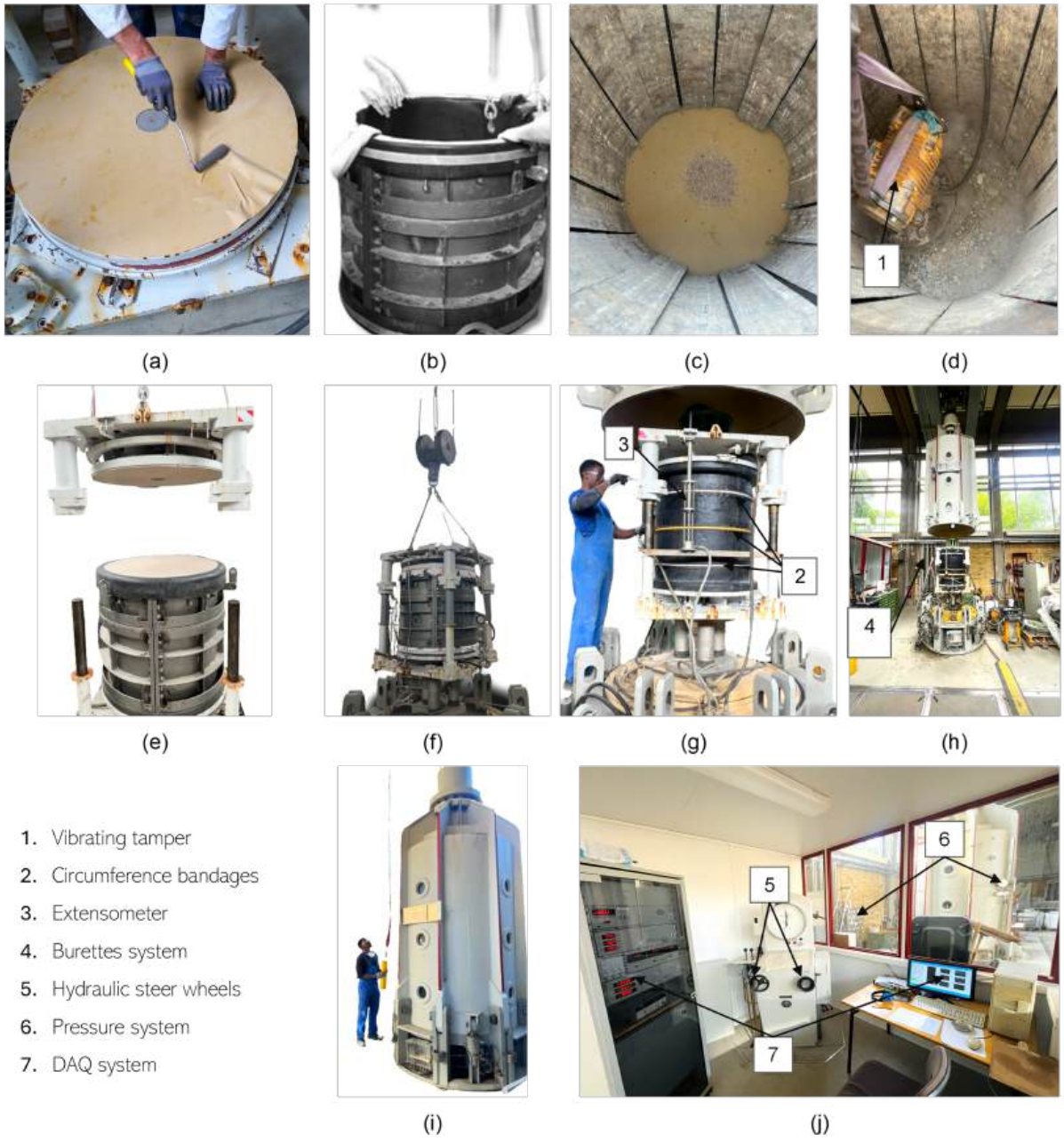

Figure 6.6 Setup of L samples: (a) adding rubber to the lubricated base platen; (b) membrane installation; (c) installing membrane protection plates and sand layer at the center to protect drainage; (d) filling the material inside and compacting; (e) adding a sand layer to level the top surface; (f) sample transportation to the testing pedestal; (g) placing circumference bandages and vertical displacement extensometers; (h) installing the cell; (i) sample ready for testing; (j) data acquisition system.

In all L samples, the attained γ_d varied between 21.15 and 21.98 kN/m^3. Thus, $I_D \geq 0.9$

was achieved in materials having d_{max} = 30 and 60 mm, as in S and M samples. After the results shown in *Figure* 6.4a, it is assumed that PSDs with d_{max} =100 mm reached similar I_D, since equivalent particle shapes are involved and the same compaction method was used. A 2 cm thick layer of sand was added on top of the last layer, to level the top surface and prevent imperfections (see *Figure* 6.6e). As shown in *Figure* 6.6f, the sample was then transferred to the testing pedestal, where the mold was removed after applying vacuum (∼90 kPa) to hold the sample. Initial measurements of the sample height at three positions were taken, as well as sample diameters at the top, middle and bottom levels. Also, circumference bandages were added on the top, middle and bottom of the sample, to track radial strain measurements (ε_r) during isotropic consolidation and shearing. In addition, three vertical displacement extensometers were positioned for ε_a measurements (*Figure* 6.6g).

Figure 6.6h presents the installation of the cell, with a built-in hydraulic system that allows the cell to close properly and apply deviatoric stress; the final installation step is shown in *Figure* 6.6i. Finally, the cell was filled with water for about 2 hours. Upon completion, the vacuum was gradually removed, while simultaneously applying a cell pressure of 100 kPa to hold the sample. The saturation step was followed by filling water during 24 $hours$ inside the sample, from bottom to top using a burette system.

In contrast with S and M samples, where the B value check was used to assess the saturation degree, "full saturation" was assumed for L samples when water flew out from the sample via a clear vinyl hose that had been attached for this end. The uncertainty in the B value for the L-samples could not be resolved experimentally. However, this is expected to have a minimal influence on the results of the drained triaxial tests, since the volumetric strain is measured using local bandages (refer to *Figure* 6.6g), which are not affected by the volumetric changes in the gas (air) that would influence a global measurement. Additionally, the drained nature of the tests prevents the generation of excess pore water pressure, further minimizing the impact of this uncertainty. L-samples were subsequently consolidated at the desired σ'_3, after which shearing proceeded at a constant rate of 0.4 mm/min. The data acquisition system (DAQ) involved a computer that recorded automatically and continuously the applied q, ε_a (through vertical extensometer readings) and σ'_3 from the pressure sensor (see *Figure* 6.6j). The readings from the circumference bandages were done manually every 5 min, and data were updated in the computer until $\varepsilon_a \sim 15\%$ was reached (around 5 $hours$).

6.3 Results

Stress-strain responses in terms of the stress ratio q/p' (p' being the mean effective stress given by $p' = (\sigma'_1 + 2\sigma'_3)/3$) are plotted against ε_a for all the materials tested; S, M and L samples are displayed in *Figures* 6.7, 6.8 and 6.9, respectively. Continuous lines designate scalped samples and dashed or pointed lines indicate truncated samples. Strain relationships represented by the volumetric strain (ε_v) plotted against ε_a are equally shown in the same figures. It is noteworthy to recall that ε_v was measured directly from drained water during shearing in S and M samples, while ε_v in L samples was estimated from ε_r readings as

$$\varepsilon_v = 1 - (1 - \varepsilon_a)(1 - \varepsilon_r)^2$$

All tests showed hardening and peak q/p' values, which were recorded around $\varepsilon_a = 3\%$ and 6% for σ'_3 =100 and 600 kPa, respectively. Softening regime followed after peak, converging toward ultimate q/p' values at large strains beyond $\varepsilon_a \geq 13\%$. As expected, peak shear strength and dilatancy decrease with σ'_3. Normalized shear strength q/p' at large strains tends to similar values for a given sample size, which is expected since the samples have equivalent relative densities and the same characteristic particle shape. All samples displayed dilatant behavior as early as $\varepsilon_a \sim 1\%$ for $\sigma'_3 = 100$ kPa, and $\varepsilon_a \sim 3\%$ for $\sigma'_3 = 600$ kPa. Interestingly, in all the cases volumetric dilatancy decreases with increasing C_u, which is a well reported observation in the literature (Ahmed et al., 2023; Muir Wood & Maeda, 2008; Yang & Luo, 2018). The maximum ε_v attained on scalped samples varied with size and σ'_3; on average, $\varepsilon_v \sim$ -11%, -8% and -3% at $\sigma'_3 = 100$ kPa, and $\varepsilon_v \sim$ -5%, -5% and -3% at $\sigma'_3 = 600$ kPa, for S, M, and L samples, respectively.

Selected S and M samples were sieved after testing to compare the amounts of particle crushing at $\sigma'_3 = 600$ kPa. The results are shown in *Figure* 6.10. In general, changes in PSD after testing are mostly not significant and particularly negligible in size fractions coarser than 1 mm. Moreover, increasing of the mass of the finest fractions are less than 5 %. The Marsal's breakage index (B_g) was computed, defined as the sum of the positive differences between the total retained percentage on each size fraction before and after a test (Marsal, 1967). B_g at $\sigma'_3 = 600$ kPa on S samples was twice higher than B_g in M samples. This is probably related to crushing promoted by more angular particle shapes in finer samples, as well as more uniform grading.

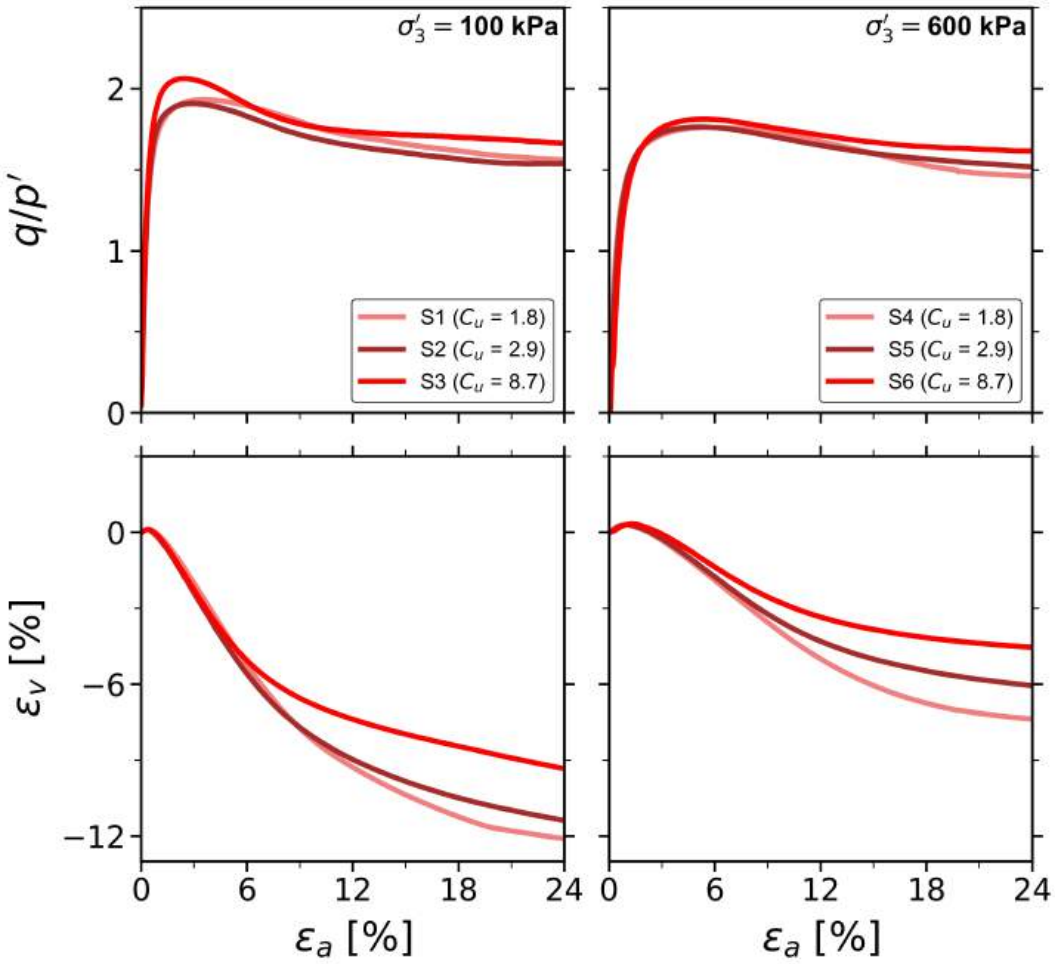

Figure 6.7 Stress-strain curves of S samples: (a) q/p' vs ε_a; (b) ε_v vs ε_a.

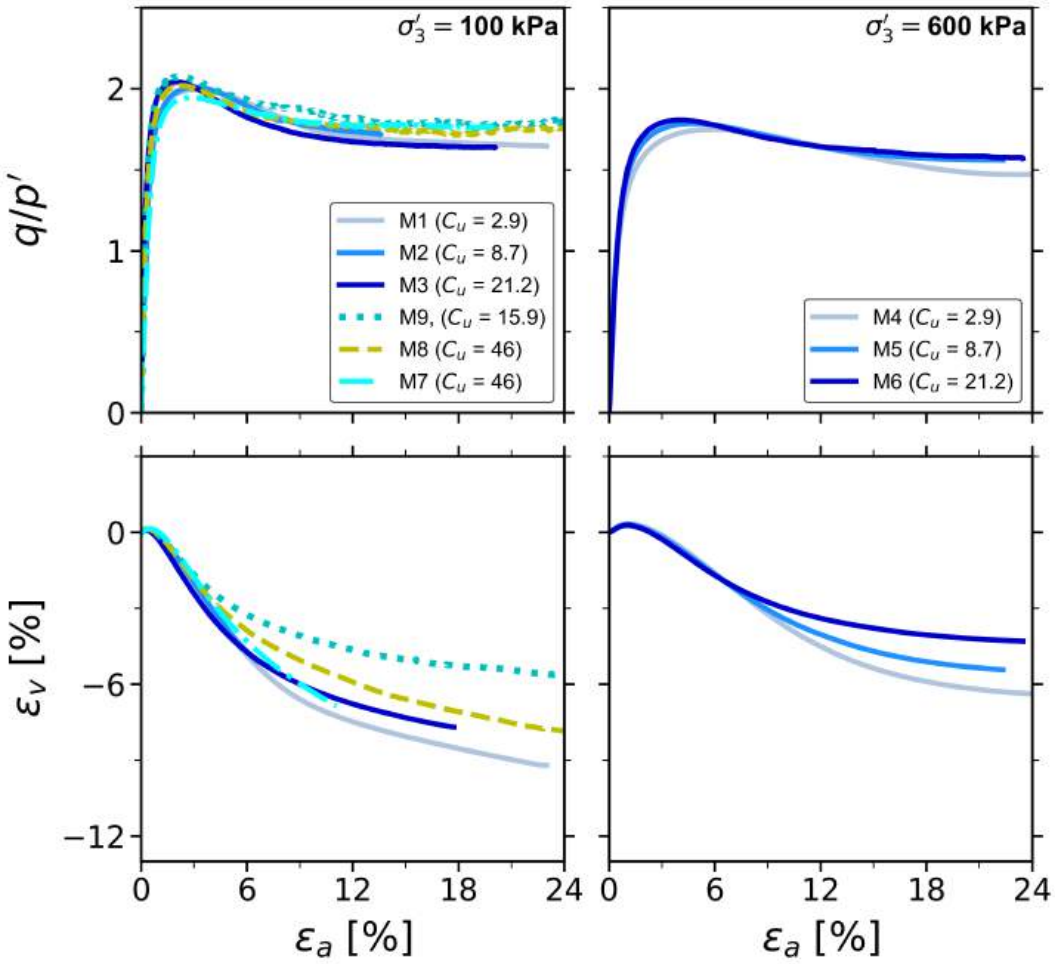

Figure 6.8 Stress-strain curves of M samples: (a) q/p' vs ε_a; (b) ε_v vs ε_a.

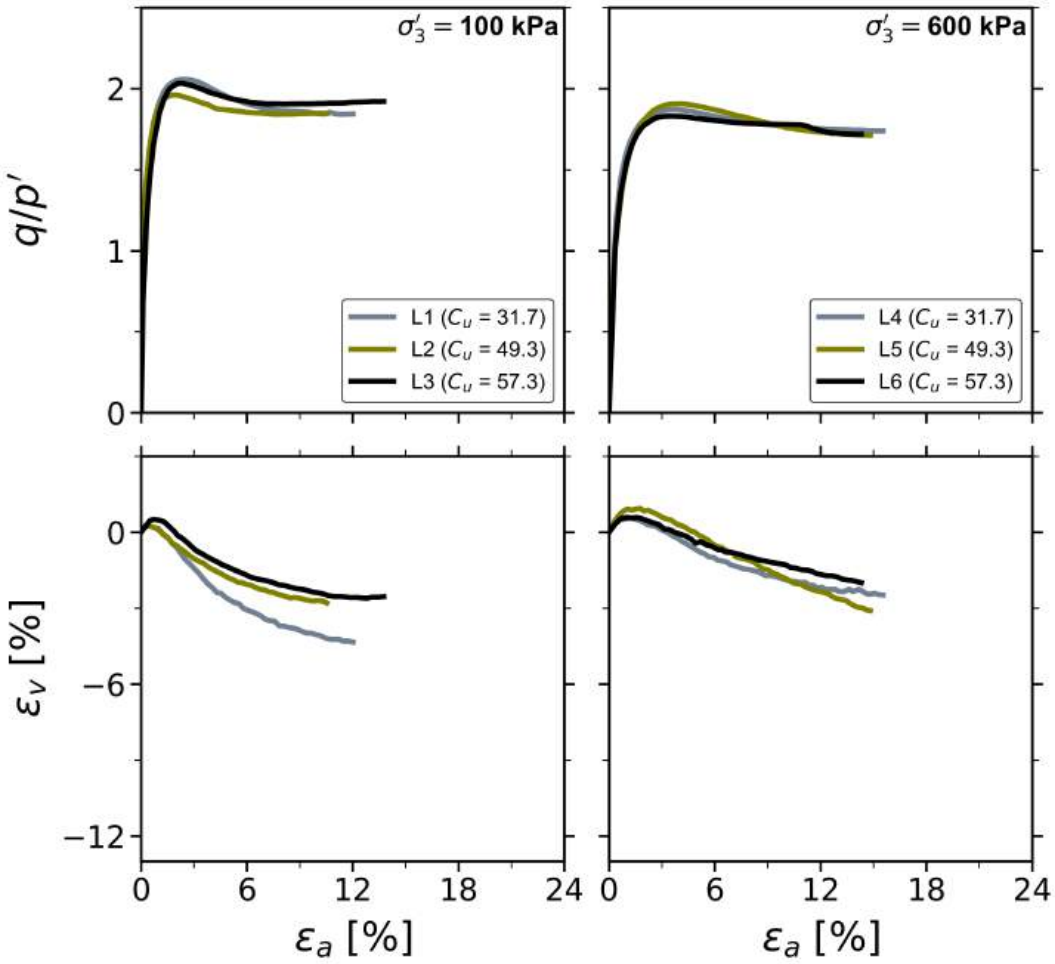

Figure 6.9 Stress-strain curves of L samples: (a) q/p' vs ε_a; (b) ε_v vs ε_a.

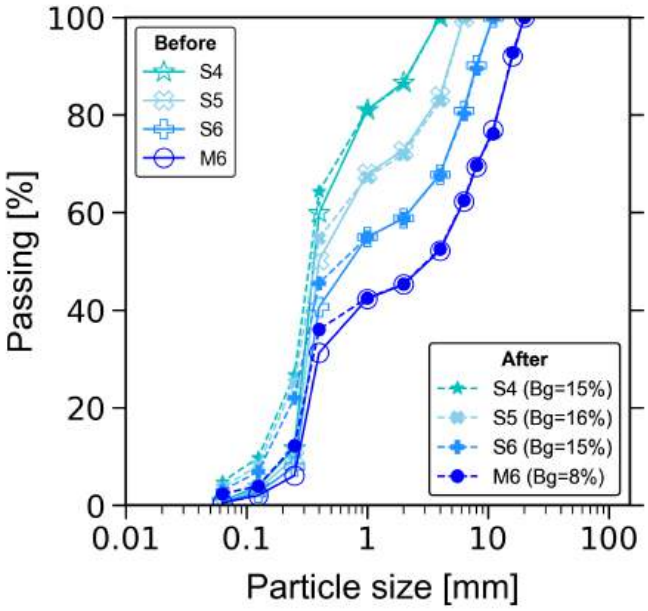

Figure 6.10 Initial and final PSD comparison for particle breakage quantification.

6.4 Analysis and Discussion

6.4.1 *Dilatancy*

The maximum dilatancy angle (ψ_{max}) mobilized is defined as (Schanz & Vermeer, 1996):

$$sin\psi_{max} = \frac{-(d\varepsilon_v/d\varepsilon_a)_p}{2-(d\varepsilon_v/d\varepsilon_a)_p}$$

where $(d\varepsilon_v/d\varepsilon_a)_p$ is the dilatancy ratio at the peak deviatoric stress. ψ_{max} is plotted in *Figure* 6.11 against C_u for all the tests carried out. The results are arranged for each σ_3' and sample size with distinct colors and markers. One can clearly observe that, regardless of the scaling technique (scalping or truncation), ψ_{max} decreases with C_u. This tendency is more marked and more scattered at lower pressure (i.e., 100 kPa). On average, ψ_{max} mobilized were $21.1°, 20.3°$ and $13.1°$ at $\sigma_3' = 100$ kPa, and $11.7°, 11.6°$ and $8.8°$ at $\sigma_3' = 600$ kPa, on S, M and L scalped samples, respectively.

These findings are consistent with previous research suggesting that, under a given shearing stress path and relative density, volumetric dilatancy decreases with grain size polydispersity (Ahmed et al., 2023; Amirpour Harehdasht et al., 2017; Cantor et al., 2018; Deng et al., 2021; Yan & Dong, 2011; Yang & Luo, 2018; Zhang et al., 2024). This is because more diverse pore sizes allow for more efficient packing, enabling easier rearrangement and filling with varying

grain sizes. On the other hand, relatively large volume of pores in uniformly graded soils lead to high volume changes upon dilation. Therefore, since small-scaling will generally generate a more uniformly graded sample, it is worth noting that the use of small-scale dense samples gives values of the volumetric deformation that should be considered non-conservative in geotechnical designs.

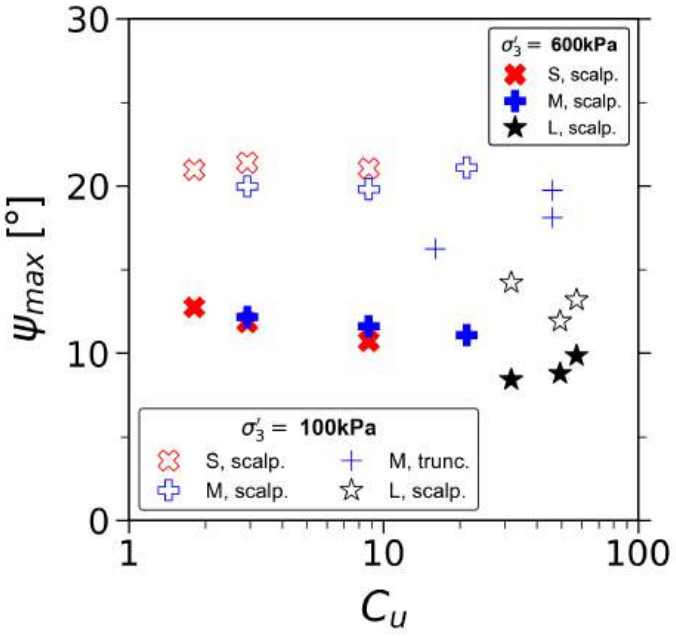

Figure 6.11 Dilatancy angle ψ_{max} against C_u for all samples.

6.4.2 *Secant Strain Modulus*

The characteristic stiffness of the samples was analyzed based on E_{50}, defined as the secant strain modulus at 50% of the peak deviatoric stress (q_{max}):

$$E_{50} = \frac{0.5 q_{max}}{\varepsilon_{a-q_{max}}}$$

Figure 6.12 presents E_{50} against C_u for all the tests in this study. Combining all the C_u values for each sample size, the average modulus of scalped samples is around $E_{50} = 59,\ 68$ and 77 MPa for $\sigma'_3 = 100$ kPa, and $E_{50} = 76,\ 180$ and 233 MPa at 600 kPa, on S, M and L samples, respectively. This suggests that for all σ'_3 used, L samples exhibit around 15 to 30% higher strain moduli compared to S and M samples. Therefore, small-scaling results in conservative values compared to the coarser material stiffness.

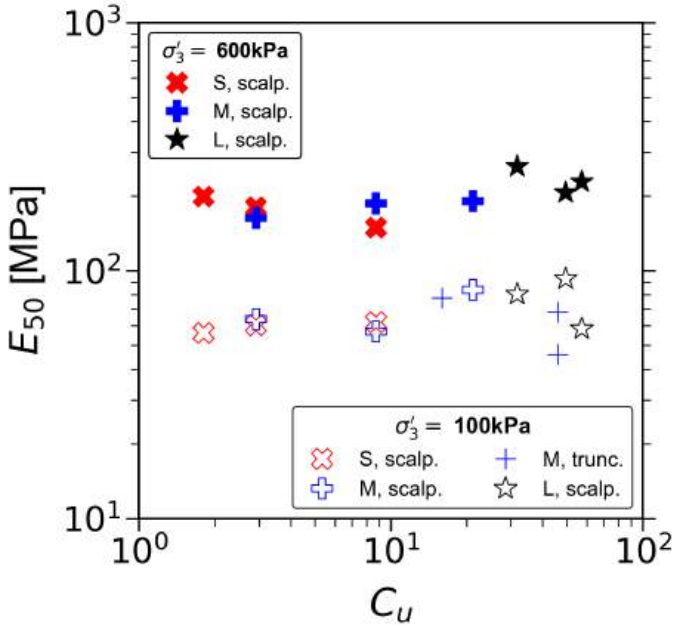

Figure 6.12 Secant strain modulus E_{50} against C_u for all samples.

A comparison of E_{50} with data of coarse rockfills ($d_{max} = 100 - 200\ mm$, from blasted and quarried rocks) compiled in Ovalle et al. (2020) is presented in *Figure* 6.13. Empirical relationships for quartz sands proposed by Schanz and Vermeer (1998) are also included. One can observe that the tested alluvial gravels exhibited much higher E_{50} than coarse rockfills, aligning with reported data on diverse gravel materials from several authors (Liu et al., 2016; Verdugo & de la Hoz, 2007; Wang et al., 2022). This is mainly due to enhanced particle crushing of highly angular rock grains and relatively weak crushed rock particles resulting from blasting. On the other hand, alluvial and fluvial gravels are typically composed by strong eroded particles.

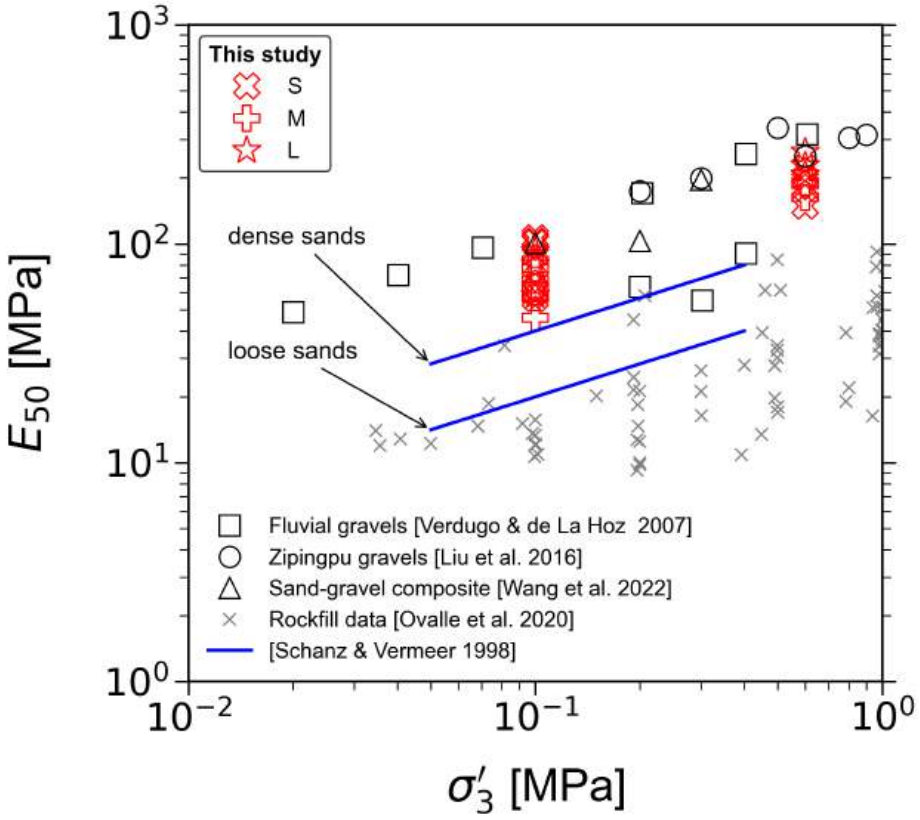

Figure 6.13 Comparison of E_{50} with reported triaxial data on rockfill and gravel materials, as a function of σ'_3.

6.4.3 *Shear Strength*

The shear strength was assessed as the mobilized effective friction angle (ϕ'), estimated according to the Mohr-Coulomb failure criterion for non-cohesive materials:

$$sin\phi' = \frac{3M}{6+M}$$

where M is q/p' at the maximum strength for the peak friction angle (ϕ'_p), and at the steady state for the critical friction angle (ϕ'_{cr}). The dilatant dense samples did not fully reach critical state, particularly in terms of volumetric strains. However, ϕ'_{cr} was assumed to mobilize at the largest vertical strain in each test, since the results in terms of q/p' are reasonably stable after $\varepsilon_a = 12\%$. For all the scalped samples at $\sigma'_3 = 100$ kPa, *Figure* 6.14 shows that ϕ'_p varied between 46.5° and 50.0°. For different sample sizes, the average ϕ'_p varied in the order S < M ≈ L, with less than 2° of dispersion around the mean value. Similar observations are found at $\sigma'_3 = 600$ kPa, with ϕ'_p ranging between 43.3° to 45.5°, and the average values in

the order S ≈ M < L. In other words, within the scope of the investigated grading methods and sample sizes, the tested alluvial gravels presented a slight size effect on ϕ'_p, where the small-scale samples exhibit lower strength values than coarser materials.

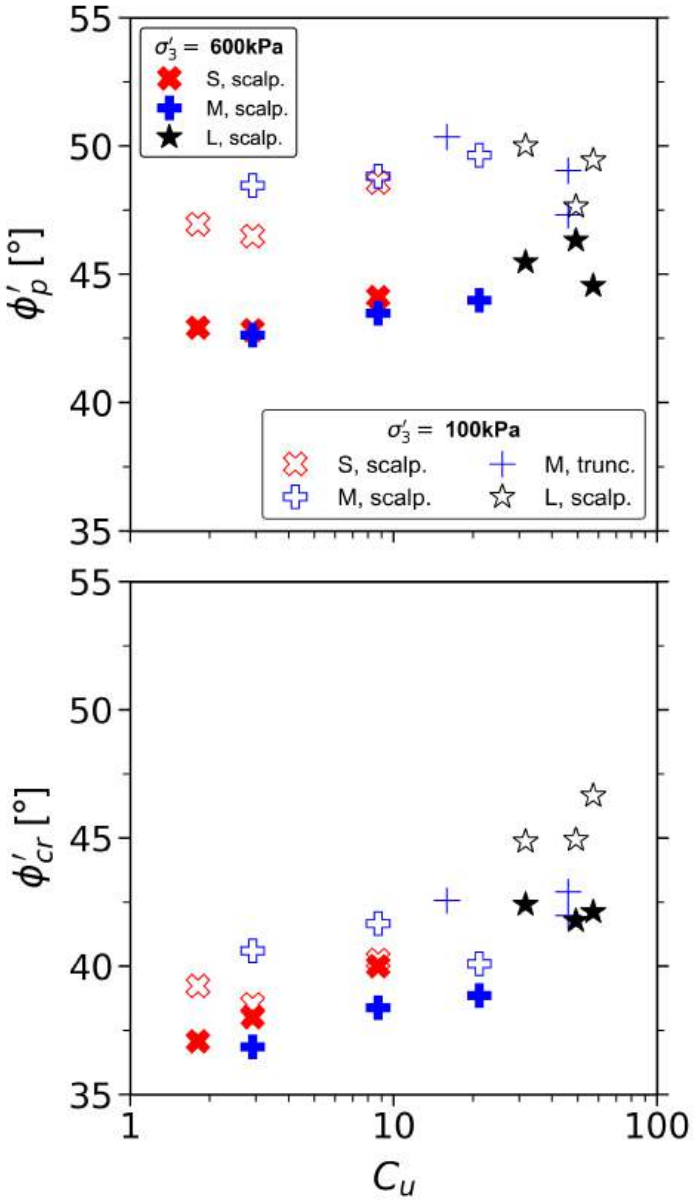

Figure 6.14 Sample size and grading effects on effective friction angles: ϕ'_p vs C_u (top) and (bottom) ϕ'_{cr} vs C_u.

Figure 6.14 also shows that ϕ'_{cr} has remarkable variations across the samples sizes and C_u, with averages values of around 39.3°, 40.8° and 45.5° at $\sigma'_3 = 100$ kPa, and 38.4°, 38.0° and 42.1° at $\sigma'_3 = 600$ kPa, for S, M, and L samples respectively. Presumed causes for such results are

proposed: (1) particle shape-size correlation shown in *Figure* 6.1c could strongly affect ϕ'_{cr}, as reported by Ovalle and Dano (2020) after large triaxial tests and by Carrasco et al. (2023) using DEM simulations; (2) samples did not fully attain the critical state conditions at the reached ε_a levels; (3) the strain fields of the samples at post-peak states might have impacted the mobilized stresses due to localized deformations. Indeed, as presented in *Figure* 6.15, a visual inspection of photos taken at the end of each test attests to different deformation modes, particularly some samples experiencing overexpansion at the top or at the bottom section. The observed heterogeneous strain fields suggest that end-restraint effects are not overcome by using lubricated plates in such strong soils. The high frictional stresses mobilized by coarse soils might require increased slenderness to avoid this effect. Consequently, in this case the critical state strength can only be considered as an estimated value.

S3, $d_{max} = 11$ mm

M3, $d_{max} = 20$ mm

L3, $d_{max} = 100$ mm

S6, $d_{max} = 11$ mm

M6, $d_{max} = 20$ mm

L5, $d_{max} = 60$ mm

Figure 6.15 Sample photos after tests: from left to right S, M & L samples, and top to bottom $\sigma'_3 = 100$ kPa & 600 kPa, respectively.

Excess friction angle, defined as $\phi'_p - \phi'_{cr}$, was correlated with ψ_{max} and compared with the expression proposed by Bolton (1986):

$$\phi'_p = \phi'_{cr} + K\psi_{max}$$

where K is an empirical parameter for a given soil (i.e., constant C_u). *Figure* 6.16 shows that $K = 0.48$, proposed by Bolton for uniform dense sands, overestimates the well graded alluvial gravels presented here (M and L). Also, data on gravel materials from the literature (Strahler et al., 2016; Xiao et al., 2014, 2016) is included for comparison, showing that the results of this study are within reported values of K = 0.21 to 0.58.

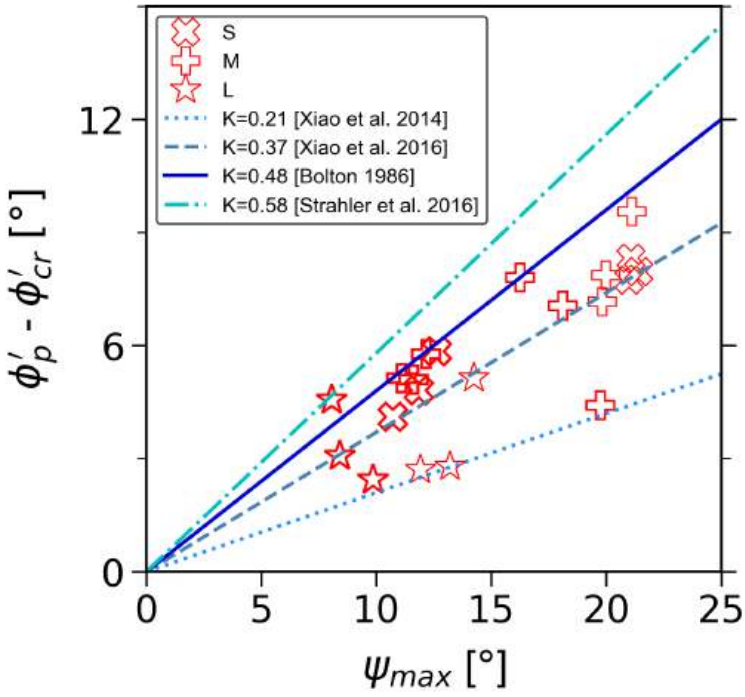

Figure 6.16 Comparison of the excess friction angle with reported values in gravels.

6.4.4 *Critical State*

Figure 6.17 presents the stress deformation path in the $e-p'$ space for all the tests carried out in this study. Although steady states were not reached completely in the tests, the critical state lines (CSL) were drawn simply by estimating the critical void ratios (e_{cr}) at the largest deformation reached in each test, in order to perform a comparative analysis. In the set of three plots presented in *Figure* 6.17, C_u for a given sample size (S, M or L) decreases from left to right. As a consequence, the volumetric dilatancy increases significantly, particularly in S samples (red marks in *Figure* 6.17). The same tendency is observed within a single plot showing different sample sizes; i.e., the lower the C_u, the higher e_{cr} and the volumetric dilatancy. This is also shown in *Figures* 6.7 to 6.9 in terms of volumetric strains. As a result, the CSL is dragged down in the volume-stress space once C_u increases, consistently with the well-known PSD effects on critical state. Also, the slope of the CSL evolves, which might be affected by diverse properties, such as initial density, particle shape varying across grain sizes and heterogeneous strain fields at large strains. To highlight the evolution of the critical state with grading, *Figure* 6.18 shows e_{cr} as a function of C_u for all tests, where the values distinctly decrease as the materials become better graded. Two fitted power laws correspond to the sets of tests at different confining pressures $\sigma'_3 = 100$ and 600 kPa, which closely match

the experimental data.

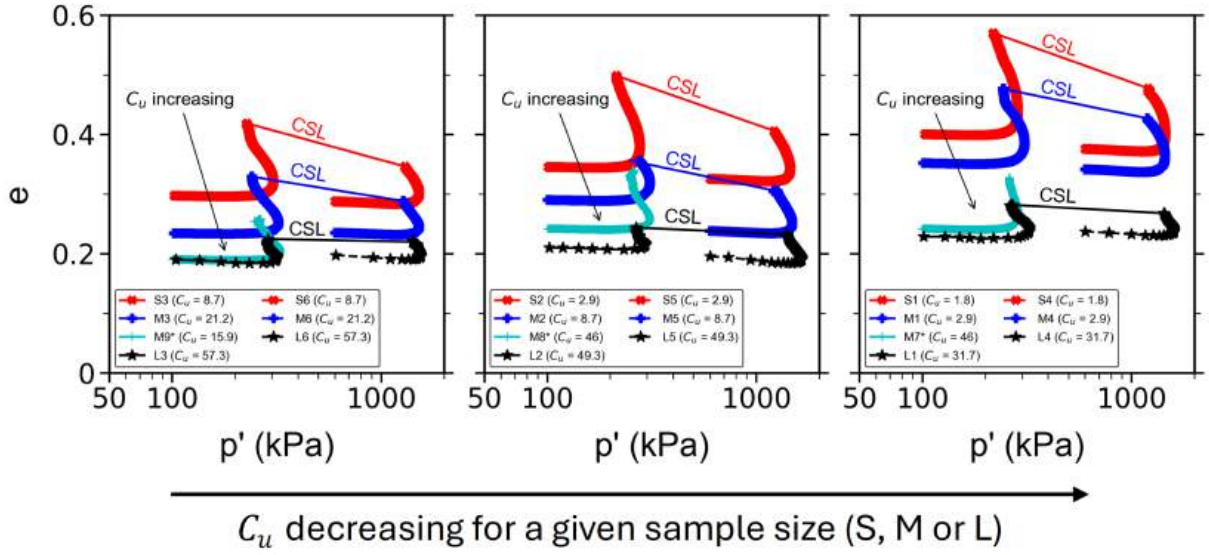

Figure 6.17 Dilatancy paths in $e - p'$ space and estimated CSL for all the tests.

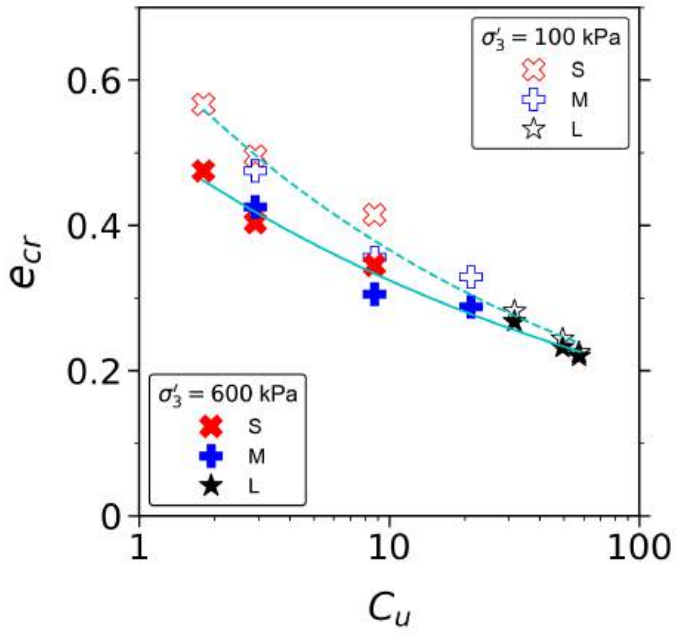

Figure 6.18 Estimated critical state void ratio e_{cr} vs C_u for all the tests on scalped samples (dashed and solid lines for power fitting of tests at $\sigma'_3 = 100$ and 600 kPa, respectively).

6.5 Conclusions

In order to assess the impacts of small-scaling and grading on the mechanical behavior of coarse soil, 21 monotonic triaxial tests were carried out on dense alluvial gravel materials under consolidated drained conditions. A field soil with a maximum grain size of 125 mm was sampled and small-scale specimens were prepared using scalping grading and truncation techniques, with C_u spanning between 1.8 to 57.3. The testing program involved 3 devices with distinct diameters: S samples of $D = 100$ mm, M samples of $D = 150$ mm, and L samples with $D = 800$ mm. The results were evaluated in terms of dilatancy, strain modulus, peak shear strength and critical states. The following conclusions can be drawn from this research:

- Since scaling granular soils entails the reduction of the grain size, grading and packing properties differ at each scale level. As a result, it is crucial to determine particle size distributions and standard maximum and minimum densities for all sample sizes generated during scaling. This provides reference values and enables the preparation of samples at equivalent relative densities. A meaningful comparison across different scales is only possible when state conditions remain equivalent. However, the lack of standardized methods for evaluating the relative densities of oversized soils necessitates result extrapolation.

- Scaling a coarse material results in a more uniformly graded smaller sample, which affects its volumetric dilatancy. Due to grading effects, dense small-scale samples at equivalent density indexes exhibit higher dilatancy and critical state void ratio than the original coarse soil. This effect should be taken into account when calibrating and modeling based on scaled parameters.

- While volumetric dilatancy increases in small-scale samples, their peak strength decreases compared to the coarser material. In this study, at the same relative density, small-scale samples show 3° to 4° decrease in the effective peak friction angle. Therefore, using small samples represents a conservative approach in terms of strength. However, this trend could be reversed if the amount of particle crushing becomes significant, due to size effects on particle fragmentation resistance. The latter is more likely in blasted and crushed rockfill than in eroded alluvial material, such as the samples tested in this study.

- Particle shape can significantly influence the results of small-scale tests on granular soils. When modifying grading after reducing the particle size, it is important to measure

grain shapes across all grain sizes involved and compare them with the original coarse soil being scaled. Drastic variations in the characteristic shapes between the coarse and fine fractions of the same soil could affect the representativeness of the scaled samples, as particle shapes are known to have a substantial impact on the mechanical behavior of soils.

Summarizing, the results presented here on dense small-scale alluvial gravel, across 3 different sample sizes and 10 distinct particle size distributions, provide insights into the impacts of scaling coarse gravels. It has been highlighted that scaling methods have limitations due to the intrinsic properties of the soil, such as grading, packing conditions and grain shapes. However, understanding these limitations can help make realistic and conservative assumptions when characterizing oversized materials in the field, particularly when large-scale testing is unavailable and geotechnical designs must rely on scaled parameters. These uncertainties are notably relevant when using data from small samples to capture the behavior of oversized soils, particularly in constitutive models developed to represent stress-strain behavior. In these models, dilatancy often serves as a crucial criterion that greatly impacts the conclusions derived from the modeling. Therefore, special caution is necessary to avoid overestimating or underestimating limit states, while taking into account a realistic particle size distribution wherever possible.

Many uncertainties remain regarding the effects of small-scale testing. Future research directions include studying size effects on granular materials with non negligible fine fractions ($< 80\mu m$), incorporating loose conditions, analyzing different stress paths and investigating materials that are highly sensitive to particle crushing. More extensive investigations are also required to assess the different percentages of replaced coarse fraction in the truncation technique, in order to establish a threshold value that allows reliable comparison with the scalping grading method. Finally, although rare and expensive, large-scale testing will still provide valuable information that will contribute to a better understanding of coarse soils.

Bibliography

Ahmed, S. S., Martinez, A., & DeJong, J. T. (2023). Effect of gradation on the strength and stress-dilation behavior of coarse-grained soils in drained and undrained triaxial compression. *Journal of Geotechnical and Geoenvironmental Engineering*, *149*(5), 04023019.

Al-Hussaini, M. M. (1970). *The influence of end restraint and method of consolidation on the drained triaxial compressive strength of crushed napa basalt* (Miscellaneous Paper No. S-70-18). U.S. Army Engineer Waterways Experiment Station. Vicksburg, Mississippi, USA.

Al-Hussaini, M. M. (1983). Effect of particle size and strain conditions on the strength of crushed basalt. *Canadian Geotechnical Journal*, *20*(4), 706–717.

Amirpour Harehdasht, S., Karray, M., Hussien, M. N., & Chekired, M. (2017). Influence of particle size and gradation on the stress-dilatancy behavior of granular materials during drained triaxial compression. *International Journal of Geomechanics*, *17*(9), 04017077.

ASTM D2487. (2017). *Standard practice for classification of soils for engineering purposes (unified soil classification system)*. ASTM International.

Barton, N., & Kjærnsli, B. (1981). Shear strength of rockfill. *Journal of the Geotechnical Engineering Division*, *107*(7), 873–891.

Biarez, J., & Hicher, P.-Y. (1994). *Elementary mechanics of soil behaviour: saturated remoulded soils*. A.A. Balkema.

Biarez, J., & Hicher, P.-Y. (1997). Influence de la granulométrie et de son évolution par ruptures de grains sur le comportement mécanique de matériaux granulaires. *Revue française de génie civil*, *1*(4), 607–631.

Bolton, M. D. (1986). The strength and dilatancy of sands. *Géotechnique*, *36*(1), 65–78.

Brauns, J., & Kast, K. (2007). Dynamic compaction of rockfill samples. In H. I. Ling, L. Callisto, D. Leshchinsky, & J. Koseki (Eds.), *Proceedings of the 10th international conference on soil mechanics and foundation engineering* (pp. 669–671). A. A. Balkema.

Brauns, J., & Reith, H. (2000). Testing the stress-strain properties and the shear strength of rockfill material. *International Journal on Hydropower and Dams*, *7*(1), 62–63.

Cantor, D., Azema, E., Radjai, F., & Sornay, P. (2018). Rheology and structure of polydisperse three-dimensional packings of spheres. *Physical Review E*, *98*(5).

Cantor, D., & Ovalle, C. (2023). Sample size effects on the critical state shear strength of granular materials with varied gradation and the role of column- like local structures. *Géotechnique*, *75*(1), 29–40.

Carrasco, S., Cantor, D., Ovalle, C., & Dubois, F. (2025). Particle shape distribution effects on the critical strength of granular materials. *Computers and Geotechnics*, *177*, 106896.

Carrasco, S., Cantor, D., Ovalle, C., & Quiroz, P. (2023). Shear strength of angular granular materials with size and shape polydispersity. *Open Geomechanics*, *4*.

Daouadji, A., Hicher, P.-Y., & Rahma, A. (2001). An elastoplastic model for granular materials taking into account grain breakage. *European Journal of Mechanics - A/Solids*, *20*(1), 113–137.

Deiminiat, A., Li, L., & Zeng, F. (2022). Experimental study on the minimum required specimen width to maximum particle size ratio in direct shear tests. *CivilEng*, *3*(1), 66–84.

Deng, Y., Yilmaz, Y., Gokce, A., & Chang, C. S. (2021). Influence of particle size on the drained shear behavior of a dense fluvial sand. *Acta Geotechnica*, *16*(7), 2071–2088.

DIN 18126. (2022). *"baugrund, untersuchung von bodenproben-bestimmung der dichte nicht bindiger boden bei lockerster und dichtester lagerung", standard test method for minimum and maximum densities (in German)*. Deutsches Institut für Normung, Beuth Verlag GmbH.

Girumugisha, G., Ovalle, C., & Ouellet, S. (2024). Grading scalping and sample size effects on critical shear strength of mine waste rock through laboratory and in-situ testing. *International Journal of Rock Mechanics and Mining Sciences*, *183*, 105915.

Hao, S., & Pabst, T. (2023). Mechanical characterization of coarse-grained waste rocks using large-scale triaxial tests and neuroevolution of augmenting topologies. *Journal of Geotechnical and Geoenvironmental Engineering*, *149*(6).

Hassan, N. A., Nguyen, N. S., Marot, D., & Bendahmane, F. (2022). Consequences of scalping and scalping/replacement procedures on strength properties of coarse-grained gap-graded soils. *Canadian Geotechnical Journal*, *59*(10), 1819–1832.

Hettler, A., & Vardoulakis, I. (1984). Behaviour of dry sand tested in a large triaxial apparatus. *Géotechnique*, *34*(2), 183–197.

Hu, W., Dano, C., Hicher, P.-Y., Le Touzo, J.-Y., Derkx, F., & Merliot, E. (2011). Effect of sample size on the behavior of granular materials. *Geotechnical Testing Journal*, *34*(3), 186–197.

Kikumoto, M., Wood, D. M., & Russell, A. (2010). Particle crushing and deformation behaviour. *Soils and foundations*, *50*(4), 547–563.

Leussink, H. (1960). *Bau eines grossen dreiaxialen shergerätes zur untersuchung grobkörniger erdstoffe (design of a large triaxial shear apparatus for investigating coarse grained soils)* (Vol. 1). Soil Mechanics Institute of the Karlsruhe Technical University Germany.

Li, G., Ovalle, C., Dano, C., & Hicher, P.-Y. (2013). Influence of grain size distribution on critical state of granular materials. In Q. Yang, J.-M. Zhang, H. Zheng, & Y. Yao (Eds.), *Constitutive modeling of geomaterials* (pp. 207–210). Springer Berlin Heidelberg.

Linero, S., Bradfield, L., Fityus, S. G., Simmons, J. V., & Lizcano, A. (2020). Design of a 720-mm square direct shear box and investigation of the impact of boundary conditions on large-scale measured strength. *Geotechnical Testing Journal*, *43*(6).

Linero, S., Palma, C., & Apablaza, R. (2007). Geotechnical characterisation of waste material in very high dumps with large scale triaxial testing. In Y. Potvin (Ed.), *Slope stability 2007: proceedings of the 2007 international symposium on rock slope stability in open pit mining and civil engineering* (pp. 59–75). Australian Centre for Geomechanics.

Linero, S., Fityus, S., Simmons, J., Lizcano, A., & Cassidy, J. (2017). Trends in the evolution of particle morphology with size in colluvial deposits overlying channel iron deposits. *EPJ Web Conf.*, *140*, 14005.

Linero, S., Azema, E., Estrada, N., Fityus, S., Simmons, J., & Lizcano, A. (2019). Impact of grading on steady-state strength. *Géotechnique Letters*, *9*(4), 328–333.

Liu, J., Zou, D., Kong, X., & Liu, H. (2016). Stress-dilatancy of zipingpu gravel in triaxial compression tests. *Science China Technological Sciences*, *59*(2), 214–224.

Lowe, J. (1964). Shear strength of coarse embankment dam materials. *Proc., 8th Int. Congress on Large Dams*, *3*, 745–761.

Marachi, N. D., Chan, C. K., & Seed, H. B. (1972). Evaluation of properties of rockfill materials. *Journal of the Soil Mechanics and Foundations Division*, *98*(1), 95–114.

Marsal, R. J. (1967). Large scale testing of rockfill materials. *Journal of the Soil Mechanics and Foundations Division*, *93*(2), 27–43.

Matsuoka, H., Liu, S., Sun, D., & Nishikata, U. (2001). Development of a new in-situ direct shear test. *Geotechnical Testing Journal*, *24*(1), 92–102.

Muir Wood, D., & Maeda, K. (2008). Changing grading of soil: effect on critical states. *Acta Geotechnica*, *3*(1), 3–14.

Ning, F., Liu, J., Zou, D., Kong, X., & Cui, G. (2024). Super-large-scale triaxial tests to study the effects of particle size on the monotonic stress–strain response of rockfill materials. *Acta Geotechnica*.

Osses, R., Pineda, J., Ovalle, C., Linero, S., & Sáez, E. (2024). Scale and suction effects on compressibility and time-dependent deformation of mine waste rock material. *Engineering Geology*, *340*, 107668.

Ovalle, C., & Dano, C. (2020). Effects of particle size–strength and size–shape correlations on parallel grading scaling. *Géotechnique Letters*, *10*(2), 191–197.

Ovalle, C., Frossard, E., Dano, C., Hu, W., Maiolino, S., & Hicher, P.-Y. (2014). The effect of size on the strength of coarse rock aggregates and large rockfill samples through experimental data. *Acta Mechanica*, *225*(8), 2199–2216.

Ovalle, C., & Hicher, P.-Y. (2020). Modeling the effect of wetting on the mechanical behavior of crushable granular materials [Grain Crushing in Geoscience Materials]. *Geoscience Frontiers*, *11*(2), 487–494.

Ovalle, C., Linero, S., Dano, C., Bard, E., Hicher, P.-Y., & Osses, R. (2020). Data compilation from large drained compression triaxial tests on coarse crushable rockfill materials. *Journal of Geotechnical and Geoenvironmental Engineering*, *146*(9), 06020013.

Polanía, O., Cabrera, M., Renouf, M., Azéma, E., & Estrada, N. (2023). Grain size distribution does not affect the residual shear strength of granular materials: an experimental proof. *Physical Review E*, *107*(5), L052901.

Quiroz-Rojo, P., Cantor, D., Renouf, M., Ovalle, C., & Azéma, E. (2024). REV assessment of granular materials with varied grading based on macro- and micro-mechanical statistical data. *Acta Geotechnica*.

Schanz, T., & Vermeer, P. A. (1996). Angles of friction and dilatancy of sand. *Géotechnique*, *46*(1), 145–151.

Schanz, T., & Vermeer, P. A. (1998). On the stiffness of sands. In *Pre-failure deformation behaviour of geomaterials* (pp. 383–387). Thomas Telford.

Strahler, A., Stuedlein, A. W., & Arduino, P. W. (2016). Stress-strain response and dilatancy of sandy gravel in triaxial compression and plane strain. *Journal of Geotechnical and Geoenvironmental Engineering*, *142*(4), 04015098.

Varadarajan, A., Sharma, K. G., Venkatachalam, K., & Gupta, A. K. (2003). Testing and modeling two rockfill materials. *Journal of Geotechnical and Geoenvironmental Engineering*, *129*(3), 206–218.

Verdugo, R., & de la Hoz, K. (2007). Strength and stiffness of coarse granular soils. In H. I. Ling, L. Callisto, D. Leshchinsky, & J. Koseki (Eds.), *Soil stress-strain behavior: measurement, modeling and analysis* (pp. 243–252). Springer Netherlands.

Wang, X., Xu, B., Meng, X., & Fan, Q. (2022). Experimental study on the dilatancy characteristics and equation of saturated sand–gravel composites during the whole shearing process. *International Journal of Geomechanics*, *22*(3), 04021310.

Xiao, Y., Liu, H., Chen, Y., & Jiang, J. (2014). Strength and deformation of rockfill material based on large-scale triaxial compression tests. i: influences of density and pressure. *Journal of Geotechnical and Geoenvironmental Engineering*, *140*(12), 04014070.

Xiao, Y., Liu, H., Zhang, W., Liu, H., Yin, F., & Wang, Y. (2016). Testing and modeling of rockfill materials: a review. *Journal of Rock Mechanics and Geotechnical Engineering*, *8*(3), 415–422.

Yan, W. M., & Dong, J. (2011). Effect of particle grading on the response of an idealized granular assemblage. *International Journal of Geomechanics*, *11*(4), 276–285.

Yang, J., & Luo, X. D. (2018). The critical state friction angle of granular materials: does it depend on grading? *Acta Geotechnica*, *13*(3), 535–547.

Zeller, J., & Wullimann, R. (1957). The shear strength of the shell materials for the go-schenenalp dam, switzerland. *4th International Conference on Soil Mechanics and Foundation Engineering*, *2*, 399–415.

Zhang, T., Wang, Y., Zhang, C., & Wang, S. (2024). DEM investigation of particle gradation effect on the stress-dilatancy behavior of granular soil. *Advanced Powder Technology*, *35*(11), 104692.

Zheng, J., & Hryciw, R. D. (2015). Traditional soil particle sphericity, roundness and surface roughness by computational geometry. *Géotechnique*, *65*(6), 494–506.

CHAPTER 7 DISCUSSION

The summary of the findings presented in *Chapters* 4-6 is discussed in this chapter. To facilitate the discussion, it is recalled that the test results carried out at the Laboratory of Mining Environment of Polytechnique Montreal are referred to as M1 (height-to-diameter H:D =300:150 mm) and L1 (H:D =600:300 mm). Equally, the end boundary conditions of the specimens are denoted by (R) for the standard rough end platens and (L) for the enlarged-lubricated platens. Thus, M1 and L1 are discussed as M1-R, M1-L and L1-R, respectively. σ'_3 and the material are indicated; for instance, M1-R45-Sed1 designates Sed1 tested in M1-R specimen at $\sigma'_3 = 45$ kPa. On the other hand, the tests carried out at the *Institut für Bodenmechanik und Felsmechanik* (IBF) (Institute of Soil Mechanics and Rock Mechanics) at the Karlsruhe Institute of Technology in Germany, are referred to as S2-L (H:D =100:100 mm), M2-L (H:D =150:150 mm) and L2-L (H:D =800:800 mm). The following analyses and discussions are focused on characteristic mechanical parameters (strain modulus, Poisson's ratio, dilatancy, shear strength) and size effects.

7.1 Strain moduli and Poisson ratio

It has been systematically shown in *Chapter* 6 that altering the PSD impacts the stress-strain properties of soils, whereby the CSL of uniformly graded PSD is steeper and in a higher void ratio range than well-graded materials. In other words, poorly graded specimens are more compressible due to the larger pore volumes. This point is discussed here for the WR specimens tested in *Chapter* 4.

First, the variation of the secant strain modulus at a given axial strain (E_{ε_a}) is presented in *Figure* 7.1 against ε_a, from $\varepsilon_a = 0.3\%$ until E_{50}; the lower limit $\varepsilon_a = 0.3\%$ is chosen due to the low precision range of the displacement transducers used in the tests. The results are arranged based on σ'_3 and material tested: Sed1, Sed2, and PO. In a given material, the stiffness increases with σ'_3. Sed1 specimens exhibit the lowest values of E_{ε_a}, presumably due to fines content, which are restricted in Sed2 and PO. As such, the scalping grading technique by restraining the minimum particle size shows enhanced characteristic stiffness. However, one cannot discern the influence of the gradation in this figure. To do so, *Figure* 7.2 is proposed, showing the secant strain modulus at $\varepsilon_a = 0.3\%$ ($E_{\varepsilon_{a,0.3\%}}$) on the *left* and E_{50} on the *right*, both plotted against C_u. For the sole purpose of better visualization, semi-

logarithmic plots are utilized. M1-R specimens show scattered strain moduli between 10-50 MPa due to different σ'_3. However, as discussed in *Chapter* 4, E_{50} (on the *right* plot) presents less scattering, still ranging from 4 to 20 MPa on all loose WR specimens tested. It is also worth noting that the values obtained are in the range reported by Maknoon (2016) (between 0.5-40 MPa), who investigated the strain modulus of WR using rigid plate loading (refer to *Figure* 2.19).

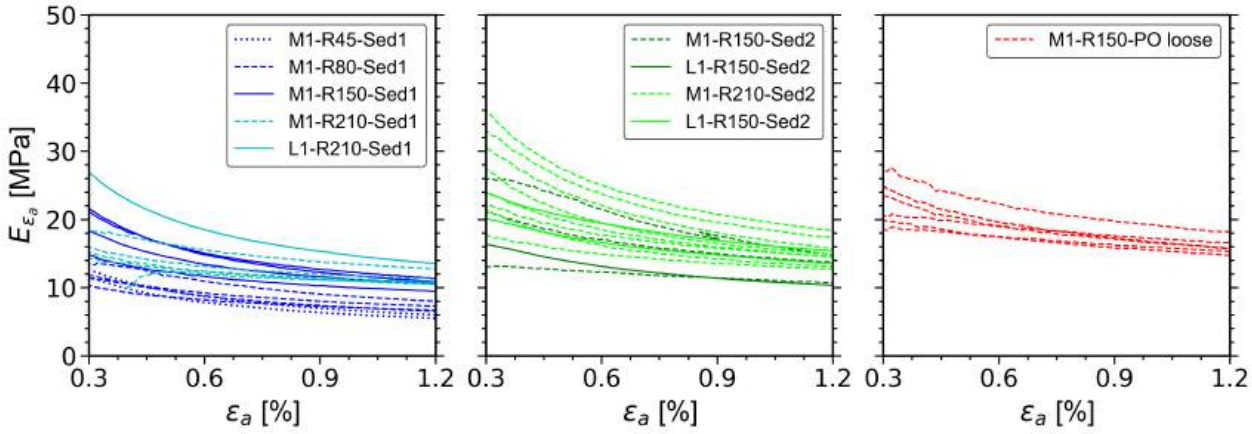

Figure 7.1 Variation of the characteristic strain modulus E_{ε_a} vs ε_a in loose WR specimens tested.

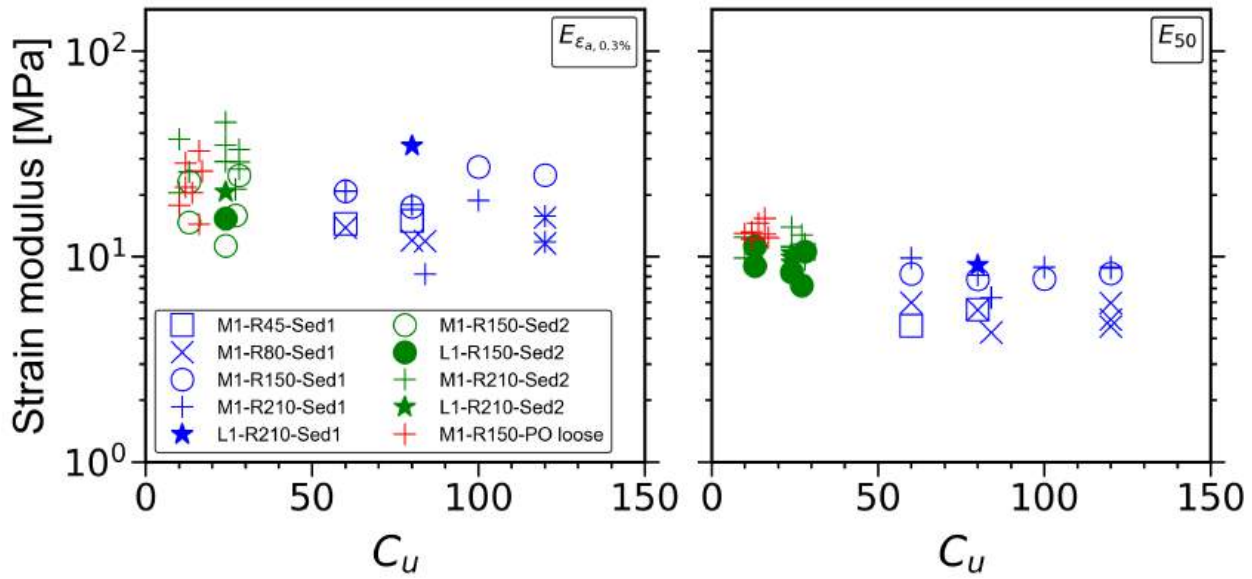

Figure 7.2 Variation of $E_{\varepsilon_{a,0.3\%}}$ (*left*) and E_{50} (*right*) vs C_u in loose WR specimens tested.

Figure 7.3 shows E_{50} of all materials tested in this thesis, as well as additional data from

the literature for comparison. Since soils present non-linear elasticity, E_{50} increases with σ'_3 and packing properties. Visibly, as discussed in *Chapter* 6, the alluvial gravels exhibit higher E_{50} values than rockfills. This is also visible in *Figure* 7.4, plotting the data against C_u. The main reason is that alluvial gravels were prepared densely, while most WR and rockfill did not. Anyhow, the exceptions are PO-dense WR specimens, which reach relatively high E_{50} values and approach the range of dense sands, with isolated cases as high as gravels. Additionally, the amount of particle crushing could also play a role in the material stiffness. As shown in *Figure* 7.5, characteristic grain shapes of alluvial gravels are more rounded than rockfills, thus less prone to crushing by attrition of edges. Gravel particles are generally more resistant to fragmentation, since they result from a long and aggressive geological process of erosion and abrasion. However, WR and rockfills are mostly damaged after blasting and excavation operations, which results in relatively low fragmentation strength.

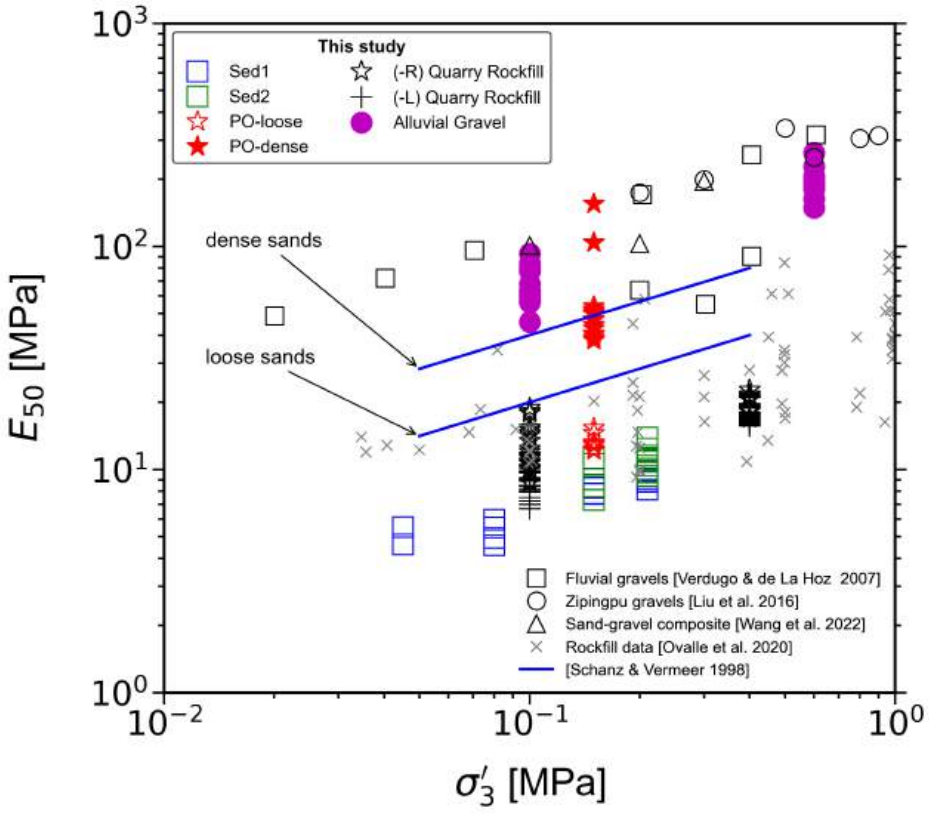

Figure 7.3 Variation of E_{50} vs σ'_3 in all investigated materials, compared with reported data.

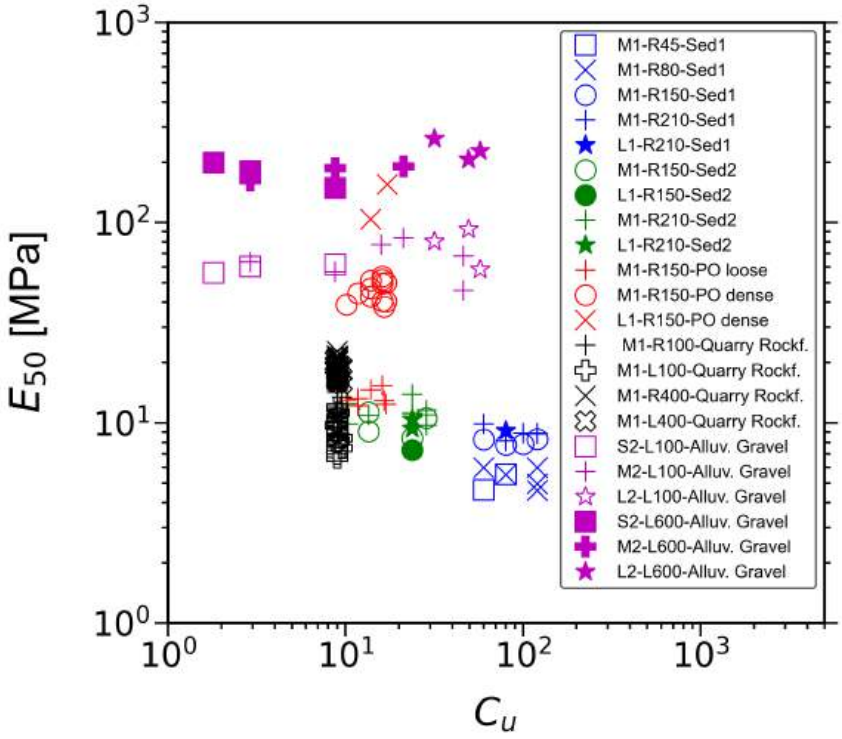

Figure 7.4 Variation of E_{50} across C_u in all investigated materials.

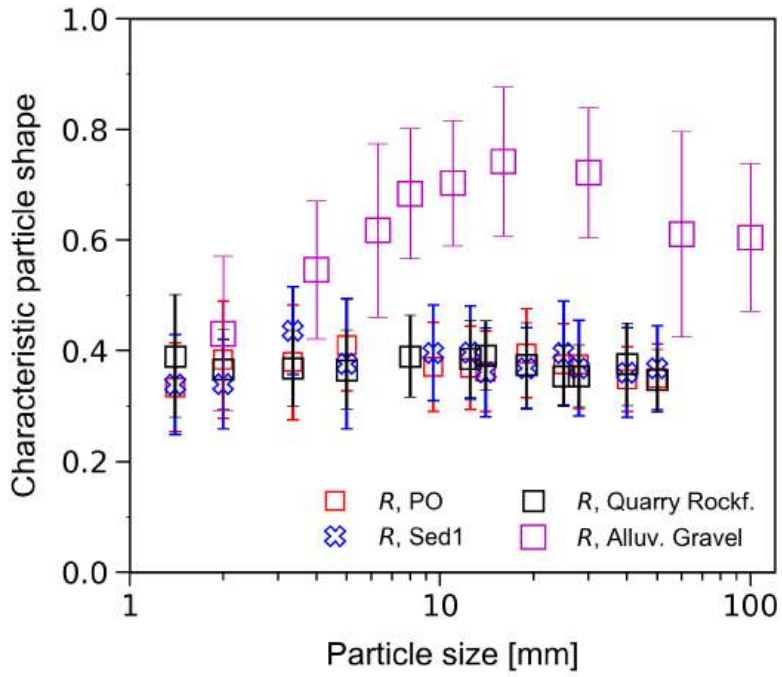

Figure 7.5 Variation of the roundness R in all investigated materials.

Following Duncan and Bursey (2013) and Yang et al. (2018), the Poisson's ratio (ν) is estimated by *Equation* 7.1 and the values are plotted against C_u in *Figure* 7.6. ν seems to increase slightly with increasing σ'_3 on a given material. All values are between 0.2 and 0.3, remaining in the range reported for gravels and WR materials (Essayad, 2021; Gercek, 2007). The dispersion of the values is due to scattering in the internal friction angle, which might be due to the combined effects of different σ'_3, mineralogy, particle shapes, and packing conditions. In addition, Poisson's ratio values were also measured from the « elastic » domain of the stress-strain in each test ($\nu_m = -\varepsilon_r/\varepsilon_a$, where ε_r is the radial strain). It is worth mentioning that the displacement transducers used could not allow precise measurement of the elastic regime in loose specimens. Therefore, the ν_m values obtained in those specimens are abnormal (e.g. $\nu_m < 0.1$) and are discarded from this discussion. *Figure* 7.7 shows ν_m of dense specimens tested, varying between $\nu_m \sim 0.2-0.4$. This is in a similar range to the estimated ν through ϕ' and other typical reported values for coarse-grained materials. However, the significant variability is explained by the low precision of the deformation measurement system, which was not intended to capture the elastic regime.

$$\nu = \frac{1 - sin\ \phi'}{2 - sin\ \phi'} \tag{7.1}$$

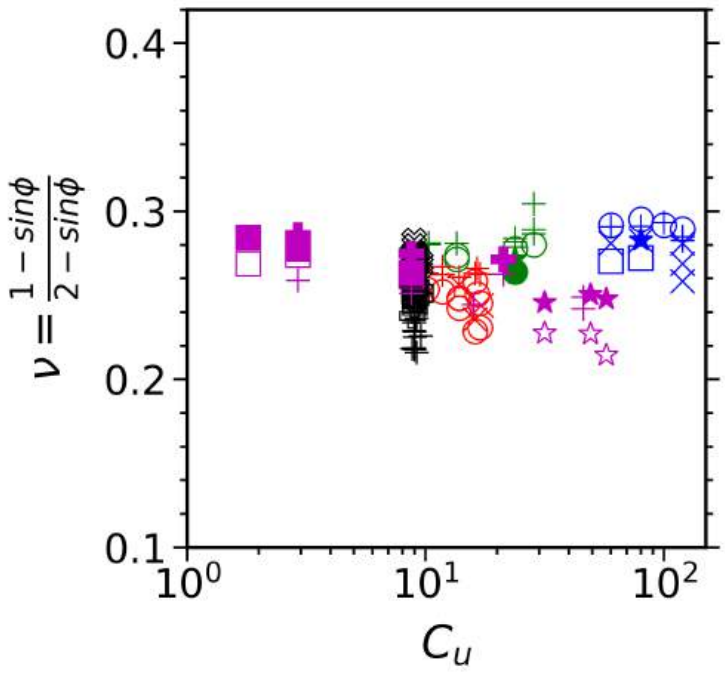

Figure 7.6 Variation of ν in all specimens tested (similar legend markers as in *Figure* 7.4).

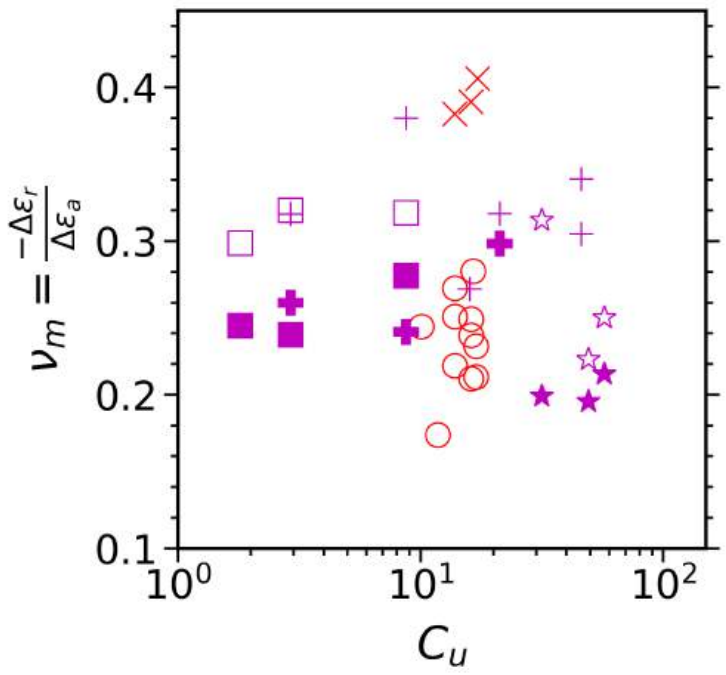

Figure 7.7 Variation of ν_m in all specimens tested (similar legend markers as in *Figure* 7.4).

7.2 Volume change

Figure 7.8 shows that loose WR and quarry rockfill exhibit lower dilatancy compared to dense alluvial gravels, in terms of the peak strain ratio $(d\varepsilon_v/d\varepsilon_a)_{max}$. This is mainly due to the initial density and is also enhanced by crushing in angular and subangular WR and rockfills Ovalle et al. (2020). Alluvial gravels are in the range of dense sands proposed by Bolton (1986) ($I_D \sim 0.7$), while WR and rockfills are comparable to sands with $I_D \sim 0.2$.

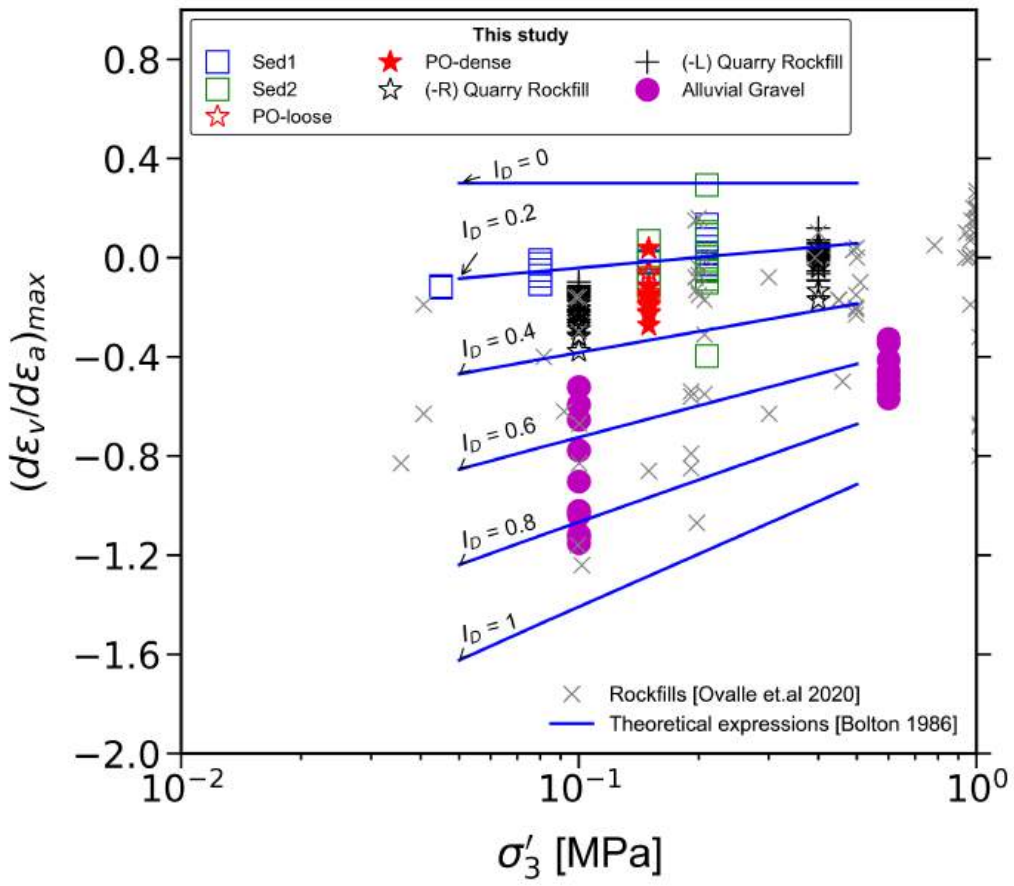

Figure 7.8 Evolution of $(d\varepsilon_v/d\varepsilon_a)_{max}$ vs σ'_3 in all investigated materials, comparing with reported data on rockfill and theoretical expressions on sand materials.

The effects of specimen scaling discussed in *Chapter* 6 for alluvial gravels reveal that volumetric dilatancy is affected by changing the PSD. Namely, at given state parameters (stress and density), the better graded the material, the lower the dilatancy upon shearing. This is because better graded materials have more efficient packing thanks to fine particles (sand or silt) efficiently fitting within pores between coarse particles. Therefore, since scaling generates lower C_u, small-scale specimens exhibit higher volumetric dilatancy upon shearing than the original coarse material.

A comparison of all materials tested in this thesis is shown in *Figure* 7.9, plotting the angle of dilatancy (ψ_{max}, where $\sin\psi_{max} = -(d\varepsilon_v/d\varepsilon_a)_{max}/(2-(d\varepsilon_v/d\varepsilon_a)_{max})$) against C_u. Again, one can notice that WR and rockfill specimens behave more contractant (mainly $\psi_{max} < 0$) and mobilize relatively low $\psi_{max} < 10°$ for all stress levels considered. Concerning specimen size, M1 specimens display higher dilatancy than L1 specimens. Similarly, alluvial gravels exhibit a consistent decreasing pattern with the specimen size for a given σ'_3 considered; for

instance, S2 and M2 specimens overestimate in $\sim 30-45\%$ the dilatancy of L2 specimens. In other words, in all the cases small-specimens overestimate dilatancy.

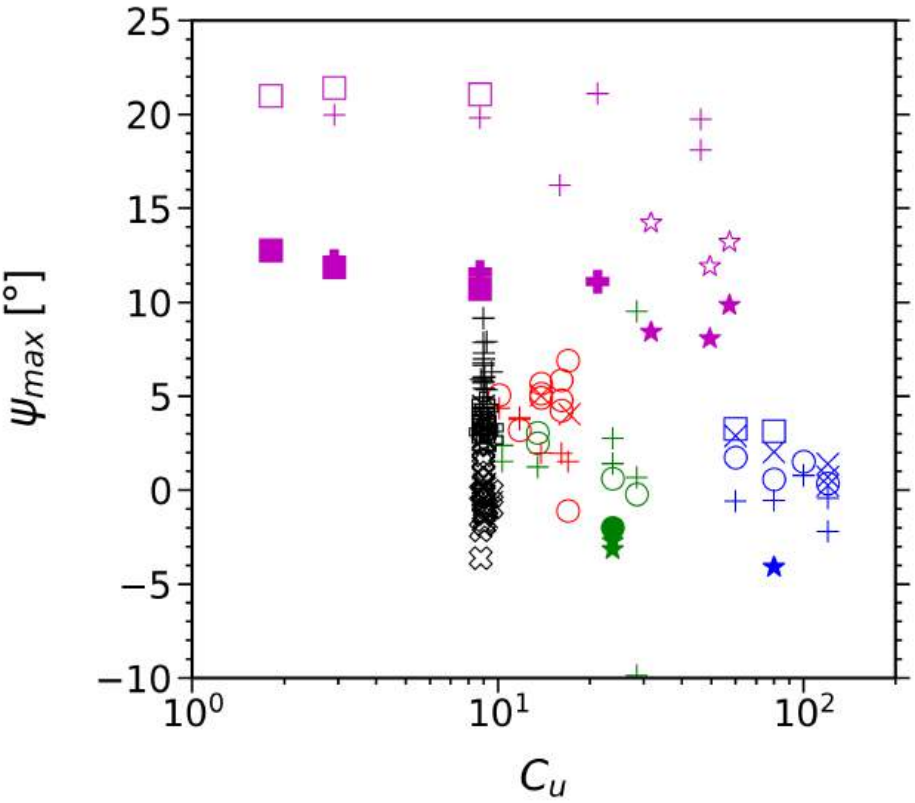

Figure 7.9 Variation of ψ_{max} with C_u on all investigated materials (similar legend markers as in *Figure* 7.4).

The source of the overestimation of dilatancy in small-scale samples could be explained not only by more uniform PSDs (that is, low C_u), but also by the slenderness of the samples (height-to-diameter H:D). A preliminary investigation of experiments carried out on H:D=2 specimens at IBF on the same alluvial soil is discussed; these results are unpublished and not included in previous Chapters of this thesis. *Figure* 7.10 compares the stress-strain curves of the specimens with H:D=2 (*discontinuous* curves), exhibiting considerable reduction in volumetric dilatancy compared to S2 specimens (H:D=1) under similar test conditions. Photos of deformed specimens are shown in *Figure* 7.11, displaying bulging and strain localization in different specimen zones with H:D=2, contrary with their counterpart S2 specimens with H:D=1. Possibly, in H:D=2 specimens the dilation is confined in narrow localized shear bands, thus the volume change measured is not representative of the whole material volume.

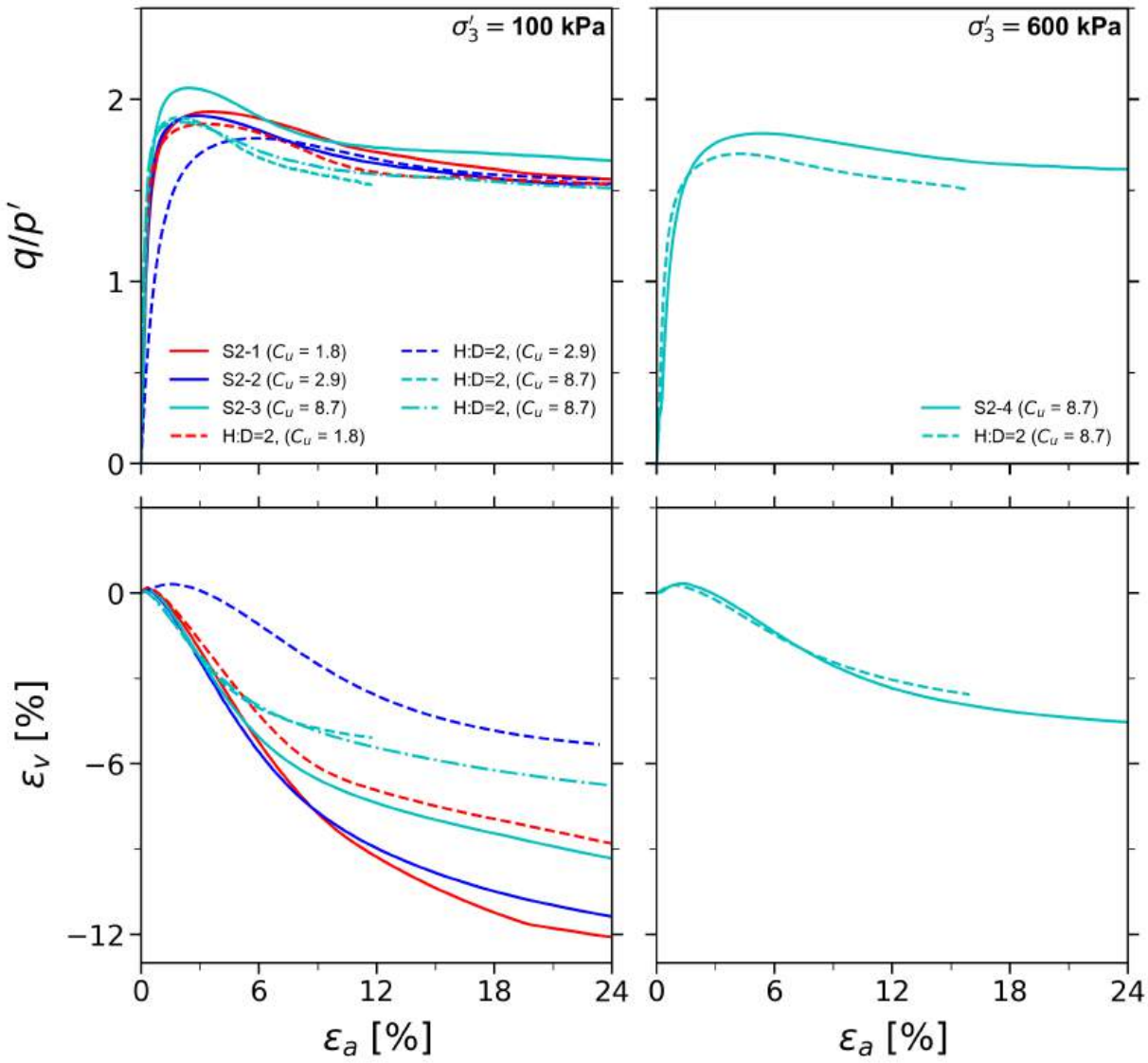

Figure 7.10 Comparison of stress-strain response of H:D=2 and H:D=1 S2 alluvial gravel specimens (D=100 mm).

H:D=2, $C_u = 1.8$

H:D=2, $C_u = 2.9$

S2 (H:D=1), $C_u = 2.9$

S2 (H:D=1), $C_u = 8.7$

Figure 7.11 Pictures of the deformation of end-lubricated alluvial gravel dense S2 specimens (D=100 mm): *top* H:D=2 ; *bottom* H:D=1.

7.3 Critical void ratio e_{cr}

The variation of the current void ratio with p' in WR specimens (analyzed in *Chapter* 4), is shown in *Figure* 7.12. The initial test program has been designed with different PSDs and σ'_3, therefore, it is impossible to estimate the critical state lines (CSL) with this dataset; this

explains why the analysis was not included in the journal article presented in *Chapter* 4. However, the evolution of individual tests suggests that the critical void ratio (e_{cr}) can be assumed in loose specimens at ε_a attained at the end of each test. *Figure* 7.13 shows the estimated e_{cr} values aligning around 0.4±0.03 for loose specimens. Conversely, dense specimens do not reach similar e_{cr}, due to inherent limitations of triaxial compression and strain localization.

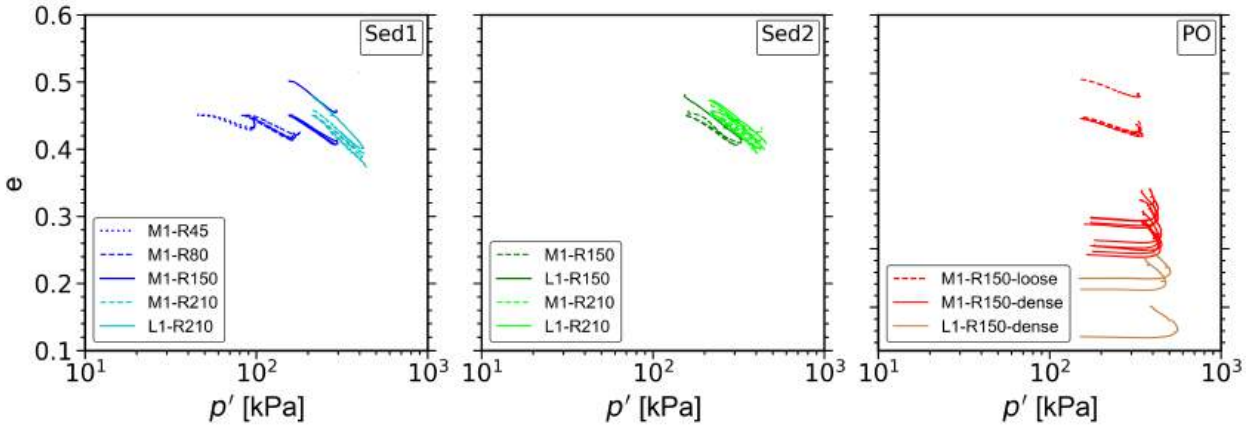

Figure 7.12 Variation of the current void ratio e vs p' in WR specimens tested.

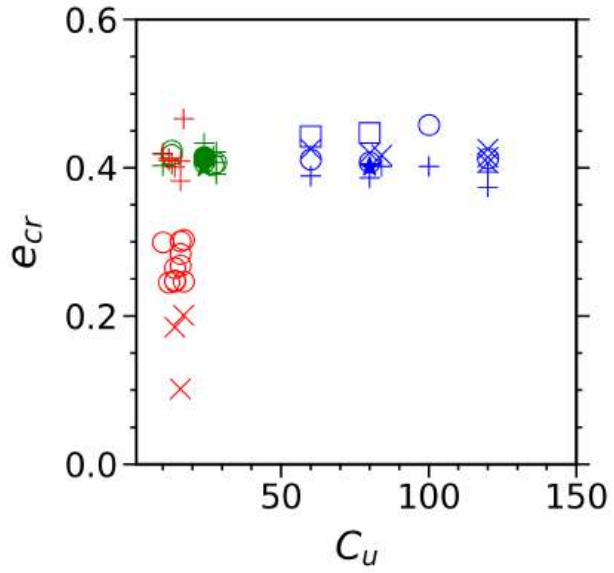

Figure 7.13 Variation of the critical void ratio e_{cr} vs C_u in WR specimens tested (similar legend markers as in *Figure* 7.4).

7.4 Effective internal critical friction angle ϕ'_{cr}

A comparative basis from the literature (see *Chapter 4, Section 4.4.1*) suggests that a REV is reached only when the scatter on the measured effective critical friction angle (ϕ'_{cr}) is less than $\leq 2°$ (around 5%). Despite the challenge to reach the critical state fully, stress-strain curves reached a stress "plateau" beyond $\varepsilon_a \geq 12\%$ in all tests. ϕ'_{cr} values were assumed at the largest ε_a achieved in each test for comparison, usually around $\varepsilon_a \geq 15\%$. Furthermore, a general definition for a REV in this doctoral project comprises a specimen that allows α sufficiently large enough, to exempt specimen size effects on ϕ'_{cr} estimates. A systematic assessment of WR material considering various specimen sizes suggests that a REV is achieved only when $\alpha \geq 12$, which is consistent with other recent studies (e.g. (Cantor & Ovalle, 2023; Quiroz-Rojo et al., 2024)). As shown in *Figures* 4.11 and 4.12 for M1 and L1 WR specimens, this is valid under similar state properties (e, σ'_3) and constant characteristic particle shapes across size fractions.

A generalization on coarse materials studied in this thesis is plotted in *Figure* 7.14. The figure combines the test results of quarry rockfill and alluvial gravel materials with varying α, showing a normalized $\phi'_{cr}/\phi'_{(\alpha=12)}$, where $\phi'_{(\alpha=12)}$ is the ϕ'_{cr} of the specimen with $\alpha = 12$. The compilation shows that the REV condition is met at $\phi'_{cr} \geq 12$, which is almost double the recommended values of α =5, 6 and 10, by the testing standards ASTM D7181; BS 1377-8/DIN 18137; JGS 0530, respectively. The data oscillate beyond the REV conditions below this threshold ($\alpha = 12$), attaining more than $\pm 10\%$ scattering. However, it is worth noting that the tests on alluvial gravels (*Chapter* 6) did not fully reach the critical state, which explains the enhanced scattering in *Figure* 7.14, compared with WR and quarry rockfill.

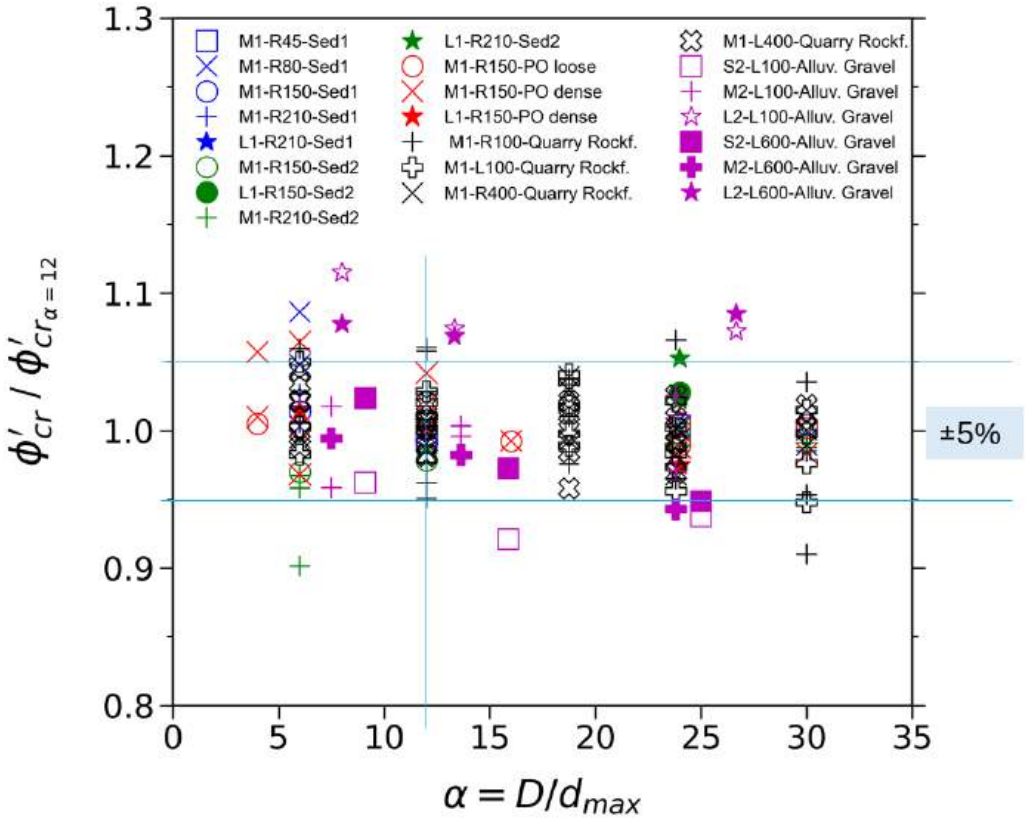

Figure 7.14 Evolution of the normalized $\phi'_{cr}/\phi'_{(\alpha=12)}$ vs α on all investigated materials.

7.5 Particle and specimen size effects

A comparison of the results obtained in this study with data sets from the pertinent literature is made in the context of the contradictions evoked earlier in *Section 2.5* (refer to *Figure* 2.71). The friction angle of the coarsest material tested in each case is taken as a reference (ϕ'_{ref}), and then the excess value ($\Delta\phi' = \phi'_{ref} - \phi'$) is compared with the scaling factor F. Under controlled similar packing properties and characteristic particle shapes, the materials tested in this thesis float around ±2°. Therefore, it is proposed that the contradicting scatter observed in the literature is presumably caused by one or several (coupled) effects of different material states, characteristic PSD, REV, grain shape and grain crushing, and not necessarily due to the size of the particles or the size of the specimens, exclusively. In other words, most prior studies have addressed small-scale effects primarily under the broad category of *particle size effects*, while overlooking the influence of other intrinsic and state material properties.

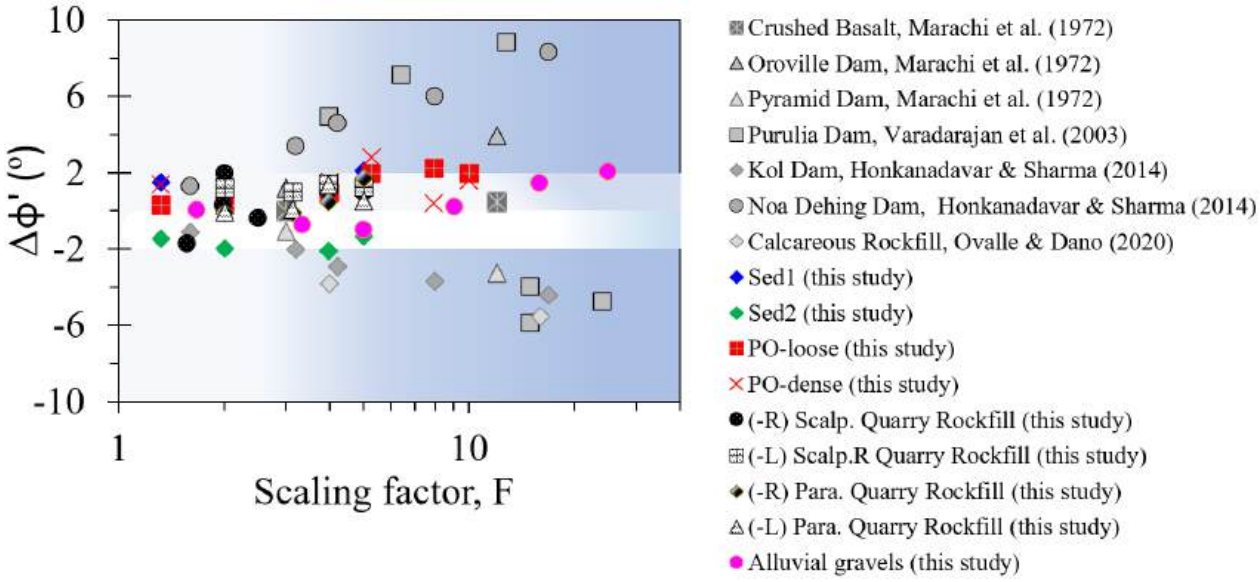

Figure 7.15 Evolution of the scatter $\Delta\phi'$ with the scaling factor F.

CHAPTER 8 CONCLUSION

Understanding the mechanical behavior of coarse mine waste rock is paramount to ensure adequate geotechnical designs of waste storage facilities, such as waste rock piles, backfilling in mining operations or co-disposal methods. Although the primary motivation for this thesis stems from the challenges associated with mine waste rock management, these are fundamentally similar to those faced in other coarse granular materials[1], including gravelly soils and quarried rockfill materials. The main challenge is related to the oversized particles contained in coarse materials. Due to size limitations of existing testing facilities, physical testing of coarse materials is not always achievable, leading to a lack of data. Thus, engineering designs are often based on a limited number of data, mostly taken from tests on small-scale specimens of the field material, or simply using published mechanical parameters from *similar* materials.

This doctoral project aimed to investigate qualitatively and quantitatively the reliability of small-scaling techniques for coarse granular materials. Additionally, the study sought to clarify the sources of the apparent contradictions found in the literature regarding *size effects* on the mechanical behavior of small-scale specimens.

A series of experimental testing campaigns were carried out, totaling 170 triaxial tests and a dozen of large-scale in-situ direct shear test (DST). Triaxial tests were performed using laboratory devices that can handle specimens of varied sizes, from diameters D=100 to 800 mm, considering coarse material of different origins: blasted waste rock (WR) from mining operations, quarry rockfill and alluvial gravel materials. In addition, a non-standard in-situ direct shear box was developed, being one of the largest ever reported in the literature, with dimensions $1200 \times 1200 \times 380\ mm^3$. The density of the specimens and the characteristic grain shapes of all the coarse materials used were controlled and measured, respectively. specimens ranged from loose to dense, as well as subangular to rounded coarse particles. The confining stress levels applied in the tests were from $\sigma'_3 = 45 - 600$ kPa. The small-scaling techniques used were scalping grading, parallel grading and truncation (replacement). The tests were performed at varied specimen and particle sizes, grading and boundary conditions. Stress-strain relationships were analyzed with respect to dilatancy, strain modulus, peak shear strength and critical states.

[1]Coarse materials in this thesis are defined as those that contain particle sizes in the range of gravels ($5 < d < 80mm$) and/or oversized boulders ($d > 80mm$)

The main conclusions drawn from this thesis are enumerated below.

- Scaling granular soils involves reducing grain size, adjusting grading and modifying density, with these properties varying at each scale level. Therefore, it is essential to establish standard maximum and minimum densities for all specimen sizes used in scaling. These reference values facilitate the preparation of specimens with equivalent density indexes. A meaningful comparison across different scales is only possible when state conditions remain consistent. However, the absence of standardized methods for evaluating the relative densities of oversized soils necessitates extrapolating results.

- The compilation of all triaxial test results in loose WR, quarry rockfill and alluvial gravels, showed that the representative elementary volume (REV) condition for the assessment of the effective internal critical friction angle (ϕ'_{cr}) is met at a specimen aspect ratio[2] $\alpha = D/d_{max} \geq 12$, which is higher than the recommended values of α =5, 6 and 10, by the international testing standards from USA (ASTM), Europe (BS and DIN) and Japan (JGS), respectively.

- The large in-situ DST allowed for very similar mean ϕ'_{cr} as in laboratory triaxial results of loose WR specimens tested at comparable normal stresses.

- Provided that REV conditions are met, triaxial laboratory results on loose WR specimens showed stable mean ϕ'_{cr} across all the scaled specimens, regardless of the particle size distribution (PSD). This is consistent with several reported experimental evidence stating that ϕ'_{cr} does not depend on grading, provided that grain mineralogy, characteristic particle shape and grain surface roughness remain constant across size fractions.

- Standard rough triaxial platens induce end-restraint effects in coarse angular materials, which is manifested in strain localization and enhanced scattering in the mechanical properties, including ϕ'_{cr}, volumetric dilatancy and secant stiffness (E_{50}). However, enlarged and lubricated ends allow for homogeneous strain fields in loose specimens with slenderness (height-to-diameter) H:D=2, resulting in relatively low dispersion of the mechanical parameters.

- End lubrication should be systematically used in triaxial tests on coarse rockfill materials. Also, it is highly advisable to use shredded sheets on lubricated caps. This promotes radial movement of the particles in contact with the triaxial caps and bases, avoiding a single sliding surface that can cause buckling of the specimen.

[2] D is the specimen diameter and d_{max} is the coarsest particle size.

- Small specimens prepared by scalping grading and tested with standard rough platens manifested the most pronounced end-restraint effects, with scattered values of ϕ'_{cr} and E_{50} compared with parallel graded materials under the same testing conditions.

- Scalping or truncating the PSD of a coarse material produces a smaller specimen with a more uniform grading, which affects its volumetric dilatancy. Due to grading effects, dense small-scale specimens with equivalent density indexes exhibit greater dilatancy and a higher critical state void ratio than the original coarse soil. This effect must be considered when calibrating and modeling based on scaled parameters.

- Although small-scaling tends to enhance the volumetric dilatancy, the peak strength appears relatively reduced compared to the coarser material at similar density index. Therefore, the reduced specimens often comprise conservative shear strength values. However, if particle crushing is predominant this trend could be transposed due to the inverse effect of particle strength-size correlations.

- The mechanical response of granular materials greatly depends on the characteristic shape of the particles. Therefore, the particle shapes should be systematically verified at all scales to ensure a reliable representation of the small-scale specimens. Practitioners should anticipate these limitations in interpreting the test results if the particle shapes of the finer fraction differ from those of the original coarse fraction; knowing that higher grain angularity gives higher shear strength and dilatancy, and vice-versa.

In summary, small-scaling of coarse materials comprises limitations given by the material properties, such as packing density conditions and grain shapes, which could vary due to grading effects. However, understanding these drawbacks can help make realistic and conservative assumptions when characterizing oversized materials in the field, or when geotechnical designs must inescapably rely on reduced specimen properties due to inaccessible large-scale testing. Consequently, practitioners should be cautious in modeling stress-strain behavior from the results issued from small-scale specimens.

Indubitably, the significant data scatter and contradicting trends observed in the literature for scaled specimens are caused by one or numerous (coupled) effects not carefully controlled: different material states, unmet REV, end boundary conditions, characteristic PSD and grain shape, and particle crushing, and not solely the sizes of the particles or specimens. The findings of this thesis indicate that ϕ'_{cr} can be assessed using scalping grading, parallel grading and truncation techniques when REV conditions are met. Furthermore, it was thoroughly

shown that the recommendations of some worldwide geotechnical standards, such as ASTM D7181; BS 1377-8; DIN 18137; JGS 0530, should be revisited.

Many uncertainties remain regarding the effects of small-scale testing. Future strategic investigations should be envisaged, considering grading effects in the context of the degradation of coarse material properties through cyclic loading. It would be valuable to verify the scaling effects observed in this study under different stress paths, particularly oedometric conditions and simple shearing, and with diverse materials that exhibit varying sensitivity to grain crushing; for instance, WR from non-metallic mines and crushable shale rockfills. Furthermore, it would be important to consider the end-restraint effects in these types of materials in specimens with different H:D ratios and density states.

Another potential avenue for research is examining the influence of rock aggregate mineralogy. These properties can vary across size fractions due to differences in morphology and geological composition, introducing additional uncertainties in predicting scaling effects. Consequently, obtaining a truly representative scaled specimen may require more than just sieving and size fraction separation, it should also consider other geometric factors (such as shape) and mineralogical aspects.

It would be also necessary to perform research to quantify the optimum amount of the replaced coarse fraction in the truncation technique, and materials having PSDs with excessive fine fractions ($< 80\mu m$). In addition, future studies could also seek to establish experimental standard methods to evaluate the minimum and maximum densities in oversized materials.

Finally, despite technical and economic constraints large-scale testing provides valuable information, contributing to a holistic understanding of coarse materials. Therefore, they remain indispensable for accurate geotechnical characterization.

REFERENCES

Aachib, M., Mbonimpa, M., & Aubertin, M. (2004). Measurement and prediction of the oxygen diffusion coefficient in unsaturated media, with applications to soil covers. *Water, Air, Soil Pollution*, *156*(1), 163–193.

Abbas, S. M., Sharma, K. G., & Varadarajan, A. (2004). Prediction of shear strength parameter of alluvial and quarried rockfill materials. *9th International Symposium on Numerical Models in Geomechanics, NUMOG 2004, August 25, 2004 - August 27, 2004*, 195–204.

Airey, D., Budhu, M., & Wood, D. (1985). Some aspects of the behaviour of soils in simple shear. In P. Banerjee & R. Butterfield (Eds.), *Developments in soil mechanics and foundation engineering* (pp. 185–213). Elsevier.

Al-Hussaini, M. M. (1983). Effect of particle size and strain conditions on the strength of crushed basalt. *Canadian Geotechnical Journal*, *20*(4), 706–717.

Altuhafi, F. N., Coop, M. R., & Georgiannou, V. N. (2016). Effect of particle shape on the mechanical behavior of natural sands. *Journal of Geotechnical and Geoenvironmental Engineering*, *142*(12), 04016071.

Amirpour Harehdasht, S., Hussien, M. N., Karray, M., Roubtsova, V., & Chekired, M. (2018). Influence of particle size and gradation on shear strength–dilation relation of granular materials. *Canadian Geotechnical Journal*, *56*(2), 208–227.

Amos, R. T., Blowes, D. W., Bailey, B. L., Sego, D. C., Smith, L., & Ritchie, A. I. M. (2015). Waste-rock hydrogeology and geochemistry. *Applied Geochemistry*, *57*, 140–156.

Anterrieu, O., Chouteau, M., & Aubertin, M. (2010). Geophysical characterization of the large-scale internal structure of a waste rock pile from a hard rock mine. *Bulletin of Engineering Geology and the Environment*, *69*(4), 533–548.

Arrieta, M., & Zhang, Z.-X. (2024). Particle size distribution (PSD) estimation using unmanned aerial vehicle (UAV) photogrammetry for rockfill shear strength characterization. *Acta Geotechnica*, *19*(9), 6239–6258.

ASTM C127. (2024). *Test method for density, relative density (specific gravity), and absorption of coarse aggregate*. ASTM International.

ASTM D2487. (2017). *Standard practice for classification of soils for engineering purposes (unified soil classification system)*. ASTM International.

ASTM D3080. (2011). *Standard test method for direct shear test of soils under consolidated drained conditions*. ASTM International.

ASTM D4253. (2016). *Standard test methods for maximum index density and unit weight of soils using a vibrating table*. ASTM International.

ASTM D4254. (2016). *Standard test methods for minimum index density and unit weight of soils and calculation of relative density*. ASTM International.

ASTM D4318. (2017). *Standard test methods for liquid limit, plastic limit, and plasticity index of soils*. ASTM International.

ASTM D5030. (2013). *Standard test methods for density of soil and rock in place by the water replacement method in a test pit*. ASTM International.

ASTM D7181. (2020). *Standard test method for consolidated drained triaxial compression test for soils*. ASTM International.

ASTM D854. (2014). *Standard test methods for specific gravity of soil solids by water pycnometer*. ASTM International.

Aubertin, M., Bussiere, B., & Chapuis, R. P. (1996). Hydraulic conductivity of homogenized tailings from hard rock mines. *Canadian geotechnical journal*, *33*(3), 470–482.

Aubertin, M., Bussière, B., & Bernier, L. (2002). Environnement et gestion des rejets miniers. *Presses Internationales Polytechnique*.

Aubertin, M., Bussière, B., James, M., Mbonimpa, M., & Chapuis, R. (2013). Revue de divers aspects liés à la stabilité géotechnique des ouvrages de retenue de résidus miniers: partie i – mise en contexte et caractéristiques générales. *Environnement, Ingénierie Développement, N°64 - Juin 2013*(64).

Aubertin, M., Fala, O., Bussière, B., Martin, V., Campos, D., Gamache-Rochette, A., Chouteau, M., & Chapuis, R. (2002). Analyse des écoulements de l'eau en conditions non saturées dans les haldes à stériles. *Défis et perspectives: Symposium*.

Aubertin, M., Fala, O., Molson, J., Gamache-Rochette, A., Lahmira, B., Martin, V., Lefebvre, R., Bussière, B., Chapuis, R. P., Chouteau, M., et al. (2005). Évaluation du comportement hydrogéologique et géochimique des haldes à stériles. *Proceedings of the Symposium sur l'Environnement et les Mines, Rouyn-Noranda, CD-ROM, CIM*.

Aubertin, M., Maknoon, M., & Ovalle, C. (2021). Waste rock pile design considerations to promote geotechnical and geochemical stability. *Canadian Geotechnique - The CGS Magazine: Fall 2021*, *2(3)*, 44–47.

Azam, S., Wilson, G. W., Fredlund, D. G., & Van Zyl, D. (2011). Geotechnical characterization of mine waste rock. International Society for Soil Mechanics; Geotechnical Engineering (ISSMGE).

Azam, S., Wilson, G. W., Herasymuik, G., Nichol, C., & Barbour, L. S. (2007). Hydrogeological behaviour of an unsaturated waste rock pile: a case study at the golden sunlight

mine, montana, usa. *Bulletin of Engineering Geology and the Environment*, *66*(3), 259–268.

Azéma, E., Linero, S., Estrada, N., & Lizcano, A. (2017). Shear strength and microstructure of polydisperse packings: the effect of size span and shape of particle size distribution. *Physical Review E*, *96*(2), 022902.

Bao, Z., Bain, J., Saurette, E., Zou Finfrock, Y., Hu, Y., Ptacek, C. J., & Blowes, D. W. (2022). Mineralogy-dependent sulfide oxidation via polysulfide and thiosulfate pathways during weathering of mixed-sulfide bearing mine waste rock. *Geochimica et Cosmochimica Acta*, *317*, 523–537.

Bar, N., Semi, J., Koek, M., Owusu-Bempah, G., Day, A., Nicoll, S., & Bu, J. (2020). Practical waste rock dump and stockpile management in high rainfall and seismic regions of papua new guinea. *Proceedings of the 2020 International Symposium on Slope Stability in Open Pit Mining and Civil Engineering*, 117–128.

Bard, E., Campaña, J., Anabalón, M., & Apablaza, R. (2007). Waste rock behavior under high pressures. *XIII Pan-American Conference on Soil Mechanics and Geotechnical Engineering, Venezuela*.

Bard, E., Anabalón, M. E., & Campaña, J. (2011). Waste rock behavior at high pressures. In *Multiscale geomechanics* (pp. 83–112).

Barton, N. (2013). Shear strength criteria for rock, rock joints, rockfill and rock masses: problems and some solutions. *Journal of Rock Mechanics and Geotechnical Engineering*, *5*(4), 249–261.

Barton, N., & Kjærnsli, B. (1981). Shear strength of rockfill. *Journal of the Geotechnical Engineering Division*, *107*(7), 873–891.

Bishop, A. W. (1945). A large shear box for testing sands and gravels. *Proceedings of the 2nd international conference on soil mechanics and foundation engineering, Rotterdam, The Netherlands*, 21–30.

Bishop, A. W., & Green, G. E. (1965). The influence of end restraint on the compression strength of a cohesionless soil. *Géotechnique*, *15*(3), 243–266.

Blight, G. E. (2009). *Geotechnical engineering for mine waste storage facilities* (1st). CRC Press.

Bolton, M. D. (1986). The strength and dilatancy of sands. *Géotechnique*, *36*(1), 65–78.

Bowles, J. E. (1997). *Foundation analysis and design*. McGraw-Hill.

BS 1377-8. (1990). *Methods of Test for Soils for Civil Engineering Purposes – Part 8: Shear Strength Tests (Effective Stress) (BS 1377-8:1990)* [Withdrawn: 13 Apr 2018]. British Standards Institution Standards Limited.

Bussière, B. (2007). Colloquium 2004: hydrogeotechnical properties of hard rock tailings from metal mines and emerging geoenvironmental disposal approaches. *Canadian Geotechnical Journal*, *44*(9), 1019–1052.

Bussière, B., & Guittonny, M. (2020). *Hard rock mine reclamation: from prediction to management of acid mine drainage*. CRC press.

Cantor, D., Azema, E., Radjai, F., & Sornay, P. (2018). Rheology and structure of polydisperse three-dimensional packings of spheres. *Physical Review E*, *98*(5).

Cantor, D., & Ovalle, C. (2023). Sample size effects on the critical state shear strength of granular materials with varied gradation and the role of column- like local structures. *Géotechnique*, *75*(1), 29–40.

Carrasco, S., Cantor, D., Ovalle, C., & Dubois, F. (2025). Particle shape distribution effects on the critical strength of granular materials. *Computers and Geotechnics*, *177*, 106896.

Casagrande, A. (1936). Characteristics of cohesionless soils affecting the stability of slopes and earth fills. *J. Boston Society of Civil Engineers*, *23*(1), 13–32.

Castellanos, B., & Brandon, T. (2013). A comparison between the shear strength measured with direct shear and triaxial devices on undisturbed and remolded soils. *Proceedings of the 18th international conference on soil mechanics and geotechnical engineering, Paris*, *1*, 317–320.

Cavarretta, I., Coop, M., & O'Sullivan, C. (2010). The influence of particle characteristics on the behaviour of coarse grained soils. *Géotechnique*, *60*(6), 413–423.

Chapuis, R. P., L'Ecuyer, M., & Aubertin, M. (1993). Field permeability tests in mine tailings. *Canadian Geotechnical Conference*, 51–59.

Cho, G.-C., Dodds, J., & Santamarina, J. C. (2006). Particle shape effects on packing density, stiffness, and strength: natural and crushed sands. *Journal of Geotechnical and Geoenvironmental Engineering*, *132*(5), 591–602.

Das, B. M. (2019). *Advanced soil mechanics* (5th). CRC Press.

Dawood, I., & Aubertin, M. (2009). A numerical investigation of the influence of internal structure on the unsaturated flow in a large waste rock pile. *62nd Canadian Geotechnical Conference and 10th Joint CGS/IAH-CNC Groundwater Specialty Conference, Halifax, Nova Scotia*.

Deiminiat, A., & Li, L. (2022). Experimental study on the reliability of scaling down techniques used in direct shear tests to determine the shear strength of rockfill and waste rocks. *CivilEng*, *3*(1), 35–50.

Deiminiat, A., Li, L., & Pabst, T. (2023). Experimental study on specimen size effect and the minimum required specimen diameter to maximum particle size ratio for constant head permeability tests. *Environmental Earth Sciences*, *82*(14).

Deiminiat, A., Li, L., & Zeng, F. (2022). Experimental study on the minimum required specimen width to maximum particle size ratio in direct shear tests. *CivilEng*, *3*(1), 66–84.

Deiminiat, A., Li, L., Zeng, F., Pabst, T., Chiasson, P., & Chapuis, R. (2020). Determination of the shear strength of rockfill from small-scale laboratory shear tests: a critical review. *Advances in Civil Engineering*, *2020*, 8890237.

Deng, Y., Yilmaz, Y., Gokce, A., & Chang, C. S. (2021). Influence of particle size on the drained shear behavior of a dense fluvial sand. *Acta Geotechnica*, *16*(7), 2071–2088.

Dimech, A., Chouteau, M., Aubertin, M., Bussière, B., Martin, V., & Plante, B. (2019). Three-dimensional time-lapse geoelectrical monitoring of water infiltration in an experimental mine waste rock pile. *Vadose Zone Journal*, *18*(1), 180098.

DIN 18137. (2011). *Soil, investigation and testing – determination of shear strength – part 2: triaxial test (din 18137-2:2011-04)* [Withdrawn, replaced by DIN EN ISO 17892-8:2018 and DIN EN ISO 17892-9:2018]. Deutsches Institut für Normung, Beuth Verlag GmbH.

Donaghe, R., & Townsend, F. (1976). Scalping and replacement effects on the compaction characteristics of earth-rock mixtures. In *Soil specimen preparation for laboratory testing*. ASTM International.

Dorador, L., & Villalobos, F. A. (2020). Analysis of the geomechanical characterization of coarse granular materials using the parallel gradation method. *Obras y Proyectos*, (27), 50–63.

Duncan, J. M., & Bursey, A. (2013). Soil modulus correlations. *Foundation Engineering in the Face of Uncertainty: Honoring Fred H. Kulhawy*, 321–336.

Duncan, J. M., & Dunlop, P. (1968). The significance of cap and base restraint. *Journal of the Soil Mechanics and Foundations Division*, *94*(1), 271–290.

Essayad, K. (2021, August). *Évaluation multi-échelle de l'instabilité interne et de la migration des résidus à travers les inclusions de roches stériles* [Doctoral dissertation, Polytechnique Montréal].

Essayad, K., & Aubertin, M. (2021). Consolidation of hard rock tailings under positive and negative pore-water pressures: testing procedures and experimental results. *Canadian Geotechnical Journal*, *58*(1), 49–65.

Estaire, J., & Santana, M. (2018). Large direct shear tests performed with fresh ballast. *Symposium on Railroad Ballast Testing and Properties*, 144–161.

Estaire, J., & Olalla, C. (2006). Analysis of the strength of rockfills based on direct shear tests made in 1 m3 shear box. *Ingeniería Civil*, *144*, 73–79.

Fakhimi, A., Boakye, K., Sperling, D. J., & Mclemore, V. T. (2008). Development of a modified in situ direct shear test technique to determine shear strength parameters of mine rock piles. *Geotechnical Testing Journal*, *31*(3), 269–273.

Fala, O. (2008). *Analyses des conditions d'écoulement non saturé dans les haldes à stériles* [Doctoral dissertation, École Polytechnique de Montréal].

Fala, O., Molson, J., Aubertin, M., Bussiere, B., & Chapuis, R. P. (2006). Numerical simulations of long term unsaturated flow and acid mine drainage at waste rock piles. *7th International Conference on Acid Rock Drainage 2006, ICARD 2006, Also Serves as the 23rd Annual Meetings of the American Society of Mining and Reclamation, March 26, 2006 - March 30, 2006*, *1*, 582–597.

Fannin, R. J., Eliadorani, A., & Wilkinson, J. M. T. (2005). Shear strength of cohesionless soils at low stress. *Géotechnique*, *55*(6), 467–478.

Feda, J., Bohac, J., & Herle, I. (1993). End restraint in triaxial testing of soils. *Acta Technica CSAV*, *38*, 197–197.

Franklin, M., Fernandes, H. M., & Van Genuchten, M. T. (2008). Modeling the water flow in unsaturated waste rock pile: an important step in the overall closure planning of the first uranium mining site in brazil. In B. J. Merkel & A. Hasche-Berger (Eds.), *Uranium, mining and hydrogeology* (pp. 177–186). Springer.

Fredlund, D., & Xing, A. (1994). Equations for the soil-water characteristic curve. *Canadian Geotechnical Journal*, *31*(4), 521–532.

Frost, R. (1973). Some testing experiences and characteristics of boulder-gravel fill in earth dams. In *Evaluation of relative density and its role in geotechnical projects involving cohesionless soils*. ASTM International.

Gamache-Rochette, A. (2004). *Une étude de caractérisation en laboratoire et sur le terrain des écoulements de l'eau dans les roches stériles* [Master's thesis, École Polytechnique de Montréal].

Garcia-Torres, S., Ovalle, C., & Girumugisha, G. (2024). Stability assessment of end/push dumping mine waste rock piles in open-pit backfilling. *77th Canadian Geotechnical Conference & 16th Joint CGS/IAH-CNC Groundwater Conference (GeoMontreal 2024)*.

Gercek, H. (2007). Poisson's ratio values for rocks. *International Journal of Rock Mechanics and Mining Sciences*, *44*(1), 1–13.

Goto, S., & Tatsuoka, F. (1988, January). Effects of end conditions on triaxial compressive strength for cohesionless soil. In *Advanced triaxial testing of soil and rock* (p. 14). ASTM International.

Griffith, A. A. (1921). The Phenomena of Rupture and Flow in Solids. *Philosophical Transactions of the Royal Society of London Series A*, *221*, 163–198.

Grimard, L.-P. (2018, March). *Étude de laboratoire du comportement de résidus miniers soumis à des essais de compression non drainés et à une baisse du confinement, avec mesures de vitesse des ondes de cisaillement* [Master's thesis, École Polytechnique de Montréal].

Hassan, N. A., Nguyen, N. S., Marot, D., & Bendahmane, F. (2022). Consequences of scalping and scalping/replacement procedures on strength properties of coarse-grained gap-graded soils. *Canadian Geotechnical Journal*, *59*(10), 1819–1832.

Hawley, M., & Cunning, J. (2017). *Guidelines for mine waste dump and stockpile design*. CSIRO Publishing.

Hennes, R. G. (1957). The strength of gravel in direct shear. In G. P. Tschebotarioff (Ed.). ASTM International.

Hernandez-Orellana, A. M. (2007). *Une étude expérimentale des propriétés hydriques des roches stériles et autres matériaux à granulométrie étalée* [Master's thesis, École Polytechnique de Montréal].

Hettler, A., & Vardoulakis, I. (1984). Behaviour of dry sand tested in a large triaxial apparatus. *Géotechnique*, *34*(2), 183–197.

Holtz, R. D., & Kovacs, W. D. (1981). *An introduction to geotechnical engineering*. Prentice Hall.

Holtz, W. G., & Gibbs, H. J. (1956). Triaxial shear tests on pervious gravelly soils. *Journal of the Soil Mechanics and Foundations Division*, *82*(1), 867–1–867–22.

Hu, W., Dano, C., Hicher, P.-Y., Le Touzo, J.-Y., Derkx, F., & Merliot, E. (2011). Effect of sample size on the behavior of granular materials. *Geotechnical Testing Journal*, *34*(3), 186–197.

Iabichino, G., Barbero, M., Cravero, M., Fidelibus, C., & Usai, G. (2014). Experimental tests for the assessment of the shear strength of marble waste dumps. *Environmental Earth Sciences*, *71*(7), 3259–3271.

Indraratna, B., Ionescu, D., & Christie, H. D. (1998). Shear behavior of railway ballast based on large-scale triaxial tests. *Journal of Geotechnical and Geoenvironmental Engineering*, *124*(5), 439–449.

Indraratna, B., Wijewardena, L. S. S., & Balasubramaniam, A. S. (1993). Large-scale triaxial testing of greywacke rockfill. *Géotechnique*, *43*(1), 37–51.

Jacobson, D. E., Valdes, J. R., & Evans, T. M. (2007). A numerical view into direct shear specimen size effects. *Geotechnical Testing Journal*, *30*(6), 512–516.

Jain, S. P., & Gupta, R. C. (1974). In-situ shear test for rock fills. *Journal of the Geotechnical Engineering Division*, *100*(9), 1031–1050.

James, M. (2009). *The use of waste rock inclusions to control the effects of liquefaction in tailings impoundments* [Doctoral dissertation, École Polytechnique de Montréal].

James, M., Aubertin, M., & Bussière, B. (2013). On the use of waste rock inclusions to improve the performance of tailings impoundments. *Proceedings of the 18th International conference soil mechanics and geotechnical engineering, Paris, France*, 2–6.

Jewell, R. A., & Wroth, C. P. (1987). Direct shear tests on reinforced sand. *37*(1), 53–68.

JGS 0530. (2015). *Preparation of specimens of coarse granular materials for triaxial tests*. Japanese Geotechnical Society (JGS).

Kang, X., Xia, Z., Chen, R., Ge, L., & Liu, X. (2019). The critical state and steady state of sand: a literature review. *Marine Georesources Geotechnology*, *37*(9), 1105–1118.

Klinkmüller, M., Schreurs, G., Rosenau, M., & Kemnitz, H. (2016). Properties of granular analogue model materials: a community wide survey. *Tectonophysics*, *684*, 23–38.

Klohn Leonoff Ltd. (1991). *Operation and Monitoring of Mine Dumps, Interim Guidelines*. British Columbia Mine Dump Committee.

Krumbein, W. C., & Sloss, L. L. (1963). *Stratigraphy and sedimentation* (2nd). Freeman; Company.

Lade, P. V. (2016). *Triaxial testing of soils*. John Wiley & Sons.

Lade, P. V., & Duncan, J. M. (1976). Stress-path dependent behavior of cohesionless soil. *Journal of the Geotechnical Engineering Division*, *102*(1), 51–68.

Lahmira, B., Lefebvre, R., Aubertin, M., & Bussière, B. (2016). Effect of heterogeneity and anisotropy related to the construction method on transfer processes in waste rock piles. *Journal of Contaminant Hydrology*, *184*, 35–49.

Lambe, W. T. (1967). Stress path method. *Journal of the Soil Mechanics and Foundations Division*, *93*(6), 309–331.

Lèbre, É., Corder, G., & Golev, A. (2017). The role of the mining industry in a circular economy: a framework for resource management at the mine site level. *Journal of Industrial Ecology*, *21*(3), 662–672.

Leps, T. M. (1970). Review of shearing strength of rockfill. *Journal of the Soil Mechanics and Foundations Division*, *96*(4), 1159–1170.

Leussink, H. (1960). *Bau eines grossen dreiaxialen shergerätes zur untersuchung grobkörniger erdstoffe (design of a large triaxial shear apparatus for investigating coarse grained soils)* (Vol. 1). Soil Mechanics Institute of the Karlsruhe Technical University Germany.

Li, G., Liu, Y.-J., Dano, C., & Hicher, P.-Y. (2015). Grading-dependent behavior of granular materials: from discrete to continuous modeling. *Journal of Engineering Mechanics*, *141*(6), 04014172.

Li, G., Ovalle, C., Dano, C., & Hicher, P.-Y. (2013). Influence of grain size distribution on critical state of granular materials. In Q. Yang, J.-M. Zhang, H. Zheng, & Y. Yao (Eds.), *Constitutive modeling of geomaterials* (pp. 207–210). Springer Berlin Heidelberg.

Linero, S., Bradfield, L., Fityus, S. G., Simmons, J. V., & Lizcano, A. (2020). Design of a 720-mm square direct shear box and investigation of the impact of boundary conditions on large-scale measured strength. *Geotechnical Testing Journal*, *43*(6).

Linero, S., Palma, C., & Apablaza, R. (2007). Geotechnical characterisation of waste material in very high dumps with large scale triaxial testing. In Y. Potvin (Ed.), *Slope stability 2007: proceedings of the 2007 international symposium on rock slope stability in open pit mining and civil engineering* (pp. 59–75). Australian Centre for Geomechanics.

Lini Dev, K., Pillai, R. J., & Robinson, R. G. (2016). Drained angle of internal friction from direct shear and triaxial compression tests. *International Journal of Geotechnical Engineering*, *10*(3), 283–287.

Liu, S. (2009). Application of in situ direct shear device to shear strength measurement of rockfill materials. *Water Science and Engineering*, *2*(3), 48–57.

Lottermoser, B. G. (2010). *Mine wastes: characterization, treatment and environmental impacts*. Springer: Berlin, Germany.

Lowe, J. (1964). Shear strength of coarse embankment dam materials. *Proc., 8th Int. Congress on Large Dams*, *3*, 745–761.

Majdanishabestari, K. (2023). *Slope stability analysis of high waste rock piles constructed by push/end dumping using 2d and 3d fem simulations* [Ph.D. Thesis]. Polytechnique Montréal.

Majdanishabestari, K., Girumugisha, G., Ovalle, C., Aubertin, M., & Saez, E. (2022). Slope stability and safety distance for mine waste rock piles built by end/push dumping. *75th Canadian Geotechnical Conference (GeoCalgary 2022)*.

Maknoon, M., & Aubertin, M. (2021). On the use of bench construction to improve the stability of unsaturated waste rock piles. *Geotechnical and Geological Engineering*, *39*(2), 1425–1449.

Maknoon, M. (2016, September). *Slope stability analyses of waste rock piles under unsaturated conditions following large precipitations* [Doctoral dissertation, École Polytechnique de Montréal].

Marachi, N. D., Chan, C. K., & Seed, H. B. (1972). Evaluation of properties of rockfill materials. *Journal of the Soil Mechanics and Foundations Division*, *98*(1), 95–114.

Marsal, R. J. (1967). Large scale testing of rockfill materials. *Journal of the Soil Mechanics and Foundations Division*, *93*(2), 27–43.

Marsal, R. J. (1968). Closure to "large scale testing of rockfill materials". *Journal of the Soil Mechanics and Foundations Division*, *94*(4), 1042–1047.

Martin, V. (2003). *Étude des propriétés non saturées des stériles miniers* [Master's thesis, École Polytechnique de Montréal].

Martin, V., Aubertin, M., & Lessard, G. (2019). An assessment of hydrogeological properties of waste rock using infiltration tests and numerical simulations. *GeoStJohn's*, *2019*, 72nd.

Matsuoka, H., & Liu, S. (1998). Simplified direct box shear test on granular materials and its application to rockfill materials. *Soils and Foundations*, *38*(4), 275–284.

Matsuoka, H., Liu, S., Sun, D., & Nishikata, U. (2001). Development of a new in-situ direct shear test. *Geotechnical Testing Journal*, *24*(1), 92–102.

McKeowen, R., Barbour, S. L., Rowlett, D., & Herasymuik, G. (2000). Characterization of the grain-size distribution for waste rock from metal mines–a review of existing grain size data and an evaluation of the implications for hydrogeologic behaviour. *Proceedings of the Canadian Society of Civil Engineers (CSCE) Annual Conference*, 203–209.

McLemore, V. T., Fakhimi, A., van Zyl, D., Ayakwah, G. F., Anim, K., Boakye, K., Ennin, F., Felli, P., Fredlund, D., & Gutierrez, L. A. (2009). Literature review of other rock piles: characterization, weathering, and stability. *J Questa Rock Pile Weathering Stability Project. New Mexico Bureau of Geology and Mineral Resources. New Mexico Tech, USA*.

MERN. (2016). Guidelines for preparing mine closure plans in Québec, Canada [Publication No: M08-03a-1711, ISBN: 978-2-550-79804-0]. *Ministère de l'Énergie et des Ressources naturelles (MERN)*.

Ministère de l'Environnement, de la Lutte contre les changements climatiques, de la Faune et des Parcs (MELCCFP). (2021). *Directive 019 sur l'industrie minière* [Disponible en ligne : https://www.quebec.ca/gouv/politiques-orientations/directives-environnementales/industrie-miniere-directive-019]. Gouvernement du Québec.

Mitchell, J. K., & Soga, K. (2005). *Fundamentals of soil behavior* (3rd). Wiley.

Morin, K. A., Gerencher, E., Jones, C. E., & Konasewich, D. E. (1991). *Critical literature review of acid drainage from waste rock* (Technical Report No. MEND (NEDEM) Project No. 1.11.1). CANMET, Department of Energy, Mines and Research Canada.

Mozaffari, M., Liu, W., & Ghafghazi, M. (2022). Influence of specimen nonuniformity and end restraint conditions on drained triaxial compression test results in sand. *Canadian Geotechnical Journal*, *59*(8), 1414–1426.

Mugele, L., Niemunis, A., & Stutz, H. H. (2024). Neohypoplasticity revisited. *International Journal for Numerical and Analytical Methods in Geomechanics*, *48*, 311–331.

Muir Wood, D., & Maeda, K. (2008). Changing grading of soil: effect on critical states. *Acta Geotechnica*, *3*(1), 3–14.

NAVFAC. (1982). *Soil mechanics, dm 7.1*. Naval Facilities Engineering Command.

Ning, F., Liu, J., Zou, D., Kong, X., & Cui, G. (2024). Super-large-scale triaxial tests to study the effects of particle size on the monotonic stress–strain response of rockfill materials. *Acta Geotechnica*.

Oldecop, L., & Alonso, E. (2003). Suction effects on rockfill compressibility. *Géotechnique*, *53*(2), 289–292.

Osses, R., Majdanishabestari, K., Ovalle, C., & Pineda, J. (2021). Testing and modelling total suction effects on compressibility and creep of crushable granular material. *Soils and Foundations*, *61*(6), 1581–1596.

Osses, R., Pineda, J., Ovalle, C., Linero, S., & Sáez, E. (2024). Scale and suction effects on compressibility and time-dependent deformation of mine waste rock material. *Engineering Geology*, *340*, 107668.

Ouellet, S., Chapuis, S., & Ovalle, C. (2021). Le projet de co-déposition dans la fosse canadian malartic. *Symposium Rouyn-Noranda 2021 sur l'environnement et les mines*.

Ovalle, C. (2018). Role of particle breakage in primary and secondary compression of wet and dry sand. *Géotechnique Letters*, *8*(2), 161–164.

Ovalle, C., Girumugisha, G., Cantor, D., & Ouellet, S. (2023). Size effects assessment of mine waste-rock shear strength combining numerical, laboratory and in situ approaches [Place: Perth]. In P. Dight (Ed.), *SSIM 2023: Third International Slope Stability in Mining Conference* (pp. 291–300). Australian Centre for Geomechanics.

Ovalle, C. (2013). *Contribution à l'étude d la rupture des grains dans les matériaux ranulaires* [Thesis]. Ecole Centrale de Nantes (ECN).

Ovalle, C., Dano, C., Hicher, P.-Y., & Cisternas, M. (2015). Experimental framework for evaluating the mechanical behavior of dry and wet crushable granular materials based on the particle breakage ratio. *Canadian Geotechnical Journal*, *52*(5), 587–598.

Ovalle, C., Frossard, E., Dano, C., Hu, W., Maiolino, S., & Hicher, P.-Y. (2014). The effect of size on the strength of coarse rock aggregates and large rockfill samples through experimental data. *Acta Mechanica*, *225*(8), 2199–2216.

Ovalle, C., & Hicher, P.-Y. (2020). Modeling the effect of wetting on the mechanical behavior of crushable granular materials [Grain Crushing in Geoscience Materials]. *Geoscience Frontiers*, *11*(2), 487–494.

Ovalle, C., Linero, S., Dano, C., Bard, E., Hicher, P.-Y., & Osses, R. (2020). Data compilation from large drained compression triaxial tests on coarse crushable rockfill materials. *Journal of Geotechnical and Geoenvironmental Engineering*, *146*(9), 06020013.

Oyanguren, P. R., Nicieza, C. G., Fernández, M. Á., & Palacio, C. G. (2008). Stability analysis of llerin rockfill dam: an in situ direct shear test. *Engineering Geology*, *100*(3-4), 120–130.

Parsons, J. D. (1936). Progress report on an investigation of the shearing resistance of cohesionless soils. *1st Int. Conf. on Soil Mechanics and Foundation Engineering*, *2*, 133–138.

Peregoedova, A. (2012, October). *Étude expérimentale des propriétés hydrogéologiques des roches stériles à une échelle intermédiaire de laboratoire* [Master's thesis, École Polytechnique de Montréal].

Peri, E., Ibsen, L. B., & Nordahl Nielsen, B. (2019). Influence of sample slenderness and boundary conditions in triaxial test - a review. *E3S Web Conf.*, *92*, 02009.

Phoon, K.-K., & Kulhawy, F. H. (1999). Evaluation of geotechnical property variability. *Canadian Geotechnical Journal*, *36*(4), 625–639.

Piteau Engineering Ltd. (1991). *Mined Rock and Overburden Piles, Investigation and Design Manual, Interim Guidelines*. British Columbia Mine Dump Committee.

Polanía, O., Cabrera, M., Renouf, M., Azéma, E., & Estrada, N. (2023). Grain size distribution does not affect the residual shear strength of granular materials: an experimental proof. *Physical Review E*, *107*(5), L052901.

Qiu, P., & Pabst, T. (2023). Characterization of particle size segregation and heterogeneity along the slopes of a waste rock pile using image analysis. *Environmental Earth Sciences*, *82*(23), 573.

Qiu, P., & Pabst, T. (2024). Effect of construction method and bench height on particle size segregation during waste rock disposal. *International Journal of Mining, Reclamation and Environment*, *38*(9), 677–700.

Quezada, J. C., & Villavicencio, G. (2024). Characterisation of the internal friction angle of waste rock material from large triaxial tests using the contact dynamics method. *International Journal of Mining, Reclamation and Environment*, 1–20.

Quiroz-Rojo, P., Cantor, D., Renouf, M., Ovalle, C., & Azéma, E. (2024). REV assessment of granular materials with varied grading based on macro- and micro-mechanical statistical data. *Acta Geotechnica*.

Raju, V., Sadasivan, S., & Venkataraman, M. (1972). Use of lubricated and conventional end platens in triaxial tests on sands. *Soils and Foundations*, *12*(4), 35–43.

Raymond, K. E., Seigneur, N., Su, D., & Mayer, K. U. (2021). Investigating the influence of structure and heterogeneity in waste rock piles on mass loading rates—a reactive transport modeling study. *Frontiers in Water*, *3*.

Razavi, S. K. (2023, December). *Constitutive modeling of flow liquefaction of tailings* [Doctoral dissertation, Polytechnique Montréal].

Rodriguez, J. M., Johansson, J. M. A., & Edeskar, T. (2012). Particle shape determination by two-dimensional image analysis in geotechnical engineering. *Proceedings of the Nordic Conference on Soil Mechanics and Geotechnics*, 207–218.

Roscoe, K. H., Schofield, A. N., & Wroth, C. P. (1958). On the yielding of soils. *Géotechnique*, *8*(1), 22–53.

Rowe, P. W. (1962). The Stress-Dilatancy Relation for Static Equilibrium of an Assembly of Particles in Contact. *Proceedings of the Royal Society of London Series A*, *269*(1339), 500–527.

Rowe, P. W., & Barden, L. (1964). Importance of free ends in triaxial testing. *Journal of the Soil Mechanics and Foundations Division*, *90*(1), 1–27.

Roy, M., & Lo, K. (1971). Effect of end restraint on high pressure tests of granular materials. *Canadian Geotechnical Journal*, *8*(4), 579–588.

Schmertmann, J. H. (1978). *Guidelines for cone penetration test performance and design* (Report No. FHWA-TS-78-209). U.S. Department of Transportation. Washington, DC.

Schultze, E. (1957). Large-scale shear tests. *Proc. of the Fourth International Conference on Soil Mechanics and Foundation Engineering*, *1*, 193–199.

Seed, H. B., & Goodman, R. E. (1964). Earthquake stability of slopes of cohesionless soils. *Journal of the Soil Mechanics and Foundations Division*, *90*(6), 43–74.

Shibuya, S., Mitachi, T., & Tamate, S. (1997). Interpretation of direct shear box testing of sands as quasi-simple shear. *Géotechnique*, *47*(4), 769–790.

SME. (2011). *SME mining engineering handbook* (P. Darling, Ed.; 3rd).

Smith, L. J., Blowes, D. W., Jambor, J. L., Smith, L., Sego, D. C., & Neuner, M. (2013). The diavik waste rock project: particle size distribution and sulfur characteristics of low-sulfide waste rock. *Applied Geochemistry*, *36*, 200–209.

Stark, T. D., Swan Jr, R. H., & Yuan, Z. (2014). Ballast direct shear testing. *ASME/IEEE Joint Rail Conference*, *45356*, V001T01A003.

Statistics Canada. (2022). Table 38-10-0285-01: natural resources satellite account, indicators (x 1,000,000) [Accessed [December 2024]].

Terzaghi, K., Peck, R. B., & Mesri, G. (1996). *Soil mechanics in engineering practice* (3rd ed.). Wiley-Interscience.

TolouKian, A. R., Sadeghi, J., & Zakeri, J.-A. (2018). Large-scale direct shear tests on sand-contaminated ballast. *Proceedings of the Institution of Civil Engineers - Geotechnical Engineering*, *171*(5), 451–461.

USGS (Ed.). (2022). *Mineral commodity summaries* (3rd). U.S. Geological Survey (USGS).

Valenzuela, L., Bard, E., Campaña, J., & Anabalón, M. (2008). High Waste Rock Dumps — Challenges and Developments [Place: Perth]. In A. Fourie (Ed.), *Rock Dumps 2008: Proceedings of the First International Seminar on the Management of Rock Dumps, Stockpiles and Heap Leach Pads* (pp. 65–78). Australian Centre for Geomechanics.

Varadarajan, A., Sharma, K. G., Venkatachalam, K., & Gupta, A. K. (2003). Testing and modeling two rockfill materials. *Journal of Geotechnical and Geoenvironmental Engineering*, *129*(3), 206–218.

Varadarajan, A., Sharma, K., Abbas, S., & Dhawan, A. (2006). The role of nature of particles on the behaviour of rockfill materials. *Soils and Foundations*, *46*(5), 569–584.

Verdugo, R., & de la Hoz, K. (2007). Strength and stiffness of coarse granular soils. In H. I. Ling, L. Callisto, D. Leshchinsky, & J. Koseki (Eds.), *Soil stress-strain behavior: measurement, modeling and analysis* (pp. 243–252). Springer Netherlands.

Verdugo, R., & Ishihara, K. (1996). The steady state of sandy soils. *Soils and Foundations*, *36*(2), 81–91.

Voivret, C., Radjaï, F., Delenne, J. Y., & El Youssoufi, M. S. (2009). Multiscale force networks in highly polydisperse granular media. *Physical Review Letters*, *102*(17), 178001.

Wadell, H. (1932). Volume, shape, and roundness of rock particles. *The Journal of Geology*, *40*(5), 443–451.

Weibull, W. (1939). A statistical theory of the strength of materials. *Proceedings of the Royal Swedish Institute for Engineering Research*, *151*, 1–45.

Wightman, A., Dickinson, S., Jeong, C.-G., Shanmugarajah, T., & Billings, M. (2024). Importance of sample height–diameter ratio in triaxial testing with free ends for determination of the critical state of sands. *Geotechnical Testing Journal*, *48*(2).

Wijeyesekera, D. C., Siang, A. J. L. M., & Yahaya, A. S. B. (2013). Advanced statistical analysis for relationships between particle morphology (size and shape) and shear (static and dynamic) characteristics of sands. *International Journal of Geosciences*, *04*(10), 27–36.

Wilson, J., Wilson, G., & Fredlund, D. (2000). Numerical modeling of vertical and inclined waste rock layers. *Proc 5th Int Conf Acid Rock Drainage, Society for Mining, Metallurgy & Exploration, Inc.(SME), Denver*, 257–266.

Wilson, S. D., & Squier, R. (1969). Earth and rockfill dams. *11th Int. Conf. on Soil Mech. and Found. Engrg.*

Wu, M., Wang, J., Russell, A., & Cheng, Z. (2021). DEM modelling of mini-triaxial test based on one-to-one mapping of sand particles. *Géotechnique*, *71*(8), 714–727.

Xiao, Y., Long, L., Evans, T. M., Zhou, H., Liu, H., & Stuedlein, A. W. (2019). Effect of particle shape on stress-dilatancy responses of medium-dense sands. *Journal of Geotechnical and Geoenvironmental Engineering*, *145*(2), 04018105.

Xu, Y., Williams David, J., Serati, M., & Vangsness, T. (2018). Effects of scalping on direct shear strength of crusher run and crusher run/geogrid interface. *Journal of Materials in Civil Engineering*, *30*(9), 04018206.

Yang, J., & Luo, X. D. (2015). Exploring the relationship between critical state and particle shape for granular materials. *Journal of the Mechanics and Physics of Solids*, *84*, 196–213.

Yang, J., & Luo, X. D. (2018). The critical state friction angle of granular materials: does it depend on grading? *Acta Geotechnica*, *13*(3), 535–547.

Yang, P., Li, L., & Aubertin, M. (2018). Theoretical and numerical analyses of earth pressure coefficient along the centerline of vertical openings with granular fills. *Applied Sciences*, *8*(10), 1721.

Zeller, J., & Wullimann, R. (1957). The shear strength of the shell materials for the go-schenenalp dam, switzerland. *4th International Conference on Soil Mechanics and Foundation Engineering*, *2*, 399–415.

Zevgolis, I. E. (2018). Geotechnical characterization of mining rock waste dumps in central evia, greece. *Environmental Earth Sciences*, *77*(16).

Zhang, X., Baudet, B. A., & Yao, T. (2020). The influence of particle shape and mineralogy on the particle strength, breakage and compressibility. *International Journal of Geo-Engineering*, *11*(1).

Zheng, J., & Hryciw, R. D. (2015). Traditional soil particle sphericity, roundness and surface roughness by computational geometry. *Géotechnique*, *65*(6), 494–506.

Zheng, J., & Hryciw, R. (2016). Roundness and sphericity of soil particles in assemblies by computational geometry. *Journal of Computing in Civil Engineering*, *30*(6), 04016021.

Zheng, J., & Hryciw, R. D. (2018). Identification and characterization of particle shapes from images of sand assemblies using pattern recognition. *Journal of Computing in Civil Engineering*, *32*(3), 04018016.

APPENDICES

APPENDIX A – Additional figures of CTC test results of WR specimens

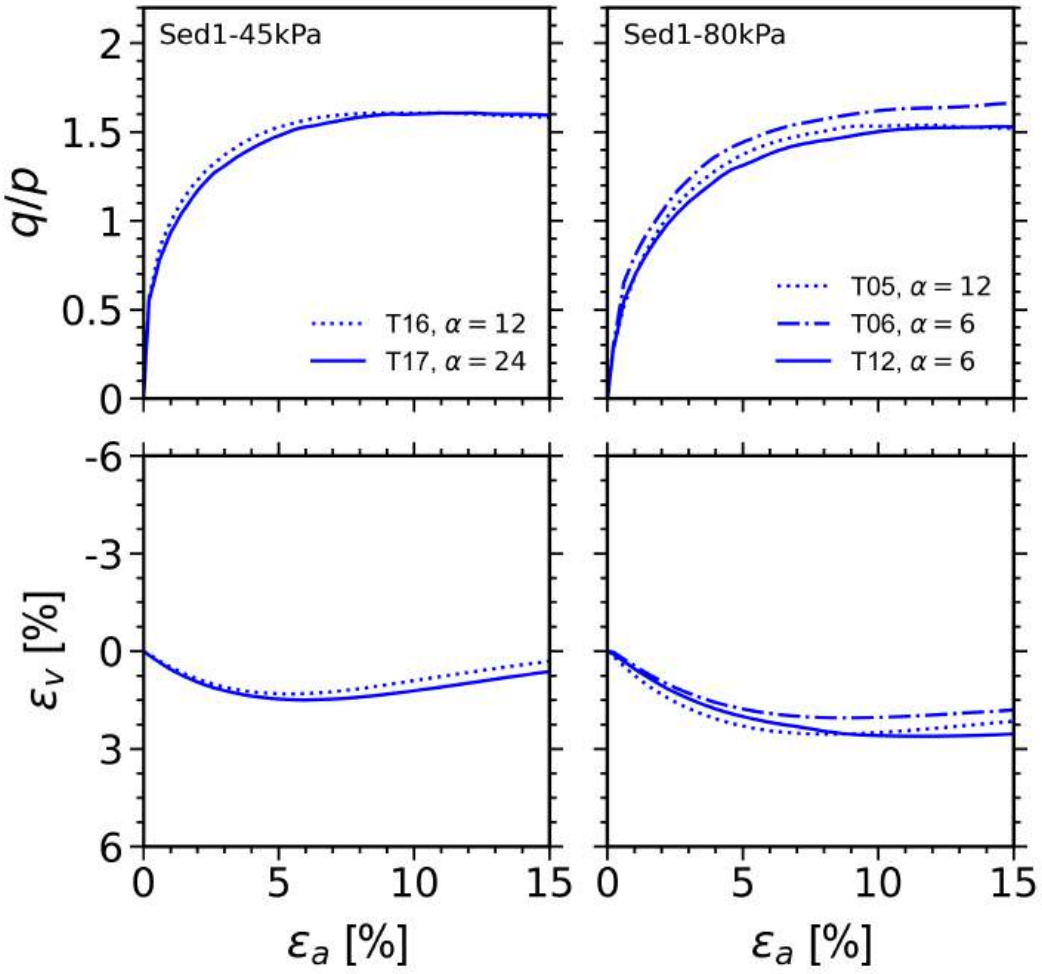

Figure 8.1 Stress-strain curves for Sed1 specimens tested at $\sigma_3' = 45$ kPa (*left*) and $\sigma_3' = 80$ kPa (*right*).

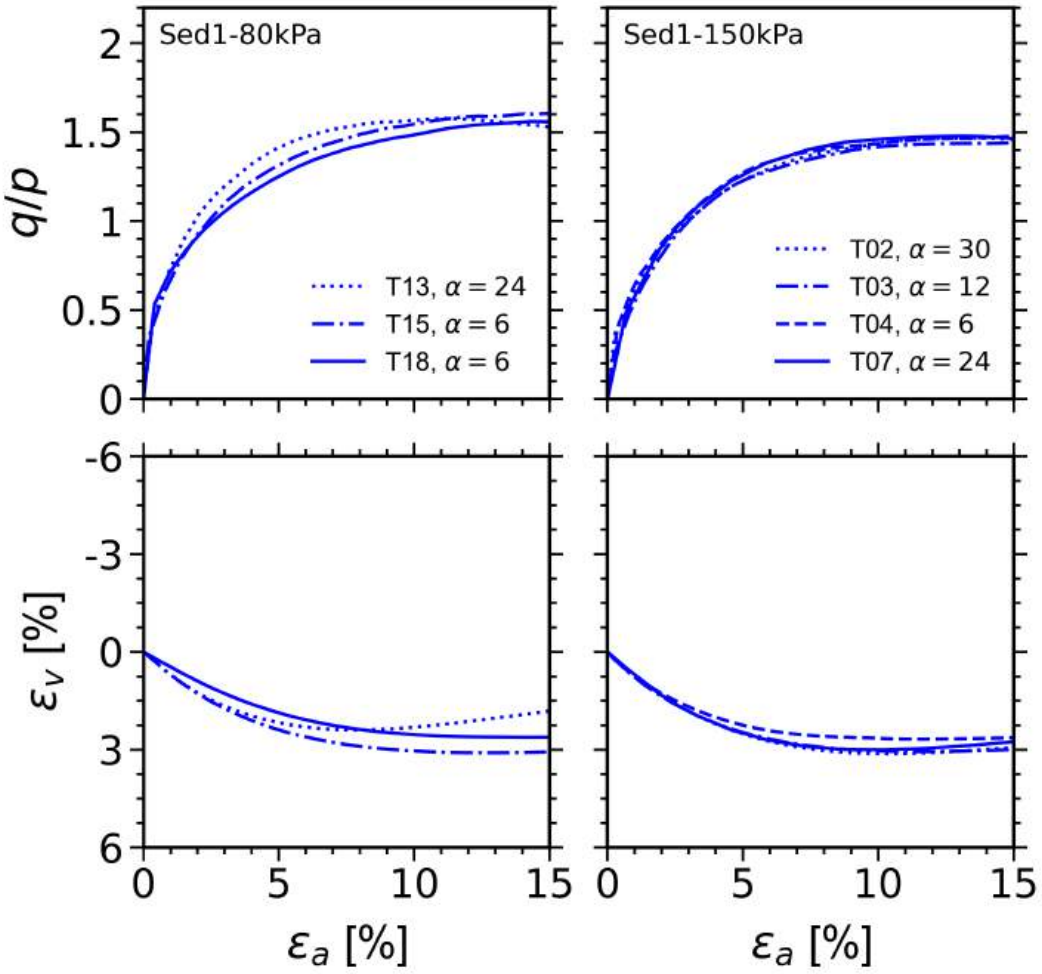

Figure 8.2 Stress-strain curves for Sed1 specimens tested at $\sigma'_3 = 80$ kPa (*continued*) (*left*) and $\sigma'_3 = 150$ kPa (*right*).

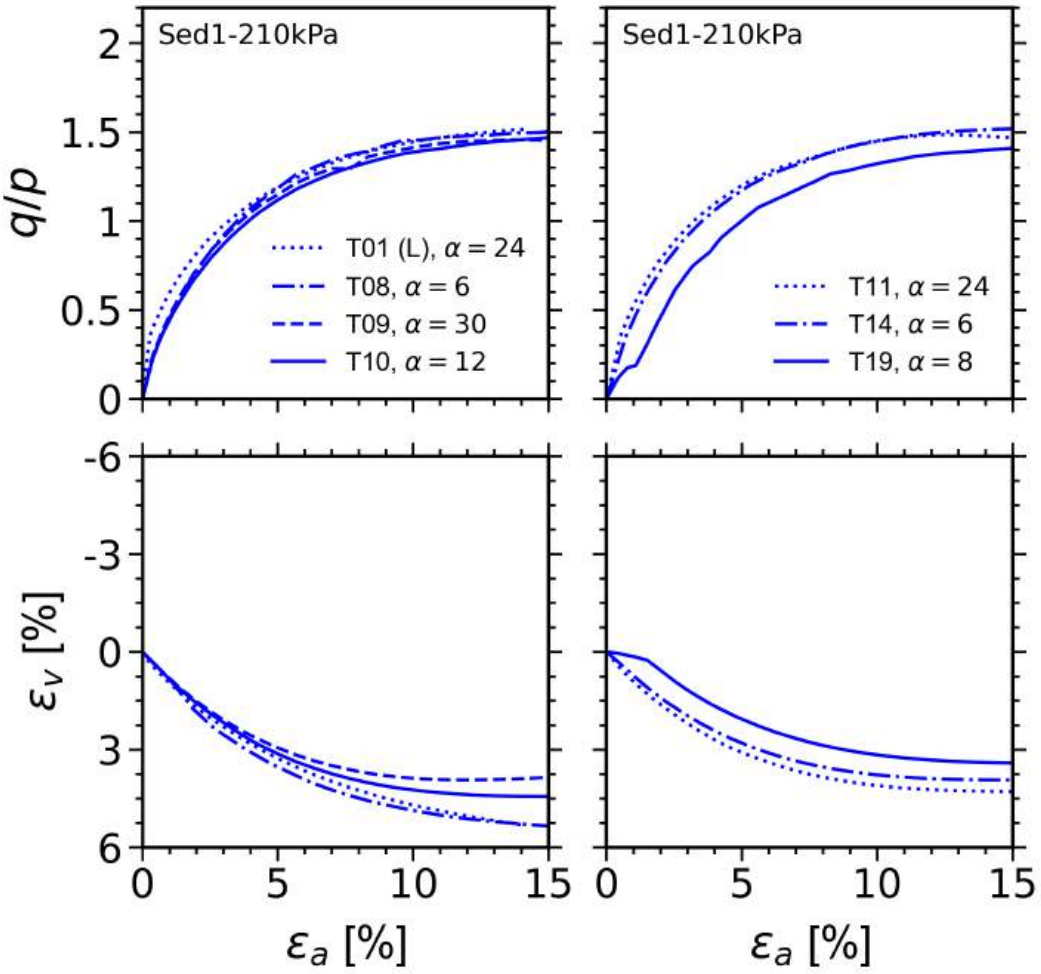

Figure 8.3 Stress-strain curves for Sed1 specimens tested at $\sigma_3' = 210$ kPa.

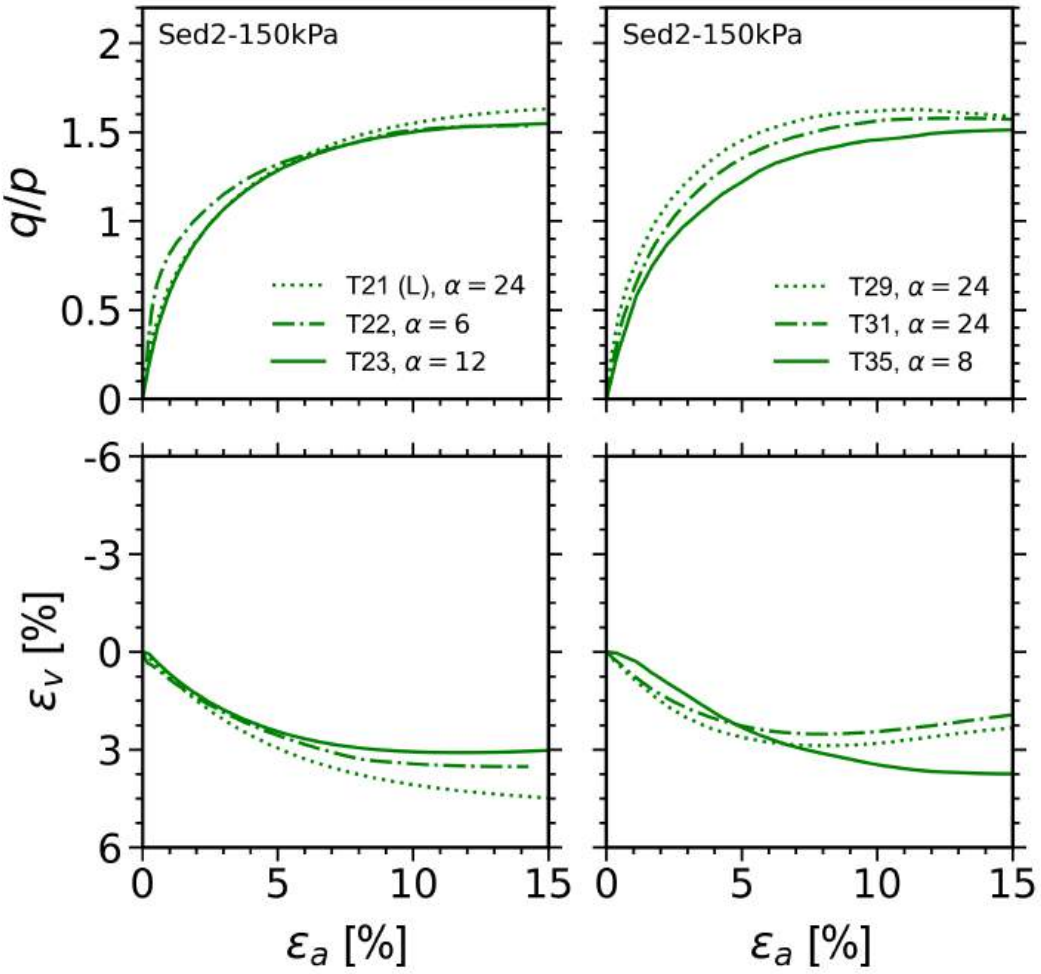

Figure 8.4 Stress-strain curves for Sed2 specimens tested at $\sigma_3' = 150$ kPa.

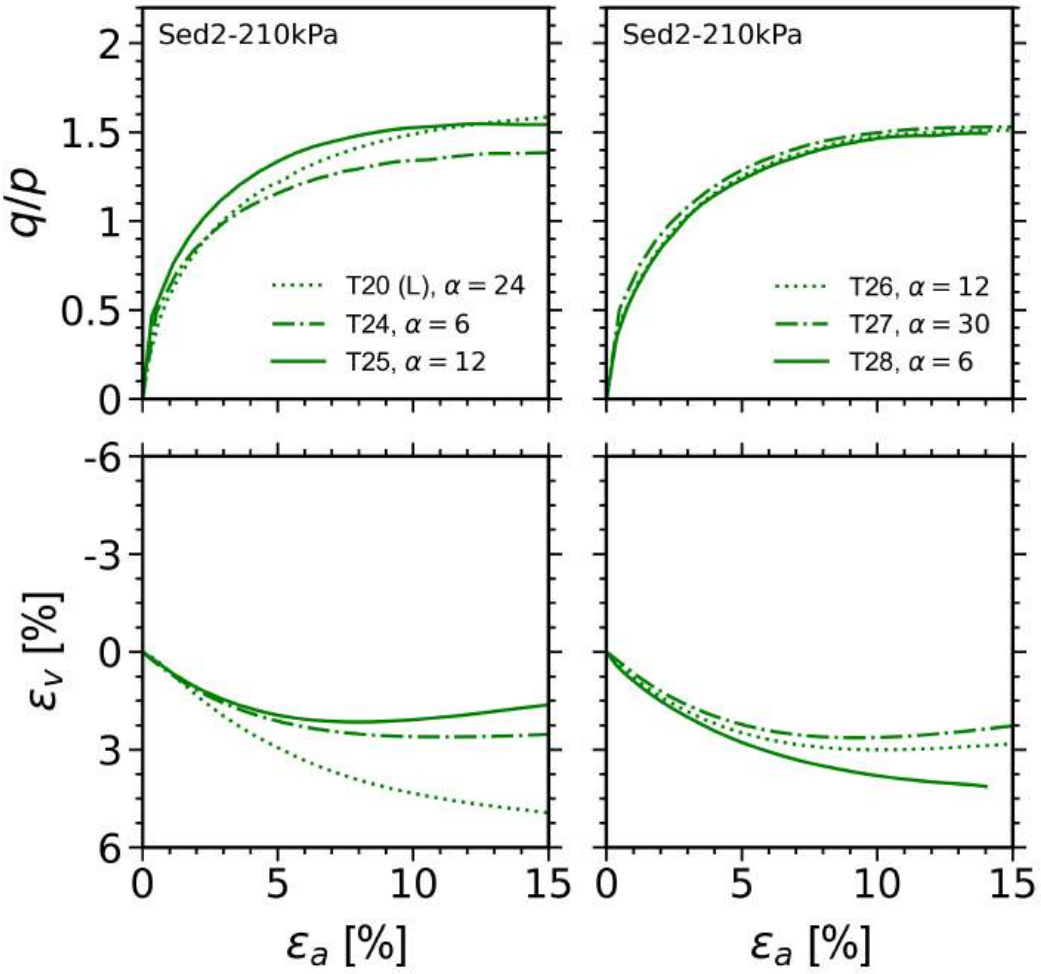

Figure 8.5 Stress-strain curves for Sed2 specimens tested at $\sigma_3' = 210$ kPa.

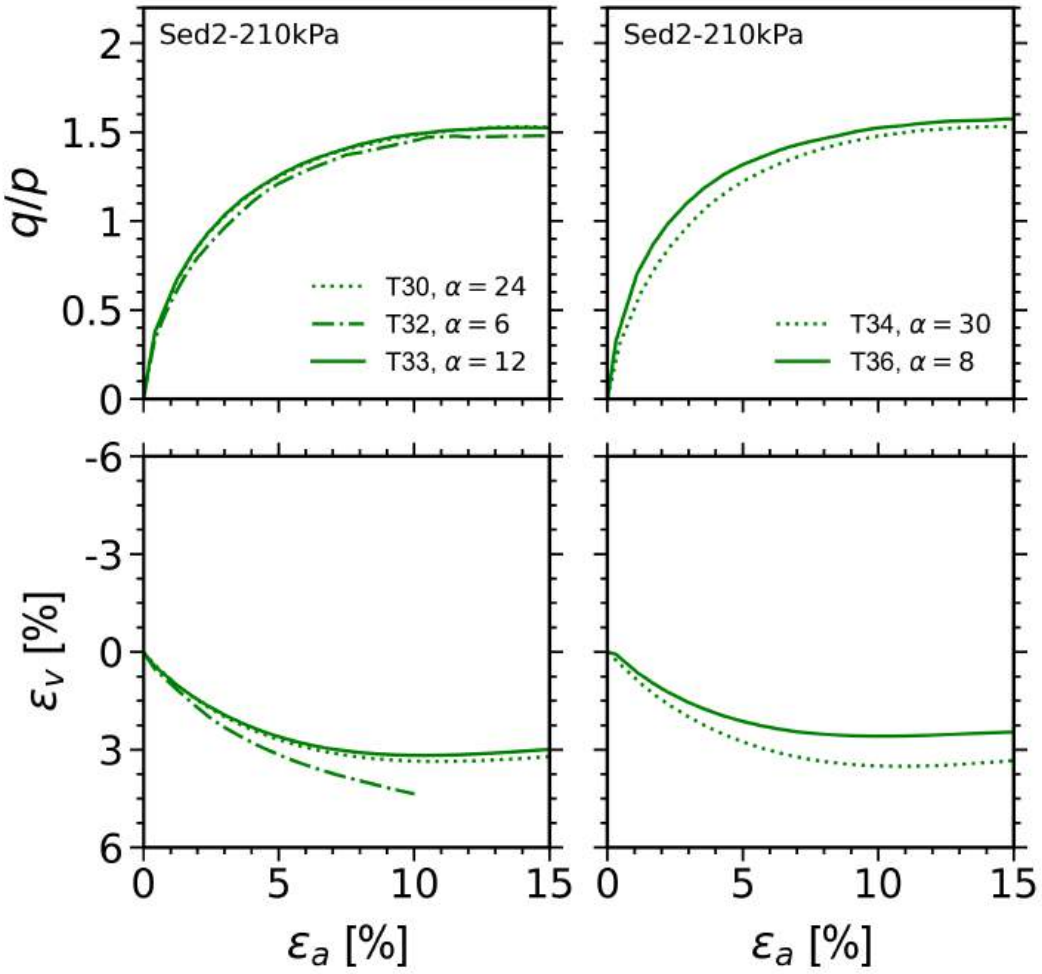

Figure 8.6 Stress-strain curves for Sed2 specimens tested at $\sigma_3' = 210$ kPa (*continued*).

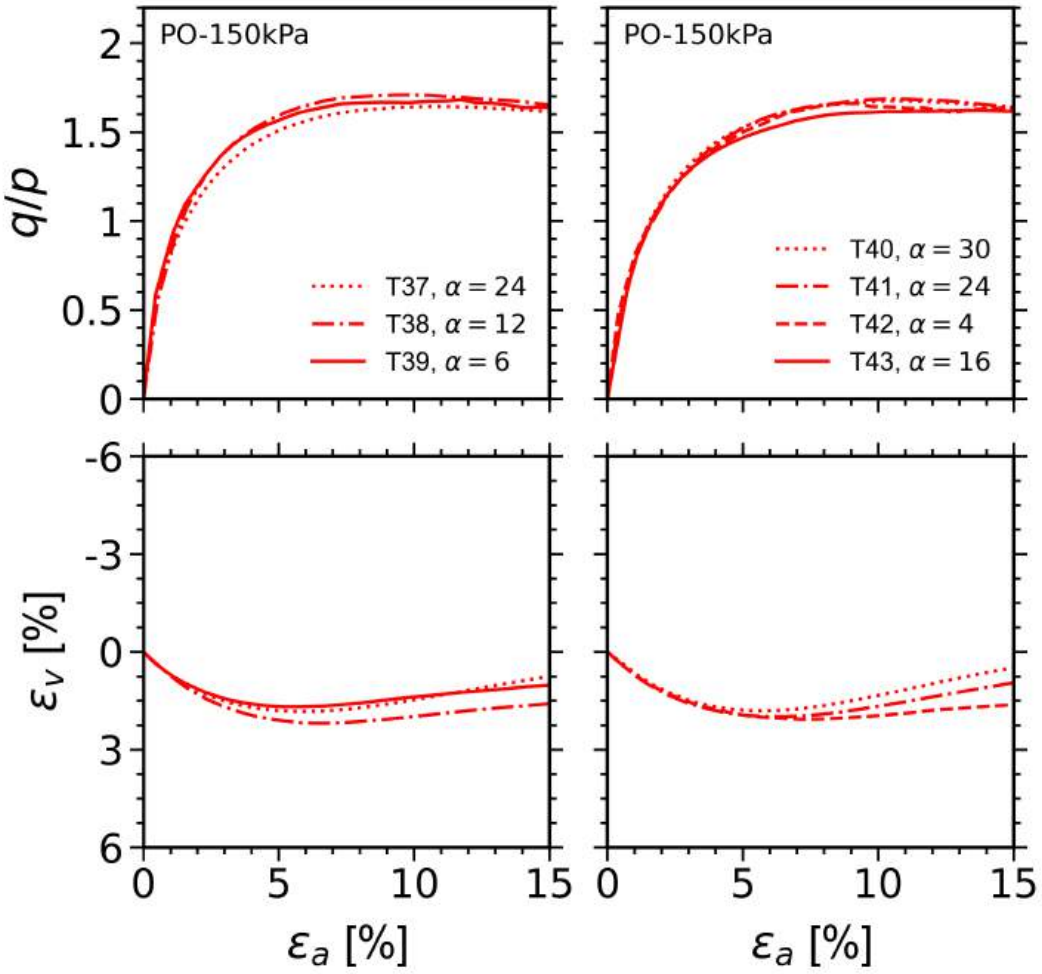

Figure 8.7 Stress-strain curves for loose PO specimens tested at $\sigma_3' = 150$ kPa.

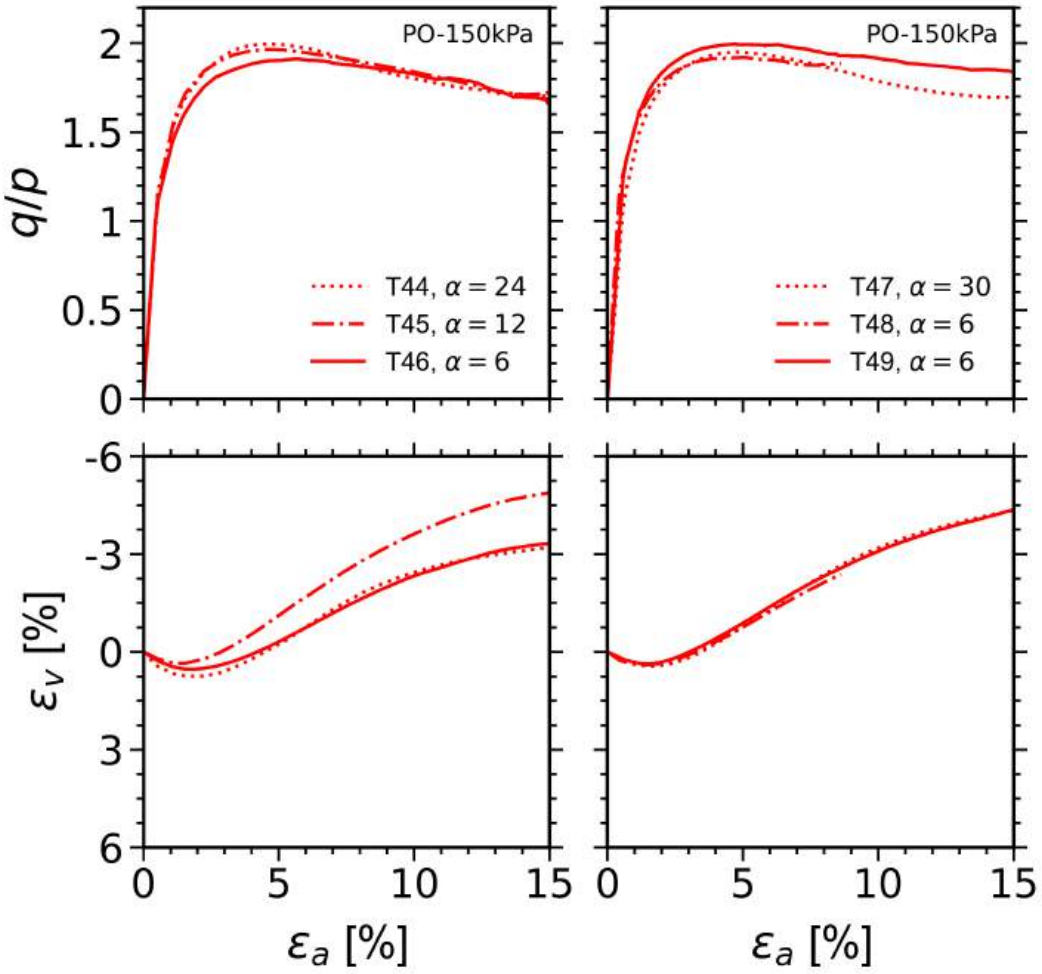

Figure 8.8 Stress-strain curves for dense PO specimens tested at $\sigma_3' = 150$ kPa.

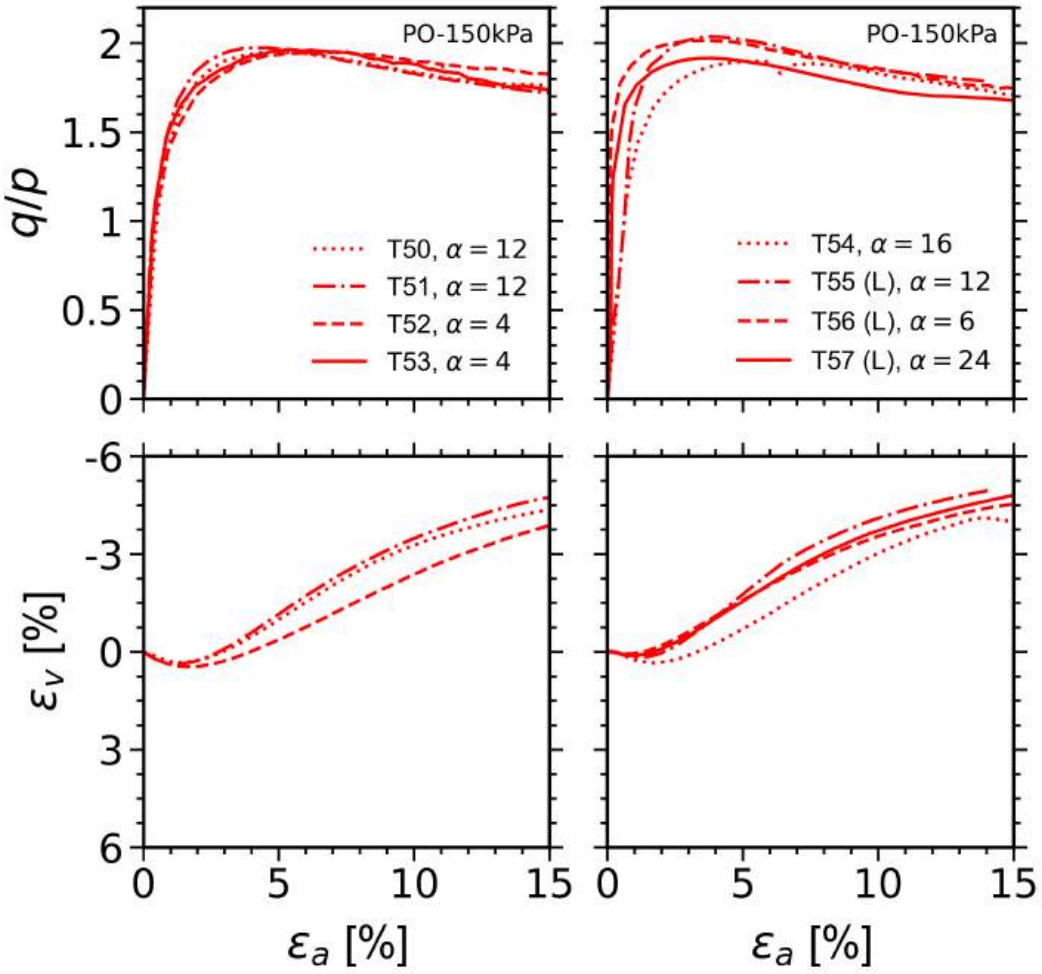

Figure 8.9 Stress-strain curves for dense PO specimens tested at $\sigma'_3 = 150$ kPa (*continued*): (L) designate large specimens having a diameter D=300 mm.

APPENDIX B – Additional figures of in-situ DST results of WR specimens

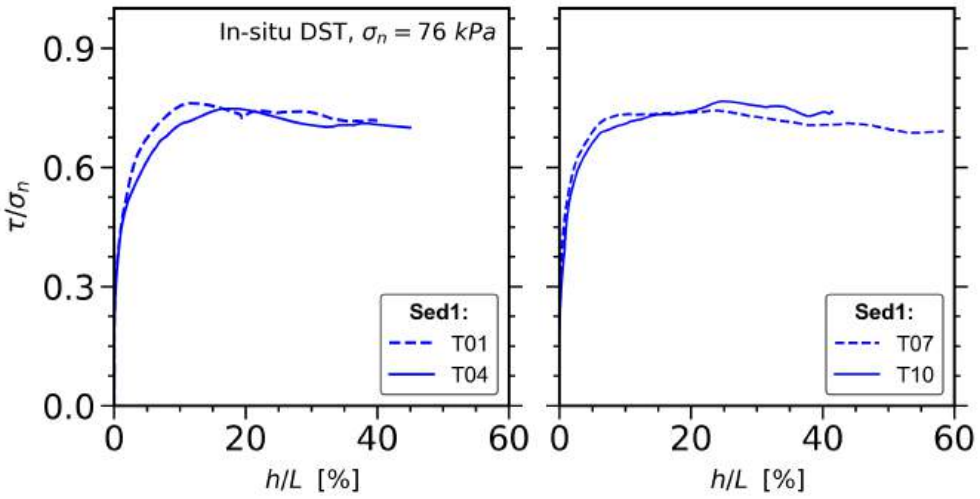

Figure 8.10 Stress ratio-normalized deformation curves for Sed1 DST specimens tested at $\sigma_n = 76$ kPa.

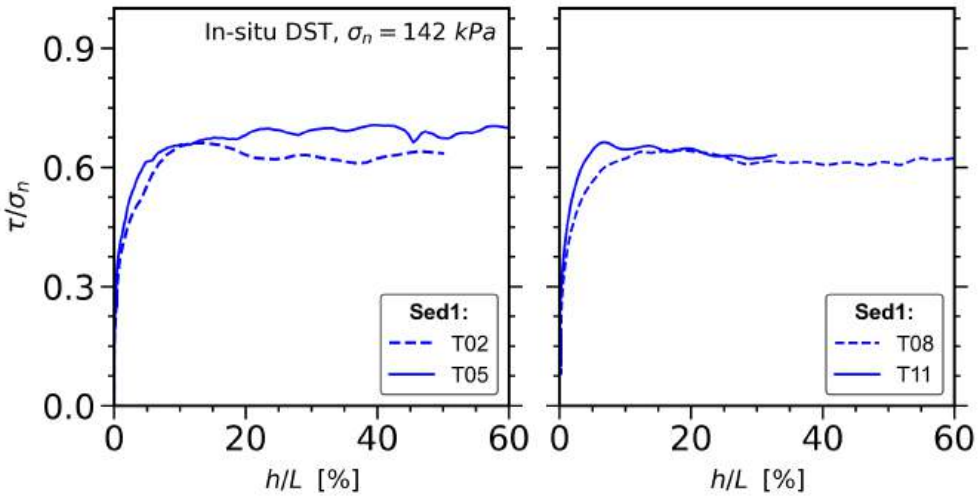

Figure 8.11 Stress ratio-normalized deformation curves for Sed1 DST specimens tested at $\sigma_n = 142$ kPa.

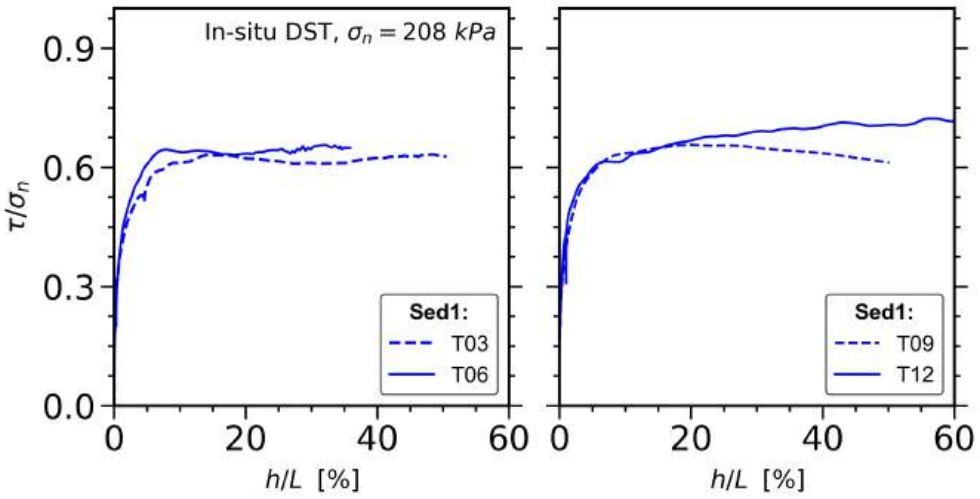

Figure 8.12 Stress ratio-normalized deformation curves for Sed1 DST specimens tested at $\sigma_n = 208$ kPa.

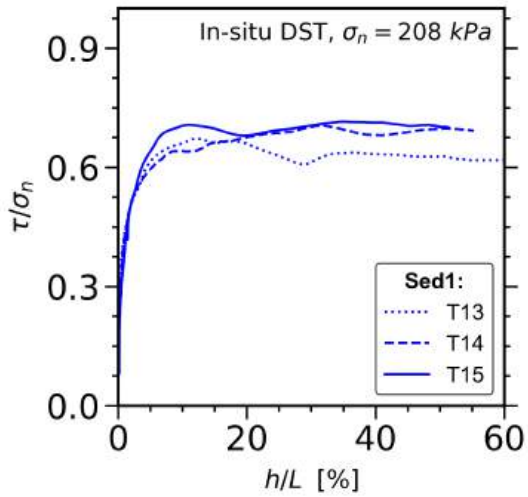

Figure 8.13 Stress ratio-normalized deformation curves for Sed1 DST specimens tested at $\sigma_n = 208$ kPa (*continued*).

APPENDIX C – Additional figures of CTC test results of quarry rockfill specimens

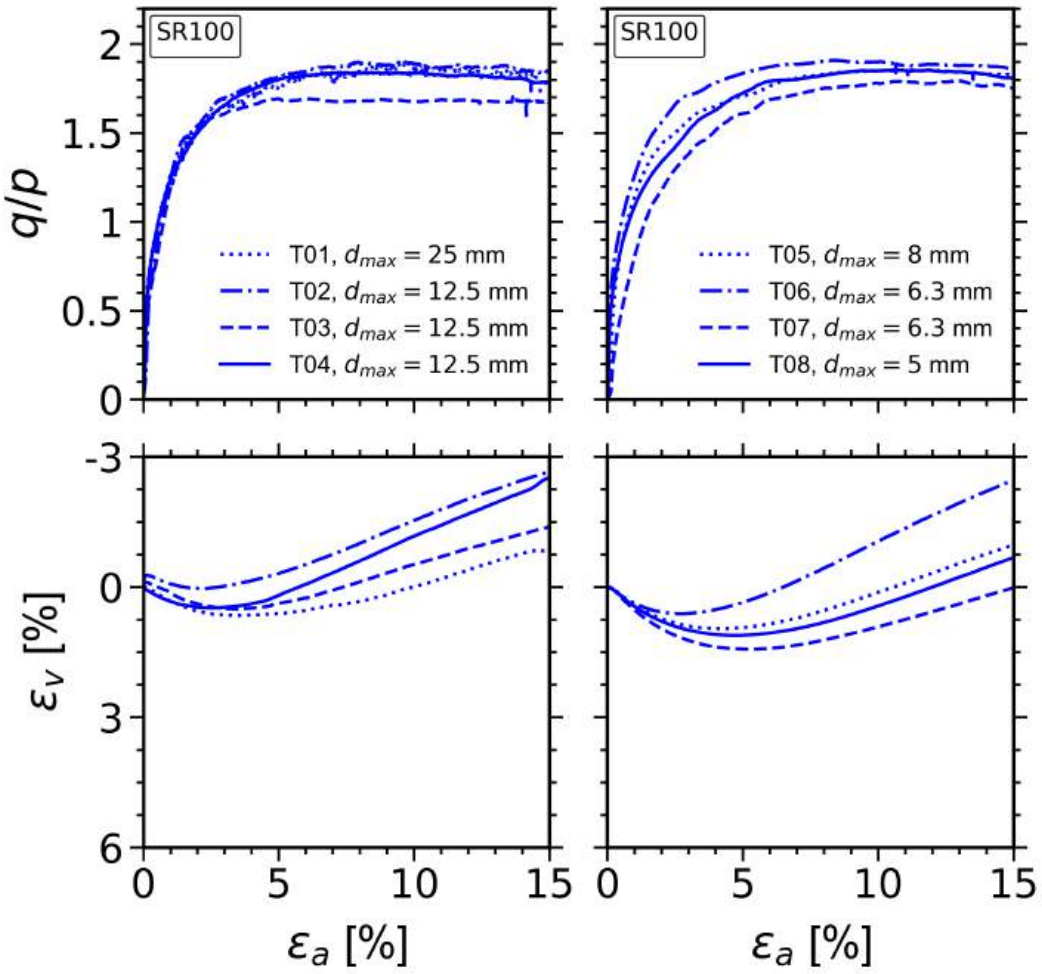

Figure 8.14 Stress-strain curves of scalped quarry rockfill specimens, tested at $\sigma'_3 = 100$ kPa using standard rough platens (SR100).

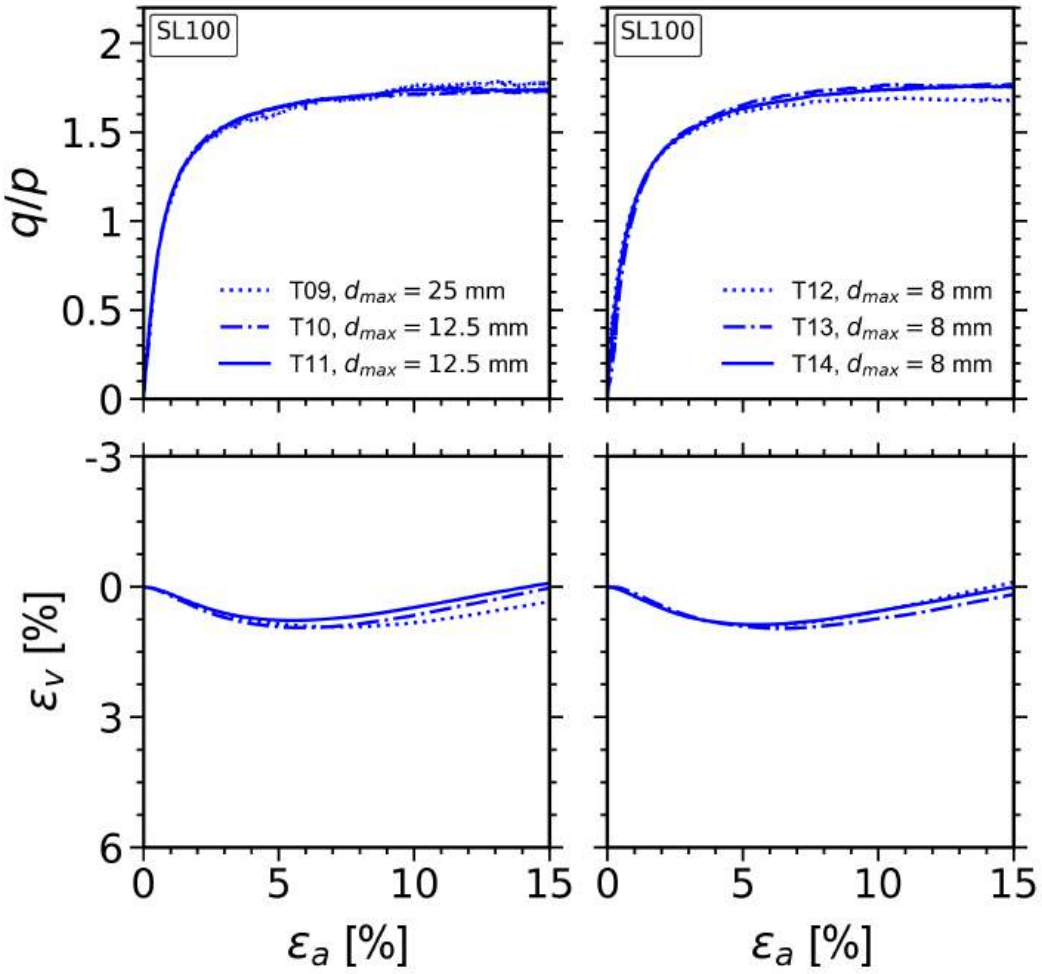

Figure 8.15 Stress-strain curves of scalped quarry rockfill specimens, tested at $\sigma'_3 = 100$ kPa using lubricated platens (SL100).

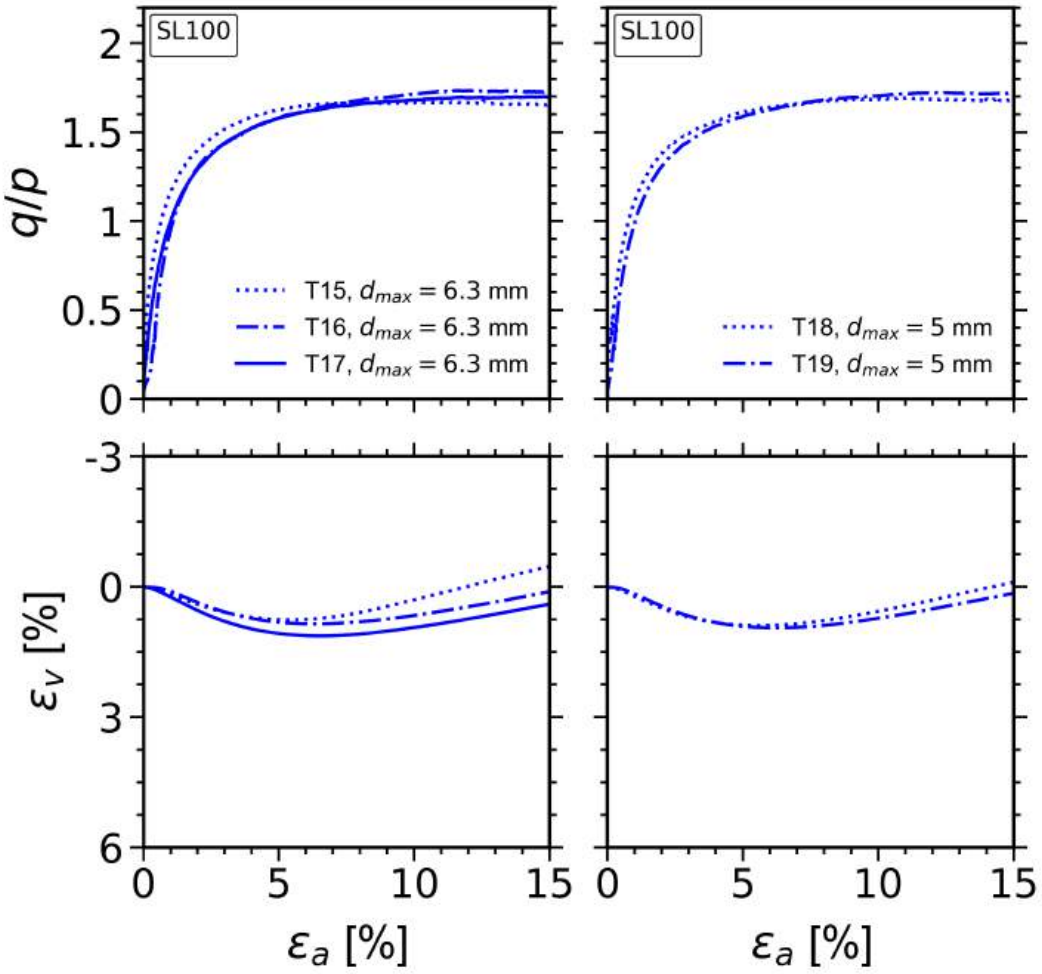

Figure 8.16 Stress-strain curves of SL100 (*continued*).

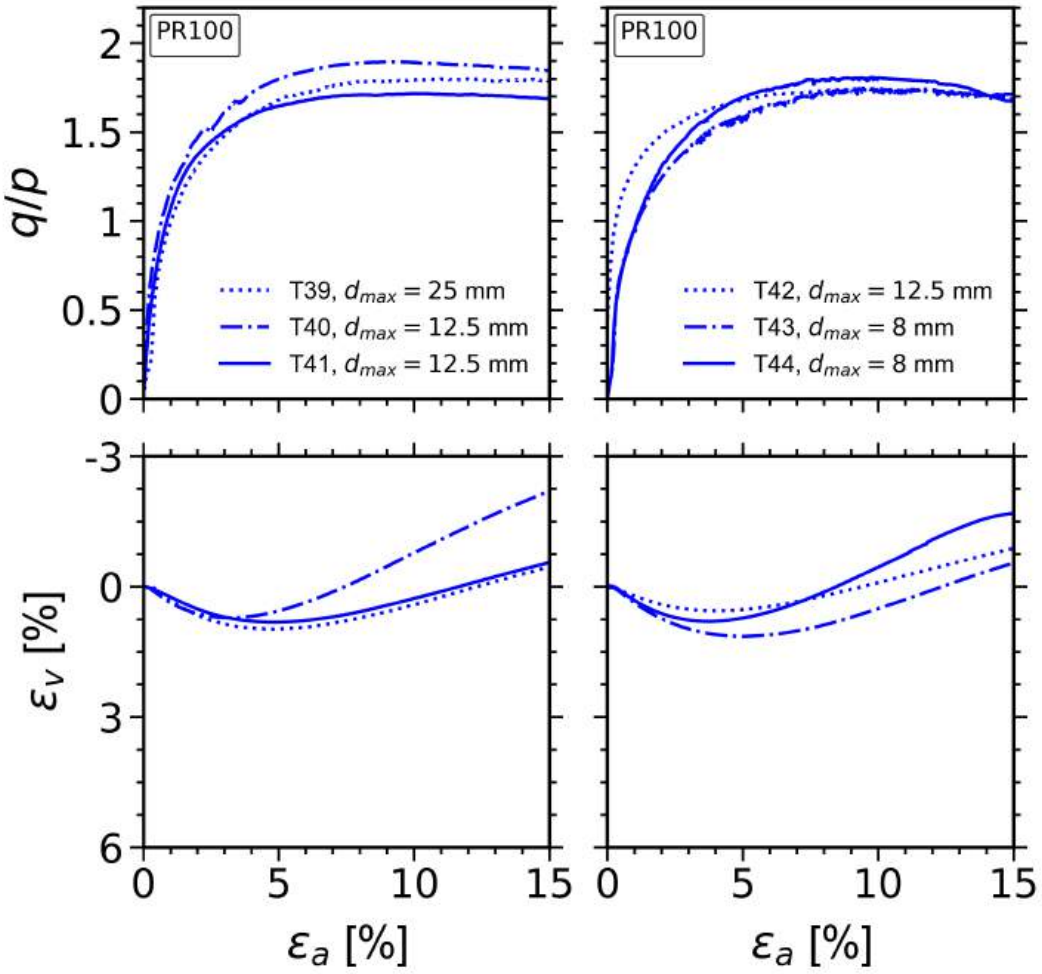

Figure 8.17 Stress-strain curves of parallel-graded quarry rockfill specimens, tested at σ'_3 = 100 kPa using standard rough platens (PR100).

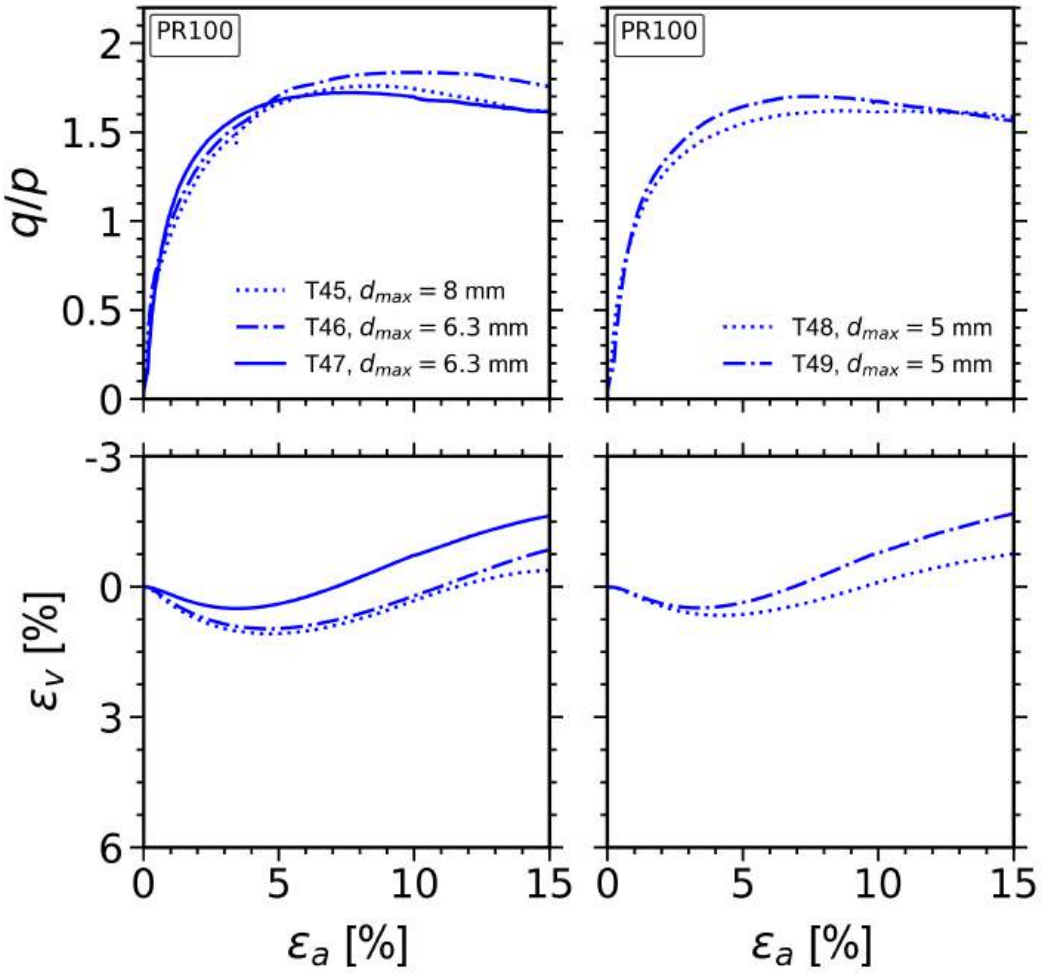

Figure 8.18 Stress-strain curves of PR100 (*continued*).

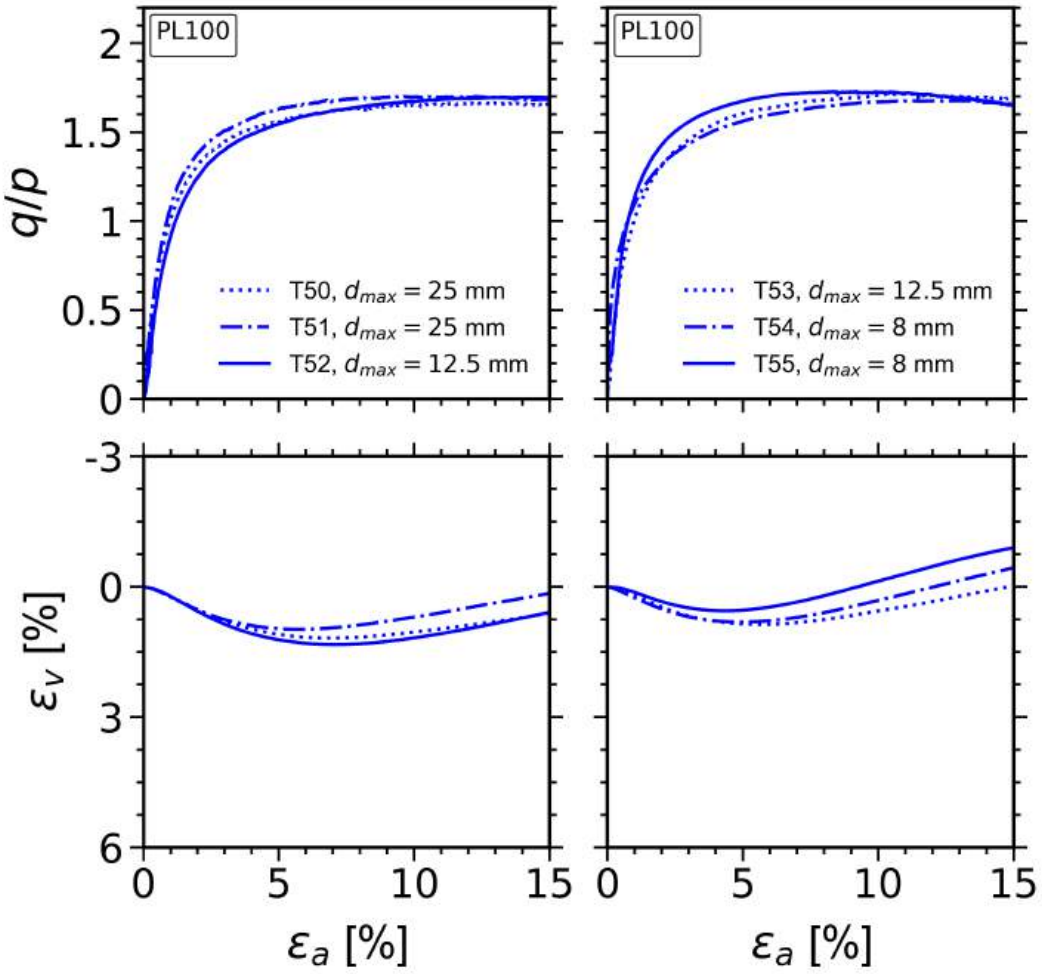

Figure 8.19 Stress-strain curves of parallel-graded quarry rockfill specimens, tested at σ'_3 = 100 kPa using lubricated platens (PL100).

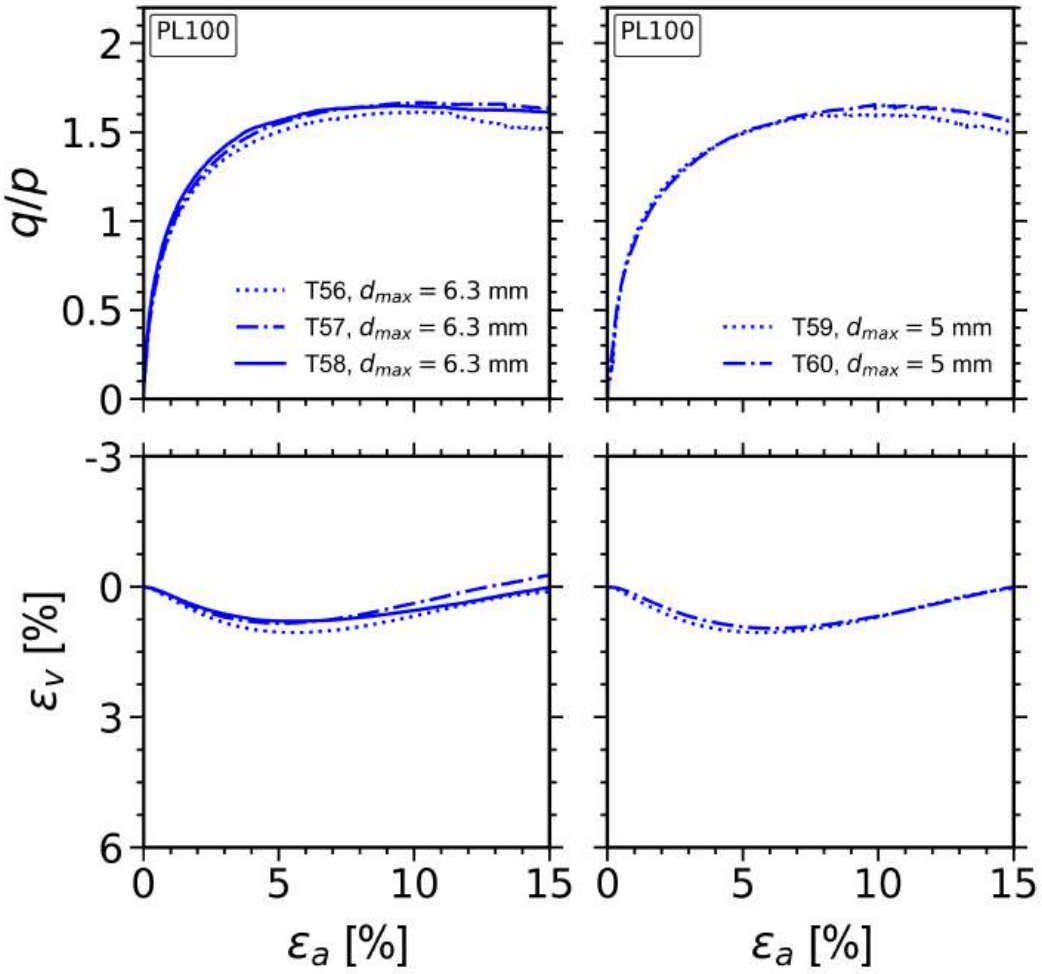

Figure 8.20 Stress-strain curves of PL100 (*continued*).

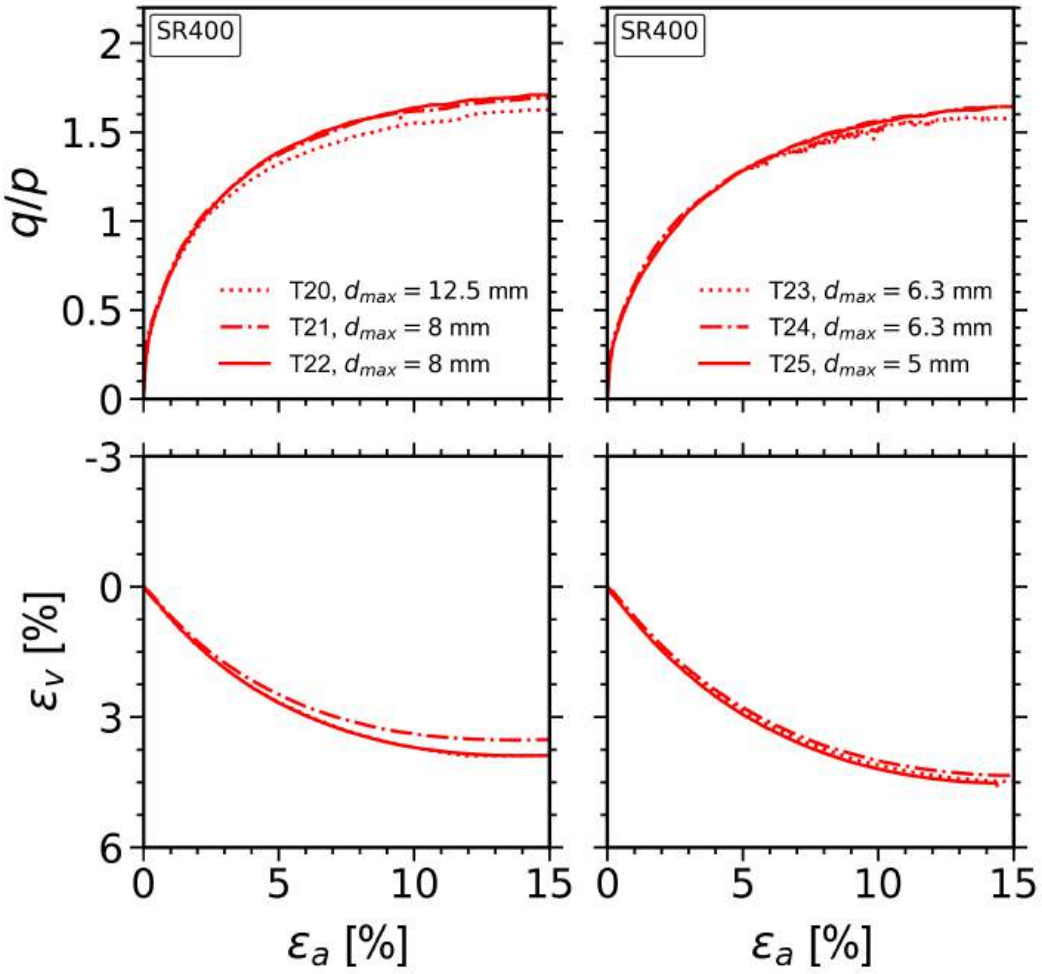

Figure 8.21 Stress-strain curves of scalped quarry rockfill specimens, tested at $\sigma'_3 = 400$ kPa using standard rough platens (SR400).

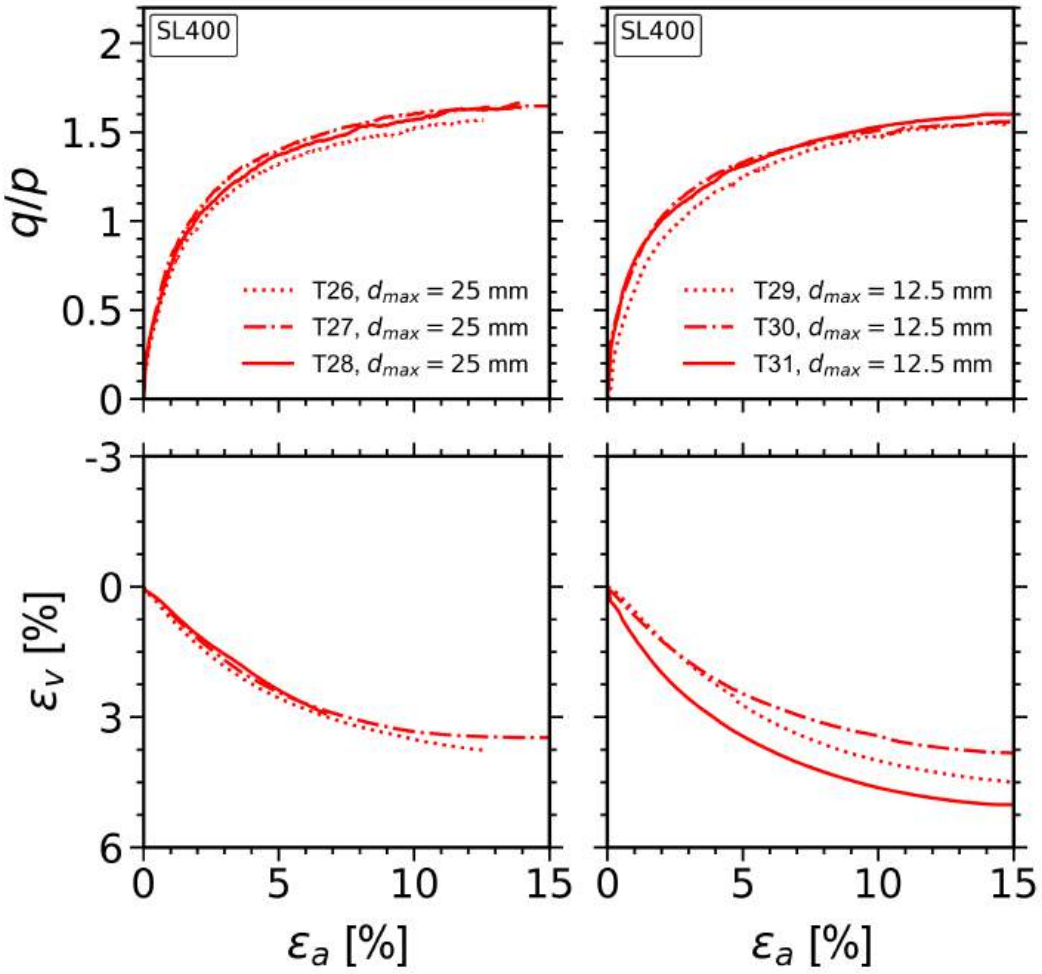

Figure 8.22 Stress-strain curves of scalped quarry rockfill specimens, tested at $\sigma'_3 = 400$ kPa using lubricated platens (SL400).

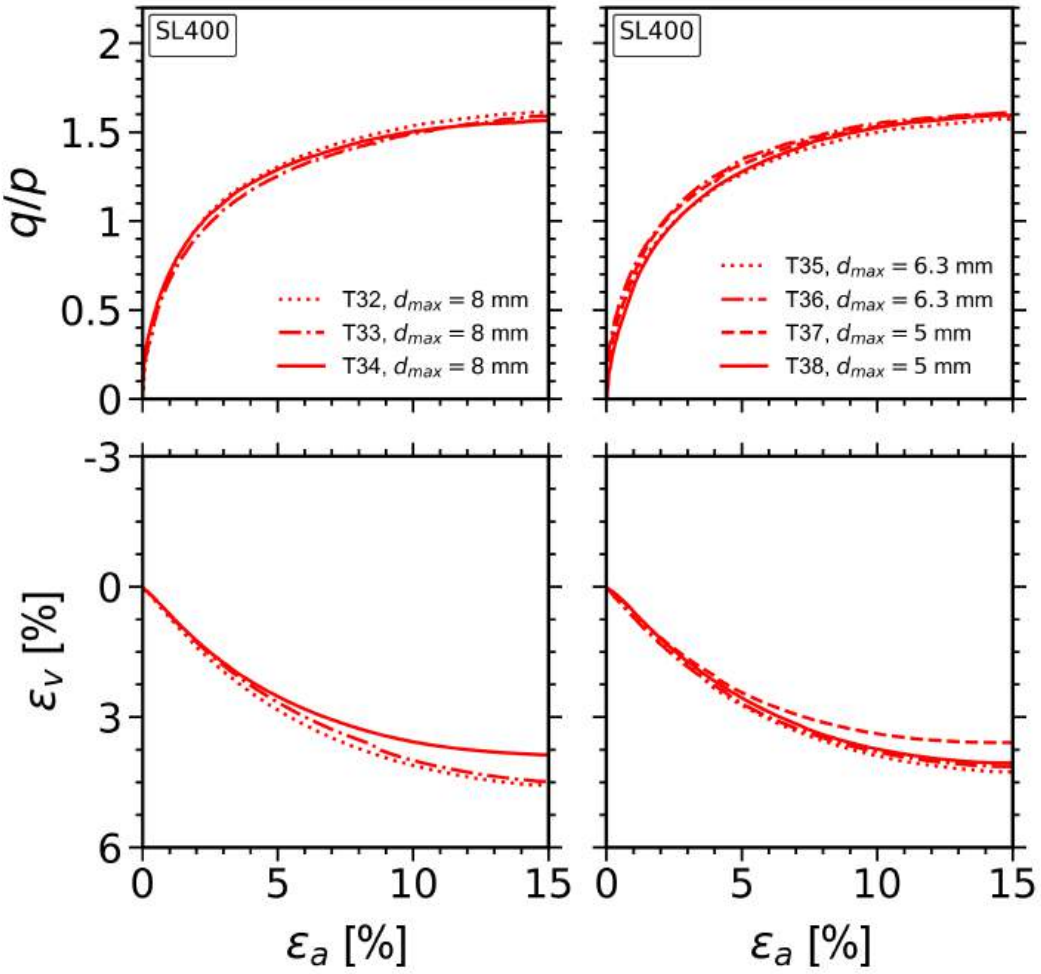

Figure 8.23 Stress-strain curves of SL400 (*continued*).

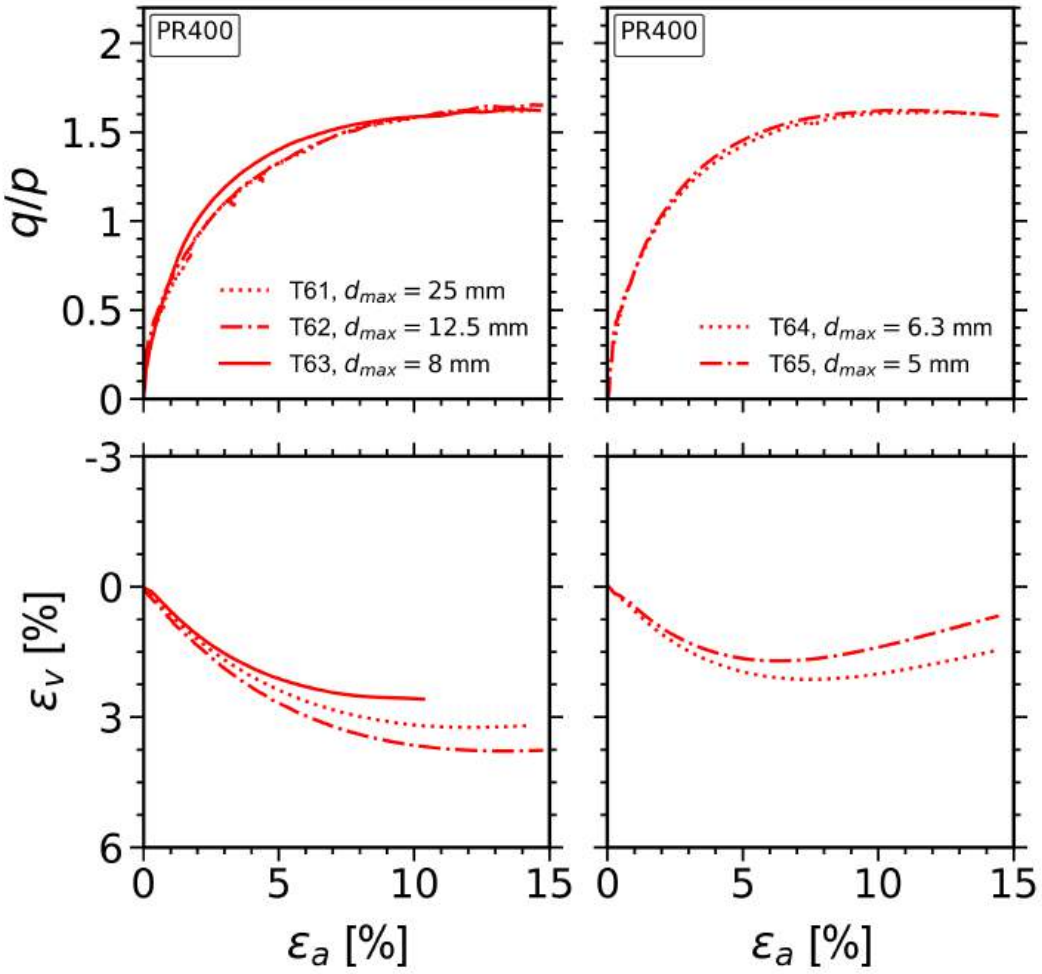

Figure 8.24 Stress-strain curves of parallel-graded quarry rockfill specimens, tested at σ'_3 = 400 kPa using standard rough platens (PR400).

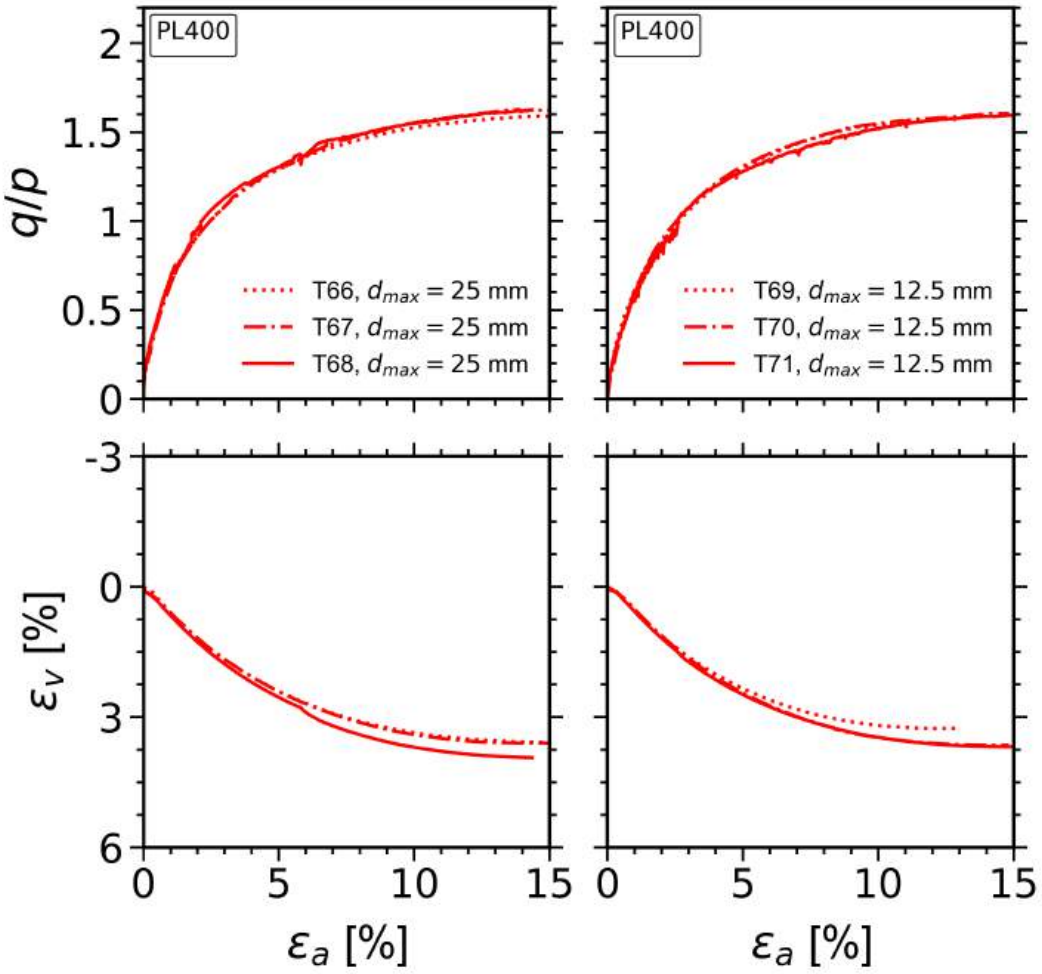

Figure 8.25 Stress-strain curves of parallel-graded quarry rockfill specimens, tested at σ'_3 = 400 kPa using lubricated platens (PL400).

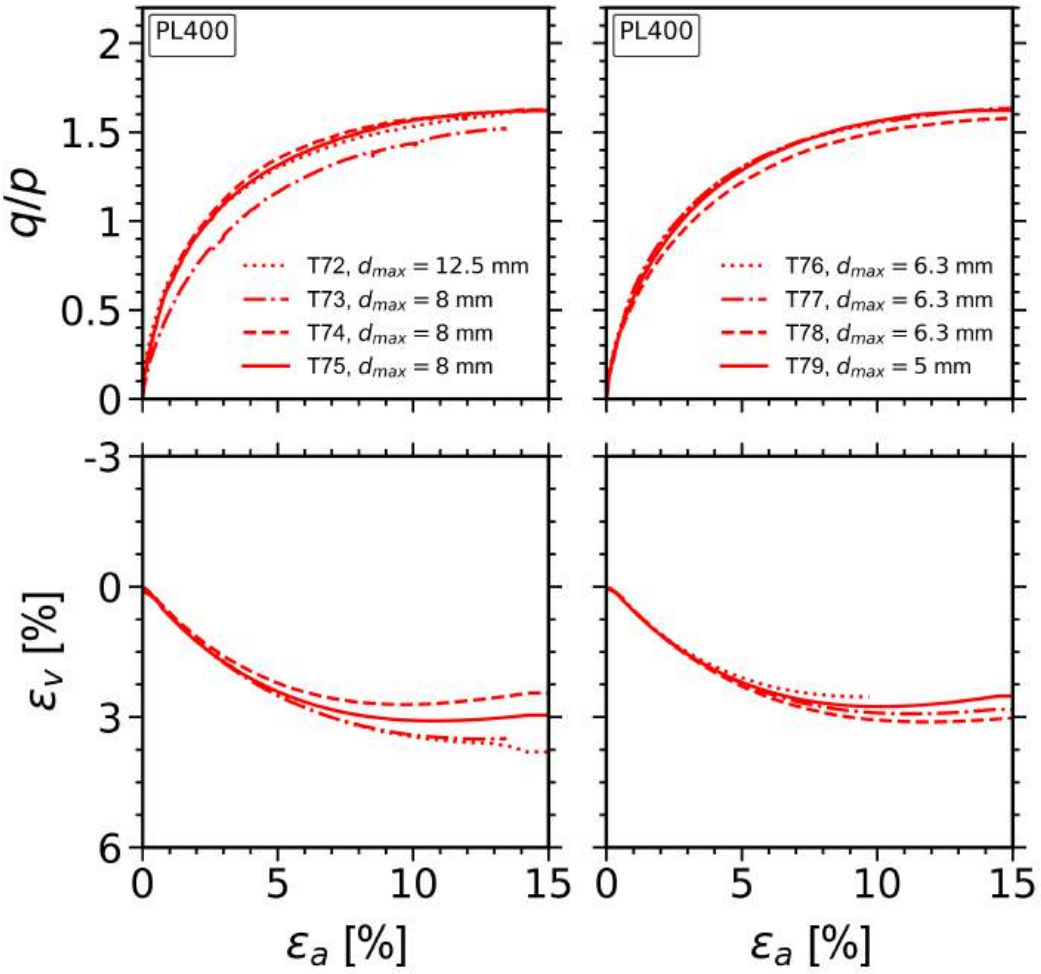

Figure 8.26 Stress-strain curves of PL400 (*continued*).